

Staircase structures in fluid dynamical systems



Paul Edward Pružina

The University of Leeds
School of Mathematics

Submitted in accordance with the requirements for the degree of
Doctor of Philosophy

November 2023

Declaration

The candidate confirms that the work submitted is their own, except where work which has formed part of jointly authored publications has been included. The contribution of the candidate and the other authors to this work has been explicitly indicated below. The candidate confirms that appropriate credit has been given within the thesis where reference has been made to the work of others.

Chapters 2 and 3 contain material from the jointly authored publication

- Pružina, P, Hughes, D.W. Pegler, S.S. (2022). Development and long-term evolution of density staircases in stirred stratified turbulence. *Physical Review Fluids* 7, 104801.

Chapters 5 and 7 contain material from the jointly authored publication

- Pružina, P, Hughes, D.W., Pegler, S.S. (2023). Salt fingering staircases and the three-component Phillips effect. *Journal of Fluid Mechanics* 968, A16.

The co-authors provided ideas and guidance surrounding this work and aided with the writing of these papers. All mathematical and scientific research contained in these works was undertaken by the candidate himself.

This copy has been supplied on the understanding that it is copyright material and that no quotation from the thesis may be published without proper acknowledgement.

The right of Paul Edward Pružina to be identified as Author of this work has been asserted by Paul Edward Pružina in accordance with the Copyright, Designs and Patents Act 1988.

Paul Edward Pružina
November 2023

Acknowledgements

I would first like to thank my supervisors David Hughes and Sam Pegler for all your support and guidance. Your knowledge and ideas have been a great help while working on this thesis, and your enthusiasm has made it an enjoyable few years. I would also like to thank my examiners Stephen Griffiths and Colm-cille Caulfield for stimulating discussion in my viva, and several useful comments that helped me think about my work from a different angle.

Working in the University of Leeds has been a great experience, and I found the department a very welcoming environment in my first months here. The regular seminars and talks have helped broaden my horizons, as well as providing a welcome break from other work in many post-lunchtime slumps.

I am also incredibly grateful to all my family and friends for all the good times I've had over the years. And especially to Helen, who has been by my side (at least figuratively) with love and support every step of the way.

This work was supported by the Natural Environment Research Council Panorama Doctoral Training Programme (Grant No. NE/S007458/1).

Abstract

Stratified turbulent fluids exhibit a wide variety of fascinating behaviours. One of the most interesting is the phenomenon of staircase formation, where the density field spontaneously evolves into a series of well-mixed layers separated by sharp interfaces with high gradients. Staircases appear in a wide range of contexts, from the geophysical examples of oceanic thermohaline staircases and atmospheric potential vorticity staircases, to the $\mathbf{E} \times \mathbf{B}$ staircase of plasma physics.

In this thesis we present models for staircases in stirred stratified convection and double diffusive convection. We derive a one-dimensional horizontally-averaged mixing-length model from the Boussinesq equations, which we apply first to layering in stirred stratified convection, and then to double-diffusive layering.

In stirred stratified convection, the model consists of equations for the buoyancy and kinetic energy, closed via a length scale parameterised in terms of the variables. We investigate the linear stability of the system, determining the effects of varying the viscous and molecular diffusivities. A novel choice of boundary conditions allows us to investigate the behaviour of numerical solutions to very late times. Staircase solutions undergo layer mergers, which we demonstrate occur on a logarithmic timescale, providing a link with other models of layering. We also present an experimental study to test predictions of the theory.

For double-diffusive convection, the model consists of three equations, for temperature, salinity and energy. We present a linear stability analysis for a general three-component flux-law system, which we apply to our specific model. A suitable parameterisation for the length scale allows the model to produce staircases in salt fingering convection without the need for any external forcing. In diffusive convection, some energy source is required for layering. Temperature and salinity fluxes through staircases increase during layer mergers, accounting for heightened fluxes in observed staircases in comparison with non-layered states.

Table of contents

List of figures	ix
List of tables	xviii
1 Introduction	1
1.1 Introduction	1
1.2 The Phillips effect	3
1.3 Double-diffusive convection	6
1.3.1 Suggested mechanisms for DDC layering	8
1.3.2 The Phillips effect in double-diffusive convection	11
1.4 Experimental studies of staircases	13
1.5 Outline of thesis	15
2 Formulation of a model for staircase formation	17
2.1 Introduction	17
2.2 Model formulation	18
3 Layering in stirred stratified convection	23
3.1 Introduction	23
3.2 Model formulation	27
3.3 Conditions for initial layer development	28
3.3.1 Uniform-gradient steady states	28
3.3.2 Stability and conditions for layering	30
3.3.3 Implications for typical values of Pe^{-1} and Re^{-1}	34
3.4 Long-term evolution of layered solutions	35
3.4.1 The effects of fixed-buoyancy boundary conditions on the long-term behaviour	37
3.4.2 Evolution to late times	41
3.5 Discussion	45
4 Experimental study of stirred stratified layering	48
4.1 Introduction	48
4.2 Experimental method	51

4.2.1	Double bucket method	51
4.2.2	Layer formation	53
4.3	Results	54
4.4	Discussion	56
5	The three-component Phillips effect	60
5.1	Introduction	60
5.2	A general three-component system	60
5.2.1	Instability at small wavenumbers	62
5.2.2	Instability at high wavenumbers	63
5.2.3	Condition for marginal stability	64
5.2.4	Conditions for layering	64
5.2.5	Comparison with Radko's γ -instability	64
5.3	Hyperdiffusion can regularise the high wavenumber instability	67
5.4	Discussion	68
6	Stirred double-diffusive layering	70
6.1	Introduction	70
6.2	A model for stirred double-diffusive layering	71
6.3	Uniform-gradient steady states	73
6.3.1	Steady-state solutions $g_0(e_0; G_0)$	74
6.3.2	Unstable regions for the three-component system	76
6.3.3	Why is there such a difference between SF and DC?	77
6.3.4	Suppressing the high wavenumber instability with hyperdiffusion	79
6.3.5	The effect of changing parameters	79
6.4	Numerical Solutions	83
6.4.1	Numerical method to include hyperdiffusion	83
6.5	Numerical solutions in the salt fingering regime	85
6.6	Numerical solutions in the diffusive convection regime	88
6.6.1	Solution with high wavenumber instability	88
6.6.2	Solution with Phillips instability	89
6.7	Discussion	91
7	Thermohaline staircases: Salt fingering	92
7.1	Introduction	92
7.2	A three-component model for thermohaline staircases	93
7.3	Steady states and their stability	96
7.3.1	Steady states	98
7.3.2	Linear stability	99
7.4	Nonlinear evolution and long-term merger behaviour	102
7.4.1	Nonlinear evolution	103

7.4.2	Merger dynamics	103
7.4.3	Increase of the buoyancy flux	107
7.4.4	Variation of parameter values	108
7.5	Discussion	110
8	Thermohaline staircases: Diffusive convection	112
8.1	Introduction	112
8.2	Model for DC layering incorporating an energy source	113
8.3	Steady states and their stability	114
8.3.1	Uniform gradient steady states	114
8.3.2	Stability	115
8.4	Nonlinear evolution	117
8.4.1	Profile of the layers and interfaces	118
8.5	Difference in behaviour between salt fingering and diffusive convection .	123
8.6	Discussion	124
9	Conclusions	128
	Bibliography	132

List of figures

1.1	Global distribution of the occurrence of thermohaline staircases, coloured by number of steps, in the salt finger regime (red dots) and diffusive convection regime (blue dots). Taken from van der Boog <i>et al.</i> (2021). . . .	2
1.2	The solid lines show the flux-gradient relations used by Posmentier (black) and BLY (red). The black dashed line shows the minimum value $g = g_c$ for which Posmentier's flux satisfies the instability condition (1.2). The red dashed lines show the boundaries of the finite region in which the flux in the BLY model satisfies condition (1.5).	4
1.3	Stability boundaries resulting from the classical stability analysis. The boundary for direct instabilities given by (1.7) is labelled SF; the boundary for oscillatory instabilities given by (1.8) is shown by the line labelled DC. Unstable modes exist above and to the left of these two lines. After Turner (1973).	6
1.4	Observational data from (a) Schmitt <i>et al.</i> (1987), showing the temperature profile in a section of the western tropical North Atlantic, from the C-SALT programme; and (b) Timmermans <i>et al.</i> (2008), showing temperature and conductivity profiles (from which salinity can be deduced) in the Arctic, from the pan-Arctic Beringia 2005 Expedition.	9
1.5	Numerical simulations from Stellmach <i>et al.</i> (2011), showing (a)–(c) snapshots in three different phases of the evolution. The system first evolves into salt fingers, which become unstable to large scale gravity waves that saturate at finite amplitude. Eventually convective layers form, separated by thin interfaces. The top panels show the temperature perturbation on the data-cube faces, with the lower ones showing the internal structure. (d) Time series of the Nusselt number $Nu = 1 - f$ and flux ratio $\gamma = f/c$, where f and c are the temperature and salinity fluxes respectively.	10

- 1.6 Shadowgraph images from Park *et al.* (1994), showing the evolution of a staircase in a salt-stratified fluid stirred with a rod. Layers can be seen as darker regions, separated by bright interfaces. The two lowermost interfaces in (a)-(c) gradually move closer together, and have merged to form a single interface in (d). The black strip at the side of each image is the stirring rod. 14
- 3.1 Reproduction of numerical results using the BLY model (3.1)–(3.2), showing the initial development of the layered state, layer mergers, and expansion of the edge regions. The plots show the spatial profile of the dimensionless buoyancy gradient $g(z,t) = b_z(z,t)$ across the depth of the layer at regular time intervals. The scale bar at the top of the panel indicates the magnitude of g . Panel (a) reproduces the simulation of Fig. 6 of BLY, while panel (b) shows the continued long-term evolution to $t = 10^6$. The edge regions expand at a rate $\propto t^{1/2}$ into the interior, eventually destroying the entire layered region and filling the domain. In both panels, the solution at $t = 2 \times 10^4$ is shown in red; this denotes the first time at which consistent layers exist across the entire interior region. 24
- 3.2 Steady-state energy e_0 (solutions to (3.16)) as a function of buoyancy gradient g_0 . In (a), $r = 50$ is fixed and Pe^{-1} varies; in (b), $\text{Pe}^{-1} = 0.1$ is fixed and r varies. 29
- 3.3 (a) Flux-gradient relations for a selection of values of Pe^{-1} , for $r = 50$, calculated by substituting the steady-state energy e_0 (found as exact solutions of (3.16)) into the buoyancy flux $f(g,e)$ given by (3.19). The N-shaped curve required for the layering instability is displayed by the smaller values of Pe^{-1} . (b) Loci of $F'(g_0;r) = 0$, for a range of Pe^{-1} (constant on each curve). For each value of r , the gradients g_0 inside the curve are unstable. 31
- 3.4 Growth rate plotted as a function of wavenumber, for $r = 50$ and $g_0 = 0.0218$. In (a), $\text{Re}^{-1} = 0$ is fixed and Pe^{-1} varies; in (b), $\text{Pe}^{-1} = 0$ is fixed and Re^{-1} varies. Since the parameters are linked by $\text{Pe} = \text{PrRe}$, (a) corresponds to the limit of $\text{Pr} = 0$, and (b) to $\text{Pr} \rightarrow \infty$. The dashed black curve represents the diffusionless system. The lower set of curves represents the damped energy mode. 33
- 3.5 Growth rate plotted as a function of wavenumber, for (a) temperature- and (b) salt-stratified fluids, for $r = 50$, $g_i = 0.0218$, with three different choices of Re^{-1} and a range of values of Prandtl and Schmidt numbers. The values of Pr and Sc are chosen to be representative of water under common terrestrial conditions, as seen in Table 3.1. For comparison with Fig. 3.4, note that in (a), $\text{Pe}^{-1} = (\text{PrRe})^{-1}$, and in (b), $\text{Pe}^{-1} = (\text{ScRe})^{-1}$. 36

- 3.6 Time evolution of the buoyancy gradient $g(z, t) = b_z(z, t)$, resulting from solution of the system (3.12)–(3.14) for fixed-buoyancy boundary conditions (3.26), and initial conditions (3.30)–(3.31), with $n = 45$, background buoyancy gradient $g_0 = 0.0218$, dissipation parameter $r = 50$, and domain thickness $H = 2000$. Zero-energy-flux boundary conditions (3.27) are adopted in (a) and (b); fixed energy conditions (3.28) are adopted in (c) and (d). The scale bar at the top left of each panel indicates the magnitude of the gradient $g(z, t)$ 40
- 3.7 Long-time evolution of the buoyancy gradient $g(z, t)$, resulting from solution of the system (3.12)–(3.14) with diffusion included; in the basic state $g_0 = 0.0218$. Panel (a) shows a typical temperature-stratified case with $Pe^{-1} = 0.01$, $Re^{-1} = 0.1$, and $n = 40$ initial interfaces; (b) a typical salt-stratified case with $Pe^{-1} = 0.0001$, $Re^{-1} = 0.1$, $n = 43$; (c) $Pe^{-1} = 0.001$, $Re^{-1} = 1$, $n = 24$; (d) $Pe^{-1} = 0.1$, $Re^{-1} = 1$, $n = 6$. In each case, the dissipation parameter $r = 50$. The scale bar at the top left of each panel indicates the magnitude of the gradient $g(z, t)$ 42
- 3.8 Plots showing variation in the interfaces over time, obtained using a numerical peak finder to count peaks in the buoyancy gradient b_z . Panel (a) shows the maximum gradient at each time, corresponding to the gradient at the centre of the sharpest interface. Panel (b) shows the number of interfaces at each time, plotted against the natural logarithm $\log(t)$. The dashed lines show the best fits to relation (3.32). Parameters used for each curve are reported in Table 3.3. 46
- 4.1 Diagram summarising experimental runs of Park *et al.* (1994) and Zatssepín *et al.* (1999) in Re – Ri plane: \times - layers (L), $+$ - no layers (N) (Park *et al.*, 1994), \square - (L), \circ - (N) (Zatssepín *et al.*, 1999). The dashed vertical line approximately separates runs with turbulence (to the left) from those without (to the right). The solid line separates runs with (above) and without layers (below). (Taken from Zatssepín *et al.*, 1999) 50
- 4.2 Stability boundary in Re – Ri space for the stirred stratified system considered in Chapter 3, with dissipation parameter $r = 50$. For each value of Re , there are upper and lower values of Ri_c , between which the system is unstable to layering. Dashed lines show $Ri = 0.0142$ and $Ri = 0.0360$, the asymptotic limits of Ri_c as $Re \rightarrow \infty$ 51
- 4.3 Diagram showing double bucket setup for filling the cylindrical experimental tank. 52
- 4.4 Diagram showing the rotating table setup. A metal rod of diameter d is suspended in the fluid at radius R_s , and the rotating table is turned on, thus stirring the fluid. 52

- 4.5 Shadowgraph images of a single experiment run at several different times, rotating at different rates. (a) Initial speed $U = 0.035\text{ms}^{-1}$ with mostly non-turbulent fluid. (b)–(d) Progressively higher rotation rates $U = 0.052, 0.071, 0.091\text{ms}^{-1}$. A large amount of turbulent fluid is visible, but no layers form. (e)–(f) Images taken 4, 12, 18 and 50 minutes after increase in rotation rate to $U = 0.12\text{ms}^{-1}$. An interface is visible as a long-lasting bright band in the lower part of the images. The stirring rod is visible as a dark stripe on the left hand-side of each image. The bright horizontal bands visible in every image are not interfaces, but are likely due to refraction in the tank. 55
- 4.6 Results of thirteen experimental runs, varying background buoyancy gradient b_z (s^{-2}) and characteristic speed U (ms^{-1}). For each run, b_z was fixed, and U gradually increased. Blue crosses represent points where layers formed, red plus signs represent conditions where no layers were evident. Scatter plot on (a) b_z – U axes, (b) Ri – Re axes.) 56
- 5.1 (a) Sketch of a region of instability in g_0 – d_0 space, shaded pink. The locus of marginal stability is shown in black. The blue line shows an arbitrary cross-section through the unstable region. Panel (b) shows the value of $F_g C_d - F_d C_g$ along the blue path — it is negative only in the finite region between the two points shown in red, giving a finite region only where condition (5.17a) is satisfied 65
- 6.1 Steady-state energies for constant G_0 , found using the expression for $g_0(e_0)$ given in (6.24). For this plot, $\text{Pt}^{-1} = 0.01$, $\text{Ps}^{-1} = 0.0001$ and $\varepsilon = 0.02$. (a) shows small values of G_0 , where e_0 is multivalued for some negative values of g_0 ; (b) shows the behaviour of the solutions in (a) for small e_0 ; (c) shows larger values of G_0 , where e_0 is always single-valued; (d) shows a selection of very small values of g_0 , near the point where they all take a similar value, and shows that the maximum G_0 for which there are values of g_0 with multiple solutions is 0.012. 75
- 6.2 Loci of marginal stability in g_0 – G_0 space, for parameter values $\text{Pt}^{-1} = 0.01$, $\text{Ps}^{-1} = 0.0001$ and $\varepsilon = 0.02$. Found by solving simultaneously (6.24) with the conditions for marginal stability $F_g C_d - F_d C_g = 0$, $p_e = 0$, $f_g c_d - f_d c_g = 0$ and $F_g + C_d = 0$ 76
- 6.3 Wavenumber-growth rate plots for the three-component system, demonstrating different types of instability, for parameter values $\text{Pt}^{-1} = 0.01$, $\text{Ps}^{-1} = 0.0001$, $\varepsilon = 0.02$ and $\text{Re}^{-1} = 0$. (a) $F_g C_d - F_d C_g < 0$; (b) $F_g C_d - F_d C_g < 0$ and $F_g + C_d < 0$; (c) $f_g c_d - f_d c_g < 0$. Panels (d)–(f) correspond to three different energies for the same values of g and d ; (d) and (f) show stable modes; (e) shows the energy mode instability $-p_e < 0$ 78

- 6.4 Wavenumber-growth rate plots for $(g_0, d_0, e_0) = (-0.6, -0.63, 0.0022)$, for a range of values of A and parameter values $Pt^{-1} = 0.01$, $Ps^{-1} = 0.0001$, $\varepsilon = 0.02$ and $Re^{-1} = 0$. For perturbations to this steady state, increasing A beyond 10^{-4} is sufficient to suppress the high wavenumber instability for all wavenumbers. 80
- 6.5 Comparison of instability conditions (as shown in Fig. 6.2) for a range of values of τ , taking $Pt^{-1} = 0.01$ in panels (a)–(d), and $Ps^{-1} = 0.01$ in panels (e) and (f). $Re^{-1} = 0$ and $\varepsilon = 0.02$. Increasing τ ‘flattens’ the profile of the region, until $g - d$ does not vary with g when $\tau = 1$. Note that the plots in (e) and (f) are reflections of those in (c) and (b) respectively. 81
- 6.6 Comparison of wavenumber-growth rate plots for a range of values of τ , taking $Pt^{-1} = 0.01$, $Re^{-1} = 0$ and $\varepsilon = 0.02$. Each plot is for the same point $(g_0, d_0) = (0.1, 0.075)$, roughly in the centre of the SF unstable region. Increasing τ increases both the range of unstable wavenumbers and the maximum growth rate 82
- 6.7 Comparison of instability conditions for a range of values of Pt^{-1} , taking $\tau = 0.01$, $Re^{-1} = 0$ and $\varepsilon = 0.02$. Increasing Pt^{-1} shrinks the size of the unstable region (of both regimes) in g_0 – G_0 space. 82
- 6.8 Long-term evolution of the buoyancy gradient $b_z(z, t)$ in solutions of the three-component stirred system (6.13)–(6.15) with length scale (6.16), for parameter values $Pt^{-1} = 0.01$, $Ps^{-1} = 0.0001$, $\varepsilon = 0.02$ and $Re^{-1} = 0$. (a) Background state $(g_0, d_0, e_0) = (0, 1, 0, 0.075, 0, 11)$ and an $n = 33$ sinusoidal perturbation, near the centre of the SF unstable region; (b) $(g_0, d_0, e_0) = (0.005, -0.03, -0.043)$ and $n = 22$, with both temperature and salinity gradients stable; (c) $(g_0, d_0, e_0) = (0.23, 0.205, 0.17)$ and $n = 6$, near the right-hand boundary of the unstable region seen in Fig. 6.2. All three panels share a common time axis. 87
- 6.9 Profiles of the temperature and salinity gradients in solutions to the three-component stirred system (6.13)–(6.15), at time $t = 10^7$, normalised by their background gradients. Each panel contains a snapshot at $t = 10^7$ of the solution with background gradients $(g_0, d_0) = (0.1, 0.075)$, with (a) $e_0 = 0.11$, $\tau = 0$; (b) $e_0 = 0.11$, $\tau = 0.01$; and (c) $e_0 = 0.095$, $\tau = 0.5$. Temperature and salinity fields track each other closely, with the normalised gradients being identical in all three cases. 88

- 6.10 Solutions to (6.32)–(6.36) in the DC regime, with background steady state $(g_0, d_0, e_0 = -0.6, -0.63, 0.0022)$ and parameter values $Pt^{-1} = 0.01$, $Ps^{-1} = 0.0001$, $\varepsilon = 0.02$ and $Re^{-1} = 0$. In this background state, a high wavenumber instability is expected. (a) Solution at time $t = 100$ for the system solved without hyperdiffusion terms to counter the HWI (i.e. $A = 0$). (b) Solution at time $t = 100$ for hyperdiffusion coefficient $A = 0.01$. The initial condition is shown in red for comparison. 89
- 6.11 Solutions to (6.32)–(6.36) in the DC regime, with background steady state $(g_0, d_0, e_0 = -0.1, -0.13, 0.032)$ and parameter values $Pt^{-1} = 0.01$, $Ps^{-1} = 0.0001$, $\varepsilon = 0.02$ and $Re^{-1} = 0$. In this background state, the Phillips instability is predicted by the linear stability analysis. (a) Solution at time $t = 10000$ for the system solved without hyperdiffusion terms (i.e. $A = 0$). Interfaces sharpen to the scale of the spatial mesh owing to the effect of the HWI. (b) Solution at time $t = 10000$ for hyperdiffusion coefficient $A = 0.01$. The hyperdiffusion regularises the sharpening, producing well-resolved layers. Note the plots show only a portion of the depth, to demonstrate most clearly the resolution of the interfaces. (c) Comparison of temperature and salinity gradients, normalised by their background gradients $T_z / -0.1$ and $S_z / 0.13$, at time 10000, for the case with hyperdiffusion. 90
- 7.1 Steady-state solutions to (7.25) with $\tau = 0.01$, $\sigma = 10$. (a) Energy e_0 and corresponding value of the length scale l_0 given by (7.18), as functions of R_0 for $\varepsilon = 1$, $\delta = 0.001$. For small R_0 , e_0 and l_0 are large; as R_0 increases, e_0 decreases, with l_0 initially decreasing but $l_0 \rightarrow \infty$ as $e_0 \rightarrow 0$. Inset plot shows behaviour of e_0 and l_0 near $R_0 = 1$, with red and blue dotted lines showing the values $e_0 = \sigma / \varepsilon - 1 = 9$ and $l_0 = \sqrt{\sigma / \varepsilon - 1} = 3$. (b) e_0 as a function of R_0 , for a range of values of δ with $\varepsilon = 1$ fixed. (c) e_0 as a function of R_0 , for a range of values of ε with $\delta = 0.001$ fixed. Sufficiently small values of δ and large values of ε lead to $e_0(R_0)$ being multi-valued. 97
- 7.2 (a) Various stability measures of the uniform steady state as R_0 varies, with $\tau = 0.01$, $\sigma = 10$, $\varepsilon = 1$, $\delta = 0.001$. The quantity $-p_e$ is shown in red, $F_g C_d - F_d C_g$ in black, $F_g + C_d$ in yellow, and $f_g c_d - f_d c_g$ in purple. The red circles mark the minimum and maximum values of R_0 for which condition (5.17) is satisfied. (b) The growth rate s against wavenumber m for the steady state with $R_0 = 1.8$ (marked with a dotted black line in (a)). There is a single unstable mode with maximum growth rate $s = 4.6 \times 10^{-4}$ at wavenumber $m = 0.363$ 100

- 7.3 Effect on the layering instability of changing (a) the diffusivity ratio τ , and (b) the Prandtl number σ . Black lines show the boundary of the unstable range of R_0 , as (a) τ is changed with fixed $\sigma = 10$, and (b) σ is changed for fixed $\tau = 0.01$. In each case, changing the value of the other parameter leads to no qualitative differences. The other model parameter values are $\delta = 0.001$ and $\varepsilon = 1$; for these choices of δ and ε , there is no energy mode instability. The dashed line in (b) shows $R_0 = 1$, the lower boundary of the salt fingering regime. 102
- 7.4 Nonlinear evolution of the system (7.15)–(7.17), with length scale (7.18), subject to boundary conditions (7.27)–(7.29) and initial conditions (7.30)–(7.32), for parameter values $\tau = 0.01$, $\sigma = 10$, $\delta = 0.001$, $\varepsilon = 1$, $R_0 = 1.8$. (a) Depth profiles of the overall buoyancy field $b = T - S$ at a range of times logarithmically distributed between $t = 10^4$ and $t = 10^7$; (b) profiles of the buoyancy gradient $b_z = T_z - S_z$ scaled by the range of its values at each time, plotted at the same times as in (a); (c) range of gradients, i.e. $\max(b_z) - \min(b_z)$. The solution evolves from the initial condition into a dense stack of layers (seen as the first solution presented in (b)). At $t \approx 6 \times 10^5$, the layers begin to undergo mergers, which cause the maximum gradient to increase, until by $t \approx 2 \times 10^6$, only a single interface remains at $z \approx 350$, with $b_z \approx 120$ 104
- 7.5 (a) Potential $U(e)$ found by integrating (7.41) with respect to D , and coupling with (7.42) to find corresponding values of e . The red line has two peaks at e_1 and e_2 , where $U(e_1) = U(e_2)$. Parameter values are $f_0 = 0.45$, $\tau = 0.01$, $\sigma = 10$, $\varepsilon = 1$ and $\delta = 0.001$. (b) Plot of the ratio λ_B/λ_H calculated in the small-gradient case given by equation (7.43), for the solutions presented in Fig 7.4. The dotted line marks $\lambda_B/\lambda_H = 1$: above this line, the B-merger dominates; below it, the H-merger dominates. 106
- 7.6 Evolution of the buoyancy flux field for the solution shown in Fig. 7.4(a). The black dashed line shows the vertical mean of the upward buoyancy flux ($c - f$) defined by (7.44), plotted against time on the lower horizontal axis. The spatial profile of the buoyancy flux (with z on the upper horizontal axis) is also shown at a range of times, with the corresponding mean flux at each time marked with a dot of the same colour. 108

- 7.7 Evolution of solutions to (7.15)–(7.17) with length scale (7.18), subject to boundary conditions (7.27)–(7.29) and initial conditions (7.30)–(7.32). (a) Very high Prandtl number case, with $\tau = 0.0001$, $\sigma = 10^4$, $\delta = 0.001$, $\varepsilon = 1$ and $R_0 = 3.64$, showing wide, smooth interfaces and layers. (b) No overall background buoyancy gradient, with $\tau = 0.01$, $\sigma = 1$, $\delta = 0.01$, $\varepsilon = 1$, $R_0 = 1$, in which the timescale for mergers is similar to that for layer growth. Layers merge quickly, eventually giving way to a single convective state across the entire domain. 109
- 8.1 (a) Steady-state solutions $e_0(R_0)$ to the DC steady-state equation (8.5), for a range of values of the constant power source W . Other parameter values are $\tau = 0.01$, $\sigma = 10$, $\varepsilon = 1$ and $\delta = 0.001$. The black dotted line shows the boundary of the DC region $R_0 < 1$. (b) Values of $l_0(R_0)$, corresponding to each line shown in (a). 116
- 8.2 (a) Stability conditions for the state $(g_0, d_0, e_0) = (-1, -1/R_0, e_0(R_0))$, for parameters $\tau = 0.01$, $\sigma = 10$, $\varepsilon = 1$, $\delta = 0.001$ and $W = 1$. Condition (5.17a) is satisfied for values of R_0 between the red dots. (b) Growth rate of perturbations to the steady state with $R_0 = 0.9$. There is a single unstable mode, with maximally unstable wavenumber $m = 0.222$ 117
- 8.3 Nonlinear evolution of the system (8.1)–(8.3), with length scale (8.4), subject to boundary conditions (7.27)–(7.29) and initial conditions (7.30)–(7.32), for parameter values $R_0 = 0.9$, $\tau = 0.01$, $\sigma = 10$, $\varepsilon = 1$, $\delta = 0.001$ and $W = 1$. (a) Overall buoyancy field $b = T - S$; (b) buoyancy gradient $b_z = T_z - S_z$ scaled by the range of its values at each time; (c) range of gradients, i.e. $\max(b_z) - \min(b_z)$. The time axes of all panels are aligned. Profiles in (a) and (b) are shown corresponding to the time at which they intersect the time axis. The solution evolves from the initial condition into a dense stack of layers (seen as the first solution presented in (b)). At $t \approx 10^6$, the layers begin to undergo mergers, which cause the maximum gradient to increase, until by $t \approx 10^{13}$ two interfaces remain on the edges of the domain. Interfaces are characterised by two spikes of equal magnitude in the buoyancy gradient b_z , with a lower gradient region in between. 119
- 8.4 Snapshot of the solution from Fig. 8.3, showing (a) the density ratio R and length scale l ; (b) T , S and b ; and (c) T_z , S_z and b_z at $t = 10^8$. The b and b_z fields have been normalised to have the same scale as S and S_z . The box outlined in blue in (c) shows a larger scale view of the range $630 \leq z \leq 660$. 120
- 8.5 Snapshots of solutions to (8.1)–(8.3) at time $t = 10^{10}$, for (a) $R_0 = 0.8$ and (b,c) $R_0 = 0.6$. T_z , S_z and b_z are plotted, with the buoyancy gradient fields been normalised to have the same scale salinity gradient. (b) and (c) show the same solution, with (c) giving a close-up view of the profile of a single interface. 121

-
- 8.6 Regions of Ra – Rs space unstable to the layering instability (5.17*a*), with parameter values $\tau = 0.01$, $\sigma = 10$, $\varepsilon = 1$, $\delta = 0.001$ in (a) the unforced SF system (7.15)–(7.17), and (b) the forced DC system (8.1)–(8.3) with $W = 1$. Dashed lines show $g_0 = d_0$; above these lines the fluid is statically unstable. 123

List of tables

3.1	Prandtl and Schmidt numbers of water at various temperatures (in degrees Celsius) and salinities (in parts per thousand). The values of Pr are taken from Nayar <i>et al.</i> (2016); Sharqawy <i>et al.</i> (2010) and those of Sc from Ramsing & Gunderson (2020).	35
3.2	Predicted dimensionless wavenumbers of the mode of maximum growth rate m_{\max} , and the corresponding dimensionless growth rates, for characteristic values of Pr , Sc and Re^{-1} , with $r = 50$, $g_0 = 0.0218$. For $Pr \lesssim 1$, there is little difference from the $Pr = 0$ case. Plots of wavenumber versus growth rate are shown for selected parameter choices in Fig. 3.5.	37
3.3	Parameter values for the plots in Fig. 3.8, and corresponding values of α and β for the trend law (3.32).	46

Chapter 1

Introduction

1.1 Introduction

The dynamics of stratified turbulent flows presents a rich variety of behaviour. One of the most striking examples is the spontaneous development of density staircases: given an initially uniform density gradient, stirring the fluid can lead to the formation of well-mixed layers, in which the density is nearly constant, separated by sharp interfaces with strong density gradients. The interfaces are narrow, but the density field across them is smooth, with a well-defined finite thickness. Experimental work has produced such layered structures by dragging a rod or grid back and forth through an initially stable gradient of salt concentration (Linden, 1979; Ruddick *et al.*, 1989; Park *et al.*, 1994).

One of the most fascinating aspects of staircase formation is its appearance in a number of ostensibly different areas of physics. One of the most important geophysical examples is oceanic thermohaline staircases, with well-documented layered structures observed in temperature and salinity measurements over large areas of the oceans (e.g. Tait & Howe, 1968; Timmermans *et al.*, 2008). As a specific example, the Caribbean Sheets and Layers Transects (C-SALT) programme (Schmitt *et al.*, 1987) found a system of about 10 well-mixed layers 5-30m thick, existing on a lateral scale of 200–400km. The survey ran for a continuous eight-month period, with the staircase remaining essentially unchanged throughout this time. These layered structures appear in areas of ocean with competing temperature and salinity gradients, i.e. where the contribution to the density gradient from temperature acts to stabilise the fluid, whereas that from salinity is destabilising, or vice versa. In such regions, a phenomenon called ‘double-diffusive convection’ (DDC) can occur, where an instability stems from the difference in the rates of thermal and saline diffusion. Soon after the discovery of thermohaline staircases, a link was made with DDC, with Turner (1967) suggesting that layers could form due to a double-diffusive process. A more detailed introduction to DDC is given in Sec. 1.3. Thermohaline staircases are found across incredibly large areas of the Earth’s oceans; Fig. 1.1 shows the distribution of staircases across the world, with colour intensity corresponding to number of steps. The area of the C-SALT study can be seen around 10°N, 50°W. Other notable areas include a

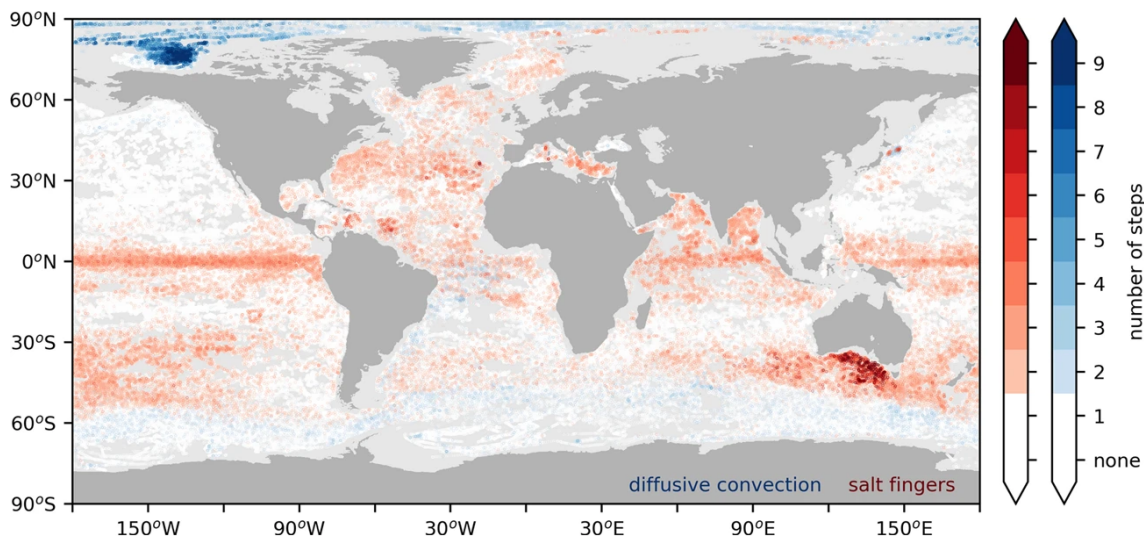


Fig. 1.1 Global distribution of the occurrence of thermohaline staircases, coloured by number of steps, in the salt finger regime (red dots) and diffusive convection regime (blue dots). Taken from van der Boog *et al.* (2021).

large region of staircases south of Australia (40°S , 130°E), and another significant area in the Canada Basin (75°N , 140°W). In astrophysics, similar double-diffusive staircase structures may be found in the interiors of stars and giant planets, where instead of salt, the solutal gradient is provided by heavy elements dissolved in a mixture of hydrogen and helium (e.g. Garaud, 2018).

In an atmospheric context, rotating stratified flow can give rise to a potential vorticity (PV) staircase, where wide regions with small PV gradients are separated by strong zonal jets where the PV gradient is high (e.g. Dritschel & McIntyre, 2008). These strong jets can be observed most clearly in the atmosphere of Jupiter, leading to a characteristic pattern of stripes (e.g. Marcus, 1993). Closer to home, PV layers have been observed in the terrestrial stratosphere (e.g. Haynes & Shuckburgh, 2000), and can be produced in laboratory experiments (e.g. Sommeria *et al.*, 1989). The jets in PV staircases act as barriers to eddy transport, and so they are important in understanding the exchange of atmospheric chemicals, as well as being an important problem for our understanding of atmospheric dynamics.

In hot magnetised plasmas, turbulence can generate permeable localised transport barriers that globally organise into the so-called ' $\mathbf{E} \times \mathbf{B}$ staircase'. This was first established in the results of gyro-kinetic simulations (Dif-Pradalier *et al.*, 2010). Staircases were later found experimentally in the Tore Supra tokamak (Dif-Pradalier *et al.*, 2015). With layers in the $\mathbf{E} \times \mathbf{B}$ staircase acting as barriers to heat and momentum transport, understanding its dynamics may be key to plasma confinement — a vital problem to solve to make nuclear fusion viable.

That staircases should form in a turbulent fluid may be surprising, with fine structure being generated from coarser initial conditions. Understanding how layers can form, and how they evolve over time, is clearly therefore a problem of considerable scientific

interest. With such a range of physical systems displaying staircase structures, it is still unclear whether the same process causes layering in every case, and if it is possible to produce a unified model for layering in all its physical contexts. This would be a significant breakthrough in our understanding of several areas of physics, allowing predictions to be made for one system on the basis of observations from completely different fields.

Furthermore, layered systems exhibit very different transport properties to those of familiar weakly inhomogeneous systems, with significantly larger turbulent fluxes through a system that has evolved into staircases compared with the flux through more homogeneous systems (see, for example Stellmach *et al.*, 2011; Rosenblum *et al.*, 2011; Hughes & Brummell, 2021). Thus, understanding the physics of layering is also crucial to developing an accurate description of transport in oceanographic and atmospheric flows, in stellar interiors and in magnetically-confined plasmas. The parameterisation of transport through oceans and atmospheres is a key component of climate and weather modelling. Given how common staircases are in the Earth's oceans, a fuller understanding of layering could play a large role in informing better climate models in the future.

In this thesis we investigate staircases in geophysical systems, taking a mostly theoretical approach. We present horizontally-averaged, one-dimensional models for layering in stirred stratified flow with a single component of density, and in double-diffusive convection. Our models encapsulate the so-called 'Phillips effect' (Phillips, 1972), in which layering results from a specific dependence of the turbulent density flux on the density gradient. We investigate both the initial generation of staircases, and their evolution to late times. While we are primarily motivated by oceanic examples, the following work is equally applicable to astrophysical thermocompositional staircases, with the only difference being in parameter values. While the bulk of the work is theoretical, we also present an experimental study of stirred stratified layering, to test the predictions of the theory against real fluid behaviour.

1.2 The Phillips effect

The formation of layers is *anti-diffusive*, with up-gradient transport, and so represents behaviour contrary to the naïvely expected case of homogenisation. Early work on layering by Phillips (1972) and Posmentier (1977) (independently) proposed a mechanism for the development of staircases. They appealed directly to this anti-diffusive property, based on the turbulent diffusion of buoyancy with a diffusion coefficient that could be negative. Specifically, Phillips and Posmentier modelled the evolution of the buoyancy profile $b(z, t) = (\rho_0 - \rho) g / \rho_0$ (where ρ is the fluid density, ρ_0 a reference density, and g the gravitational acceleration) by the one-dimensional diffusion equation

$$\frac{\partial b}{\partial t} = \frac{\partial}{\partial z} (f(b_z)) = \frac{\partial f}{\partial b_z} \frac{\partial^2 b}{\partial z^2}, \quad (1.1)$$

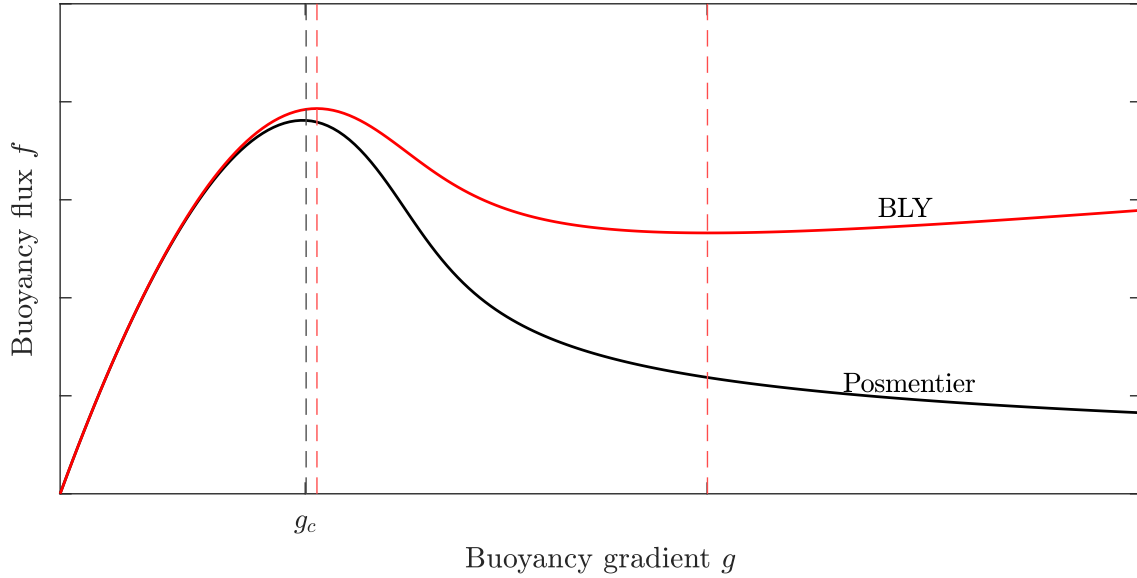


Fig. 1.2 The solid lines show the flux-gradient relations used by Posmentier (black) and BLY (red). The black dashed line shows the minimum value $g = g_c$ for which Posmentier's flux satisfies the instability condition (1.2). The red dashed lines show the boundaries of the finite region in which the flux in the BLY model satisfies condition (1.5).

where z is height, t is time, and the specified function $f(b_z)$ relates the local flux of buoyancy to the local buoyancy gradient $b_z(z, t)$. Equation (1.1) admits uniform steady state solutions $b_z = g_0$, which are linearly unstable to perturbations if the diffusivity is negative, i.e.

$$\frac{\partial f}{\partial b_z}(g_0) < 0. \quad (1.2)$$

If condition (1.2) holds, then a perturbation that increases the local buoyancy gradient b_z acts to decrease the buoyancy flux f , which further increases the buoyancy gradient through negative diffusion, in accordance with (1.1). Further, Posmentier proposed a flux-gradient relation, $f(b_z)$, of the form shown in Fig. 1.2, such that there is a critical value g_c above which condition (1.2) is satisfied. For a background gradient $b_z > g_c$, a small perturbation will grow in amplitude. If the perturbation acts to increase b_z , then it may grow without constraint, as inequality (1.2) is satisfied for all $b_z > g_c$. However, if the perturbation acts to decrease b_z , then the amplitude of the perturbation will grow only until $b_z = g_c$ locally, at which point the instability is arrested. Hence, perturbations can develop into a stepped structure, with alternating regions of large and small buoyancy gradients — a process commonly known as the ‘Phillips effect’. The argument advanced above is based on linear stability considerations and hence provides information on the initial evolution to a layered state. Once the perturbations attain a sufficiently large amplitude, nonlinear dynamics will come into play.

The model described by equation (1.1) provides a good starting point to describe a mechanism for layering. However, it relies on specifying the buoyancy flux function, and hence cannot give a full description of the physics from first principles, nor of the

intricacies of layer evolution. For example, (1.1) takes no account of the impact of the buoyancy on the velocity field; nor does it provide a mechanism to arrest the steepening of the interface, meaning that the buoyancy field eventually develops discontinuities. A particular mathematical difficulty of the model is that the linearised version of (1.1) becomes a negative diffusion equation for b in regions where $f'(b_z) < 0$. The growth rate of perturbations therefore diverges as the wavenumber increases, causing the problem to be ill-posed.

To look beyond the initial formation of layers, and investigate their longer-term evolution, the problem needs to be regularised. One possibility is to add a time delay, so that the flux does not adjust immediately to changes in the gradient, but takes a finite time to react (Barenblatt *et al.*, 1993; Kosuga *et al.*, 2013). More specifically, the flux $F(t)$ can be prescribed to depend on the buoyancy gradient $b_z(t - \tau)$, for some small delay time τ . This removes the high-wavenumber instability, but the solutions still develop discontinuities in finite time.

To regularise the dynamics, Balmforth *et al.* (1998) (hereinafter BLY) coupled the buoyancy equation (1.1) to an energy equation, considering the system

$$g_t = f_{zz}, \quad (1.3)$$

$$e_t = (\kappa e_z)_z + p, \quad (1.4)$$

where $g(z, t)$ is the buoyancy gradient, $f(g, e)$ is some flux function, $e(z, t)$ is the turbulent kinetic energy, κ is a turbulent diffusion coefficient, $p(g, e)$ is a general source (production) of energy, and $(\cdot)_t$ and $(\cdot)_z$ represent partial derivatives with respect to time and height. In the absence of double-diffusive effects, a parameterisation for p must include an energy source to drive the layering process. For linear instability in the system (1.3)–(1.4), BLY showed that the equivalent of the Phillips condition (1.2) is

$$\frac{df}{dg} \equiv \frac{f_g p_e - f_e p_g}{p_e} < 0. \quad (1.5)$$

The high-wavenumber instability inherent to the Phillips model (1.1) is avoided by parameterisations such that $df/dg < 0$ but $\partial f/\partial g > 0$. With this regularisation, (1.3)–(1.4) provide a complete model that can be used to analyse layer formation, evolution and merger in a stirred singly-stratified fluid. A crucial aspect to the model is the dependence of the turbulent fluxes on a turbulent mixing length $l(g, e)$, used to close the system.

To prevent the formation of infinite buoyancy gradients, BLY specified that the buoyancy flux should be an N-shaped function of the buoyancy gradient, so that condition (1.5) is satisfied for only a finite range of b_z . This is shown by the curve labelled ‘BLY’ in Fig. 1.2. The layering instability occurs only in the finite range of g between the red dashed lines; interfaces thus steepen only to a finite value, at which point the instability is arrested.

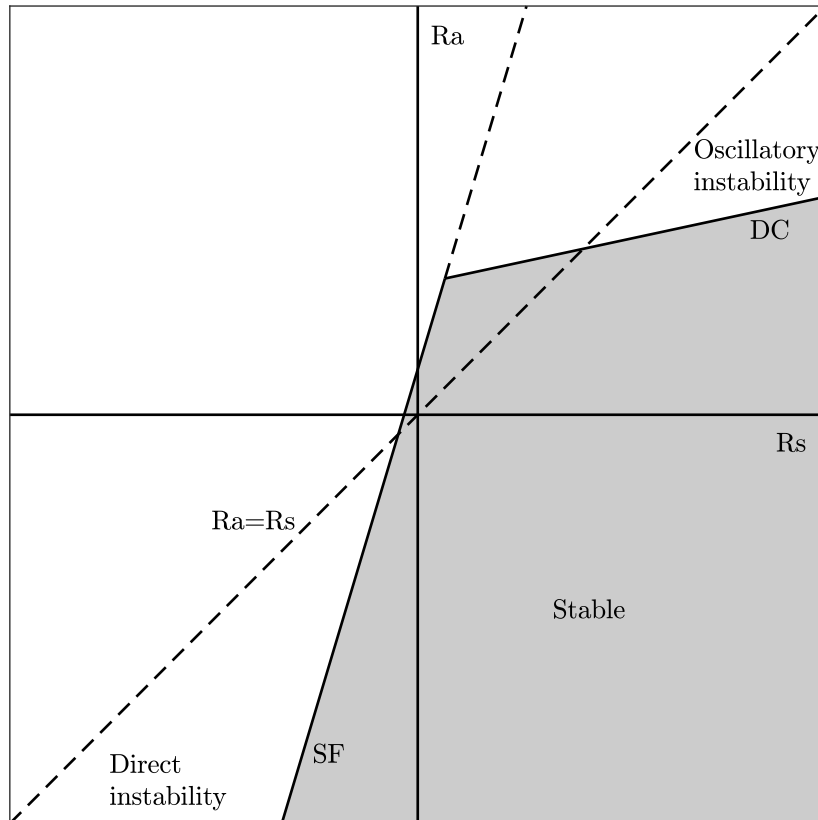


Fig. 1.3 Stability boundaries resulting from the classical stability analysis. The boundary for direct instabilities given by (1.7) is labelled SF; the boundary for oscillatory instabilities given by (1.8) is shown by the line labelled DC. Unstable modes exist above and to the left of these two lines. After Turner (1973).

1.3 Double-diffusive convection

Double-diffusive convection (DDC) is the name given to convection driven by opposing gradients of two scalar quantities that contribute to the fluid density, with each component diffusing at a different rate. These are commonly referred to as ‘temperature’ and ‘salt’, reflecting an oceanic context, where the thermal diffusivity is a factor of one hundred larger than the saline diffusivity. However, DDC can exist in any system with a stratification provided by two scalars, with another notable example being in stellar interiors, where, alongside the temperature, the concentration of a solute such as helium controls the buoyancy. In laboratory experiments, sugar-salt stratifications are commonly used to avoid the effects of heat loss (Stern & Turner, 1969).

Oceanic thermohaline staircases (with layers in both the heat and salinity fields) were first reported in the late 1960s (e.g. Tait & Howe, 1968). At a similar time, similar staircases were found in laboratory experiments on DDC (e.g. Turner, 1967), and the existence of oceanic staircases was quickly attributed to double-diffusive convection.

DDC occurs in two different regimes. Salt fingering (SF) refers to the case where the density differences driving the instability are due to salinity, with the temperature gradient acting to stabilise the overall density gradient. Diffusive convection (DC), also

called semiconvection in astrophysical contexts, refers to the opposite case, where the temperature gradient is destabilising, with a statically stable salt gradient. The regimes are commonly defined in terms of the Rayleigh numbers

$$\text{Ra} = \frac{g\alpha\Delta T d^3}{\kappa_T \nu}, \quad \text{Rs} = \frac{g\beta\Delta S d^3}{\kappa_T \nu}, \quad (1.6)$$

where g is the gravitational acceleration, α and β the thermal and solutal expansion coefficients of the fluid, d the fluid depth, κ_T the thermal diffusivity, ν the kinematic viscosity and $\Delta T = T(z=0) - T(z=H)$ and $\Delta S = S(z=0) - S(z=H)$ the temperature and salinity differences across the fluid of depth H . We further define the diffusivity ratio $\tau = \kappa_T/\kappa_S$, where κ_S is the saline diffusivity. Letting ρ be the fluid density and T and S the temperature and salinity respectively, we assume the linear equation of state $\rho = -\alpha g T + \beta g S$, such that a positive temperature gradient and a negative salinity gradient contribute to a stable (negative) density gradient. Hence the salt fingering regime is defined by $\text{Ra}, \text{Rs} < 0$, where the temperature gradient is stabilising, and the diffusive convection regime is defined by $\text{Ra}, \text{Rs} > 0$, where the salinity gradient is stabilising. The overall density gradient is stable (negative) if $\text{Ra} < \text{Rs}$. Figure 1.3 shows a regime diagram, taken from Turner (1973), showing the regions for instability in both the SF and DC regimes. A linear stability analysis of uniform gradient solutions to the governing equations leads to the stability boundaries in the Rs – Ra plane

$$\text{SF: } \text{Ra} = \frac{\text{Rs}}{\tau} + \frac{27\pi^4}{4}, \quad (1.7)$$

$$\text{DC: } \text{Ra} = \frac{\sigma + \tau}{\sigma + 1} \text{Rs} + (1 + \tau) \left(1 + \frac{\tau}{\sigma}\right) \frac{27\pi^4}{4}. \quad (1.8)$$

Points in the region between the unit slope line $\text{Rs} = \text{Ra}$ and the boundary (1.7) are unstable to salt fingering, while those between $\text{Rs} = \text{Ra}$ and the boundary (1.8) are unstable to diffusive layering. In the shaded region, the system is stable, while outside the shaded region and above the unit slope line, Rayleigh Bénard convection (RBC) occurs (Rayleigh, 1916). Note that in classical RBC (i.e. convection in a fluid layer driven by a temperature difference between the top and the bottom), the critical Rayleigh number for instability is $27\pi^4/4$. By considering $\text{Ra} - \tau^{-1}\text{Rs}$ to be an effective Rayleigh number, the SF boundary (1.7) reduces to this critical number for Rayleigh-Bénard convection.

There are well documented, long lasting (on the order of months) density staircases in regions of the ocean susceptible to both types of double-diffusive instability. For example, measurements have been taken for several decades of salt fingering staircases in the Mediterranean outflow and western tropical North Atlantic (e.g. Tait & Howe, 1968; Schmitt *et al.*, 1987; Schmitt, 1994), and diffusive convection staircases in the Arctic (Neal *et al.*, 1969; Timmermans *et al.*, 2008). Figure 1.4 shows some observational results. The two-dimensional temperature profile in the C-SALT study of Schmitt *et al.* (1987) is shown

in Fig. 1.4(a). Layers are clearly visible, and they are coherent across the entire horizontal distance. Observations from Timmermans *et al.* (2008) are shown in Fig. 1.4(b), showing clear diffusive staircases in both the temperature and salinity profiles.

Staircases have also been observed in numerical simulations of double-diffusion, in both SF (Radko, 2003; Stellmach *et al.*, 2011) and DC regimes (Rosenblum *et al.*, 2011; Mirouh *et al.*, 2012; Hughes & Brummell, 2021). As an example, the results of Stellmach *et al.* (2011) are reproduced in Fig. 1.5. An initial salt fingering instability is first seen, followed by a phase where the dynamics are dominated by gravity waves. Finally, the system develops into a clear stack of well-mixed layers separated by sharp interfaces. Fig. 1.5(d) shows time series of the Nusselt number Nu , which measures the ratio of convective to diffusive transport, and the ratio γ of the temperature and salinity fluxes. The transition to the staircase phase is associated with a simultaneous increase in Nusselt number, giving a significantly larger turbulent temperature flux in the staircase than in the previous unlayered state. This heightened flux is also seen in the numerical studies of Rosenblum *et al.* (2011) and Hughes & Brummell (2021).

1.3.1 Suggested mechanisms for DDC layering

Several theories have been proposed for the driving mechanism behind layering, which are well-documented in reviews by Merryfield (2000) and Radko (2013). An early hypothesis was that of collective instability (Stern, 1969), in which growing salt fingers excite large-scale internal waves that overturn and generate a stepped structure. It has also been suggested that staircases are the long-time state of thermohaline intrusions (Zhurbas & Ozmidov, 1984; Merryfield, 2000), or that they are metastable equilibria of the system, requiring a finite amplitude perturbation from an initial linearly stable state (Veronis, 1965; Stern & Turner, 1969). Other models rely on heating a stably stratified fluid from below, with convective layers forming sequentially from the bottom upwards due to the applied flux (Turner & Stommel, 1964; Huppert & Linden, 1979). All of these suggestions provide good explanations for layering, and studies have shown that they do indeed produce staircases. However, none of them is responsible for all layering behaviour — for example staircases are found in regions of oceans with very little internal wave activity, suggesting that collective instability cannot be the main driver of layering. The intrusion theory would require the existence of lateral gradients, but staircases can be produced in models with no horizontal variation. Numerical simulations have shown that staircases can form from a linear perturbation of a background stable state (e.g. Stellmach *et al.*, 2011), so the metastable equilibria argument is not essential for layering. Likewise, rather than staircases being controlled by an applied temperature flux, simulations show that the increase in flux follows the development of staircases. Of course, it is possible that multiple different mechanisms are in play, depending on the physical setup.

A further idea is that of Radko (2003), who proposed that the driving factor behind staircases is the result of an instability arising from variation of the ratio of the thermal to

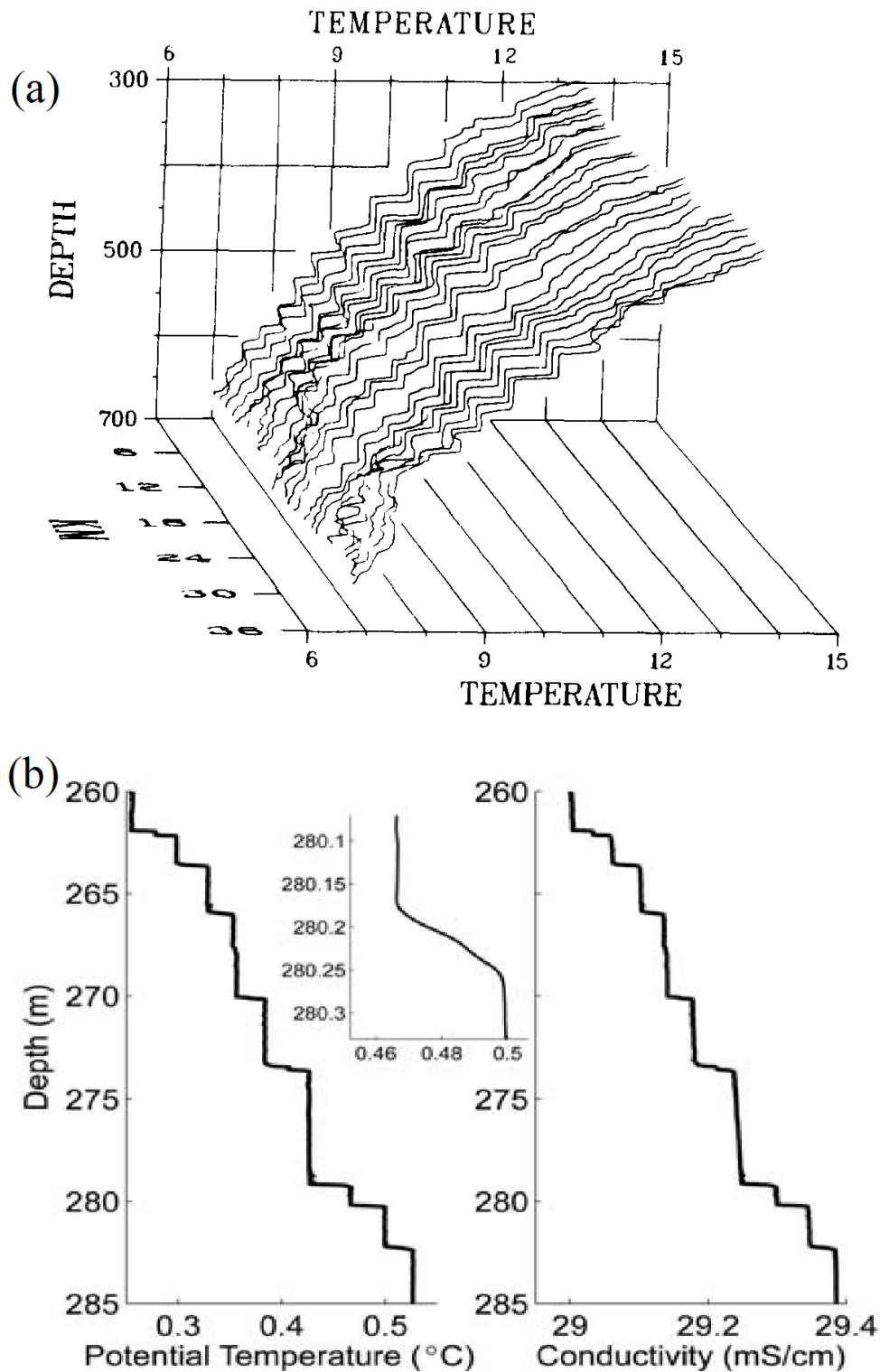


Fig. 1.4 Observational data from (a) Schmitt *et al.* (1987), showing the temperature profile in a section of the western tropical North Atlantic, from the C-SALT programme; and (b) Timmermans *et al.* (2008), showing temperature and conductivity profiles (from which salinity can be deduced) in the Arctic, from the pan-Arctic Beringia 2005 Expedition.

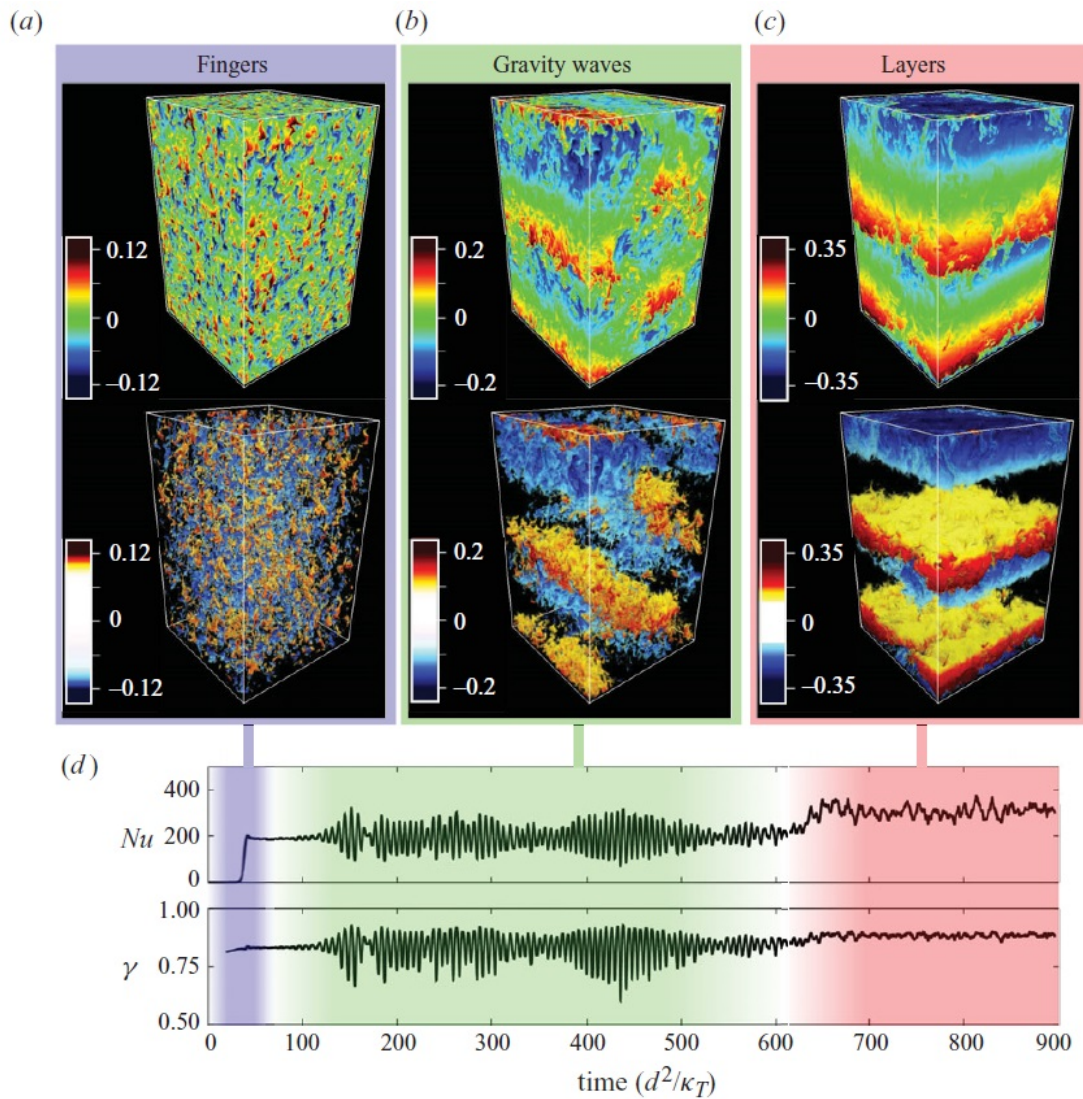


Fig. 1.5 Numerical simulations from Stellmach *et al.* (2011), showing (a)–(c) snapshots in three different phases of the evolution. The system first evolves into salt fingers, which become unstable to large scale gravity waves that saturate at finite amplitude. Eventually convective layers form, separated by thin interfaces. The top panels show the temperature perturbation on the data-cube faces, with the lower ones showing the internal structure. (d) Time series of the Nusselt number $Nu = 1 - f$ and flux ratio $\gamma = f/c$, where f and c are the temperature and salinity fluxes respectively.

solutorial fluxes. With $T(z, t)$ and $S(z, t)$ representing the horizontally-averaged temperature and salinity fields, and subscripts of t and z denoting partial derivatives with respect to time and height, Radko (2003) models the two components contributing to the density by

$$T_t = f_z, \quad S_t = c_z, \quad (1.9)$$

where $f(R)$ is the temperature flux and $c(R)$ the salinity flux, dependent on the density ratio $R = T_z/S_z$; the flux ratio $\gamma(R)$ is defined by $\gamma = f/c$. The growth rate of perturbations is found to be positive if and only if $d\gamma/dR$ is negative. On the basis of numerical simulations, Radko (2003) argues that $\gamma(R)$ should be non-monotonic with a single minimum, so that there is an unstable range of R , but the instability is arrested in regions where $d\gamma/dR > 0$. Radko's model provides a helpful conceptual framework for relating the condition for instability in terms of properties of the buoyancy fluxes. However, it describes only the conditions for an initial linear instability, with a growth rate that diverges at infinite wavenumber. As identified by Radko (2019a), such an ultraviolet catastrophe precludes the identification of a preferred wavelength or maximal growth rate, and prevents its use to study the dynamics of larger scale layers. A more complex regularised physical theory is required to model the full evolution from initial perturbation to staircase. In addition, the flow velocity is absent from the model, with the fluxes depending only on the density ratio R . To regularise the high wavenumber instability, Radko (2019a) proposed a model based on an asymptotic multiscale analysis, which leads to hyperdiffusion terms in the temperature and salinity equations, giving negative growth rates at high wavenumbers. Thus, the flux-gradient model can be adapted to study the evolution beyond an initial instability to a large scale staircase structure.

1.3.2 The Phillips effect in double-diffusive convection

It has been suggested that the same mechanism of negative density diffusion modelled by Phillips (1972) and Balmforth *et al.* (1998) (BLY) may also be of importance in double-diffusion (e.g. Schmitt, 1994). This makes some intuitive sense: the double-diffusive instability is due to release of potential energy, which acts to reduce the density of relatively lighter fluid, and increase the density of heavier fluid in a column — the eddy diffusion is negative. Hence, as we have seen that negative diffusion drives a layering instability in stirred stratified fluids, it is natural to suggest that it may also be of importance in DDC layering.

Models of the general form (1.3)–(1.4) have been used to study layering in several contexts. Malkov & Diamond (2019) produced a similar style of model to describe the formation of potential vorticity staircases. We will refer to these as *two-component models*. However, to study double-diffusive convection, the buoyancy field must be split into two independent components (e.g. temperature and salt). Hence, to produce a BLY-style model for double-diffusion, a third equation must be added to account for the second component

of buoyancy. Paparella & von Hardenberg (2014) adapted the BLY model to a double-diffusive context by arguing, on the basis of their previous numerical simulations (Paparella & von Hardenberg, 2012), that the flux ratio γ remained constant, and hence that the evolution of the temperature and salinity fields could be investigated with a single equation for the total buoyancy. This assumption reduces their model to a two-component model similar to that of BLY. The model of Paparella & von Hardenberg (2014) is forced by a constant up-gradient salt finger flux, with an eddy diffusivity term representing stirring due to ‘clusters’ of salt fingers. The constant salt finger flux has no effect on the buoyancy equation, but contributes a positive source in the energy equation. As such, while the underlying physics is different, the model of Paparella & von Hardenberg (2014) takes a very similar form to that of BLY, modelling salt fingering staircases with a forced system, and only one independent component of buoyancy.

However, it is useful to investigate whether layering is also possible without such forcing, instead including double-diffusion explicitly. In this case, a third equation is necessary that allows temperature and salinity to be described individually. There has been some limited use of three-component models to study $\mathbf{E} \times \mathbf{B}$ staircases in plasma drift-wave turbulence (Ashourvan & Diamond, 2016, 2017; Guo *et al.*, 2019). In these systems, the instability takes place in only two of the equations, so the modelling of instability again reduces to a form similar to the two-component BLY framework.

For a uniform buoyancy gradient to develop into a more complex layered structure, some energy input is necessary. BLY included an explicit source term to represent stirring, while Paparella & von Hardenberg (2014) included a constant background salt-finger flux. However, several computational studies of DDC have shown that no such external energy input is necessary for staircases to form. Instead, the double-diffusive instability provides a mechanism for the transfer of potential energy into kinetic energy. This is true in both the salt fingering regime (e.g. Stellmach *et al.*, 2011) and the diffusive convection regime (e.g. Rosenblum *et al.*, 2011; Hughes & Brummell, 2021). As such, we seek to formulate a model with no prescribed external forcing.

Ma & Peltier (2022) note that the values of the density ratio R found in observed oceanic staircases in the diffusive convection regime ($2 < 1/R < 7$) differ significantly from the values predicted by classical linear stability theory ($1 < 1/R < 1.14$) (e.g. Turner, 1973). By contrast, in the salt fingering regime, the values of R in observed staircases match well with linear theory. On this basis, Ma & Peltier (2022) suggest that the instability in diffusive convection is not actually the driver behind diffusive staircases, instead proposing that the layering instability relies on external forcing from a background flow, with double-diffusive effects being important only in the regularisation and stabilisation of layers.

1.4 Experimental studies of staircases

As well as the large volume of theoretical work discussed above, there have been several experimental studies of layering, most commonly in stirred stratified convection. Ruddick *et al.* (1989) performed experiments in which a fluid with a uniform stable salt gradient was stirred by the oscillation of a grid of rods. With the amplitude of oscillations fixed, high stirring rates caused the gradient to decrease over time while remaining smooth, gradually mixing the fluid. Lower stirring rates cause the uniform gradient to break down into a series of well-mixed layers. Park *et al.* (1994) developed this study in a more quantitative manner, varying the Reynolds number $Re = Ud/\nu$ by varying the speed of the rod, and the Richardson number $Ri = N^2 d^2 / U^2$ by changing the stratification and speed of the rod. Both Ruddick *et al.* (1989) and Park *et al.* (1994) found that at sufficiently high Ri , long lasting staircases formed.

Holford & Linden (1999*b*) built upon the work of Park *et al.* (1994), finding a difference in the evolution to layers, depending on the value of Ri . At low values of Re and low values of Ri , layers formed by the Phillips mechanism, but with higher values of Ri the development of layers followed a process dominated by the interaction of vortex sheets, as described by Holford & Linden (1999*a*).

For each value of Re , there is a critical value of Ri above which layering occurs, i.e. a critical $N^2 = b_z$. Park *et al.* (1994) estimated this stability boundary at

$$Ri_c \approx \exp(Re/900). \quad (1.10)$$

Figure 1.6 is taken from Park *et al.* (1994), and shows shadowgraph images of a staircase in stirred salt-stratified convection. Interfaces can be seen as bright bands separating darker layers. Figure 1.6 shows an early time while layers are still forming, while Figs. 1.6(b)–(d) show a fully developed staircase. A layer merger can be seen between (c) and (d), where the lowermost two interfaces drift and combine to form a single interface.

The experimental studies mentioned above have all produced staircases by stirring the fluid locally with a rod or grid of rods. With different geometries, different forcing methods are possible. Oglethorpe *et al.* (2013) conducted experiments in turbulent Taylor-Couette flow, where fluid is contained between two cylinders, with turbulence being generated by rotation of the inner cylinder, finding that an initially linear stratification spontaneously evolves into layers and interfaces. The measured density flux had a non-monotonic dependence on the Richardson number, confirming that layers form by the Phillips mechanism. Manucharyan & Caulfield (2015) applied forcing using a rotating disc on the surface of the fluid. As well as a surface mixed layer forming in contact with the disc, the Phillips effect led to the formation of a series of transient secondary mixed layers. These secondary layers appeared, then gradually merged with the main mixed layer, before a new secondary layer formed lower down and the process repeated.

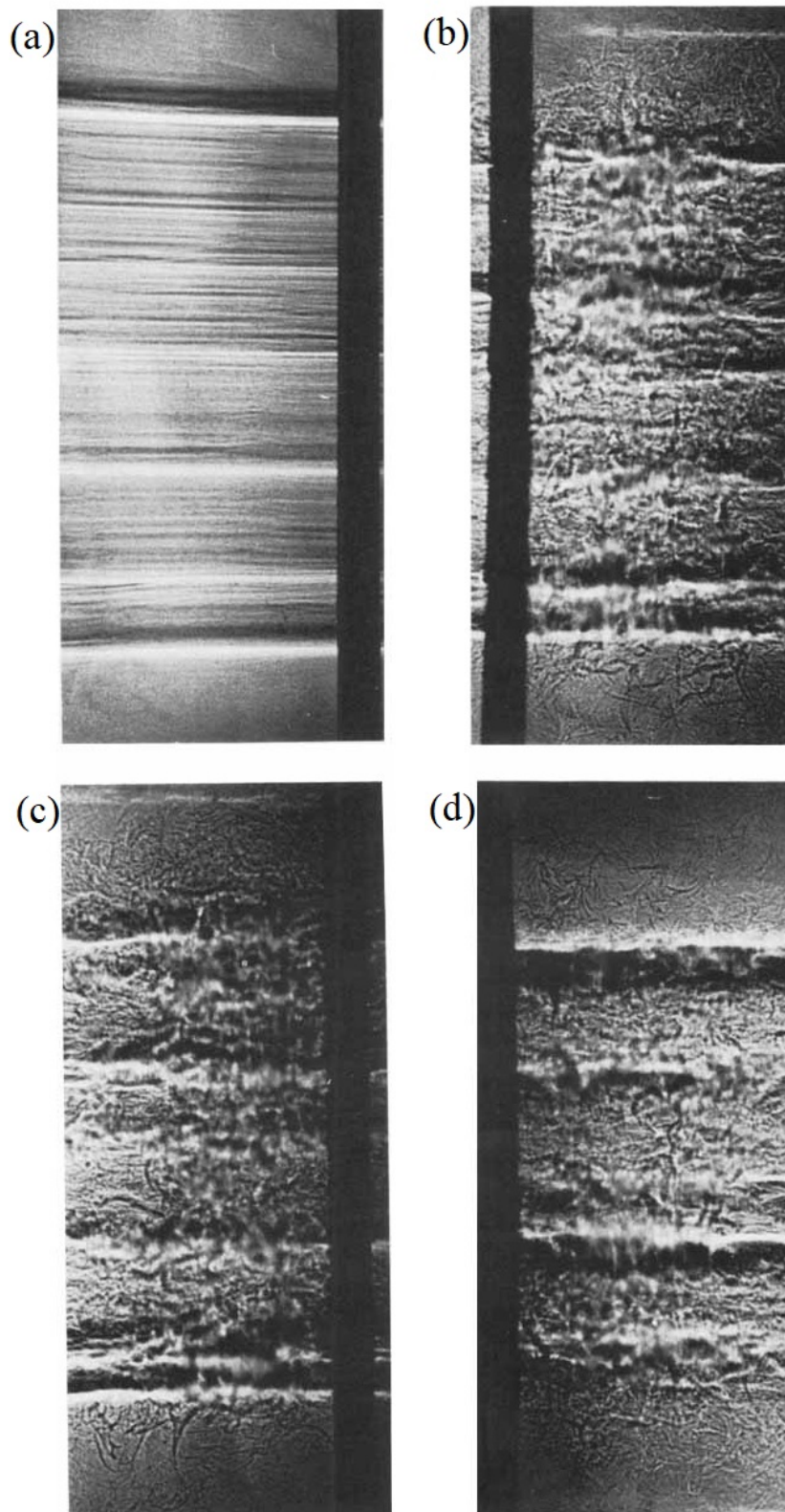


Fig. 1.6 Shadowgraph images from Park *et al.* (1994), showing the evolution of a staircase in a salt-stratified fluid stirred with a rod. Layers can be seen as darker regions, separated by bright interfaces. The two lowermost interfaces in (a)-(c) gradually move closer together, and have merged to form a single interface in (d). The black strip at the side of each image is the stirring rod.

1.5 Outline of thesis

This thesis focuses on layering in the geophysical contexts of stirred stratified convection and double-diffusive convection. In Chapter 2 we present the derivation of a general one-dimensional model for the formation of density staircases, by applying a horizontal averaging process to the Boussinesq equations. This contrasts with the model of Balmforth *et al.* (1998), which was obtained using phenomenological and dimensional arguments. This model is then adapted throughout the rest of the thesis to model layering first in stirred stratified flow, and both SF and DC regimes of double-diffusive convection.

In Chapter 3 we adapt the model to study the long-term behaviour of layers in stirred stratified convection — the problem first considered by Phillips (1972) and Posmentier (1977), and extended by Balmforth *et al.* (1998). In previous work, the behaviour of solutions of this style of model has not been investigated to late times, because of the existence of *edge regions* with low gradients, linking the boundaries to the layered interior. These edge regions expand into the interior at a rate of $z \propto t^{1/2}$, gradually engulfing layers from the outside inwards. This means that for a domain of depth H , all the layers will be destroyed by a time $t \propto H^2$, so any investigation of the layers' dynamics beyond this point is impossible. We show that by adopting different boundary conditions to BLY, the edge regions are removed, allowing the investigation of the behaviour of layers to long times. Further, the number of layers has an approximate inverse logarithmic dependence on time — the same as is found in Cahn-Hilliard (CH) models of layering, providing a link between BLY-style and CH models. The model of Chapter 3 is derived from the Boussinesq equations, as shown in Chapter 2, and includes both viscous and molecular diffusion directly, allowing it to be tailored to specific physical parameters. This work has been published as Pružina *et al.* (2022).

To test the prediction that layers will form only from a finite range of buoyancy gradients, we present an experimental study in Chapter 4. So far, experiments have demonstrated only the existence of a minimum gradient, but the results of Chapter 3 predict that a maximum gradient also exists, above which layers will not form. We show that this maximum gradient does appear to exist. However, more experimental work is necessary to establish the stability boundary more quantitatively.

So far, no BLY-style model has been used to study double-diffusion, except that of Paparella & von Hardenberg (2014), in which certain assumptions reduced the dynamics to a two-component stirred system. To study layering caused by double-diffusive convection, rather than stirring, an extra equation must be added to the system to model the second component of buoyancy, and the linear stability analysis of Balmforth *et al.* (1998) (for a two-component buoyancy–energy system) is no longer valid. We begin in Chapter 5 by demonstrating the Phillips effect in a three-component system for energy and two independent components of buoyancy. While three-component systems have been used before (e.g. Ashourvan & Diamond, 2017), the instability has always been as a function

of only two components, relying on BLY's stability analysis presented in Sec. 3.3.2. We categorise the different modes of instability that can occur, and make comparisons with previous theories. We show that the γ -instability of Radko (2003) and the Phillips effect are mathematically equivalent, and depend on the same instability condition. These are two separate physical processes however, and can be distinguished by specific parameterisations in the model equations.

To form a model for DDC layering, we take the same approach as we did for stirred stratified layering, deriving our model in the same way. Initially we keep the stirring term, and use BLY parameterisations for the length scale and dissipation terms, as a 'halfway house' between the BLY-style model of Chapter 3 and a fully double-diffusive model. These results are presented in Chapter 6. This model produces clean layers in the salt fingering regime, but suffers a high wavenumber instability in the diffusive convection regime, which can be countered by the addition of hyperdiffusion terms. In both regimes, the temperature and salinity fields evolve almost identically, suggesting that the major physical effect is that of stirred layering, rather than any double-diffusive effects being important.

To model staircases that form due to double-diffusion, rather than the forced Phillips instability, the forcing must be removed. In Chapter 7, we present a model for DDC layering without stirring. By parameterising the turbulent fluxes in terms of the density ratio R and turbulent kinetic energy e , we produce a model with the appropriate release of potential energy from the background density fields to drive the layering instability, without the need for an external energy source. We analyse the linear stability of steady states, and demonstrate that the γ -instability is active in the SF regime, producing staircase solutions, in which the temperature and salinity fields evolve independently. This work is under review for publication.

In agreement with the results of Ma & Peltier (2022) we find that the model of Chapter 7 does not lead to layering in the DC regime unless a forcing term is reintroduced. In Chapter 8 we reintroduce a simple forcing term that is sufficient to produce staircase structures in the DC regime, and discuss the similarities and differences between these solutions and those found in the SF regime in Chapter 7.

In Chapter 9 we present a summary of this work, detailing our key conclusions and suggesting some promising avenues for future work.

Chapter 2

Formulation of a model for staircase formation

2.1 Introduction

In this chapter, we present a detailed derivation of a model for layering. As discussed in the introduction, Balmforth *et al.* (1998) (BLY) developed a model for staircases in stirred stratified flow with a single component of buoyancy, extending the Phillips condition (1.2) to a model able to describe the full evolution of layers. Using dimensional and physical arguments, they obtained the following dimensionless system for the evolution of the horizontally averaged buoyancy $b(z, t)$ and turbulent kinetic energy $e(z, t)$:

$$b_t = \left(l e^{1/2} b_z \right)_z, \quad (2.1)$$

$$e_t = \left(l e^{1/2} e_z \right)_z - l e^{1/2} b_z - \frac{\epsilon e^{3/2}}{l} + P, \quad (2.2)$$

where $l = l(b_z, e)$ is a suitably parameterised mixing length and $P = P(b_z, e)$ is the energy production term representing stirring. Equations (2.1)–(2.2) form a system of turbulent diffusion equations, with the first term on each right hand side representing eddy diffusion. In the energy equation (2.2), the second term on the right hand side is necessarily the same as the buoyancy flux on the right-hand side of (2.1), accounting for the transfer between potential and kinetic energy. The penultimate term in (2.2) describes the dissipation of turbulent kinetic energy.

The BLY model (2.1)–(2.2) was developed using phenomenological and scaling arguments. In this chapter, we derive a similar model for layering, by applying a spatial averaging process to the governing Boussinesq equations. In our derivation, we retain viscous and molecular diffusion in the equations, allowing the model to be tailored to specific fluids, in contrast with the BLY model where no physical parameters remain, except in the parameterisations of l and P . Further, the inclusion of molecular diffusion allows us to

extend our model to multiple components of buoyancy with different diffusivities, so that layering can be studied in double-diffusive fluids.

Beginning with the Boussinesq equations, we use a spatial averaging process and simple closure assumptions, giving a system of one-dimensional partial differential equations for the horizontally averaged turbulent kinetic energy and buoyancy fields in terms of time and height. The system is closed using a mixing length, to be parameterised in terms of the dependent variables. While we present the derivation for a fluid with only one component of density, the process can be simply extended to an arbitrary number of independent components. We do this for a double-diffusive fluid with two components in Chapters 6–8.

2.2 Model formulation

We consider the evolution of a density-stratified fluid, defined by velocity $\mathbf{u}(\mathbf{x}, t) = (u, v, w)$ and buoyancy $b(\mathbf{x}, t) = g(\rho_0 - \rho)/\rho_0$, where g is gravitational acceleration, and $\rho(\mathbf{x}, t)$ and ρ_0 are the fluid density and a reference density respectively. In general, the fluid may be subject to a body forcing $\Phi(\mathbf{x})$ (for example due to stirring by an oscillating rod or grid). The dynamics are governed by the Boussinesq equations:

$$\frac{\partial \mathbf{u}}{\partial t} + \mathbf{u} \cdot \nabla \mathbf{u} = -\frac{1}{\rho_0} \nabla p + b \hat{\mathbf{z}} + \nu \nabla^2 \mathbf{u} + \frac{1}{\rho_0} \Phi, \quad (2.3)$$

$$\frac{\partial b}{\partial t} + \mathbf{u} \cdot \nabla b = \kappa \nabla^2 b, \quad (2.4)$$

$$\nabla \cdot \mathbf{u} = 0, \quad (2.5)$$

where ν is the kinematic viscosity and κ the molecular diffusivity. The pressure $p(\mathbf{x}, t)$ represents the perturbation away from the reference hydrostatic pressure $-\rho_0 g z$. While in later chapters we will work with these equations in dimensionless form, the choice of nondimensionalisation will vary. As such, we present the derivation of the model for layering with the dimensional form of the equations. For the purpose of developing our horizontally averaged model, we consider a horizontally periodic domain.

We now develop, via suitable averaging and parameterisations, a one-dimensional model for layering in a stratified fluid. Oceanic observations of density staircases show that they exhibit little variation over horizontal length scales much greater than the thickness of a typical layer (e.g. Timmermans *et al.*, 2008). Hence, a horizontally averaged model is an appropriate approximation to gain phenomenological insight, while being significantly easier to solve computationally than the full Boussinesq equations.

Let

$$\langle q \rangle \equiv \frac{1}{A} \int_A q(\mathbf{x}, t) \, dA \quad (2.6)$$

denote the horizontal spatial average of a quantity $q(\mathbf{x}, t)$ over a horizontal cross-section A at a given height z of the domain; $\langle q \rangle$ is thus a function of z and t . Let $\mathbf{u}_h = (u, v)$

represent the horizontal velocity, and ∇_h the horizontal gradient operator. The variables will be considered in terms of the sum of their horizontal mean and fluctuation components: $b = \langle b \rangle + b'$, $\mathbf{u}_h = \langle \mathbf{u}_h \rangle + \mathbf{u}'_h$, $w = \langle w \rangle + w'$.

Taking the average of the incompressibility condition (2.5) we obtain

$$\langle \nabla_h \cdot \mathbf{u}_h \rangle + \left\langle \frac{\partial w}{\partial z} \right\rangle = 0. \quad (2.7)$$

Assuming periodic boundary conditions on the horizontal velocity (appropriate for a phenomenon with such a large aspect ratio), the average of the horizontal divergence $\langle \nabla_h \cdot \mathbf{u}_h \rangle$ vanishes, and hence

$$\frac{\partial \langle w \rangle}{\partial z} = 0. \quad (2.8)$$

Thus, the horizontally averaged vertical velocity is uniform across the height of the domain. Assuming impermeability conditions on the top and bottom boundaries, it follows that $\langle w \rangle = 0$. Thus there is no mean vertical velocity and $w = w'$.

Our aim is to obtain a model purely in terms of horizontal averages of the buoyancy b and kinetic energy $e = \frac{1}{2} \mathbf{u} \cdot \mathbf{u}$. To this end, we first apply an averaging process to equations (2.3)–(2.4), and then parameterise any terms involving products of fluctuations in terms of mean quantities.

Splitting the variables into both mean/perturbation and horizontal/vertical components, the buoyancy equation (2.4) becomes

$$\langle b \rangle_t + b'_t + \left(\langle \mathbf{u}_h \rangle \cdot \nabla_h + \mathbf{u}'_h \cdot \nabla_h + w' \frac{\partial}{\partial z} \right) (\langle b \rangle + b') = \kappa \nabla^2 \langle b \rangle + \kappa \nabla^2 b', \quad (2.9)$$

where the subscripts $(\cdot)_t$ and $(\cdot)_z$ represent partial derivatives with respect to time and height. Once again assuming a horizontally periodic domain, the horizontal derivative of the horizontal average terms (i.e. $\nabla_h \langle b \rangle$ and $\nabla_h^2 \langle b \rangle$) vanish, leaving

$$\langle b \rangle_t + b'_t + \langle \mathbf{u}_h \rangle \cdot \nabla_h b' + \mathbf{u}'_h \cdot \nabla_h b' + w' \langle b \rangle_z + w' b'_z = \kappa \langle b \rangle_{zz} + \kappa \nabla^2 b'. \quad (2.10)$$

Using the incompressibility equation (2.5) to write $(\langle \mathbf{u}_h \rangle + \mathbf{u}'_h) \cdot \nabla_h b = \nabla_h \cdot ((\langle \mathbf{u}_h \rangle + \mathbf{u}'_h) b')$, and once again appealing to periodic boundary conditions so that its average vanishes, we take the horizontal average of (2.10) to obtain

$$\langle b \rangle_t + \langle w' b' \rangle_z = \kappa \langle b \rangle_{zz}. \quad (2.11)$$

Expression (2.11) is a diffusion equation for the mean buoyancy $\langle b \rangle$, forced by the eddy flux term $\langle w' b' \rangle_z$. The equation for b' is obtained by subtracting the mean equation (2.11) from the full equation (2.4) to give

$$b'_t + \langle \mathbf{u}_h \rangle \cdot \nabla_h b' + \mathbf{u}'_h \cdot \nabla_h b' + w' \langle b \rangle_z + w' b'_z - \langle w' b' \rangle_z = \kappa \nabla^2 b'. \quad (2.12)$$

As layering is a strongly one-dimensional phenomenon, we assume that the horizontal velocity \mathbf{u}_h is small, and use a quasilinear approximation to neglect both the terms $\langle \mathbf{u}_h \rangle \cdot \nabla_h b' + \mathbf{u}'_h \cdot \nabla_h b'$ and the perturbation buoyancy flux $w b'_z - \langle w b' \rangle_z$. This gives the following equation for the perturbation buoyancy

$$b'_t + w \langle b \rangle_z = \kappa \nabla^2 b'. \quad (2.13)$$

To parameterise the term $\langle w b' \rangle$ in (2.11) in terms of mean quantities, we use a scaling argument to represent the derivatives algebraically. We assume that the mean of the square of the vertical velocity is a constant multiple of the mean total kinetic energy $\langle e \rangle = \langle \mathbf{u} \cdot \mathbf{u} \rangle / 2$, i.e.

$$\langle w'^2 \rangle = \beta^2 \langle \mathbf{u} \cdot \mathbf{u} \rangle / 2 = \beta^2 \langle e \rangle, \quad (2.14)$$

for some dimensionless constant β . While, in general, the value of β may vary between layers and interfaces, we assume it is constant here to avoid overcomplicating the system. We assume that the turbulence varies on a mixing length scale l (to be parameterised as a function of the dependent variables) and on the dynamical timescale $\tau \sim l / \beta \langle e \rangle^{1/2}$, defined as the characteristic time to move a distance l vertically. These length and time scales are designed to provide approximations of the characteristic values for the derivatives $\partial_t \sim 1/\tau = \beta \langle e \rangle^{1/2} / l$ and $\nabla^2 \sim -1/l^2$. With these scalings, the fluctuation equation (2.13) becomes

$$\frac{\beta \langle e \rangle^{1/2}}{l} b' + w \langle b \rangle_z = -\frac{\kappa}{l^2} b'. \quad (2.15)$$

We multiply (2.15) by w and take the horizontal average, then rearranging to obtain an expression for the turbulent buoyancy flux $\langle w' b' \rangle$

$$\langle w' b' \rangle = -\frac{l^2 \langle w'^2 \rangle}{\beta l \langle e \rangle^{1/2} + \kappa} \langle b \rangle_z. \quad (2.16)$$

Using (2.14), this flux can be written in terms of $\langle b \rangle$ and $\langle e \rangle$ as

$$\langle w' b' \rangle = -\beta \frac{l^2 \langle e \rangle}{l \langle e \rangle^{1/2} + \kappa / \beta} \langle b \rangle_z. \quad (2.17)$$

Finally, combining (2.11) and (2.17) gives the equation for the averaged buoyancy:

$$\frac{1}{\beta} \langle b \rangle_t = \left(\frac{l^2 \langle e \rangle}{l \langle e \rangle^{1/2} + \kappa / \beta} \langle b \rangle_z \right)_z + \frac{\kappa}{\beta} \langle b \rangle_{zz}. \quad (2.18)$$

The first term on the right-hand side of (2.18) represents the turbulent transport of $\langle b \rangle$, and the second term molecular diffusion. To complete the model, we must couple equation (2.18) with an evolution equation for the horizontally averaged kinetic energy $\langle e \rangle$, and provide a parameterisation for the mixing length l .

We formulate the energy equation by taking the scalar product of the momentum equation (2.3) with \mathbf{u} , giving

$$e_t + \nabla \cdot (\mathbf{u}e) = -\frac{1}{\rho_0} \nabla \cdot (\mathbf{u}p) + w'b + \nu (\nabla^2 e - |\nabla \mathbf{u}|^2) + \frac{1}{\rho_0} \mathbf{u} \cdot \Phi. \quad (2.19)$$

The terms on the right-hand side of (2.19) represent, in order, the effect of pressure, the conversion from potential to kinetic energy, diffusion of kinetic energy, viscous dissipation $D = -\nu |\nabla \mathbf{u}|^2$ and production through stirring $P = (1/\rho_0) \mathbf{u} \cdot \Phi$. Following the same process as for the buoyancy equation, taking the horizontal average of (2.19) and assuming periodic boundary conditions on the energy gives

$$\langle e \rangle_t + \langle w'e' \rangle_z - \nu \langle e \rangle_{zz} = -\frac{1}{\rho_0} \langle w'p \rangle + \langle w'b' \rangle - \langle D \rangle + \langle P \rangle. \quad (2.20)$$

The fluctuation buoyancy flux $\langle w'b' \rangle$ is given by (2.17). The fluctuation turbulent energy flux $\langle w'e' \rangle$ can be parameterised in a similar way to the buoyancy flux: we subtract (2.20) from (2.19) and use a quasilinear approximation to neglect the terms $\langle \mathbf{u}_h \rangle \cdot \nabla_h \langle e \rangle + \mathbf{u}'_h \cdot \nabla_h \langle e \rangle$, $\mathbf{u}_h \cdot \nabla_h p / \rho_0$, $w'e'_z - \langle w'e'_z \rangle$ and $(w'p_z - \langle w'p_z \rangle) / \rho_0$, obtaining

$$e'_t + w' \langle e \rangle_z - \nu e'_{zz} = w'b' - D' + P'. \quad (2.21)$$

Once again, we approximate the time and space derivatives with $\partial_t \sim \beta \langle e \rangle^{1/2} / l$ and $\nabla^2 \sim -1/l^2$, multiply by $w'/2$, and make a quasilinear approximation to neglect the terms quadratic in fluctuation quantities ($w'^2 b'$, $w' D'$ and $w' P'$), giving

$$\frac{\beta \langle e \rangle^{1/2}}{2l} w' e' + \frac{w'^2}{2} \langle e \rangle_z + \frac{\nu}{2l^2} w' e' = 0. \quad (2.22)$$

Once again, we take the average, apply (2.14) and rearrange to give the energy flux

$$\langle w'e' \rangle = -\beta \frac{l^2 \langle e \rangle}{l \langle e \rangle^{1/2} + \nu / \beta} \langle e \rangle_z. \quad (2.23)$$

Combining (2.20) with (2.17) and (2.23) gives the following equation for the horizontally averaged kinetic energy.

$$\frac{1}{\beta} \langle e \rangle_t = \left(\frac{l^2 \langle e \rangle}{l \langle e \rangle^{1/2} + \nu / \beta} \langle e \rangle_z \right)_z - \frac{l^2 \langle e \rangle}{l \langle e \rangle^{1/2} + \kappa / \beta} \langle b \rangle_z + \frac{\nu}{\beta} \langle e \rangle_{zz} - \frac{1}{\beta} \langle D \rangle + \frac{1}{\beta} \langle P \rangle. \quad (2.24)$$

To close the system, a parameterisation is required for the turbulent length scales l in terms of the dependent variables $\langle b \rangle$ and $\langle e \rangle$. The choice of parameterisation is a vital part of the model. The length scale must be prescribed to model both small scales in interfaces, where the density gradient is large and energy small, and larger scales in layers, where

the gradient is small and the energy large. At this stage, we leave the length general, with more detailed discussions in later chapters.

To parameterise the dissipation $\langle D \rangle$ we follow BLY. The only combination of e and l that provides the correct dimensions for D is $D = \varepsilon e^{3/2}/l$, where ε is a dimensionless number that is treated as a parameter. This parameterisation of dissipation is commonly used in k - ε models of turbulence (e.g. Jones & Launder, 1972).

The dimensionless parameter β in equations (2.18) and (2.24) acts simply as a scale factor on the time derivative, effectively setting a new time variable $\tilde{t} = \beta t$, with new dimensionless parameters defined similarly: $\tilde{\kappa} = \kappa/\beta$, $\tilde{v} = v/\beta$ and $\tilde{\varepsilon} = \varepsilon/\beta$. With these rescalings, all factors of β disappear from (2.18) and (2.24), including in the parameterisations for the terms $\langle D \rangle/\beta$ and $\langle P \rangle/\beta$.

By adopting these rescaled forms of time and the dissipation and source terms, and dropping tildes and angled brackets from (2.18) and (2.24), we obtain the full model as

$$b_t = \left(\frac{l^2 e}{le^{1/2} + \kappa} b_z \right)_z + \kappa b_{zz}, \quad (2.25)$$

$$e_t = \left(\frac{l^2 e}{le^{1/2} + v} e_z \right)_z - \frac{l^2 e}{le^{1/2} + \kappa} b_z + v e_{zz} - \varepsilon \frac{e^{3/2}}{l} + P. \quad (2.26)$$

The system (2.25)–(2.26) forms a coupled nonlinear diffusion model describing the evolution of the horizontally averaged buoyancy $b(z, t)$ and energy density $e(z, t)$, dependent on turbulent fluxes parameterised using a mixing length $l(b_z, e)$. The second term in the energy equation (2.26) is necessarily the same as the turbulent buoyancy flux, and accounts for transfer between potential and kinetic energy. The final terms in (2.26) represents the effects of viscous dissipation and any energy source from stirring.

We have shown this derivation for a single component of density, leading to a two-component model. In Chapter 3 we will discuss the conditions for layering in this two-component framework, and investigate the behaviour of solutions. However, to study double-diffusive convection, it is necessary to treat the temperature and salinity fields independently. In this case, temperature and salinity are both governed by advection-diffusion equations of the form (2.4), but with different values of κ . Applying the same averaging process yields equations to model the turbulent transport of temperature and salt independently, yielding a three-component model. We will discuss three variants of this three-component model in Chapters 5–7.

Chapter 3

Layering in stirred stratified convection

3.1 Introduction

In this chapter, we present a model for layering in the simplest possible physical system — a stirred stratified fluid with a single component of density. This is the system considered by Phillips (1972) and Posmentier (1977). As discussed in the introduction, BLY developed a more detailed model (2.1)–(2.2) to extend the Phillips condition (1.2) to a fuller model for layering. Taking the stirring term to be $P = \varepsilon e^{1/2}/l$, where ε is a dimensionless mixing parameter, the BLY model is given in dimensionless form by:

$$b_t = \left(l e^{1/2} b_z \right)_z, \quad (3.1)$$

$$e_t = \left(l e^{1/2} e_z \right)_z - l e^{1/2} b_z - \varepsilon (e - 1) \frac{e^{1/2}}{l}, \quad (3.2)$$

The parameterisation of the length scale $l(b_z, e)$ is a crucial component of the model. In the initial non-layered state, the key length scale is that of the turbulent eddies induced by stirring, which is non-dimensionalised to unity ($l = 1$). As a result of the stirring, a shorter length scale emerges in regions where the buoyancy gradient is high. This is represented by the Ozmidov length scale $l_O = (e/b_z)^{1/2}$, defined as the characteristic size of the largest eddy that is not significantly affected by buoyancy in a stably stratified fluid (Ozmidov, 1965). The parameterisation for $l(b_z, e)$ interpolates between these two scales, taking the stirring length when the stratification is weak, and the Ozmidov length in strongly stratified regions. The particular dimensionless form chosen by BLY is

$$l(b_z, e) = \frac{e^{1/2}}{(e + b_z)^{1/2}}, \quad (3.3)$$

which appropriately transitions from the stirring length $l \sim 1$ for $b_z \ll e$ to the Ozmidov length as $b_z \gg e$.

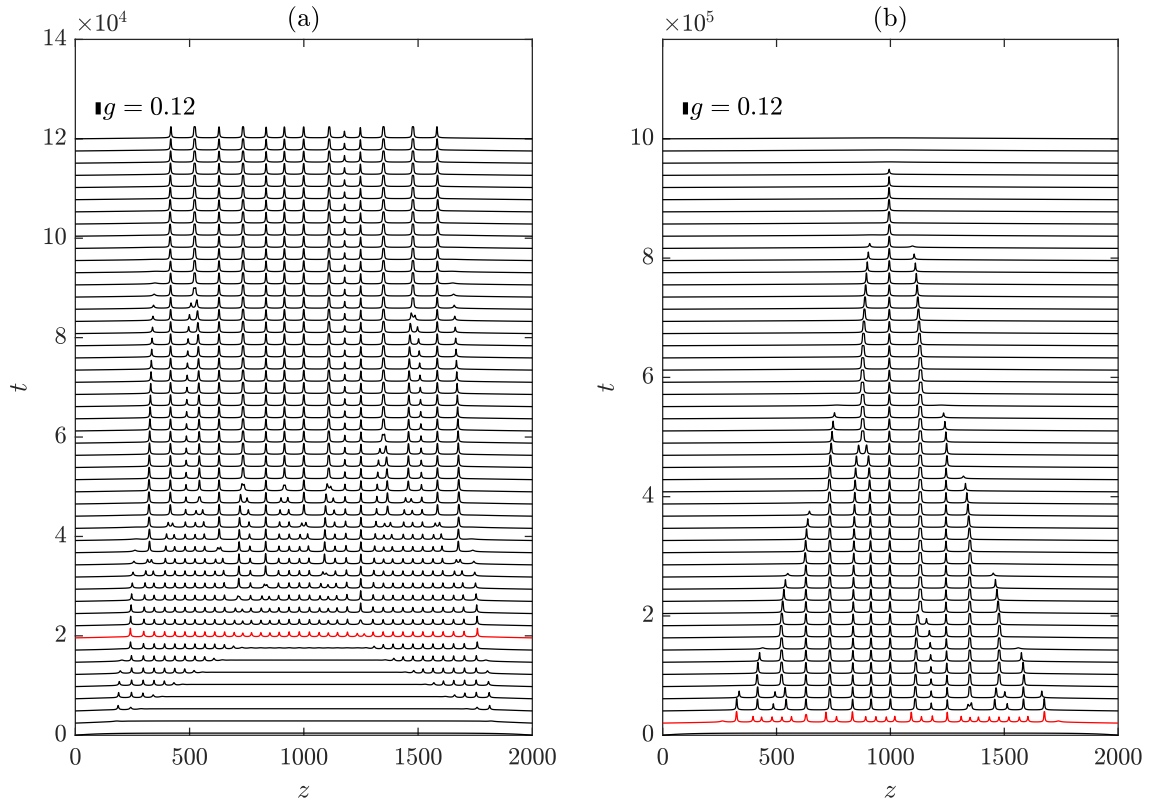


Fig. 3.1 Reproduction of numerical results using the BLY model (3.1)–(3.2), showing the initial development of the layered state, layer mergers, and expansion of the edge regions. The plots show the spatial profile of the dimensionless buoyancy gradient $g(z, t) = b_z(z, t)$ across the depth of the layer at regular time intervals. The scale bar at the top of the panel indicates the magnitude of g . Panel (a) reproduces the simulation of Fig. 6 of BLY, while panel (b) shows the continued long-term evolution to $t = 10^6$. The edge regions expand at a rate $\propto t^{1/2}$ into the interior, eventually destroying the entire layered region and filling the domain. In both panels, the solution at $t = 2 \times 10^4$ is shown in red; this denotes the first time at which consistent layers exist across the entire interior region.

The system (3.1)–(3.3) is solved in the domain $0 < z < H$. BLY prescribe no-flux boundary conditions on both buoyancy and energy, as specified by

$$b_z(0,t) = b_z(H,t) = 0, \quad e_z(0,t) = e_z(H,t) = 0. \quad (3.4)$$

These no-flux conditions imply that the total energy is changed only by dissipation and stirring.

The coupling of the buoyancy $b(z,t)$ to the energy $e(z,t)$ in the BLY model (3.1)–(3.2) is found to suppress the high wavenumber instability inherent in equation (1.1), thereby ensuring that the problem is well posed. To prevent the formation of infinite buoyancy gradients, BLY’s model specifies an N-shaped flux-gradient relation, so that condition (1.2) is satisfied for only a finite range of b_z . This is shown by the curve labelled ‘BLY’ in Fig. 1.2. The layering instability occurs only in the finite range of g between the red dashed lines; interfaces thus steepen only to a finite value, at which point the instability is arrested.

A reproduction of a numerical solution to the system (3.1)–(3.4) with $H = 2000$ is shown in Fig. 3.1. Figure 3.1(a) shows the initial development of the layered region, while Fig. 3.1(b) shows the long-time evolution of the solution. Layers initially start to develop across the interior of the domain, beginning at a distance of ≈ 200 from the top and bottom of the domain. By $t \approx 2 \times 10^4$ (shown red in both panels), a pack of layers of a regular wavelength and amplitude has formed across the full depth of the domain, with the exception of two smooth non-layered regions extending from the top and bottom of the domain to the interior pack of layers. Over time, the layers within the pack undergo sporadic merger events, in which two adjacent interfaces move together and join to form a single interface. At the same time, smooth regions, referred to herein as *edge regions*, expand from the two boundaries of the domain towards the interior at a rate of $z \propto t^{1/2}$, engulfing layers from the outside inwards. Eventually, the edge regions take up the entire domain, meeting in the middle to form a single well-mixed layer across the full depth of the fluid. By totally engulfing the layered region by $t \sim H^2/4$, the development of the edge regions limits investigation into the dynamics of layer mergers beyond this time.

In this chapter we present a model obtained using the averaging process detailed in Chapter 2, and use it to investigate the long-term behaviour of layers in stratified turbulence. We retain the parameterisations used by BLY for the dissipation, stirring, and mixing-length. We investigate the predictions of our generalised model, establishing the general effects of viscosity and molecular diffusivity on the conditions for layer formation. Diffusion and viscosity both have a stabilising effect on the system, reducing the range of unstable gradients and the maximum growth rates.

As an inroad towards investigating trends in long-term merger dynamics, we also demonstrate that the adoption of different boundary conditions to those used by BLY can eliminate the expanding edge regions, allowing the long-term dynamics of the layers to be apparent. As noted above, the no-flux conditions of (3.4) resulted in the development

of edge regions that engulf the entire layered region by time $t \sim H^2/4$. We show that the alternative boundary conditions of fixed buoyancy, equivalent to specifying the temperature at the top and bottom of the domain, prevents the expansion of edge regions. The layered region is then changed only by merging behaviour. The removal of the time constraint imposed by the edge regions thus allows us to investigate long-term trends in the dynamics of layer mergers. Each group of mergers approximately halves the number of interfaces, until eventually only a single interface remains. We show that for long times, the number of layers remaining, $N(t)$, is consistent with the scaling $1/N \sim \log t$. An inverse logarithmic dependence of this form has been found previously to arise in solutions to the Cahn-Hilliard (CH) equation for phase separation (Kawakatsu & Munakata, 1985), and an analogy can be made between kinks (separating phases) and interfaces (separating layers of density), allowing the CH equation to be used to model layering (e.g. Balmforth & Young, 2005). BLY demonstrated that the model (3.1)–(3.2) can be reduced asymptotically to the CH equation by perturbing the governing equations about the critical point of marginal stability. The logarithmic timescale that we demonstrate here further consolidates and extends this link.

This chapter is organised as follows. Section 3.2 discusses the derivation of the diffusive model. To begin our analysis of this system, we first find uniform steady solutions in Sec. 3.3.1. We investigate the linear stability of these steady states in Sec. 3.3.2, discussing how the stability is affected by changing the viscosity and molecular diffusivity. In Sec. 3.3.3, we consider parameter values relevant to water, where the stratification is due to either a salinity gradient at constant temperature, or a temperature gradient at constant salinity, and compare the differences between these two cases. In Sec. 3.4, we investigate the long-term behaviour of solutions. We begin in Sec. 3.4.1 by showing that the adoption of fixed-buoyancy boundary conditions allows layer dynamics to be observed for very long times without the intrusion of edge regions. In Sec. 3.4.2 we discuss such long-term numerical solutions of the model in detail, making comparisons with the linear stability predictions described in Sec. 3.3.2, and investigating the long-term merger dynamics of the interfaces. We demonstrate that the long-term dynamics of our model are consistent with predictions from Cahn-Hilliard models of layering. Our conclusions and a discussion of possible extensions of the work are contained in Sec. 3.5. The results contained in this chapter have been published as Pružina *et al.* (2022).

3.2 Model formulation

To derive the model, we follow the process outlined in Chapter 2, beginning with the dimensional Boussinesq equations:

$$\mathbf{u}_t + \mathbf{u} \cdot \nabla \mathbf{u} = -\frac{1}{\rho_0} \nabla p + b \hat{\mathbf{z}} + \nu \nabla^2 \mathbf{u} + \frac{1}{\rho_0} \Phi, \quad (3.5)$$

$$b_t + \mathbf{u} \cdot \nabla b = \kappa \nabla^2 b, \quad (3.6)$$

$$\nabla \cdot \mathbf{u} = 0, \quad (3.7)$$

where ν is the kinematic viscosity and κ the molecular diffusivity. The pressure $p(\mathbf{x}, t)$ represents the perturbation away from the reference hydrostatic pressure $-\rho_0 g z$. We non-dimensionalise the system through the scalings

$$\hat{t} = \frac{U}{d} t, \quad \hat{z} = \frac{1}{d} z, \quad \hat{\mathbf{u}} = \frac{1}{U} \mathbf{u}, \quad \hat{b} = \frac{d}{U^2} b, \quad \hat{p} = \frac{1}{\rho_0 U^2} p, \quad \hat{\Phi} = \frac{d}{\rho_0 U^2} \Phi, \quad (3.8)$$

where hats denote dimensionless variables, and d and U are characteristic length and velocity scales of the stirring. Note that the dimensionless buoyancy gradient $\hat{b}_z = d^2 b_z / U^2$ can be interpreted as a Richardson number, although the velocity used is that of a stirring device, not an imposed shear. On substituting from (3.8) into equations (3.5)–(3.7), and dropping hats, we obtain the non-dimensional Boussinesq equations:

$$\mathbf{u}_t + \mathbf{u} \cdot \nabla \mathbf{u} = -\nabla p + b \hat{\mathbf{z}} + \text{Re}^{-1} \nabla^2 \mathbf{u} + \Phi, \quad (3.9)$$

$$b_t + \mathbf{u} \cdot \nabla b = \text{Pe}^{-1} \nabla^2 b, \quad (3.10)$$

$$\nabla \cdot \mathbf{u} = 0, \quad (3.11)$$

where Re is the Reynolds number Ud/ν , and Pe is the Péclet number Ud/κ . Note that the Reynolds and Péclet numbers are related by $\text{Pe} = \text{Pr} \text{Re}$, where $\text{Pr} = \nu/\kappa$ is the Prandtl number. For the purpose of developing our horizontally averaged model, we can assume either impermeability conditions on the sidewalls of the domain, or, for the case of a rectangular cross-section, a horizontally periodic domain.

We apply the averaging process of Chapter 2 to (3.9)–(3.11) to obtain the following system:

$$b_t = \left(\frac{l^2 e}{le^{1/2} + \text{Pe}^{-1}} b_z \right)_z + \text{Pe}^{-1} b_{zz}, \quad (3.12)$$

$$e_t = \left(\frac{l^2 e}{le^{1/2} + \text{Re}^{-1}} e_z \right)_z - \frac{l^2 e}{le^{1/2} + \text{Pe}^{-1}} b_z + \text{Re}^{-1} e_{zz} - \varepsilon (e - 1) \frac{e^{1/2}}{l}, \quad (3.13)$$

$$l = l(b_z, e) = \frac{e^{1/2}}{(e + b_z)^{1/2}}. \quad (3.14)$$

The energy production term has been parameterised as $P = \varepsilon e^{1/2}/l$. BLY describe this as an ‘equipartition’ model for production, formulated such that the eddy speed $e^{1/2}$ adjusts to the velocity scale of the stirring device on the eddy turnover timescale $l/e^{1/2}$, and which provides an N-shaped flux-gradient relation.

Also following BLY, we adopt a length scale of the form (3.3), but it should be noted that this is not the only possible parameterisation for the length scale. We anticipate that any monotonic function that interpolates between the stirring length when the stratification is weak, and a smaller length when the stratification is strong, would serve the same purpose. We choose here to adopt the BLY length scale in the form (3.3) as it allows us to compare the results of our model directly with those of BLY, so that our study of the effects of diffusion and different boundary conditions is not affected by the further complication of adopting a different mixing length.

The system (3.12)–(3.14) forms a coupled nonlinear diffusion model describing the evolution of the horizontally averaged buoyancy $b(z, t)$ and energy density $e(z, t)$, dependent on turbulent fluxes parameterised using a mixing length $l(b_z, e)$. The second term in the energy equation (3.13) is necessarily the same as the turbulent buoyancy flux, and accounts for transfer between potential and kinetic energy. The final term in (3.13) represents the combined effects of viscous dissipation and the energy source from stirring. When $e = 1$, dissipation balances production. If $e < 1$, there is a net source of energy; if $e > 1$, there is a net sink. The BLY model can be recovered from the system (3.12)–(3.14) by setting $\text{Pe}^{-1} = \text{Re}^{-1} = 0$, which turns off both viscous and molecular diffusion.

3.3 Conditions for initial layer development

In this section, we consider the initial development of layers, and investigate the effects of viscosity and diffusion on the system through varying the inverse Reynolds number Re^{-1} and inverse Péclet number Pe^{-1} . We saw in Sec. 3.2 that these parameters appear not only as standard diffusion terms, but also in the flux terms in equations (3.12)–(3.13).

We begin, in Sec. 3.3.1, by seeking steady solutions that have uniform b_z and e . We then proceed to analyse their linear stability in Sec. 3.3.2, finding that larger values of Pe^{-1} and Re^{-1} both suppress the instability. In Sec. 3.3.3, we consider the combined effects of changing Pe^{-1} and Re^{-1} together, using values relevant for water, with the stratification provided either by a salinity gradient at constant temperature, or a temperature gradient at constant salinity.

3.3.1 Uniform-gradient steady states

To begin our linear stability analysis, we return to the full system (3.12)–(3.14), and seek uniform steady states $b = g_0 z$, $e = e_0$, where g_0 and e_0 are constants. For such basic states,

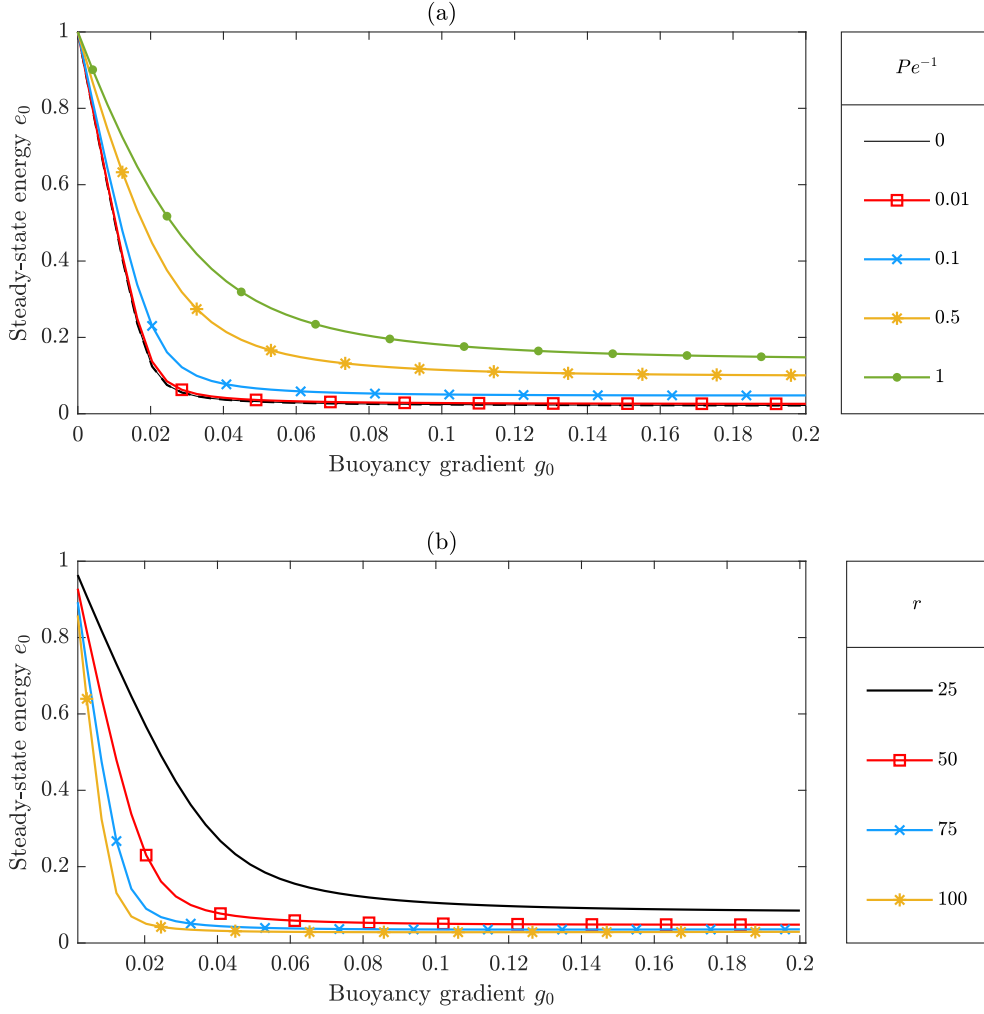


Fig. 3.2 Steady-state energy e_0 (solutions to (3.16)) as a function of buoyancy gradient g_0 . In (a), $r = 50$ is fixed and Pe^{-1} varies; in (b), $Pe^{-1} = 0.1$ is fixed and r varies.

the buoyancy equation (3.12) is trivially satisfied, and the energy equation (3.13) becomes

$$0 = -\frac{l^2 e_0}{l e_0^{1/2} + Pe^{-1}} g_0 - \varepsilon \frac{e_0^{1/2}}{l} (e_0 - 1). \quad (3.15)$$

On substituting for l from (3.14), rearranging and writing $r = 1/\varepsilon$, we obtain the steady-state energy equation

$$0 = r e_0^2 g_0 + (e_0 - 1)(e_0 + g_0) e_0 + Pe^{-1} (e_0 - 1)(e_0 + g_0)^{3/2}. \quad (3.16)$$

Figure 3.2 shows the solutions to (3.16) as solid lines, for a range of values of Pe^{-1} and r . In Fig. 3.2(a) we fix $r = 50$ while varying Pe^{-1} . In every case, $e_0 = 1$ at $g_0 = 0$, corresponding to a dimensional energy of $U^2/2$ — the energy is set by the stirring speed. As g_0 increases, the energy decreases monotonically. For small values of Pe^{-1} , the solutions are similar to the BLY solution (shown black), but for larger Pe^{-1} the profile is significantly shallower, with $e_0(g_0)$ decreasing more gradually.

Figure 3.2(b) also shows the steady-state energy $e_0(g_0)$, this time fixing $\text{Pe}^{-1} = 0.1$ while varying r . Here we see that larger values of r produce profiles for which $e_0(g_0)$ decreases more steeply. For large values of r (small ε), the combined viscous dissipation and stirring term $\varepsilon e_0^{1/2} (e_0 - 1) / l$ in the steady-state energy equation (3.15) is $O(\varepsilon)$. For the equation to be satisfied, the buoyancy flux term $-l^2 e_0 g_0 / (l e_0^{1/2} + \text{Pe}^{-1})$ must therefore also be small. This requires either e_0 or g_0 to be sufficiently small, producing the sharp decrease in $e_0(g_0)$ shown in the figure.

3.3.2 Stability and conditions for layering

We now proceed to investigate the linear stability of the uniform-gradient steady states found in Sec. 3.3.1. To do this, we will consider results derived by BLY for a more general system, and show how they apply to our model. The system (3.12)–(3.13) can be written in the form

$$g_t = f_{zz}, \quad (3.17)$$

$$e_t = (\kappa e_z)_z + p, \quad (3.18)$$

where the functions $f(g, e)$, $p(g, e)$ and $\kappa(g, e)$ are defined as

$$f = \left(\frac{l^2 e}{l e^{1/2} + \text{Pe}^{-1}} + \text{Pe}^{-1} \right) g, \quad (3.19)$$

$$p = -\frac{l^2 e}{l e^{1/2} + \text{Pe}^{-1}} g - \varepsilon \frac{e^{3/2}}{l} + \varepsilon \frac{e^{1/2}}{l}, \quad (3.20)$$

$$\kappa = \frac{l^2 e}{l e^{1/2} + \text{Re}^{-1}} + \text{Re}^{-1}. \quad (3.21)$$

BLY presented a linear stability analysis of the general system (3.17)–(3.18), which can be applied for any given specification of $f(g, e)$, $p(g, e)$ and $\kappa(g, e)$. Considering the more general form (3.17)–(3.18) thus allows us to apply the linear stability results obtained by BLY to our generalised situation allowing for viscosity and molecular diffusion, as given by (3.19)–(3.21). The general form also means that the results remain valid if we change any parameterisations in the system, such as presenting a different formulation of the mixing length l .

BLY showed that the steady state $g = g_0$, $e = e_0$, is linearly unstable if

$$F'(g_0) := \frac{f_g p_e - f_e p_g}{p_e} < 0, \quad (3.22)$$

where the partial derivatives $f_g(g, e)$, $f_e(g, e)$, $p_g(g, e)$, $p_e(g, e)$ are evaluated in the steady state (g_0, e_0) , and $F'(g_0)$ is defined as the total derivative of f with respect to g , evaluated at $(g_0, e_0(g_0))$. In essence, this represents the Phillips effect (cf. condition (1.2)), but generalised to a more complex, physically-derived diffusion problem. BLY further proposed

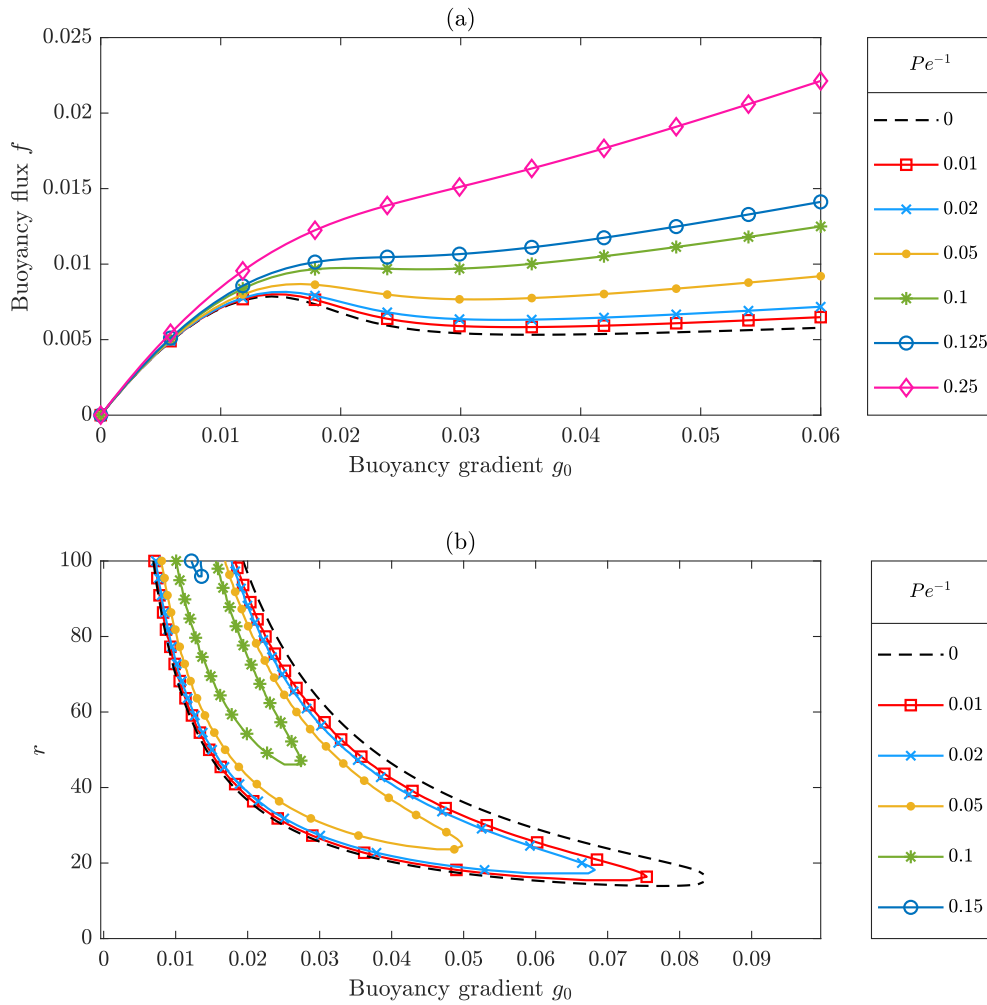


Fig. 3.3 (a) Flux-gradient relations for a selection of values of Pe^{-1} , for $r = 50$, calculated by substituting the steady-state energy e_0 (found as exact solutions of (3.16)) into the buoyancy flux $f(g, e)$ given by (3.19). The N-shaped curve required for the layering instability is displayed by the smaller values of Pe^{-1} . (b) Loci of $F'(g_0; r) = 0$, for a range of Pe^{-1} (constant on each curve). For each value of r , the gradients g_0 inside the curve are unstable.

that, in order for layering to occur, the flux-gradient relation $F'(g)$ should be N-shaped, so that there is instability only for an intermediate range of g , with very low and very high gradients being stable.

The system (3.17)–(3.18) contains two time derivatives, so the linear stability analysis produces two growth rates. The first is positive if condition (3.22) is satisfied. The second, ‘energy mode’, growth rate is equal to p_e , and allows for the possibility of an instability arising from the energy equation (3.18) alone, without any interaction with the buoyancy equation. This could happen if the forcing were too strong, or the buoyancy gradient were negative, for example. For the model to be an accurate representation of the layering mechanism, it is necessary that the only instability comes from the Phillips effect. Hence the energy mode must be stable, so we require $p_e < 0$.

For the functions relevant to our model (3.19)–(3.21), the condition $p_e < 0$ is satisfied for all values of (g_0, e_0) , Pe^{-1} and Re^{-1} . Hence the energy mode is damped, with the only instability arising from the Phillips effect. Note that the inverse Péclet number Pe^{-1} affects f and p , while the inverse Reynolds number Re^{-1} is contained only in κ . Because the condition for instability (3.22) depends only on f and p , this means that varying Re^{-1} independently of Pe^{-1} does not change whether or not the system is unstable, but only affects the range of unstable wavenumbers.

Figure 3.3(a) shows flux-gradient relations $f(g)$ for a range of values of Pe^{-1} , for the illustrative case $r = 50$. The plots display the clear N-shape required for the layering instability for values of $\text{Pe}^{-1} < 0.113$ (a critical value that depends on r). As Pe^{-1} increases, the N-shape flattens. For all $\text{Pe}^{-1} > 0.113$, $f(g)$ is a monotonically increasing function. Thus, with all other conditions identical, a sufficiently high density diffusion (sufficiently large Pe^{-1}) eventually suppresses the layering instability.

Figure 3.3(b) shows the loci on which $F'(g_0; r) = 0$ for a range of values of Pe^{-1} . These lines correspond to the top of the peak and bottom of the trough of the N-shape in Fig. 3.3(a). It is clear that for any value of r , the unstable range of g_0 is greatest when $\text{Pe}^{-1} = 0$. As Pe^{-1} increases, the unstable range of g_0 at fixed r decreases, and the critical value of r above which instability occurs increases. The loci in Fig. 3.3(b) illustrate that when the stratification is too weak, no layering is possible — physically it seems reasonable that without a strong enough gradient, mixing will simply destroy the stratification and lead to homogeneous turbulence. On the other hand, when the gradient is too large, the stratification cannot be sufficiently disturbed by the mixing, so no layers form. Using the expressions for f and p given by (3.19)–(3.20), we find that the outermost (black, $\text{Pe}^{-1} = 0$) locus is represented by

$$r(g_0) = \frac{4 - 3g_0 \pm 2\sqrt{1 - 12g_0}}{3g_0}. \quad (3.23)$$

The case with the $-$ sign represents the left-hand part of the locus; the $+$ sign represents the right-hand part. The tip of the locus is at $g_0 = 1/12$, where both expressions are equal.

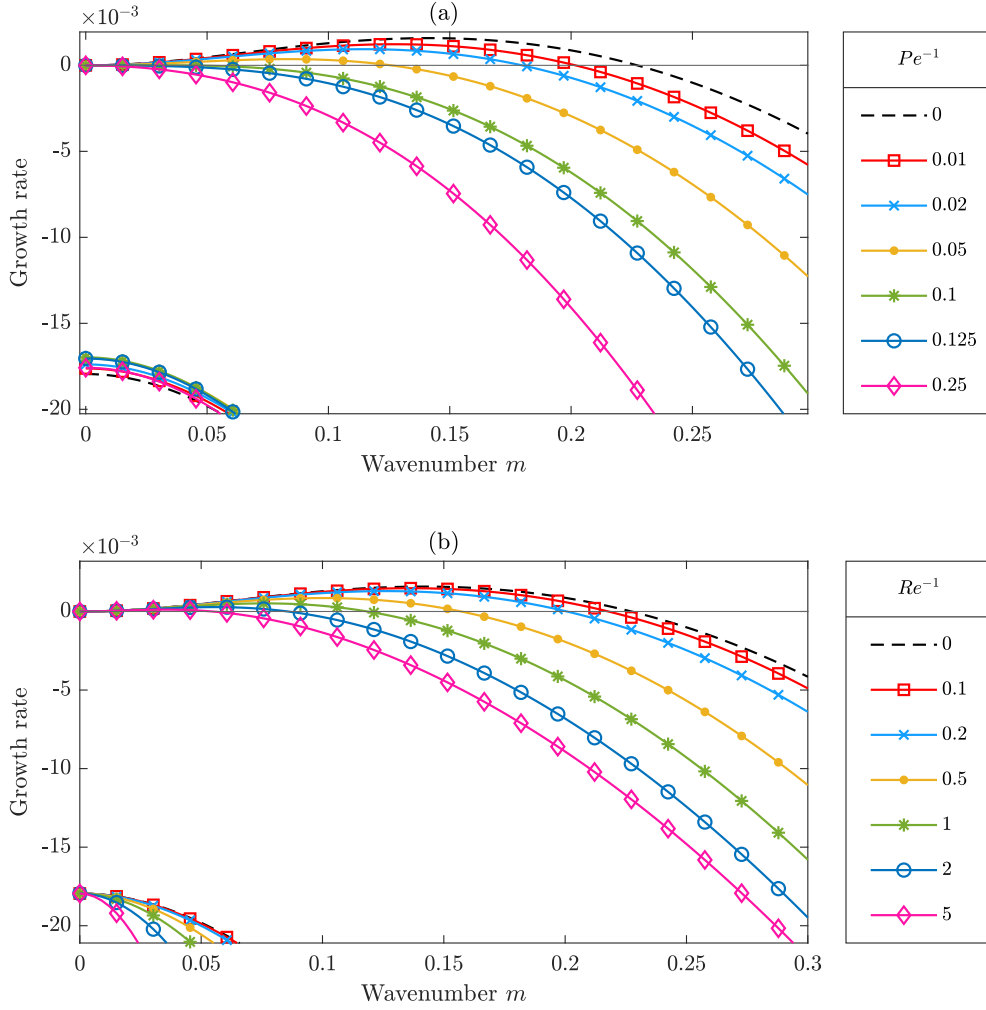


Fig. 3.4 Growth rate plotted as a function of wavenumber, for $r = 50$ and $g_0 = 0.0218$. In (a), $Re^{-1} = 0$ is fixed and Pe^{-1} varies; in (b), $Pe^{-1} = 0$ is fixed and Re^{-1} varies. Since the parameters are linked by $Pe = PrRe$, (a) corresponds to the limit of $Pr = 0$, and (b) to $Pr \rightarrow \infty$. The dashed black curve represents the diffusionless system. The lower set of curves represents the damped energy mode.

Across all values of r and Pe^{-1} , this is the maximum possible gradient for layering. For $r \rightarrow 0$, expression (3.23) reduces to the two asymptotes

$$g_1(r) \sim \frac{2}{3r}, \quad g_2(r) \sim \frac{2}{r}. \quad (3.24)$$

Thus, for any finite value of r , there is a positive range of g_0 for which the stratification is too weak for layering, as well as a finite range of g_0 for which layering is possible. We can see from Fig. 3.3 that increasing the value of Pe^{-1} shrinks the locus of marginal stability, both by increasing the critical value of r for instability (i.e. the tip of the curve), and by decreasing the unstable range of g_0 for each value of r .

The plots in Fig. 3.4 show how the growth rate of perturbations depends on the wavenumber. In panel (a), $Re^{-1} = 0$ is fixed and Pe^{-1} varies, while panel (b) has $Pe^{-1} = 0$ while Re^{-1} varies. The parameters are linked by the relation $Pe = PrRe$, so panel (a)

shows the limit of $Pr = 0$, panel (b) the limit of $Pr \rightarrow \infty$. In both cases, there is one set of unstable modes, as well as a second stable set of growth rates representing the energy mode. We see that, in accordance with the stability criteria discussed in Sec. 3.3.2, higher values of Pe^{-1} suppress the instability entirely. Furthermore, increasing Re^{-1} has no effect on the criterion for instability, but alters the range of unstable wavenumbers.

To summarise, the introduction of either molecular diffusivity or viscosity suppresses the layering instability, as might be expected. Viscosity does not change whether or not a steady state is unstable, but reduces the unstable range of wavenumbers and, consequently, the wavenumber of maximum growth rate. Hence, we expect larger values of Re^{-1} to produce staircases with thicker layers and fewer interfaces. Incorporating molecular diffusivity has the same effect of decreasing the unstable range of wavenumbers, but can also suppress the instability entirely by reducing the unstable range of buoyancy gradients. We conclude that introducing diffusion to the system will make staircases less pronounced, by increasing the gradient in layers, and decreasing the gradient in interfaces.

3.3.3 Implications for typical values of Pe^{-1} and Re^{-1}

To examine simultaneously the combined effects of viscosity and diffusion, we consider some realistic parameters for both temperature- and salt-stratified water. Here, temperature-/salt-stratified means that the density gradient is caused by a variation in temperature/salt alone. Note that for a temperature-stratified fluid,

$$Pe = PrRe, \quad (3.25)$$

where $Pr = \nu/\kappa$ is the Prandtl number. For a salt-stratified fluid with solutal diffusivity κ_S , the analogue of Pr is the Schmidt number $Sc = \nu/\kappa_S$. Some characteristic values of Pr and Sc are shown in Table 3.1, for typical conditions relevant to both oceanic and laboratory settings. For a reasonable range of temperatures and salinities, $Pr \sim 10$, while $Sc \sim 100$ - 1000 . Hence, for a given Reynolds number, the Péclet number is 10-100 times smaller for salt-stratified water than for the temperature-stratified case. For the ranges shown in Table 3.1, variations in salinity have only a small effect on Pr and Sc compared to variations in temperature. In a typical turbulent terrestrial flow, $Re \gtrsim O(1000)$, but Fig. 3.4 shows that even for $Re^{-1} = 0.1$, the growth rate profile is very close to that for $Re^{-1} = 0$. As such, to demonstrate fully the effect of parameter choices we will consider a range of larger values of Re^{-1} .

Figure 3.5 shows plots of growth rate versus wavenumber for three values of Re^{-1} and for a range of values of Pr and Sc ; the Péclet number follows from the relations $Pe^{-1} = (PrRe)^{-1}$ and $Pe^{-1} = (ScRe)^{-1}$. In Fig. 3.5(a), we take values relevant for temperature-stratified water. Instability occurs only for sufficiently small Re^{-1} ; all the solutions for $Re^{-1} = 10$ are stable. Larger values of Pr increase both the range of unstable g_0 and the maximum growth rate, as they give smaller values of Pe^{-1} . For the case of $Re^{-1} = 1$,

Temperature/°C	Salinity/‰	Pr	Sc
0	0	13.18	1620
0	20	13.22	1680
0	40	13.34	1750
10	0	9.32	831
10	20	9.39	884
10	40	9.52	934
20	0	6.95	480
20	20	7.04	514
20	40	7.17	547

Table 3.1 Prandtl and Schmidt numbers of water at various temperatures (in degrees Celsius) and salinities (in parts per thousand). The values of Pr are taken from Nayar *et al.* (2016); Sharqawy *et al.* (2010) and those of Sc from Ramsing & Gunderson (2020).

the system is unstable only for the higher values of Pr chosen. In Fig. 3.5(b), parameter values are taken to be relevant for salt-stratified water; here, all the values considered lead to instability. There is little difference between the results for the four different Schmidt numbers, but increasing Re^{-1} does decrease the range of unstable g_0 and the maximum growth rates. This is because the Schmidt numbers are large and hence the inverse Péclet numbers are small; e.g. for $Re^{-1} = 0.1$, the values of Sc used correspond to $Pe^{-1} = O(10^{-4})$. In contrast, the values of Pr used in the temperature-stratified case correspond to $Pe^{-1} = O(10^{-2})$. Hence, changing the background temperature, and therefore Pr, has a much greater effect on Pe^{-1} in the temperature-stratified case than changing Sc in a salt stratification. The existence of the layering instability is therefore more sensitive to the background temperature, and requires larger Reynolds numbers, in a temperature-stratified fluid than in a salt-stratified fluid.

Table 3.2 shows maximum growth rates and their corresponding wavenumbers, for characteristic values of Pr and Sc in oceanic configurations, as well as for two smaller choices of Pr. There is only a very slight difference between the results for $Pr = 1$ and $Pr = 0$, so a more detailed study of the small Pr region of parameter space is unlikely to reveal any new behaviour. From Table 3.2 and Figs. 3.3-3.5, we see that increasing density diffusion decreases the area in (g_0, r) parameter space that is unstable. Increasing density diffusion or viscosity decreases the range of unstable wavenumbers for each background gradient, as well as decreasing the wavenumber of maximum growth rate and the maximum growth rate itself.

3.4 Long-term evolution of layered solutions

In this section, we present solutions to the model (3.12)–(3.14), focusing on the long-term dynamics. In Sec. 3.4.1, we demonstrate that the adoption of fixed-buoyancy boundary

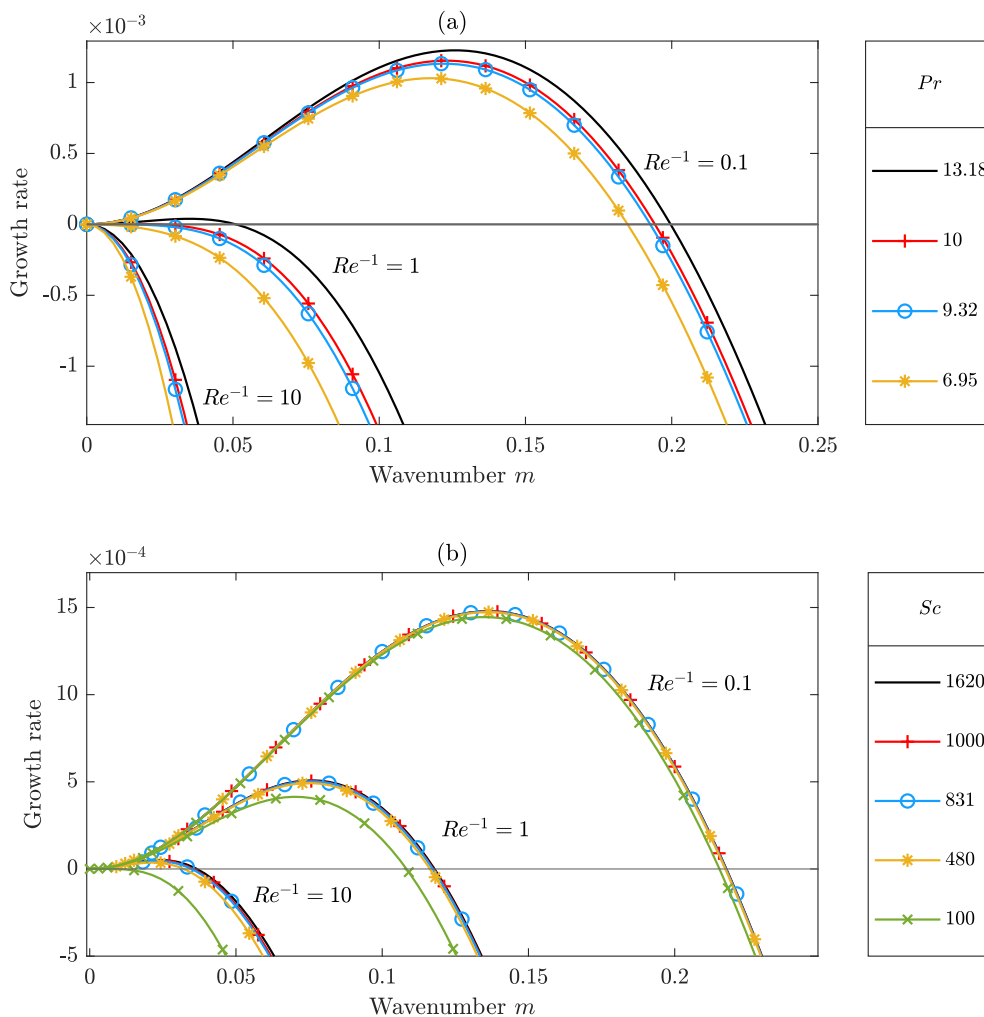


Fig. 3.5 Growth rate plotted as a function of wavenumber, for (a) temperature- and (b) salt-stratified fluids, for $r = 50$, $g_i = 0.0218$, with three different choices of Re^{-1} and a range of values of Prandtl and Schmidt numbers. The values of Pr and Sc are chosen to be representative of water under common terrestrial conditions, as seen in Table 3.1. For comparison with Fig. 3.4, note that in (a), $Pe^{-1} = (PrRe)^{-1}$, and in (b), $Pe^{-1} = (ScRe)^{-1}$.

	Re^{-1}	Pe^{-1}	m_{\max}	$n = \frac{Hm}{2\pi}$	$L = \frac{2\pi}{m}$	growth rate
BLY case	0	0	0.14	45	44	1.6×10^{-3}
Pr = 10	0.1	0.01	0.12	40	51	1.1×10^{-3}
Pr = 10	1	0.1	0.018	5.8	350	2.6×10^{-6}
Pr = 10	10	1	stable			
Sc = 1000	0.1	10^{-4}	0.14	43	46	1.5×10^{-3}
Sc = 1000	1	10^{-3}	0.076	24	83	5.0×10^{-4}
Sc = 1000	10	10^{-2}	0.024	7.7	26	4.7×10^{-5}
Pr = 1	0.001	0.01	0.13	41	48	1.2×10^{-3}
Pr = 1	0.01	0.1	0.027	8.6	230	6.6×10^{-6}
Pr = 1	0.1	1	stable			
Pr = 0	0	0.01	0.13	41	48	1.2×10^{-3}
Pr = 0	0	0.1	0.027	8.6	230	6.9×10^{-6}
Pr = 0	0	1	stable			

Table 3.2 Predicted dimensionless wavenumbers of the mode of maximum growth rate m_{\max} , and the corresponding dimensionless growth rates, for characteristic values of Pr, Sc and Re^{-1} , with $r = 50$, $g_0 = 0.0218$. For $\text{Pr} \lesssim 1$, there is little difference from the $\text{Pr} = 0$ case. Plots of wavenumber versus growth rate are shown for selected parameter choices in Fig. 3.5.

conditions prevents the formation of the expanding regions that appear in solutions to the BLY model (3.1)–(3.4), thus allowing the observation of layer dynamics to long times. An investigation of the long-term dynamics is presented in Sec. 3.4.2, where we show how the predictions of Sec. 3.3.3 are manifest in the solutions at long times. Furthermore, we demonstrate a general trend for the long-term behaviour.

3.4.1 The effects of fixed-buoyancy boundary conditions on the long-term behaviour

We begin by investigating the effects of fixed-buoyancy boundary conditions on the system. For simplicity, and to isolate the effects of the boundary conditions, we take $\text{Pe}^{-1} = \text{Re}^{-1} = 0$ in this section, reducing the model (3.12)–(3.13) to the BLY system (3.1)–(3.2) exactly. Once the effects of the boundary conditions are understood, we will reincorporate finite molecular diffusivity and viscosity.

The no-flux boundary conditions (3.4) ensure that the total energy is changed only by dissipation and stirring. For a temperature-stratified fluid, this is equivalent to the upper and lower boundaries being insulated and impermeable. The no-flux conditions admit an approximate similarity solution describing the growth of the edge region towards the centre of the domain, represented by $b_z = g(z/t^{1/2})$, $e = e(z/t^{1/2})$. This prediction was confirmed numerically by BLY, who demonstrated that the edge regions expand into the interior at a rate of $z \sim t^{1/2}$. For such a similarity solution to exist, it is necessary that

boundary conditions are imposed on the buoyancy gradient $g = b_z$, rather than on the buoyancy itself, b . Hence it is of interest to determine how the edge regions behave, and indeed if they even exist, if different boundary conditions are imposed.

In the case of a temperature-stratified fluid, a common experimental setup is a fluid layer between two conducting plates held at constant temperatures. For a statically stable gradient, we consider a hot plate above a cold plate, and adopt the Dirichlet conditions

$$b(0,t) = 0, \quad b(H,t) = g_0 H, \quad (3.26)$$

forming a uniform stable stratification. Here, g_0 is the initial uniform background buoyancy gradient, and H is the fluid depth. Without loss of generality, the buoyancy on the bottom boundary can be taken as zero, as the equations depend only on buoyancy gradients. In contrast to the choice of no-flux boundary conditions, the fixed-buoyancy condition (3.26) allows us to take a uniform background buoyancy gradient $g(z) = g_0$, which we use as a basic state for the system, creating a uniform stratification. Taking this solution to be a steady basic state gives $e(z) = e_0(g_0)$, uniform throughout the domain. Thus a no-flux (Neumann) condition on the energy is possible:

$$e_z(0) = e_z(H) = 0. \quad (3.27)$$

Alternatively, we can choose to fix the energy on the boundaries with the Dirichlet condition

$$e(0,t) = e(H,t) = e_0. \quad (3.28)$$

In considering appropriate initial conditions, we begin by noting that (3.26) admits steady-state solutions with both b_z and e uniform with height, for either choice of condition on the energy, (3.27) or (3.28). Assuming that $b = g_0 z$ and $e = e_B$, we find steady solutions to (3.12)–(3.14) by setting time derivatives to zero. Taking a uniform buoyancy gradient and uniform energy means that all the spatial derivatives also vanish, leaving a quadratic equation for $e_B(g_0)$, with solution

$$e_B(g_0) = \frac{1}{2} \left(1 - g_0(1+r) + \sqrt{(1 - g_0(1+r))^2 + 4g_0} \right), \quad (3.29)$$

where $r = 1/\varepsilon$ (Balmforth *et al.*, 1998). For the case of no stratification ($g_0 = 0$), the steady-state energy $e_B = 1$ is associated with the non-dimensional stirring length scale. As $g_0 \rightarrow \infty$, $e_B \rightarrow 0$, thereby demonstrating the damping of motion as the stratification is increased.

For the buoyancy initial condition, we take a uniform gradient steady state plus a sinusoidal perturbation of amplitude a and wavenumber $2\pi n/H$:

$$b(z, 0) = g_0 \left[z - a \sin \left(\frac{2\pi n z}{H} \right) \right], \quad (3.30)$$

$$e(z, 0) = e_B(g_0), \quad (3.31)$$

where $e_B(g_0)$ is given by (3.29). We set the amplitude to be $a = 0.001$. The integer n is chosen to produce the maximum linear growth rate for perturbations about this steady state (cf. Sec. 3.3.2), ensuring that layers develop quickly from the perturbations, with little interference from other wavenumbers. BLY used the parameter values $g_0 = 0.0218$, $r = 50$, $H = 2000$, and demonstrated that, for these values, the dominant wavenumber corresponds to $n = 45$. To facilitate comparison with BLY's results, we will adopt the same values.

All the numerical solutions of the full nonlinear system were obtained using the MATLAB pdepe solver. Figure 3.6 shows the short- and long-time evolution of solutions to equations (3.12)–(3.14). All plots have 4000 spatial mesh points. The early evolution plots have 1000 time steps, while long-time solutions were calculated using a series of nine integrations, each with 1000 time steps. There are 1000 linearly spaced time steps between each time labelled on the vertical axis, giving a piecewise linear time axis, with the size of a time step increasing by a factor of 10 or 100 between each label. The solutions are not sensitive to finer spatial resolutions or integration tolerances, and the pdepe solver chooses timesteps dynamically to ensure that the solutions are well resolved in time.

Figures 3.6(a,b) show the integration carried out with no-flux (Neumann) boundary conditions on the energy (3.27). The initial perturbation grows into a regular pattern of spikes in the buoyancy gradient $g(z, t)$, separating regions in which the fluid is well mixed and the gradient is small. The spikes represent smeared interfaces separating the well-mixed layers. At this stage, the evolution is similar to that arising from the no-flux buoyancy boundary conditions (3.4) (cf. Fig. 3.1). A key difference, however, is that the region in which layers form extends across the full depth of the domain, with little influence from the boundaries (an aspect that becomes increasingly important at later times). Initially 45 spikes (layer interfaces) develop in the buoyancy gradient profile $g(z, t)$. The wavenumber of this initial pattern of layering matches that of the initial perturbation $m = 45(2\pi/H)$. The interfaces begin to merge at $t \approx 1.6 \times 10^5$, with mergers happening evenly across the domain. After the first merger, the spike height (i.e. the maximum gradient in an interface) is approximately double that of the initial spikes. After subsequent mergers take place, the height of the spikes remains constant, with successive mergers doubling the width of each spike, as the maximum unstable gradient has been reached. These merger events follow the ‘H-merger’ pattern described by Radko (2007), where neighbouring mergers drift and combine, in contrast with the ‘B-merger’ where strong interfaces grow at the expense of weaker ones. The state at $t \approx 1 \times 10^{16}$ is not the final

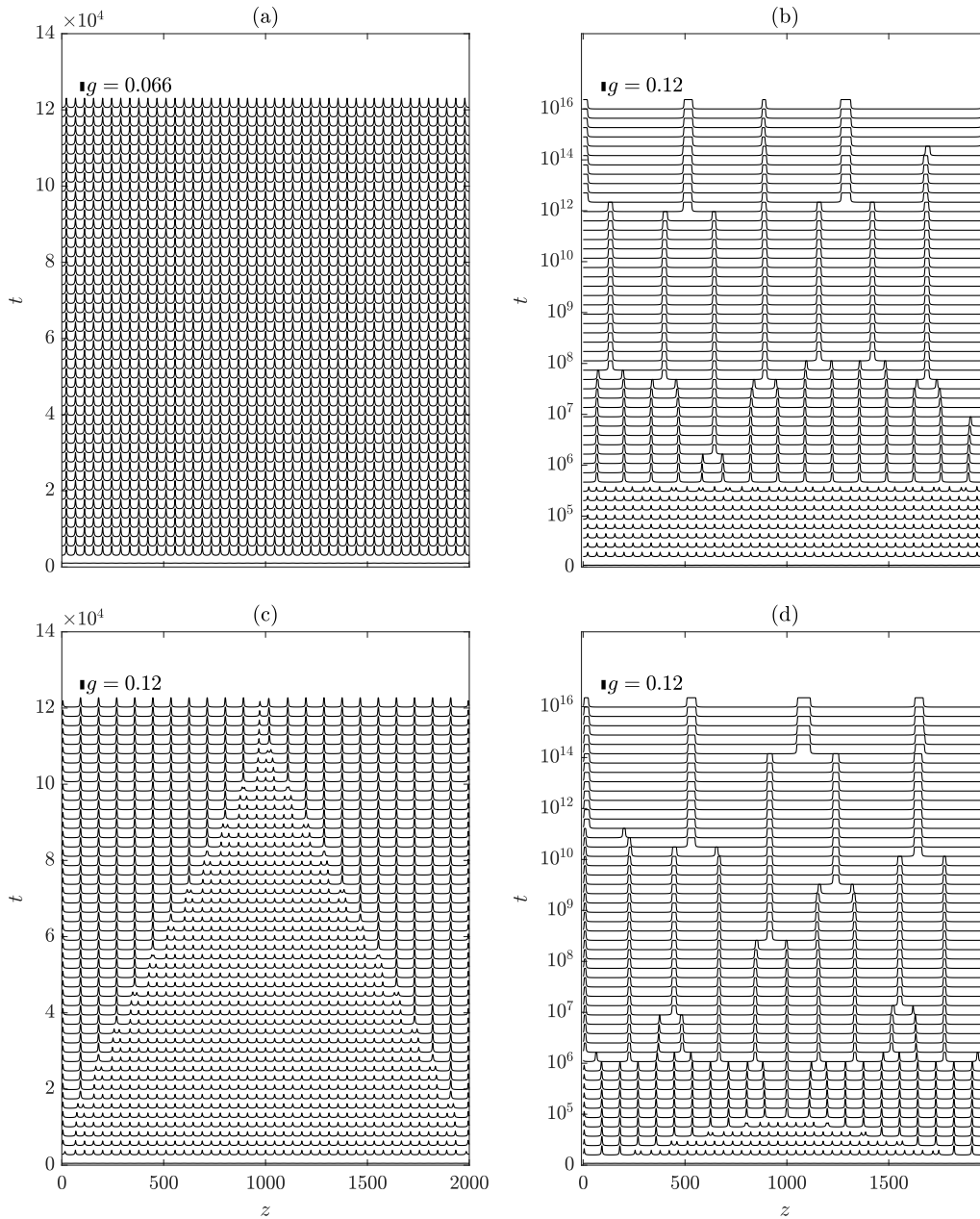


Fig. 3.6 Time evolution of the buoyancy gradient $g(z, t) = b_z(z, t)$, resulting from solution of the system (3.12)–(3.14) for fixed-buoyancy boundary conditions (3.26), and initial conditions (3.30)–(3.31), with $n = 45$, background buoyancy gradient $g_0 = 0.0218$, dissipation parameter $r = 50$, and domain thickness $H = 2000$. Zero-energy-flux boundary conditions (3.27) are adopted in (a) and (b); fixed energy conditions (3.28) are adopted in (c) and (d). The scale bar at the top left of each panel indicates the magnitude of the gradient $g(z, t)$.

state of the system — the solution will continue to evolve through mergers until eventually a single interface remains.

Figures 3.6(c,d) show the integration carried out with fixed-energy (Dirichlet) boundary conditions (3.28) instead of no-flux (Neumann) conditions (3.27), with all other parameters and conditions identical to those used in the simulation shown in Figs. 3.6(a,b). As with the Neumann conditions, the initial perturbation develops into 45 spikes, which undergo mergers. However, the first mergers now appear at the earlier time of $t \approx 15000$, first near the boundaries, and progress inwards towards the centre of the domain, until all but one spike has merged with its neighbours by $t \approx 110000$. After the initial development of the layers, the outermost interfaces move to the boundaries, resulting in a thicker layer. This thicker layer provokes the second spike from the boundary to merge with the third, creating another thicker layer. In turn this provokes a merger of the next two spikes, with the process continuing into the interior. After this first group of mergers, the dynamics are very similar to those in Figs. 3.6(a,b). Successive mergers take place evenly across the domain, and the most notable difference from Figs. 3.6(a,b) is the time at which mergers happen — which is a consequence of the different times at which the first mergers are complete.

The key conclusion to be drawn is that, for fixed-buoyancy boundary conditions, the evolution of layers is largely unaffected by the boundaries (except at early times, in the case of fixed-energy boundary conditions). The layered region evolves independently through merger events until a single interface remains in the middle of the domain. This behaviour differs from the situation of BLY, where edge regions moved into the interior (cf. Fig. 3.1), gradually engulfing the layers until a uniform state exists across the entire domain. Further numerical simulations with more complex initial conditions show that even for initial conditions that do produce edge regions, fixed-buoyancy boundary conditions prevent the intrusion of the edge regions into the interior.

3.4.2 Evolution to late times

We now turn our attention to the long-term nonlinear evolution of solutions to the full system (3.12)–(3.14), for non-zero values of Pe^{-1} and Re^{-1} . As discussed in Sec. 3.4.1, we take boundary conditions (3.26) and (3.27) to prevent the development of expanding edge regions and provide a clean framework in which to analyse the dynamics of layers. For the buoyancy, we take initial condition (3.30), namely a uniform buoyancy gradient perturbed by the wavenumber of maximum growth rate. For numerical convenience, we initialise the energy with the steady-state energy corresponding to $Pe^{-1} = 0$ — this is appropriate because the values of Pe^{-1} that we consider are sufficiently small that the true steady-state energy is close to the energy for $Pe^{-1} = 0$. In the numerical solutions, the energy adjusts rapidly to its true steady-state value.

One aim of our numerical simulations is to demonstrate how the predicted wavenumbers of maximum growth rate, and the growth rates themselves, are manifest in the

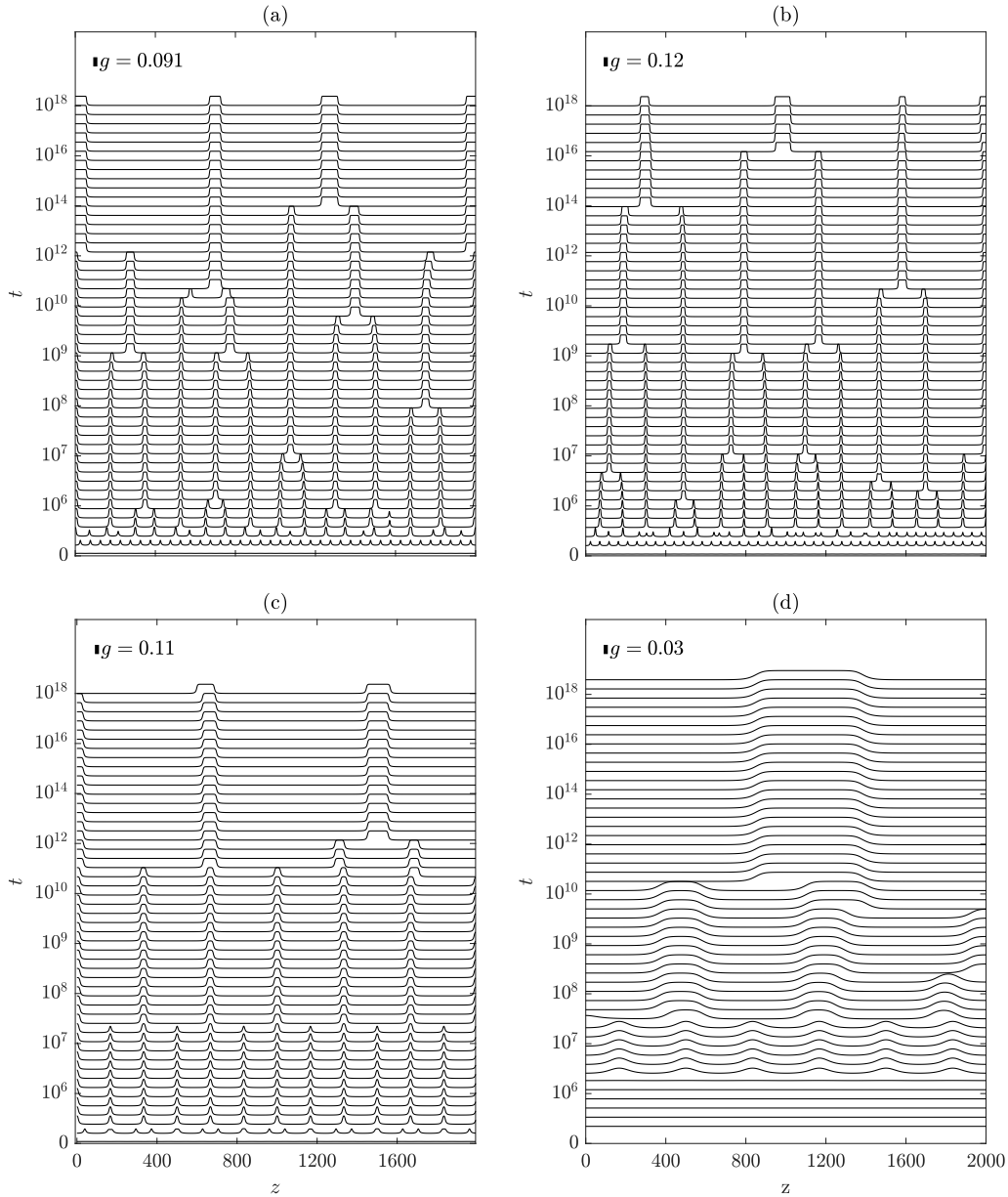


Fig. 3.7 Long-time evolution of the buoyancy gradient $g(z, t)$, resulting from solution of the system (3.12)–(3.14) with diffusion included; in the basic state $g_0 = 0.0218$. Panel (a) shows a typical temperature-stratified case with $Pe^{-1} = 0.01$, $Re^{-1} = 0.1$, and $n = 40$ initial interfaces; (b) a typical salt-stratified case with $Pe^{-1} = 0.0001$, $Re^{-1} = 0.1$, $n = 43$; (c) $Pe^{-1} = 0.001$, $Re^{-1} = 1$, $n = 24$; (d) $Pe^{-1} = 0.1$, $Re^{-1} = 1$, $n = 6$. In each case, the dissipation parameter $r = 50$. The scale bar at the top left of each panel indicates the magnitude of the gradient $g(z, t)$.

nonlinear solutions; these predictions are detailed in Table 3.2. First, we show solutions for parameters relevant to typical temperature- and salt-stratified water at $\text{Re}^{-1} = 0.1$. Next, we consider two choices of parameters that predict, and produce, significantly fewer layers, thereby demonstrating the behaviour of larger-scale layers and interfaces. We conclude this section by investigating the trends in the long-term evolution of layers and the occurrence of mergers, inferring a general law describing the number of interfaces with time.

In Sec. 3.3.3, we showed the effects of changing parameter values on the initial development of layers. Figure 3.7 demonstrates the effects of changing Pe^{-1} and Re^{-1} on solutions of (3.12)–(3.14), for values chosen from Table 3.2. In each case, we take the dissipation parameter $r = 50$, and choose the background buoyancy gradient to be $g_0 = 0.0218$. This value of g_0 is chosen to be approximately in the middle of the unstable range of buoyancy gradients predicted for this value of r , for a wide range of choices of Pe^{-1} , as seen in Fig. 3.3(b).

Figure 3.7(a) shows a typical temperature-stratified case with $\text{Pe}^{-1} = 0.01$ and $\text{Re}^{-1} = 0.1$, chosen such that $\text{Pr} = \text{Pe}/\text{Re} = 10$. In the initial condition (3.30), we take $n = 40$, giving a predicted linear growth rate of 1.15×10^{-3} . The initial perturbation grows into a series of 40 layers across the entire fluid depth, which undergo a set of mergers by $t \approx 0.5 \times 10^6$. Successive merger events take place, until there are four interfaces remaining by $t = 10^{18}$. The maximum gradient in an interface (shown in the plot as the height of a spike) is initially $g = 0.056$, increasing to $g = 0.91$ in the first set of mergers. After the first mergers are complete, successive mergers do not increase the maximum gradient, but instead create thicker interfaces, conserving the total density difference across an interface following a merger.

Figure 3.7(b) shows a typical salt-stratified case with $\text{Pe}^{-1} = 0.0001$ and $\text{Re}^{-1} = 0.1$, such that $\text{Sc} = \text{Pe}/\text{Re} = 1000$. Here we take $n = 43$ in the initial condition (3.30), giving a growth rate of 1.5×10^{-3} , approximately one and a half times greater than that in the temperature-stratified case shown in Fig. 3.7(a). The system initially develops into 43 layers, which merge by $t \approx 0.9 \times 10^6$, taking almost twice as long as for the temperature-stratified case. Thus, the increased linear growth rate of perturbations does not imply that mergers happen more quickly. The maximum interfacial gradient is initially $g = 0.064$, increasing to $g = 0.12$ after the first mergers — these gradients are both slightly larger than for the temperature-stratified case, reflecting the fact that smaller values of Pe^{-1} give a larger range of unstable buoyancy gradients in the linear analysis of Sec. 3.3.2.

Figures 3.7(c,d) show the evolution of the system for parameter choices that produce significantly smaller wavenumbers of maximum growth rate. In both cases, we take $\text{Re}^{-1} = 1$. Figure 3.7(c) has $\text{Pe}^{-1} = 0.001$, which predicts a wavenumber of maximum growth rate corresponding to $n = 24$. Here, the evolution resembles that in Figs. 3.7(a,b), with the main difference being the initial number of layers. The predicted growth rate is 5×10^{-4} , approximately half that for the temperature-stratified case. The first set of mergers is complete by $t \approx 4 \times 10^5$ — similar to both Figs. 3.7(a,b), demonstrating again

that the linear growth rate cannot be used to predict a timescale for mergers. Figure 3.7(d) has $\text{Pe}^{-1} = 0.1$, giving $n = 6$ as the most unstable wavenumber. The linear growth rate of 2.6×10^{-6} is significantly smaller than in any of the other plots, and clear layers are not apparent until $t > 10^6$. The first mergers occur at $t \approx 10^8$. The interfaces are very thick, with small gradients: the maximum interfacial gradient is $g = 0.03$, a factor of three smaller than for the cases shown in Figs. 3.7(a–c).

The plots in Fig. 3.8 show how the interfaces change over long timescales; they are derived from several numerical simulations across a range of parameters chosen to cover the full unstable range shown in Fig. 3.3(b). The parameters used to produce these results are given in Table 3.3. Figure 3.8(a) shows the maximum buoyancy gradient across the whole solution at each time; this corresponds to the gradient at the centre of the sharpest interfaces (and is representative of all interfaces). Figure 3.8(b) shows how the number of interfaces decreases with time; merger events can be seen as sharp downward steps in the profiles. In Fig. 3.8(a), the early phase of the evolution is marked by a smooth increase in the gradient from the initial perturbation to a value at which the first interfaces appear. The maximum gradient then remains unchanged for a prolonged period, until the first mergers occur. At this point, the maximum gradient increases sharply before settling again at a new value. In most cases, this second increase in gradient has approximately the same magnitude as the first. However, for the red and yellow lines (beginning at $\max(b_z) = 0.015$ and 0.8 respectively) the second increase is significantly smaller. Once the stable maximum gradient is reached, it remains unchanged, even with further mergers, as can be seen by comparison of Figs. 3.8(a,b). However, the density difference across two merging interfaces must be conserved, so the remaining interface is thicker than either of the two interfaces that formed it. This increase in interface thickness can be seen clearly in Figs. 3.7(a–d).

In Fig. 3.8(b), each solid line begins at the time when the initial layered state is fully formed (corresponding to the end of the first step up in Fig. 3.8(a)), and tracks the number of interfaces, including those on the boundaries. The interfaces are determined by locating all peaks in the buoyancy gradient with a magnitude above a critical value, chosen to be the steady gradient of the initial interfaces seen in Fig. 3.8(a). BLY briefly state that the timescale for successive mergers ‘becomes exponentially long’. However, the expanding edge regions in their solutions prevent a thorough investigation of long-term merger behaviour. Our choice of boundary conditions allows us to examine the long-term evolution of the solutions and, in turn, quantify this dependence more precisely. In Fig. 3.8(b), the dashed lines are fitted according to a least squares regression, and show a good fit with the general relation

$$\frac{1}{N} \sim \alpha \log t + \beta, \quad (3.32)$$

representing an inverse (natural) logarithmic dependence for the number of layers over time, $N(t)$. As shown in Fig. 3.8, the relation (3.32) captures the overall trend for $N(t)$ over several orders of magnitude of time, potentially indicating a self-similar structure to successive layer mergers. Expression (3.32) indicates the existence of a general law for how interfaces in stratified turbulence evolve, with the coefficients α and β dependent on the viscosity and diffusivity of the fluids. Values of α and β for each case are given in Table 3.3. Analysis of layering in the Cahn-Hilliard equation has demonstrated such a logarithmic timescale (Kawakatsu & Munakata, 1985), which has been confirmed by several numerical studies (e.g. Nagai & Kawasaki, 1983; Watson *et al.*, 2003). BLY showed that their model could be transformed into the Cahn-Hilliard equation through an asymptotic analysis about the point of marginal stability in g_0 - r space (the tip of the black curve in Fig. 3.3(b)). Figure 3.8(b) demonstrates such a logarithmic timescale across the entire unstable range of parameters, confirming the relevance of Cahn-Hilliard dynamics to models of layering that employ the Phillips effect.

3.5 Discussion

In this chapter, we have made four primary developments in the analysis of layering in stratified turbulent flow. First, we have presented a general horizontally averaged model derived from the Boussinesq equations using a spatial averaging approach. Our formulation retains the effects of viscosity and molecular diffusivity, and explicitly clarifies the closure assumptions required. Second, we have demonstrated how the layering instability is affected by molecular diffusivity and viscosity. Third, we have demonstrated the importance of boundary conditions on the long-term evolution of the solutions. Finally, we have shown how the long-term distribution of layers changes through merger events, with the inference of a general power law dependence describing the number of layers as a function of time.

In order to understand the essential conditions for layer formation, we investigated the linear stability of uniform gradient, uniform energy steady states. Increasing Pe^{-1} suppresses the instability by decreasing the range of unstable gradients. Increasing Re^{-1} does not affect which gradients lead to instability, but does decrease the range of unstable wavenumbers, so the instability occurs only at larger scales. Since for temperature-stratified water, Pe^{-1} is two orders of magnitude larger than for salt-stratified water, the latter is more susceptible to layering.

We have shown that fixed-buoyancy boundary conditions ensure that the layered regions extend across the entire depth of the domain for all time. This contrasts with the case of fixing the buoyancy gradient, which allows layer-free edge regions to expand into the interior, gradually engulfing the layers (Balmforth *et al.*, 1998). In our numerical solutions, multiple layer merger events take place in groups, with the general property that the maximum gradient across an interface approximately doubles after the first group of mergers. In subsequent mergers, the gradient does not increase further. Instead,

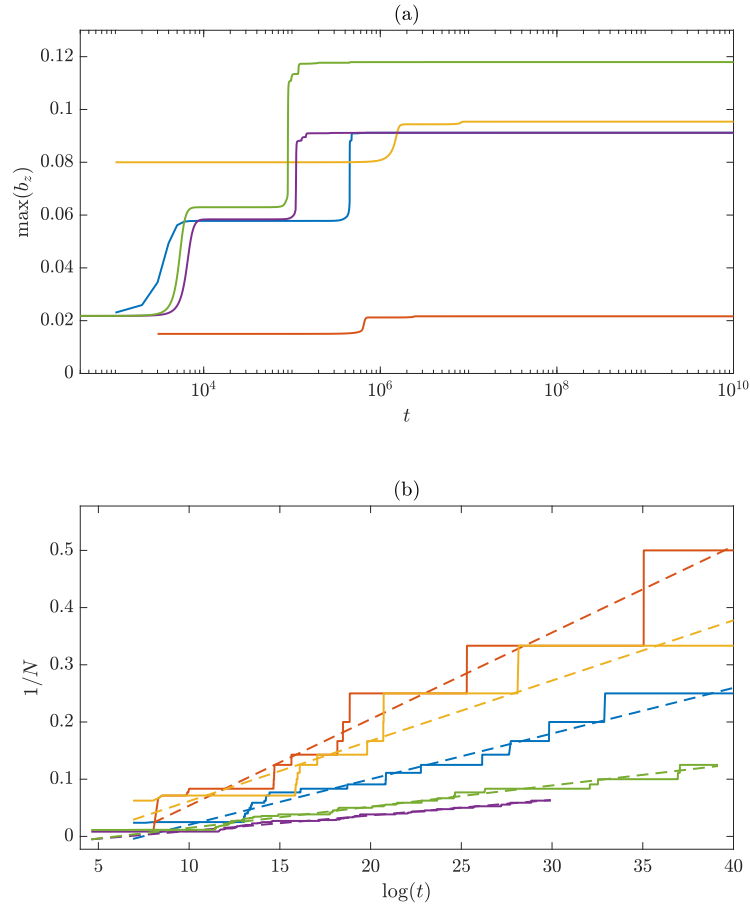


Fig. 3.8 Plots showing variation in the interfaces over time, obtained using a numerical peak finder to count peaks in the buoyancy gradient b_z . Panel (a) shows the maximum gradient at each time, corresponding to the gradient at the centre of the sharpest interface. Panel (b) shows the number of interfaces at each time, plotted against the natural logarithm $\log(t)$. The dashed lines show the best fits to relation (3.32). Parameters used for each curve are reported in Table 3.3.

Line	r	Pe^{-1}	Re^{-1}	H	n	α	β
—	50	0.01	0.1	2000	40	0.0080	-0.059
—	100	0.1	0.1	2000	12	0.015	-0.098
—	15	0	0	2000	15	0.011	-0.044
—	50	0.01	0.1	6000	119	0.0027	-0.018
—	50	0.001	0.1	4000	87	0.0037	-0.022

Table 3.3 Parameter values for the plots in Fig. 3.8, and corresponding values of α and β for the trend law (3.32).

the thicknesses of the interfaces increase, conserving the total density difference across the interface. Our analysis of the solutions over long times shows that after the initial development of layers, the number of interfaces conforms to the law $1/N \sim \log t$, thereby generalising the link to Cahn-Hilliard dynamics shown by BLY.

The model presented in this chapter is intended as a phenomenological study, rather than a direct comparison to observations. The Reynolds numbers considered in Section 3.3.2 are considerably smaller than the values required for real turbulence, but were chosen instead to demonstrate the effects of changing Re . This would not have been possible at more realistic values, as the results would have been almost identical to $Re^{-1} = 0$. To produce realistic predictions, it is necessary to calibrate the value of the parameter ε — this could be done by comparing the stability curves in Fig. 3.3(b) to the real layering boundary found in experimental or observational studies.

The mixing length formulation of BLY assumes that all the turbulent transport in the system is done by turbulent mixing, with an eddy diffusivity of $le^{1/2}$. In this chapter, we have allowed for finite Re and Pe , leading to altered flux terms. These fluxes include BLY's original $le^{1/2}$, but also take into account the small component of diffusive transport represented by Re^{-1} and Pe^{-1} in the denominator. These terms are of secondary importance in this chapter, with a single component of density, however in later chapters where we study double diffusive layering, the diffusive terms are vital, as layering is driven by the difference in diffusivities between the two components of density.

In the following chapters we extend this work in several ways. We present an experimental study to test some of the predictions of the model in Chapter 4. Next, this work on stratified layering provides a basis for generalisation to other systems where layering occurs. In particular, the two-component model for buoyancy and energy can be expanded to a double-diffusive system by the inclusion of an additional equation for the second component of buoyancy. This produces a three-component model for temperature and salinity (or any other two components of density), and energy. A general stability analysis for three-component systems is presented in Chapter 5. Two specific physical problems suggest themselves. The first, which is presented in Chapter 6, is to study a three-component model with an external forcing, as used here. This will provide insights into the second problem, in which the turbulent motions arise naturally from the double-diffusive instability of the basic state. This work is discussed in Chapter 7.

Chapter 4

Experimental study of stirred stratified layering

4.1 Introduction

As mentioned in Sec. 1.4, there is a significant body of experimental work on staircase formation, most commonly in stirred stratified convection. In this chapter we relate the model of Chapter 3 to real-world fluid systems, by presenting a new experimental study.

We saw in Sec. 3.3.2 that for any fixed set of parameter values, the model predicts that there is a finite range of dimensionless buoyancy gradients b_z that are unstable to the Phillips instability. Recall that the variables were nondimensionalised as follows:

$$\hat{b} = \frac{d}{U^2} b, \quad \hat{z} = \frac{1}{d} z, \quad (4.1)$$

where hats denote dimensionless variables, and U and d are the characteristic velocity and length scales of the stirring. As such, the dimensionless buoyancy gradient is

$$\hat{b}_z = \frac{d^2}{U^2} b_z \equiv \frac{d^2}{U^2} N^2 = \text{Ri}, \quad (4.2)$$

where N^2 is the Brunt-Väisälä frequency, and Ri is the (local) Richardson number, which measures the relative strength of the density gradient in comparison to shear. This means that the finite range of dimensionless buoyancy gradient for layering to occur corresponds to a finite range of Ri . Note that the dimensionless buoyancy gradient also defines an inverse squared Froude number Fr^{-2} (where Fr measures the ratio of inertial to gravitational forces on a fluid element to its weight); for consistency with previous literature we write $\hat{b}_z = \text{Ri}$.

From a physical perspective, it makes sense that layering will occur only for a finite range of Ri . If the density gradient is too strong compared to the shear, then the turbulence cannot disrupt the gradient enough to form layers. Conversely, if the turbulence is too

strong compared to the density gradient, the entire fluid will mix and become homogenous, rather than evolving into layers.

The experimental study of Ruddick *et al.* (1989) involved a fluid with a uniform stable salt gradient being stirred by the oscillation of a grid of rods. Low stirring rates led to the formation of layers, while higher stirring rates caused the density gradient gradually to decrease while remaining smooth, eventually homogenising. Park *et al.* (1994) developed this work, using a single stirring rod rather than a grid. Both the speed of the rod and the strength of the stratification were varied, allowing Re and Ri to be changed independently.

The experiments of Park *et al.* (1994) initially produced mixed layers at the top and bottom boundaries — this is because the no-flux condition across the boundaries required the vertical gradient to vanish. For small values of Ri , the density profile showed two advancing mixed layers moving into the interior with little interior structure. For larger initial values of Ri , interfaces first formed between the boundary mixed layers and the interior. These interfaces moved towards the interior, eventually becoming close enough and merging. For an even larger Ri , multiple interfaces formed, resembling those seen in Chapter 3. For sufficiently high Ri , long-lasting steps were easy to confirm, but for smaller values, steps did not maintain their shape for a very long time, giving a marginal region where it was unclear whether layering was occurring or not. For sufficiently small Ri , transient interfaces were sometimes observed, but dissipated quickly, leaving a generally uniform gradient. The plot in $Re - Ri$ space in Fig. 4.1 shows the parameter regions where layering occurred.

A further study by Holford & Linden (1999b) built upon the work of Park *et al.* (1994), this time stirring by moving a rake of bars through the fluid. They found that at low Ri , the density profiles remained smooth, with well-mixed boundary layers growing from the top and bottom, as found by Park *et al.* (1994). At low enough Re , layering developed by a Phillips mechanism in a certain range of Ri . However, at high values of Ri , layers formed due to mixing by vortex sheets left in the wake of the stirring rake.

Zatsepin *et al.* (1999) conducted similar experiments to Park *et al.* (1994) and Holford & Linden (1999b), stirring using oscillating vertical rods, once again producing layers from an initially linear stratification. A summary plot of their results, and those of Park *et al.* (1994), is shown in Fig. 4.1, showing a clear boundary between regions of $Re-Ri$ space where layers do and do not form.

The existence of a minimum value of Ri for layers to form has been clearly established by the numerous experimental studies detailed above. However, according to the theory of BLY and Chapter 3, an upper boundary in Ri should exist, above which the density gradient is too strong compared to the stirring speed for layers to form. No such boundary has yet been demonstrated experimentally. We saw in Fig. 3.3(b) that the unstable range of $b_z \equiv Ri$ decreases as Pe^{-1} increases. Writing $Pe = PrRe$, and assuming Pr is fixed, this means that the unstable range of Ri should increase as Re is increased. We found the form of the boundary in $r-g_0$ space to be (3.23) when $Pe^{-1} = Re^{-1} = 0$; with the appropriate value of

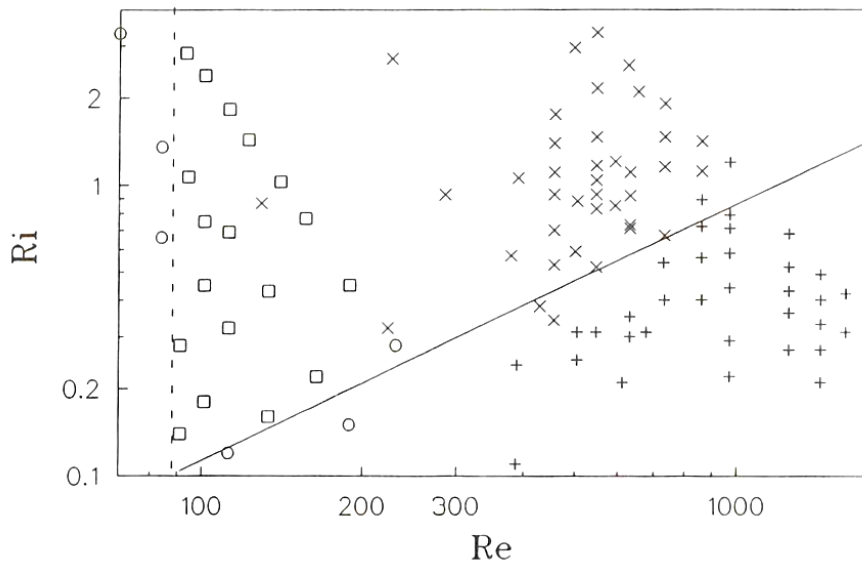


Fig. 4.1 Diagram summarising experimental runs of Park *et al.* (1994) and Zatsepin *et al.* (1999) in Re–Ri plane: \times - layers (L), $+$ - no layers (N) (Park *et al.*, 1994), \square - (L), \circ - (N) (Zatsepin *et al.*, 1999). The dashed vertical line approximately separates runs with turbulence (to the left) from those without (to the right). The solid line separates runs with (above) and without layers (below). (Taken from Zatsepin *et al.*, 1999)

r , this boundary should give the asymptotic values of the critical values Ri_c as $Re \rightarrow \infty$. Figure 4.2 shows the locus of marginal stability in Re–Ri space on which $F_g C_d - F_d C_g = 0$. There is a clear minimum value of Re for instability, and as Re increases, there are upper and lower asymptotes for Ri as $Re \rightarrow \infty$. Inverting (3.23) for $g_0 \equiv Ri$, we obtain the values for these asymptotes

$$Ri_c \sim \frac{4(r-1) \pm 2\sqrt{r^2 - 14r + 1}}{3(1+r)^2}. \quad (4.3)$$

Setting $r = 50$ gives the two values $Ri_c \sim 0.0142$ and 0.0360 . Fig. 4.2 shows the full predicted stability boundary in Re–Ri space, showing two critical values of Ri for each value of Re. Note that this is not a quantitatively accurate picture — it shows layering for very small values of Re where there will be no turbulence, and hence the turbulent model of Chapter 3 is no longer valid. However, we expect the qualitative picture to be valid, with layering occurring for only a finite range of Ri for each value of Re.

The Richardson number can be changed by varying either N^2 , d or U . Practically, it is simplest in an experimental setup to change U , as changing N^2 requires refilling the tank with a new salinity gradient, and changing d requires a change to the geometry. The velocity scale U can be varied simply by changing the speed of the motor driving the stirring. As such, to achieve high Ri requires low stirring speeds, leading to low Re. At sufficiently low Re, the fluid will no longer be turbulent, with no layering occurring. So to investigate layering at high Ri requires a particular experimental setup, with a fast enough stirring speed to ensure that Re is large enough for the fluid to be turbulent, and at the

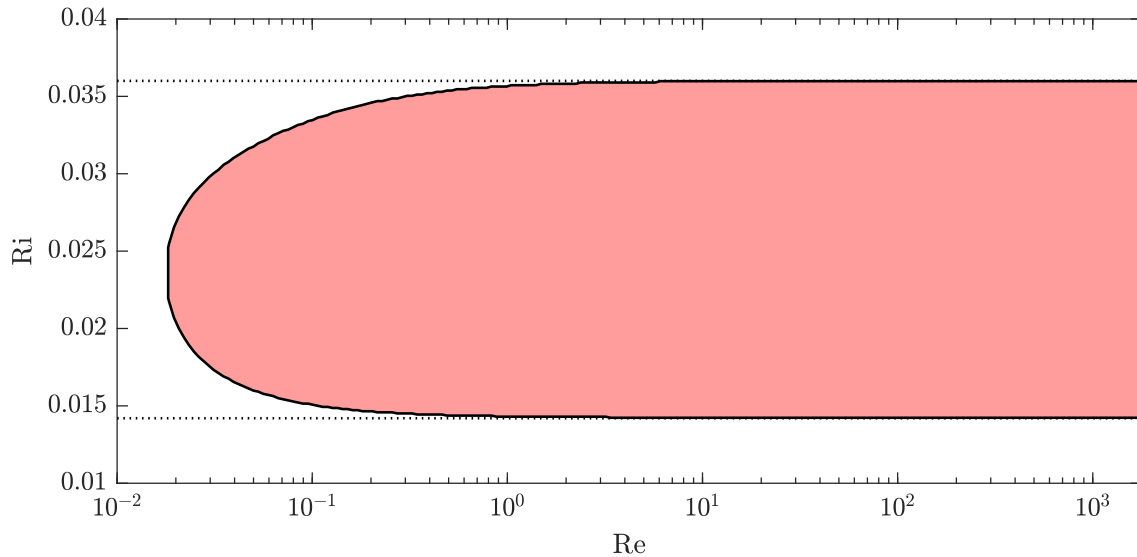


Fig. 4.2 Stability boundary in Re–Ri space for the stirred stratified system considered in Chapter 3, with dissipation parameter $r = 50$. For each value of Re, there are upper and lower values of Ri_c , between which the system is unstable to layering. Dashed lines show $Ri = 0.0142$ and $Ri = 0.0360$, the asymptotic limits of Ri_c as $Re \rightarrow \infty$.

same time strong enough buoyancy gradients that the high Ri boundary for layering can be captured.

4.2 Experimental method

We present a basic experimental study to establish the existence of the upper critical value Ri_c , above which layering does not take place. In each experiment, we create a uniform stratification, and start stirring at a low speed. We gradually increase the stirring speed, decreasing Ri, until layers form, thus establishing the existence of the upper boundary.

We employ a basic experimental setup taking advantage of equipment already available in the School of Mathematics laboratory. Instead of a back-and-forth stirrer in a rectangular tank, the stirring is provided by a stationary rod suspended in a rotating cylindrical tank. To visualise the density, we use a shadowgraph method, with a torch shining through the tank projecting an image on a sheet of tracing paper. A camera pointing at the screen photographs the shadowgraph image at fixed time intervals.

4.2.1 Double bucket method

The stratification is created in the tank using the double bucket method (Oster, 1965). Fig. 4.3 shows the setup for this process. Two buckets are filled with water: Bucket A with 4500ml fresh water, Bucket B with 4500ml salty water. The salt solution is made in advance of the experiment to allow it to regain the ambient temperature. Before creating the stratification in the cylindrical tank, the density of the salty water in Bucket B is measured

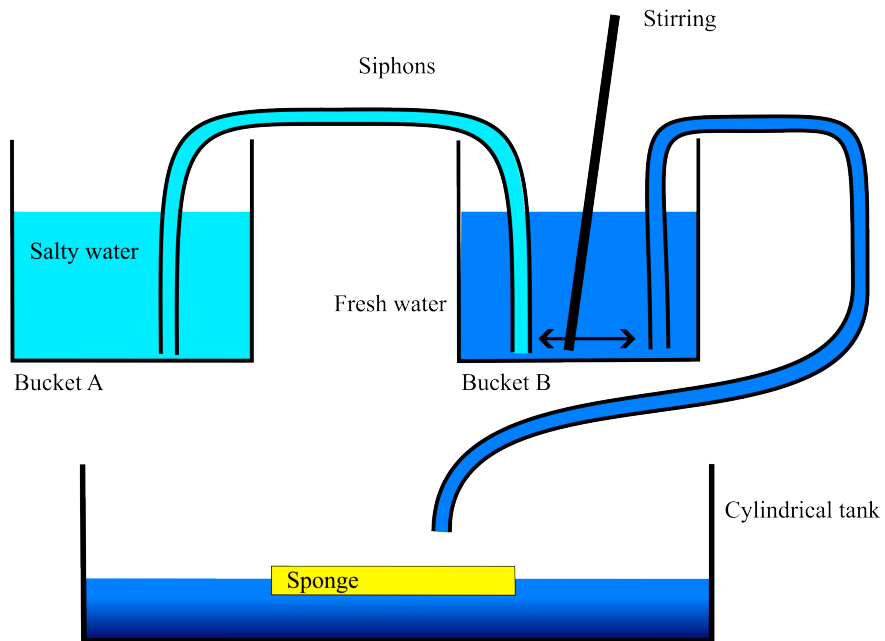


Fig. 4.3 Diagram showing double bucket setup for filling the cylindrical experimental tank.

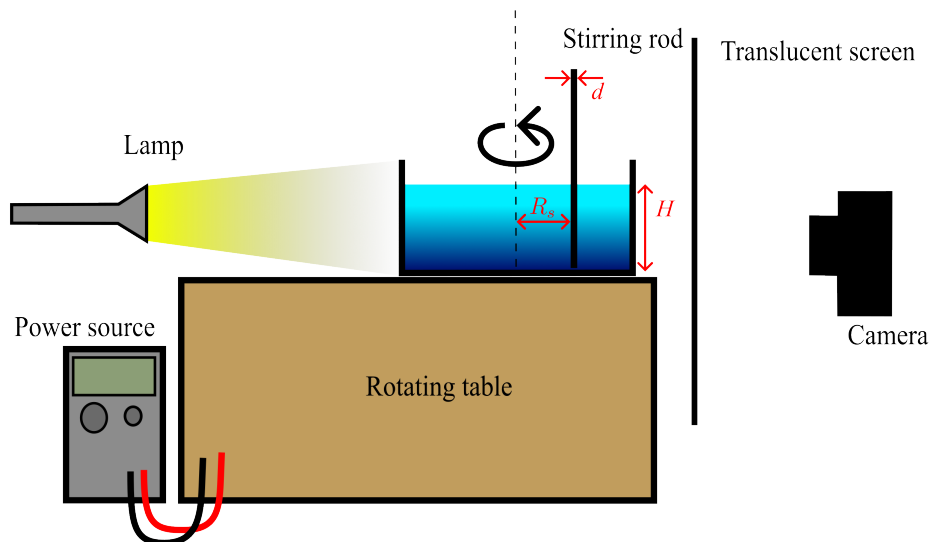


Fig. 4.4 Diagram showing the rotating table setup. A metal rod of diameter d is suspended in the fluid at radius R_s , and the rotating table is turned on, thus stirring the fluid.

using a hydrometer. Both buckets are connected by a siphon so that a reduction in water level in one bucket draws in water from the other. Salty water is siphoned out of bucket B and onto a floating sponge in the cylindrical tank. The sponge floats on the surface of the tank, so that new water spreads out on top with a low velocity, rather than penetrating into the fluid owing to its momentum. Bucket B is continuously stirred, so that it remains well mixed, while being diluted from bucket A. The tank is full when the buckets are empty.

Note: the cylindrical tank does not have a flat bottom, so a plastic base is inserted. However, the base is lighter than a saturated salt solution, so to prevent it from floating, a magnet is taped to the bottom of the base, and another magnet on outside of the bottom of the tank. There is a depression in the middle of the rotating table that the magnet fits inside, allowing the tank to sit flat.

4.2.2 Layer formation

Fig. 4.4 shows the experimental setup. The tank is placed on top of the rotating table and the stirring rod inserted halfway between the edge and the centre (7.5cm from the edge). The torch is set up to shine through the tank, and the screen attached to the opposite end of the table so that an image is projected. A camera is positioned on the opposite side of the screen from the tank, pointing towards the screen. After the water in the tank is still, the camera is set to take pictures at fixed intervals (30s, normally), and the tank set to rotate. The initial starting speed depends on the stratification, but low voltages of $\approx 4 - 5V$ are appropriate. The time period for the rotation must be measured. The initial spin-up takes several minutes before all transient behaviour dies down — during this time, there is significantly more mixing activity in the lower section of the tank, as the rotation of the bottom boundary provides forcing. We rotate at the initial speed for 30 minutes to allow time for this transient behaviour to decay. If no layers have formed after this time, the voltage is increased. We calculate the new period of rotation and rotate the tank for 15 minutes. If no layers have formed, we continue increasing the voltage every 15 minutes until layer formation is observed.

Layers can be identified by bright bands representing interfaces. These can be distinguished from normal turbulence by their continued existence over reasonably long times.

To calculate the Richardson number, we take d to be the diameter of the rod in metres, and $U = \omega R_s$ to give $Ri = \frac{d^2}{U^2} \frac{\partial b}{\partial z}$. The tank that we use has a radius of $R_o = 150\text{mm}$, and the fluid depth is $H = 125\text{mm}$. The rod of diameter of $d = 12.5\text{mm}$ is placed so that $R_s = R_o/2 = 75\text{mm}$. Writing ρ_b for the density of the salty water in Bucket B, and taking $\rho_0 = 1\text{kg m}^{-3}$ for the fresh water, the buoyancy of the salty water (in ms^{-2}) is $b_b = g(\rho_0 - \rho_b)/\rho_0 = g(1 - \rho_b)$, with $g = 9.81\text{ms}^{-2}$, and the buoyancy of fresh water is 0. The buoyancy gradient (in s^{-2}) is therefore calculated as $b_z = g(1 - \rho_b)/H$. The kinematic viscosity of salt water is taken to be $\nu = 10^{-6}\text{m}^2\text{s}^{-1}$. Experiments were carried out for initial stratifications with bottom density range $1.06 \leq \rho_b \leq 1.195\text{kg m}^{-3}$. We

measure the time period of the rotation T and density of salty water ρ_b , and use these to calculate the following

$$U = \frac{0.47}{T} \text{ms}^{-1}, \quad b_z = 78(\rho_b - 1)\text{s}^{-2}, \quad \text{Ri} = 0.055T^2(\rho_b - 1), \quad \text{Re} = 12500 \frac{0.15\pi}{T}. \quad (4.4)$$

4.3 Results

We begin by presenting the results of a single experimental run, displaying the shadowgraph results. Figure 4.5 shows the images captured at several times throughout an experiment. We begin with a slow rotation rate, with the fluid mostly non-turbulent. On increasing the rotation rate (decreasing Ri), the system attains a turbulent state, but no layers form initially. On increasing the rotation rate further, an interface begins to form. The interface can be seen first near the bottom of the image, although the true interface is higher up in the tank, with optical effects causing it to appear lower. As the stirring continues, the interface gradually moves further up the tank.

We repeat the experiment for a range of initial salinity gradients, each time starting with a slow rotation rate that is gradually increased. Each gradient/rotation speed pair is classified as either layered (L) or nonlayered (N). The scatter plot in figure 4.6 shows this classification, on (a) b_z - U axes and (b) Re-Ri axes. For each gradient, the points with the lowest values of U are classified as (N), with higher speeds giving layers (L). For three experimental runs, the speed was gradually increased further; in two of these cases a further transition to nonlayered (N) occurred at the point where the speed was fast enough to destroy the existing interface.

From Fig. 4.6(a) it is clear that, for fixed b_z , there is a critical value for U above which layers will form. However, Fig. 4.6(b) is less conclusive. For the largest values of Ri, no layers form, but for intermediate values of Ri, the layering behaviour is strongly dependent on the value of Re. Data points from each experimental run lie on lines $\text{Ri} = \text{constant}/\text{Re}$, so in Re-Ri space the points have only a small spread. By comparison with the predicted stability boundary shown in Fig. 4.2, the rough boundary seen in Fig. 4.6(b) between $600 \lesssim \text{Re} \lesssim 1000$ resembles the curved predicted boundary, but the numerical values of both Re and Ri are significantly different. However, this is to be expected — the theoretical work assumed a dissipation parameter $r \equiv 1/\varepsilon = 50$, with the stability boundaries depending strongly on r . So it is possible that the true value of r is significantly different to the one used. To produce more conclusive results it will be necessary to extend the experiment further, with more experimental runs. Using a setup with different geometry would allow a larger range of values to be investigated — for example, changing the diameter d of the stirring rod produces a linearly proportional change in Re, but a quadratic change in Ri.

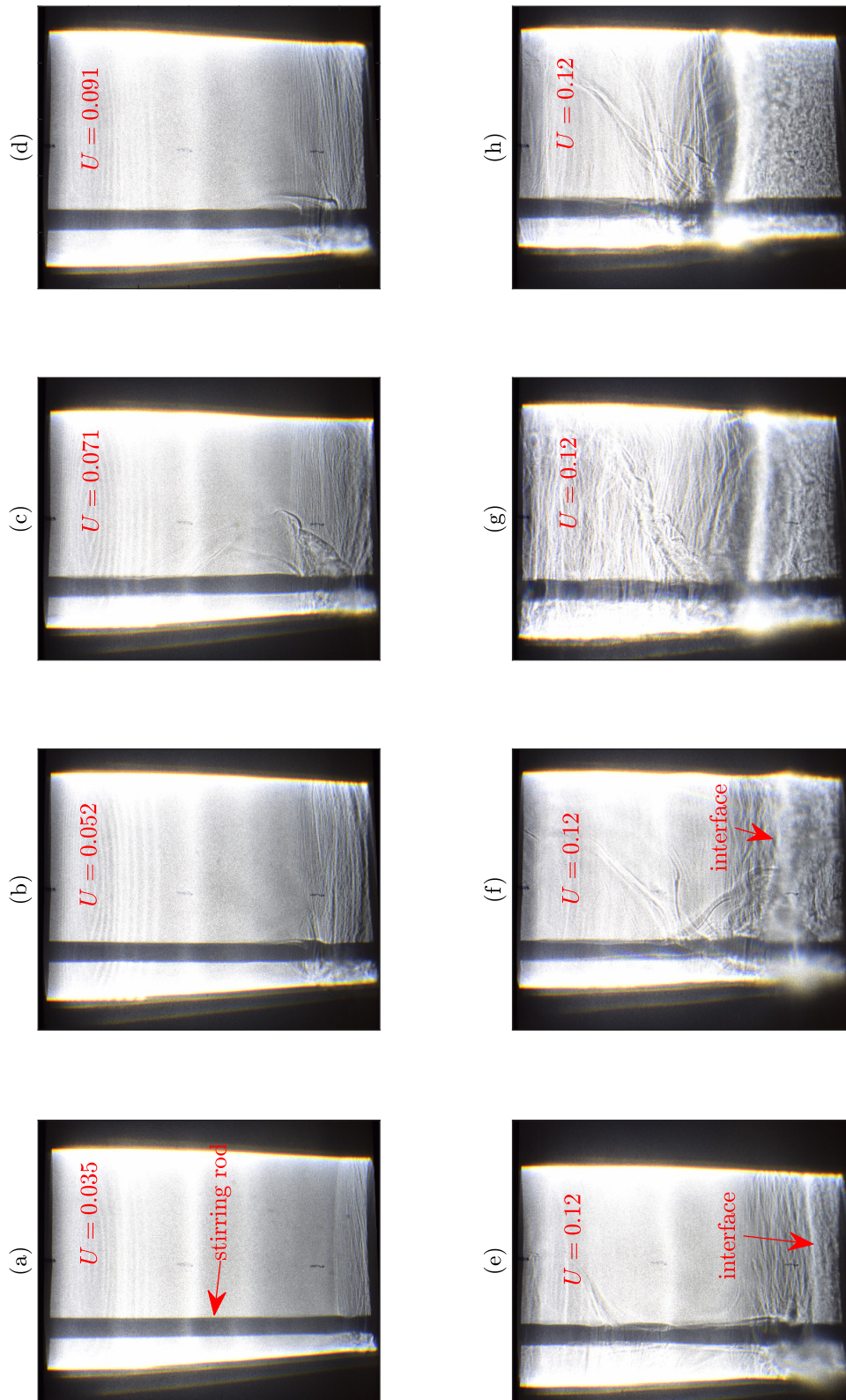


Fig. 4.5 Shadowgraph images of a single experiment run at several different times, rotating at different rates. (a) Initial speed $U = 0.035\text{ms}^{-1}$ with mostly non-turbulent fluid. (b)–(d) Progressively higher rotation rates $U = 0.052, 0.071, 0.091\text{ms}^{-1}$. A large amount of turbulent fluid is visible, but no layers form. (e)–(f) Images taken 4, 12, 18 and 50 minutes after increase in rotation rate to $U = 0.12\text{ms}^{-1}$. An interface is visible as a long-lasting bright band in the lower part of the images. The stirring rod is visible as a dark stripe on the left hand-side of each image. The bright horizontal bands visible in every image are not interfaces, but are likely due to refraction in the tank.

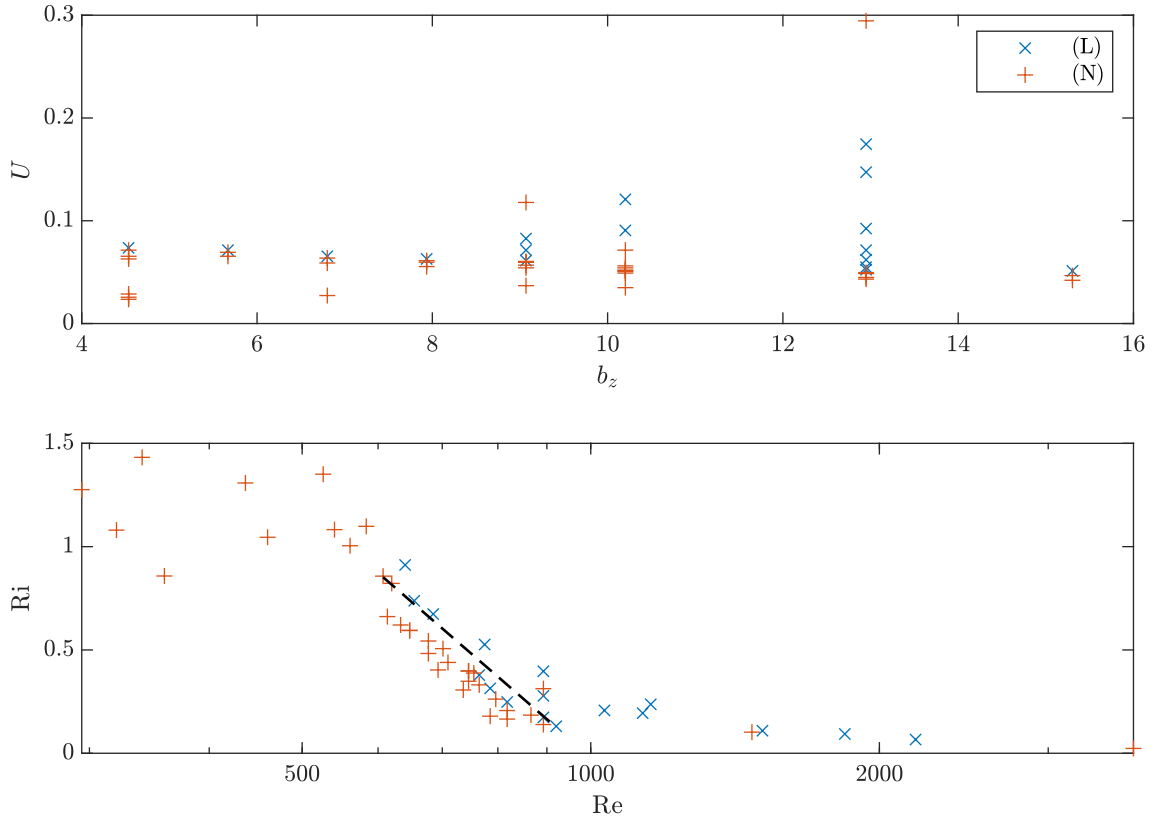


Fig. 4.6 Results of thirteen experimental runs, varying background buoyancy gradient b_z (s⁻²) and characteristic speed U (ms⁻¹). For each run, b_z was fixed, and U gradually increased. Blue crosses represent points where layers formed, red plus signs represent conditions where no layers were evident. Scatter plot on (a) b_z - U axes, (b) Ri - Re axes.)

The stability boundary seen in Fig. 4.6(b) appears to follow the logarithmic curve $Ri \sim 12.05 - 1.7472 \log(Re)$, shown as the dashed black line on the figure. However more data for smaller and larger values of Re is required to confirm this, and to find the equivalent curve for the upper boundary on Ri .

4.4 Discussion

We have conducted experimental work to test the prediction of Chapter 3 that there exists an upper limit on the Richardson number for layers to form. Previous experimental studies have established the existence of a lower limit, but no upper limit (Ruddick *et al.*, 1989; Park *et al.*, 1994; Holford & Linden, 1999a; Zatsepin *et al.*, 1999). Taken together, the lower limit of previous studies, and the upper limit that we test here, lead to a finite range of Ri in which layering takes place.

We adopted a method using a rotating table to provide the stirring motion, rather than moving a stirring rod in a stationary tank as previous studies have done. This has demonstrated a much simpler and cheaper way to investigate the problem than in previous studies, and we do not expect it to have a significant qualitative effect on the evolution after

the spin-up period. To consider the effects of the rotation, we discuss here the mathematical implications of adding Coriolis and centrifugal forces to the model discussed in Chapter 3. To account for a frame rotating at angular velocity Ω in the Boussinesq equation we add the terms

$$-2\Omega \times \mathbf{u} - \Omega \times \Omega \times \mathbf{r}, \quad (4.5)$$

to the momentum equation (2.3), where \mathbf{r} is the position vector. After taking the scalar product with \mathbf{u} to form the energy equation, the Coriolis term $-2\mathbf{u} \cdot \Omega \times \mathbf{u}$ vanishes, while the centrifugal term can be written as

$$\mathbf{u} \cdot \Omega \times (\Omega \times \mathbf{r}) - |\Omega|^2 \mathbf{u} \cdot ((\hat{\mathbf{z}} \cdot \mathbf{r}) \hat{\mathbf{z}} - (\hat{\mathbf{z}} \cdot \hat{\mathbf{z}}) \mathbf{r}) = |\Omega|^2 |\mathbf{u} \cdot \mathbf{r}_\perp|, \quad (4.6)$$

where $\mathbf{r}_\perp = (x, y, 0)$ is the horizontal position. The centrifugal contribution to the energy equation is therefore purely horizontal, and vanishes in the horizontal averaging process of Chapter 2. As such, the model (3.12)–(3.13) is identical in a rotating or inertial frame, so the results of Chapter 3 should be applicable in either case. This does not mean that the rotation has no effect, but rather that it should be accounted for in parameter choices, and possibly in the form of the length scale.

The experimental results shown in Fig. 4.5 show the development of a single interface in the middle of the tank when rotated at a sufficiently high speed. This single interface appeared alone; it is unclear whether the depth of the tank is not sufficient for more interfaces to form, or if a number of narrower layers formed initially and merged into the interface that is seen. The strength of the interface appears to increase over time, with the bright band gradually becoming brighter and thicker. Considering the results of a larger number of experimental runs, Fig. 4.6 shows that while fixing b_z , there is indeed a minimum speed U required for layers to form. However, when considered in Re–Ri space the picture is less obvious. No layers formed for the highest values of Ri, but these all correspond with low values of Re. At lower values of Ri, the value of Re has a significant effect, with layers forming only for larger values of Re.

The interface seen in Fig. 4.5(e)–(h) initially appears to form near the bottom of the tank, and gradually move upwards. The images also might be interpreted as showing more turbulent motion beneath the interface than in the layer above. These observations would be consistent with an interpretation of the results as a mixed layer forming due to interaction with the bottom boundary, with the mixed layer gradually entraining fluid above, leading to its growth upwards. We do not believe that this is the correct explanation for the results, for the following reasons. When the interface first appears, it is approximately a third of the way up the tank; the lower position seen in the images is due to optical effects caused by the cylindrical tank. If the mixed layer was generated by the bottom boundary, it would be expected that the interface would appear much lower down. In addition, during the initial spin-up phase of evolution (not pictured), some transient interfaces do appear to form in the bottom two centimetres of the fluid. These typically last for one or two minutes before

vanishing, and never form into a longer-lasting interface. These transient interfaces seem more likely to be caused by interaction with the bottom boundary, with the main central interface instead being generated by the Phillips effect. The formation of mixed layers due to bottom boundary effects has previously been studied by Manucharyan & Caulfield (2015), who demonstrated that a rotating disc applied to the top of a cylindrical tank of fluid produced expanding mixed layers. The key difference between this previous work and our current study is that in the experiments of Manucharyan & Caulfield (2015), the fluid motion was forced by a rotating top boundary, with the tank remaining stationary, where by contrast in our experiments the entire tank rotates, with only the stirring rod held stationary. The fluid and bottom boundary are moving in the same frame of reference, so we do not expect to see the same effects as are caused by a moving boundary in a stationary tank. A simple test of our interpretation would be to repeat the experiments with a rigid top boundary as well. If a second interface forms closer to the top, then the boundary-mixing interpretation is likely to be correct; if the results are the same as in our current study, then our explanation that layering is caused by the Phillips effect is more appropriate.

Several improvements could be made to this study. First, the parameter space could be extended by the use of different equipment; Ri has a quadratic dependence, and Re a linear dependence, on the diameter of the stirring rod d . Hence, changing d would allow new regions of parameter space to be accessed. Changing the solute would also produce larger ranges of density, and therefore Ri . For example, a saturated solution of potassium hydroxide has a density of 1.5kg m^{-3} , compared to the maximum density of salt water 1.2kg m^{-3} . Second, we were unable to produce quantitative measurements of the fluid density during the experiment. Detailed density profiles could be obtained using a high resolution conductivity probe, but budget constraints prevented this. Lastly, to form a direct comparison to the previous literature, the experiment could be redesigned to use a rectangular tank, with a back-and-forth stirring mechanism, as used by Park *et al.* (1994). As well as being a more direct comparison to previous experimental work, a rectangular tank would produce less distortion to the image than the cylindrical tank used in this study, and there would be no effects due to the spin-up behaviour of the fluid.

If this study had produced more conclusive results, the next step would have been to use it to tune the model of Chapter 3. By comparing the stability curves in Fig. 3.3(b) with the real stability boundary found by experiments, an empirical value of the dissipation parameter r could be found. The numerical results of Chapter 3 produced dimensional layer depths of between $40 - 50 d$; taking the characteristic stirring length $d = 0.0125\text{m}$ gives layer depths of $50 - 60\text{cm}$ —much larger than our experimental tank. The dimensionless buoyancy gradient is calculated as $b_z d^2 / U^2 \approx 0.01 b_z$, and so the range of values considered (cf. Fig. 4.6) is similar to that of Chapter 3. Hence the results of Chapter 3 are not directly comparable to these experiments, so parameters must be changed (for example, by considering more physically relevant values of Re) to make the theoretical results fully applicable to this experimental setup.

To conclude, this experimental study provides evidence to support the existence of an upper limit on Ri for layering to occur, as predicted by Balmforth *et al.* (1998) and Chapter 3. However, it cannot be viewed as a conclusive result due to the limited range of parameter space that was investigated. To produce more quantitative results, and to form an accurate estimate for this stability boundary, further experimental work is required.

Chapter 5

The three-component Phillips effect

5.1 Introduction

In the previous chapters, we have investigated the phenomenon of staircase formation in stirred single-component stratified convection. As discussed in Sec. 1.1, models of a similar form to that presented in Chapter 3 have been used to describe layering in a range of physical contexts, including atmospheric potential vorticity staircases (Malkov & Diamond, 2019) and salt fingering staircases (Paparella & von Hardenberg, 2014). However, a two-component system such as (3.12)–(3.13) is not sufficient to model the dynamics in every case. In a double-diffusive fluid, there are two independent contributions to the buoyancy. Treating these separately, and adding an equation for the energy forms a three-component system. Such three-component systems have previously been used to study $\mathbf{E} \times \mathbf{B}$ staircases in plasmas (Ashourvan & Diamond, 2016, 2017; Guo *et al.*, 2019), but in these models the instability comes from interaction between two equations, reducing the stability analysis to the two-component framework of Chapter 3. In this chapter, we develop a stability analysis for a three-component system (e.g. temperature, salinity, energy). We discuss the different possible conditions leading to linear instability of uniform basic states, and make comparisons with previous results from similar systems. The analysis presented in this chapter for a general three-component system forms a basis for subsequent chapters in which we develop specific models for layering in double-diffusive convection.

5.2 A general three-component system

To develop a theory for three-component models, we first investigate the linear stability properties of a general three-component system of the form

$$g_t = f_{zz}, \quad (5.1)$$

$$d_t = c_{zz}, \quad (5.2)$$

$$e_t = (\kappa e_z)_z + p. \quad (5.3)$$

Here, $e(z, t)$ is the kinetic energy, $g(z, t)$ and $d(z, t)$ are the independent components of the buoyancy gradient, with $f(g, d, e)$ and $c(g, d, e)$ their corresponding turbulent fluxes, and $\kappa(g, d, e)$ the turbulent kinetic energy diffusivity. To analyse the conditions for instability in this general system, we perform a linear stability analysis. We assume that (g_0, d_0, e_0) is a uniform steady state, such that $p(g_0, d_0, e_0) = 0$, and that (g', d', e') is a small perturbation. From the chain rule, we can write the z -derivative as

$$\frac{\partial}{\partial z} = \frac{\partial g}{\partial z} \frac{\partial}{\partial g} + \frac{\partial d}{\partial z} \frac{\partial}{\partial d} + \frac{\partial e}{\partial z} \frac{\partial}{\partial e}. \quad (5.4)$$

On applying (5.4), expanding $p(g, d, e)$ as a Taylor series, and neglecting terms quadratic in the perturbation quantities, we obtain the linear form of the general model:

$$g'_t \approx g'_{zz} f_g + d'_{zz} f_d + e'_{zz} f_e, \quad (5.5)$$

$$d'_t \approx g'_{zz} c_g + d'_{zz} c_d + e'_{zz} c_e, \quad (5.6)$$

$$e'_t \approx e'_{zz} \kappa + g' p_g + d' p_d + e' p_e, \quad (5.7)$$

where the partial derivatives f_g etc. are evaluated in the uniform steady state. On seeking solutions of the form $(g', d', e') \propto \exp(st + imz)$, where s is the growth rate and m the vertical wavenumber, the linearised forms of (5.1)–(5.3) may be expressed in matrix form as

$$\begin{pmatrix} s + m^2 f_g & m^2 f_d & m^2 f_e \\ m^2 c_g & s + m^2 c_d & m^2 c_e \\ -p_g & -p_d & s + m^2 \kappa - p_e \end{pmatrix} \begin{pmatrix} g_1 \\ d_1 \\ e_1 \end{pmatrix} = 0. \quad (5.8)$$

Equation (5.8) has a non-trivial solution only if the determinant of the matrix is zero, leading to the characteristic equation

$$\begin{aligned} & s^3 + s^2 [m^2 (f_g + c_d + \kappa) - p_e] \\ & + s [m^4 (f_g c_d - f_d c_g + \kappa f_g + \kappa c_d) + m^2 (f_e p_g - f_g p_e + c_e p_d - c_d p_e)] \\ & + m^6 \kappa (f_g c_d - f_d c_g) + m^4 (f_g c_e p_d - f_g c_d p_e + f_e c_d p_g - f_e c_g p_d + f_d c_g p_e - f_d c_e p_g) = 0, \end{aligned} \quad (5.9)$$

forming a cubic equation relating the growth rate to the vertical wavenumber.

We now explore the conditions for the existence of unstable wavenumbers ($\Re(s) > 0$). While solubility conditions for the cubic (5.9) can be established analytically, it is simpler, and the individual conditions can be separated more easily, by considering the asymptotic limits of small and large wavenumber m . We note that a positive growth rate $\Re(s) > 0$ in either limit is a sufficient condition for instability.

5.2.1 Instability at small wavenumbers

When $m = 0$, corresponding to infinitely long spatial scales, the characteristic equation (5.9) reduces to

$$s^3 - p_e s^2 = 0, \quad (5.10)$$

giving one root $s = p_e$ and two zero roots. If

$$-p_e < 0, \quad (5.11)$$

there is growth in the energy equation alone, without requiring interaction from the temperature equations. This *energy mode* instability was also theoretically possible in the two-component BLY formulation, but the parameterisation adopted by BLY produces $-p_e > 0$ everywhere.

To determine the stability of the two zero roots of (5.10) for small but finite m , it is necessary to include higher order terms. On taking the limit $m \rightarrow 0$, the dominant balance in (5.9) results from $s = O(m^2)$, giving

$$s^2 + (F_g + C_d)m^2 s + (F_g C_d - F_d C_g)m^4 = 0, \quad (5.12)$$

where we have adopted the following notation for simplicity:

$$F_g = \frac{f_g p_e - f_e p_g}{p_e}, \quad (5.13)$$

$$C_d = \frac{c_d p_e - c_e p_d}{p_e}, \quad (5.14)$$

$$F_d = \frac{f_d p_e - f_e p_d}{p_e}, \quad (5.15)$$

$$C_g = \frac{c_g p_e - c_e p_g}{p_e}. \quad (5.16)$$

These expressions represent the total derivatives of the fluxes $f(g, d, e)$ and $c(g, d, e)$ with respect to g and d , taking into account the contribution of the energy linked by the steady state equation $p(g, d, e) = 0$. Equation (5.12) has at least one root with positive real part if either

$$F_g C_d - F_d C_g < 0 \quad \text{or} \quad F_g + C_d < 0. \quad (5.17a,b)$$

If (5.17a) is satisfied, then there is exactly one root with positive real part, implying that the state is unstable. If (5.17b) is satisfied, but not (5.17a), then there are two roots with positive real part. Condition (5.17a) represents the direct equivalent of the Phillips effect in a three-component system; (5.17b) extends this to allow for an oscillatory instability.

These conditions can also be interpreted in a vector framework, which is helpful for generalising to an N -component system. Let \mathbf{F} be the vector function

$$\mathbf{F}(\mathbf{G}) = \begin{pmatrix} f(g, d, e(g, d)) \\ c(g, d, e(g, d)) \end{pmatrix}, \quad (5.18)$$

where $e(g, d)$ is defined implicitly via $p = 0$. The Jacobian of \mathbf{F} with respect to $\mathbf{G} = (g, d)$ is then

$$\mathbf{J} = \begin{pmatrix} F_g & F_d \\ C_g & C_d \end{pmatrix}. \quad (5.19)$$

Hence, conditions (5.17a, b) can be rewritten respectively as

$$\det(\mathbf{J}) < 0, \quad \text{tr}(\mathbf{J}) < 0. \quad (5.20)$$

Together, these conditions are equivalent to the single condition that there is instability if \mathbf{J} has at least one eigenvalue with negative real part. The same condition can be obtained by considering the system in the general form

$$\frac{\partial \mathbf{G}}{\partial t} = \frac{\partial^2}{\partial z^2} \mathbf{F}(\mathbf{G}, e(\mathbf{G})), \quad p(\mathbf{G}, e(\mathbf{G})) = 0. \quad (5.21)$$

Equation (5.21) can be readily extended into a general N -dimensional system, producing instability if the Jacobian of \mathbf{F} with respect to \mathbf{G} has at least one eigenvalue with negative real part.

5.2.2 Instability at high wavenumbers

For $m \rightarrow \infty$, the characteristic equation (5.9) simplifies at leading order to

$$s^3 + s^2 m^2 (f_g + c_d + \kappa) + s m^4 (f_g c_d - f_d c_g + \kappa f_g + \kappa c_d) + m^6 \kappa (f_g c_d - f_d c_g) = 0. \quad (5.22)$$

In this limit, all three solutions obey $s = O(m^2)$. There is at least one root s with positive real part if either the s -independent term $m^6 \kappa (f_g c_d - f_d c_g)$ is negative, or the characteristic equation (5.9) has a stationary point with $s > 0$. Assuming that f_g , c_d and κ are all positive, in order to avoid the high-wavenumber instability of Phillips (1972), both of these conditions reduce to

$$f_g c_d - f_d c_g < 0, \quad (5.23)$$

thereby providing us with a criterion for the existence of an unstable large wavenumber. Note that if there is no energy equation, then $p \equiv 0$ and $F_g = f_g$, etc. In this special case, conditions (5.17a) and (5.23) are identical, and the growth rate of the Phillips instability $s \rightarrow \infty$ as $m \rightarrow \infty$. This demonstrates how the inclusion of the energy equation (5.3) regularises the instability at high wavenumbers.

5.2.3 Condition for marginal stability

To check for instability at intermediate wavenumbers, we consider the point of marginal stability. Setting $s = 0$ in (5.9), we find the critical wavenumbers for a direct instability to be $m = 0$ and

$$m = m_* = \sqrt{\frac{p_e(F_g C_d - F_d C_g)}{\kappa(f_g c_d - f_d c_g)}}. \quad (5.24)$$

If m_* is real, then s is of one sign for $0 < m < m_*$, and the opposite sign for $m > m_*$. There is only one positive value for m_* , so as m is varied, s can change sign no more than once. Likewise, the critical wavenumber for oscillatory instability can be found by setting $\Re(s) = 0$ in (5.9). In this case, m_* is given by solutions to

$$\begin{aligned} & m^4 (f_g + c_d) (f_g c_d - f_d c_g + \kappa (f_g + c_d + \kappa)) \\ & + m^2 \left(\frac{\kappa (f_g + c_d + F_g + C_d)}{-p_e} + (f_g + c_d)^2 + \frac{(f_g f_e p_g + c_d c_e p_d + f_d c_e p_g + f_e c_g p_d)}{-p_e} \right) \\ & + (-p_e) (F_g C_d - F_d C_g) = 0. \end{aligned} \quad (5.25)$$

Assuming that $f_g > 0$ and $c_d > 0$, in order to avoid the high-wavenumber instability of Phillips (1972), the only possibility for a positive real solution m_* to exist is if one of the previous instability conditions (5.11), (5.17), (5.23) is satisfied.

Hence, the only possible instabilities are via condition (5.11) (energy mode, $m \rightarrow 0$, m_* real), conditions (5.17*a,b*) (small wavenumber Phillips instability, m_* real), or condition (5.23) (high wavenumber, m_* real). A combination of the conditions is possible, such that m_* is imaginary and there is a positive growth rate $\Re(s) > 0$ for all m .

5.2.4 Conditions for layering

We have deduced the conditions for linear instability, but have not yet demonstrated how these conditions can lead to layering. BLY proposed that, in a two-component model, layering requires an N-shaped relation between the buoyancy flux f and the buoyancy gradient g (such as that shown labelled ‘BLY’ in Fig. 1.2), so that $F_g < 0$ for only a finite range of gradients. The equivalent condition for a three-component model with independent contributions to the buoyancy is that there exists a bounded region of g - d space in which any one of the conditions for instability (5.11), (5.17) or (5.23) are met, as illustrated schematically in Fig. 5.1. On any path through the unstable region, only a finite range of points are unstable, with stable regions either side arresting the instability.

5.2.5 Comparison with Radko’s γ -instability

Radko (2003) put forward the idea that the driving factor behind layering is an instability arising from the parametric variation of the flux ratio γ as a function of the density ratio R .

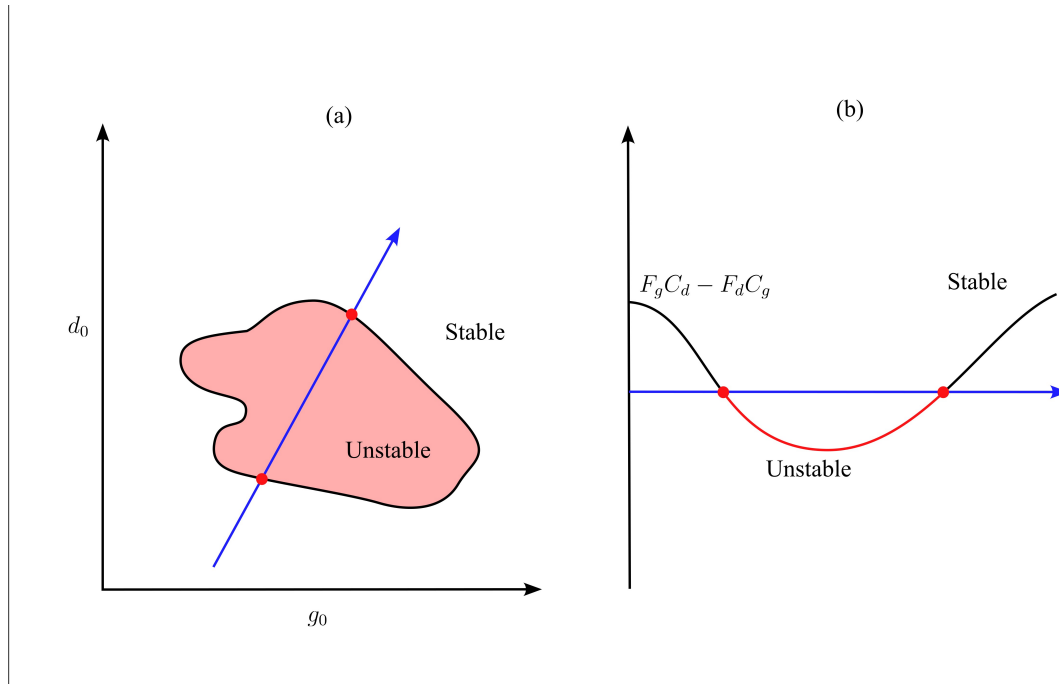


Fig. 5.1 (a) Sketch of a region of instability in g_0 - d_0 space, shaded pink. The locus of marginal stability is shown in black. The blue line shows an arbitrary cross-section through the unstable region. Panel (b) shows the value of $F_g C_d - F_d C_g$ along the blue path — it is negative only in the finite region between the two points shown in red, giving a finite region only where condition (5.17a) is satisfied

He modelled the two components of the density as

$$T_t = \frac{\partial}{\partial z} f(\gamma, Nu), \quad (5.26)$$

$$S_t = \frac{\partial}{\partial z} c(\gamma, Nu), \quad (5.27)$$

where the flux ratio $\gamma = f/c$ and the Nusselt number Nu is the ratio of convective to conductive heat transfer. The functions $\gamma(R)$ and $Nu(R)$ depend only on the density ratio $R = \alpha T_z / \beta S_z$, i.e. the ratio of the contributions to the density from temperature and salt. Steady states of the flux-gradient relations (5.26)–(5.27) are found to be linearly unstable to perturbations when

$$\frac{d\gamma}{dR} < 0, \quad (5.28)$$

representing the γ -instability.

To compare the criterion (5.28) with the conditions for instability that we have deduced in the context of our general three-component model, we formulate our system in terms of Radko's parameters. Making Radko's assumption that the equations can be parameterised in terms only of the ratio of gradients, R , we express the fluxes in terms of turbulent

diffusivities $K_T(R)$ and $K_S(R)$ as

$$f = K_T(R)g, \quad (5.29)$$

$$c = K_S(R)d, \quad (5.30)$$

with $R = g/d$. Returning to the Jacobian form of the problem (5.19) with this new notation, we obtain

$$\mathbf{J} = \begin{pmatrix} K_T + K'_T R & -K'_T R^2 \\ K'_S & K_S - K'_S R \end{pmatrix}, \quad (5.31)$$

where primes denote differentiation with respect to R . Note that \mathbf{J} does not depend on g or d independently and the only parameter of importance is the density ratio R . The trace and determinant of \mathbf{J} are given by

$$\text{tr}(\mathbf{J}) = K_T + K_S + R(K'_T - K'_S), \quad (5.32)$$

$$\det(\mathbf{J}) = K_T K_S + R(K'_T K_S - K_T K'_S). \quad (5.33)$$

With fluxes of the form (5.29)–(5.30), the flux ratio $\gamma = RK_T/K_S$, so

$$\frac{d\gamma}{dR} = \frac{d}{dR} \left(R \frac{K_T}{K_S} \right) = \frac{K_T}{K_S} + \frac{R}{K_S^2} (K'_T K_S - K_T K'_S) = K_S^2 \det(\mathbf{J}). \quad (5.34)$$

The negative determinant condition (5.20) exactly recovers Radko's γ -condition. The trace condition (5.20*b*) is new, and allows for two unstable modes, while Radko's γ -instability indicates only the onset of instability with a single mode.

To summarise, Radko's γ -condition (5.28) is mathematically equivalent to the Phillips instability, in the specific context of double-diffusive flux-gradient relations dependent on R . The three-component model (5.1)–(5.3), with instability conditions (5.11), (5.17) and (5.23), describes a generalisation of both the Phillips and γ -instabilities for a three-component system with explicit dependence on the kinetic energy e . The inclusion of e avoids the ultraviolet catastrophe inherent to the γ -instability and the single-component Phillips instability, allowing the model to capture not only the initial growth of perturbations but also the possible development of layers and their long-term evolution. Note that for a system in the general form (5.1)–(5.3), condition (5.17*a*) can lead to instability by two different physical mechanisms. If the function p is parameterised to include an energy source term, then the system describes the forced mechanism of BLY and Paparella & von Hardenberg (2014). By contrast, with no source term in p , but appropriate parameterisations for f and c such that (5.17*a*) is satisfied, the instability comes from the γ -instability of Radko (2003).

5.3 Hyperdiffusion can regularise the high wavenumber instability

The single component Phillips equation (1.1), the three component system (5.1)–(5.3), and the temperature-salinity system (5.26)–(5.27) may all be unstable at high wavenumbers, depending on the specific parameterisations of the flux terms. Such a high wavenumber instability can be regularised by the addition of hyperdiffusion terms. This is a common approach for regularisation, and we will first demonstrate it for the Phillips equation (1.1). Expressing the equation in terms of the buoyancy gradient $g = b_z$, the hyperdiffusion term takes the form of a fourth derivative, with a negative hyperdiffusion coefficient $-A$, giving the equation

$$g_t = f_{zz} - Ag_{zzzz}. \quad (5.35)$$

This altered equation admits the same uniform steady states $g = g_0$ as without hyperdiffusion. A linear stability analysis about these states, with perturbation $\propto \exp(st + imz)$, gives the following equation for the growth rate s :

$$s = -m^2 f_g - Am^4. \quad (5.36)$$

If $f_g < 0$, then this produces positive growth rates for $0 < m < \sqrt{-f_g/A}$. Above this wavenumber, the hyperdiffusion becomes dominant, and the growth rate is negative.

To regularise the high wavenumber instability in the three-equation system (5.1)–(5.3), we add hyperdiffusion only to the temperature and salinity equations. The condition for a high wavenumber instability (5.23) does not depend on any terms in the energy equation, so there is no need to alter the energy equation. The altered system with hyperdiffusion terms added is:

$$g_t = f_{zz} - Ag_{zzzz}, \quad (5.37)$$

$$d_t = c_{zz} - Bd_{zzzz}, \quad (5.38)$$

$$e_t = (\kappa e_z)_z + p. \quad (5.39)$$

The augmented growth rate equation is

$$\begin{aligned} 0 = & s^3 + s^2 [m^4 (A + B) + m^2 (f_g + c_d + \kappa) - p_e] + s [m^8 AB + m^6 (f_g B + c_d A + \kappa (A + B)) \\ & + m^4 (f_g c_d - f_d c_g + \kappa f_g + \kappa c_d - (A + B) p_e) + m^2 (f_e p_g - f_g p_e + c_e p_d - c_d p_e)] + m^{10} \kappa AB \\ & + m^8 (\kappa f_g B + \kappa c_d A - AB p_e) + m^6 \kappa (f_g c_d - f_d c_g + A (c_e p_d - c_d p_e) + B (f_e p_g - f_g p_e)) \\ & + m^4 (f_g c_e p_d - f_g c_d p_e + f_e c_d p_g - f_e c_g p_d + f_d c_g p_e - f_d c_e p_g). \quad (5.40) \end{aligned}$$

The hyperdiffusion terms do not affect the small wavenumber behaviour, but become dominant at large wavenumbers. As $m \rightarrow \infty$, (5.40) becomes

$$s^3 + s^2 m^4 (A + B) + s m^8 AB + m^{10} \kappa AB = 0. \quad (5.41)$$

The growth rates at large m are therefore

$$s = -m^4 A, \quad -m^4 B, \quad \text{and} \quad s = -m^2 \kappa. \quad (5.42)$$

As mentioned before, κ must be positive, so all three growth rates are negative as $m \rightarrow \infty$. Hence, any amount of hyperdiffusion will counter the high wavenumber instability eventually. However, this means that the choice of coefficients A and B has a significant effect on the range of wavenumbers susceptible to instability, and on the wavenumber of maximum growth rate. As seen in Chapter 3, the wavenumber of maximum growth rate corresponds directly with the initial number of layers. Hence the spatial scale for layers is set by the hyperdiffusion coefficient. This is a disadvantage of the hyperdiffusion approach, in comparison with choosing parameterisations such that there is no high wavenumber instability, in which case the layer depth depends only on the other parameterisations, rather than the arbitrary choice of hyperdiffusion coefficient.

5.4 Discussion

In this chapter we have investigated the linear stability of uniform steady states of a system of two turbulent diffusion equations based on flux laws (for two components of buoyancy, for example), coupled with a third flux-diffusion equation including a general source term (the ‘energy’ equation). There are four possible types of instability. First, the energy mode, due to instability in the energy equation alone; this mode is most unstable at wavenumber $m = 0$, leading to growth in energy across the whole domain. Next, there are three possible instabilities attributable to either the Phillips effect or the γ -instability, depending on the parameterisations of the fluxes. At low wavenumbers, there can be one or two positive growth rates, corresponding to positive eigenvalues of the Jacobian of the temperature and salinity fluxes with respect to their gradients. There is also the possibility of a high wavenumber instability, which can be avoided by suitable parameterisation of the flux terms, or by the inclusion of hyperdiffusion terms in the system.

We compare these results with those of two important previous studies. The system of Balmforth *et al.* (1998) was unstable to a single Phillips mode, and also allowed for a stable energy mode. We have shown the possibility of an extra Phillips mode, allowing for an oscillatory instability, as may be expected in the diffusive convection regime. While BLY’s use of the energy equation precluded the high wavenumber instability inherent to Phillips (1972) and Posmentier (1977), the same is not automatically true in the three-component system. Instability at high wavenumbers can be avoided through careful parameterisation

of the flux terms. An alternative approach is the introduction of hyperdiffusion terms to the temperature and salinity equations, which we have shown to suppress the high wavenumber instability entirely. This approach was taken by Radko (2019a), leading to a model that produces the key dynamics of double-diffusive layering in terms of only the temperature and salinity fields (in comparison with our three-component model).

In addition, we have demonstrated that Radko's γ -instability and the Phillips effect are mathematically equivalent, both being described by the instability condition (5.17a). The two cases are separated by the specific forms of the equations, with the Phillips effect relying on a forcing in the energy equation, while the γ -instability stems from a direct interaction between the temperature and salinity fluxes.

In the following chapters, we apply the stability analysis presented here to three different systems. First, to the problem of stirred staircase formation with two components of buoyancy in Chapter 6. In Chapter 7 we investigate double-diffusive layering without any source term, using different parameterisations for the flux terms than in Chapter 6. Finally, we reintroduce a source term in Chapter 8 to model diffusive convective staircases.

Chapter 6

Stirred double-diffusive layering

6.1 Introduction

In Chapter 2, we presented a derivation of a one-dimensional model for layering in a turbulent stratified fluid. In Chapter 3, we applied this model to the case of stirred stratified flow and studied the behaviour of its solutions to late time. This model was based on the Phillips effect, where the layering instability stems from a non-monotonic dependence of the buoyancy flux on the buoyancy gradient. Work by Balmforth *et al.* (1998) (BLY) extended the Phillips effect to a well-resolved model for layering, and our work in Chapter 3 developed this further to study the long term evolution of staircases in detail. The model of BLY has been adapted to model staircases in several physical contexts, including in double-diffusive convection. On the basis of the numerical results of Paparella & von Hardenberg (2012), Paparella & von Hardenberg (2014) made the assumption that the flux ratio $\gamma = f/c$ is constant throughout the evolution. With this assumption, the temperature and salinity equations can be reduced to a single buoyancy equation. Also based on the simulations of Paparella & von Hardenberg (2012), they suggested that the layering process in salt fingering is due to stirring by clusters of salt fingers moving together, allowing salt fingering staircases to be modelled using the BLY system, with some slightly different parameterisations.

An important point about two-component models (i.e. models for buoyancy $b(z, t)$ and energy $e(z, t)$) can be made by considering a generalised form of the energy equation, adapted from (3.13)

$$e_t = (f_e)_z - f_b + C - D. \quad (6.1)$$

Here f_e is the energy flux, f_b is the buoyancy flux, C is an energy source and D the dissipation term. The uniform, steady-state buoyancy flux is $f_b(g_0, e_0) = C(g_0, e_0) - D(g_0, e_0)$, so the form of the steady-state flux can be chosen arbitrarily through choice of C and D . Hence it is always possible to generate a flux-gradient relation with the characteristic ‘N’-shape required for layering (BLY), simply by careful parameterisation of the dissipation and source terms.

By simplifying the double-diffusive problem to a two-component model, Paparella & von Hardenberg (2014) removed any possibility for the salt and temperature fields to evolve separately, and for further double-diffusive effects to occur. To study DDC layering in detail, we propose instead a three-component model, with temperature and salinity independent of each other. In this chapter, we retain the stirring term as a bridge between the model of Chapter 3 and a fully double-diffusive model; in Chapter 7 we present a model where the energy input to the system comes directly from double-diffusive terms in the equations, without the need for stirring.

We begin in Sec. 6.2 by presenting a three-component model, derived using the method outlined in Chapter 2. We investigate uniform steady-state solutions to the model, and their linear stability, in Sec. 6.3. In the salt fingering regime, steady states are unstable to the Phillips instability for a wide range of parameters. In the diffusive convection regime, the Phillips instability is also active, but there is an additional high wavenumber instability (HWI) and energy mode instability, as discussed in Chapter 5. The HWI can be suppressed by adding hyperdiffusion terms to the equations. We consider the effect of different parameter values on the stability of the system in Sec. 6.3.5.

In Sec. 6.5 we present numerical solutions in the salt fingering (SF) regime, and demonstrate that the primary behaviour is that of stirred layering, with double-diffusion having only a minor effect. We present solutions in the diffusive convection (DC) regime in section 6.6. Even for initial conditions where the HWI is not expected, the HWI is present in the nonlinear evolution, and structures narrow to the spatial mesh scale. Adding hyperdiffusion to the system successfully suppresses the HWI, producing layered solutions. As in the SF regime, these solutions are dominated by stirring, with the salt and temperature fields evolving identically. In section 6.7 we discuss our results.

6.2 A model for stirred double-diffusive layering

The dynamics of a stirred double-diffusive fluid are governed by the Boussinesq equations for velocity $\mathbf{u}(\mathbf{x}, t)$, temperature $T(\mathbf{x}, t)$, salinity $S(\mathbf{x}, t)$ and pressure $p(\mathbf{x}, t)$:

$$\mathbf{u}_t + \mathbf{u} \cdot \nabla \mathbf{u} = -\frac{1}{\rho_0} \nabla p + g \frac{\rho - \rho_0}{\rho_0} \mathbf{e}_z + \nu \nabla^2 \mathbf{u} + \Phi, \quad (6.2)$$

$$T_t + \mathbf{u} \cdot \nabla T = \kappa_T \nabla^2 T, \quad (6.3)$$

$$S_t + \mathbf{u} \cdot \nabla S = \kappa_S \nabla^2 S, \quad (6.4)$$

$$\nabla \cdot \mathbf{u} = 0, \quad (6.5)$$

$$\frac{\rho - \rho_0}{\rho_0} = \beta S - \alpha T, \quad (6.6)$$

where Φ is a body forcing representing stirring (for example, by a rod), defining a characteristic length d and speed U . The thermal and solutal expansion coefficients α and β , and gravitational acceleration g account for the effect of temperature and salinity on buoyancy,

and ρ_0 is a reference density. We use these characteristic scales to nondimensionalise the equations via the following prescriptions:

$$\hat{t} = \frac{U}{d}t, \quad \hat{z} = \frac{1}{d}z, \quad \hat{\mathbf{u}} = \frac{1}{U}\mathbf{u}, \quad \hat{T} = \frac{\alpha g d}{U^2}T, \quad \hat{S} = \frac{\beta g d}{U^2}S, \quad \hat{p} = \frac{1}{\rho_0 U^2}p, \quad \hat{\Phi} = \frac{d}{\rho_0 U^2}\Phi, \quad (6.7)$$

where hats denote dimensionless variables. With these scalings, upon dropping hats, we obtain the Boussinesq equations in dimensionless form:

$$\frac{\partial \mathbf{u}}{\partial t} + \mathbf{u} \cdot \nabla \mathbf{u} = -\nabla p + b\hat{\mathbf{z}} + \text{Re}^{-1} \nabla^2 \mathbf{u} + \Phi, \quad (6.8)$$

$$\nabla \cdot \mathbf{u} = 0, \quad (6.9)$$

$$\frac{\partial T}{\partial t} + \mathbf{u} \cdot \nabla T = \text{Pt}^{-1} \nabla^2 T, \quad (6.10)$$

$$\frac{\partial S}{\partial t} + \mathbf{u} \cdot \nabla S = \text{Ps}^{-1} \nabla^2 S, \quad (6.11)$$

$$b = T - S. \quad (6.12)$$

These equations are governed by three dimensionless numbers: $\text{Re} = Ud/\nu$ is the Reynolds number, and $\text{Pt} = Ud/\kappa_T$ and $\text{Ps} = Ud/\kappa_S$ the thermal and solutal Péclet numbers respectively. For salt water, the solutal Péclet number Ps is $O(100)$ times larger than Pt . Using the averaging process detailed in Chapter 2, we obtain the following model for the three-component system:

$$T_t = \left(\frac{l^2 e}{le^{1/2} + \text{Pt}^{-1}} T_z \right)_z + \text{Pt}^{-1} T_{zz}, \quad (6.13)$$

$$S_t = \left(\frac{l^2 e}{le^{1/2} + \text{Ps}^{-1}} S_z \right)_z + \text{Ps}^{-1} S_{zz}, \quad (6.14)$$

$$e_t = \left(\frac{l^2 e}{le^{1/2} + \text{Re}^{-1}} e_z \right)_z - \frac{l^2 e}{le^{1/2} + \text{Pt}^{-1}} T_z + \frac{l^2 e}{le^{1/2} + \text{Ps}^{-1}} S_z + \text{Re}^{-1} e_{zz} - \varepsilon \frac{(e-1)e^{1/2}}{l}. \quad (6.15)$$

As in Chapter 3, we adopt the BLY length scale, splitting the buoyancy gradient into its constituent parts as $b_z = T_z - S_z$. Thus,

$$l = \frac{e^{1/2}}{(e + T_z - S_z)^{1/2}}. \quad (6.16)$$

In Chapter 3, there was a single component of density, so writing the length scale in terms of b_z was the only option. Here, it would be possible to consider a length scale in terms of only the temperature or salinity gradient, rather than the total buoyancy. However, the dynamics of both components will be affected by the form of the length scale, so both T_z and S_z should feed back in to the form of l . The prescription (6.16) will clearly be problematic if $T_z - S_z$ becomes negative, but when this happens the gradient is statically

unstable. As we are modelling the mixing of an initially stable gradient, we expect that the total gradient should remain stable, and this should not be an issue.

Note that by writing $b = T - S$, (6.13)-(6.15) can be rewritten as:

$$b_t = \left(\frac{l^2 e}{le^{1/2} + \text{Pt}^{-1}} b_z \right)_z + \text{Pt}^{-1} b_{zz} - (\text{Pt}^{-1} - \text{Ps}^{-1}) \left(\frac{l^2 e}{(le^{1/2} + \text{Pt}^{-1})(le^{1/2} + \text{Ps}^{-1})} S_z - S_z \right)_z, \quad (6.17)$$

$$S_t = \left(\frac{l^2 e}{le^{1/2} + \text{Ps}^{-1}} S_z \right)_z + \text{Ps}^{-1} S_{zz}, \quad (6.18)$$

$$e_t = \left(\frac{l^2 e}{le^{1/2} + \text{Re}^{-1}} e_z \right)_z - \frac{l^2 e}{le^{1/2} + \text{Pt}^{-1}} b_z + (\text{Pt}^{-1} - \text{Ps}^{-1}) \frac{l^2 e}{(le^{1/2} + \text{Pt}^{-1})(le^{1/2} + \text{Ps}^{-1})} S_z + \text{Re}^{-1} e_{zz} - \varepsilon \frac{(e-1)e^{1/2}}{l}. \quad (6.19)$$

Recall that in the case of Chapter 3 with only one component of buoyancy, staircases formed only for relatively small values of $\text{Pe}^{-1} = O(0.1)$. Assuming that Pt^{-1} is also small in the three-component case, and recalling that $\text{Ps}^{-1} = O(\text{Pt}^{-1}/100)$, then the system (6.17)–(6.19) is only an $O(\text{Pt}^{-1})$ perturbation away from the two-component system (3.12)–(3.13). As such, we expect that the results of this system will be very similar to those obtained for the two-component system.

Also recall that the Péclet numbers can be written in terms of the Reynolds, Prandtl and Schmidt numbers as

$$\text{Pt} = \text{Pr Re}, \quad \text{Ps} = \text{Sc Re}. \quad (6.20)$$

Table 3.1 gave realistic values of Pr and Sc at a variety of temperatures and salinities, showing that for a wide range of values, $\text{Pr} \approx O(\text{Sc}/100)$. To reduce the number of parameters in the system, we will henceforth assume that $\text{Ps}^{-1} = \text{Pt}^{-1}/100$, and only vary Pt^{-1} and Re^{-1} independently.

6.3 Uniform-gradient steady states

In this section we investigate steady state solutions of the system (6.13)–(6.16), with spatially uniform temperature and salinity gradients, and uniform energy. We discuss the stability of these states in Sec. 6.3.2.

6.3.1 Steady-state solutions $g_0(e_0; G_0)$

If a uniform steady state $(T_z, S_z, e) = (g_0, d_0, e_0)$ exists, then the temperature and salinity equations (6.13)–(6.14) are trivially satisfied, and the energy equation (6.15) reduces to

$$\frac{l_0^2 e_0}{l_0 e_0^{1/2} + \text{Pt}^{-1}} g_0 - \frac{l_0^2 e_0}{l_0 e_0^{1/2} + \text{Ps}^{-1}} d_0 + \varepsilon \frac{(e_0 - 1) e_0^{1/2}}{l_0} = 0, \quad (6.21)$$

where $l_0 = l(g_0, d_0, e_0)$, calculated using (6.16). Substituting for l_0 and writing the total buoyancy gradient $G_0 = g_0 - d_0$, (6.21) becomes

$$\frac{e_0^2 g_0}{e_0 \sqrt{e_0 + G_0} + \text{Pt}^{-1} (e_0 + G_0)} - \frac{e_0^2 d_0}{e_0 \sqrt{e_0 + G_0} + \text{Ps}^{-1} (e_0 + G_0)} + \varepsilon (e_0 - 1) \sqrt{e_0 + G_0} = 0. \quad (6.22)$$

In general this is a high order polynomial for $e_0^{1/2}$, which is difficult to solve, or work with analytically. First of all, note that when $G_0 = 0$, (6.22) reduces to

$$\frac{(\text{Ps}^{-1} - \text{Pt}^{-1}) e_0}{(e_0^{1/2} + \text{Pt}^{-1}) (e_0^{1/2} + \text{Ps}^{-1})} g_0 + \varepsilon (e_0 - 1) e_0^{1/2} = 0. \quad (6.23)$$

From this, it is clear that $e_0 = 0$ is a solution for any value of g_0 when $G_0 = 0$.

To find the other solutions, we write $G_0 = g_0 - d_0$ and treat G_0 as a parameter. This allows us to solve exactly for $g_0(e_0; G_0)$ to obtain steady states with the salinity gradient d_0 a known step G_0 away from the temperature gradient g_0 . Hence we obtain the exact expression for $g_0(e_0; G_0)$

$$g_0 = \frac{e_0 + \text{Pt}^{-1} \sqrt{e_0 + G_0}}{(\text{Pt}^{-1} - \text{Ps}^{-1})} \left(\frac{G_0}{\sqrt{e_0 + G_0}} + \frac{\varepsilon (e_0 - 1) (e_0 + \text{Ps}^{-1} \sqrt{e_0 + G_0}) \sqrt{e_0 + G_0}}{e_0^2} \right). \quad (6.24)$$

Expression (6.24) for g_0 is plotted in Fig. 6.1 for a range of values of G_0 . Fig. 6.1(a) shows that for $G_0 \lesssim 0.015$, there are multiple steady-state energies for some values of g_0 . For G_0 above this value, the energy is a single valued function of g_0 . Fig. 6.1(d) shows a close-up picture near the origin, for a narrow range of values of G_0 , allowing the transition from multi- to single-valued solutions to be seen clearly. Fig. 6.1(b) shows a larger scale version of (a) near $e_0 = 0$: for all positive values of G_0 , the temperature gradient $g_0 \rightarrow \infty$ as $e_0 \rightarrow 0$. In Fig. 6.1(c) the energy is plotted for larger values of G_0 : as g_0 increases, $e_0 \rightarrow \infty$ at an increasing rate (although it is not exponential). Note that the scale on the g_0 -axis is significantly larger than that on the e_0 -axis in both these plots. Steady-state solutions exist for very large temperature gradients, as similarly large salinity gradients ensure that the overall buoyancy gradient is substantially weaker than either of its components.

When the steady-state solution is multivalued (as seen in Fig. 6.1 for $G_0 \lesssim 0.15$), there are multiple solutions $e_0(g_0, d_0)$ of $p(g, d, e) = 0$. The limiting case for multiple solutions

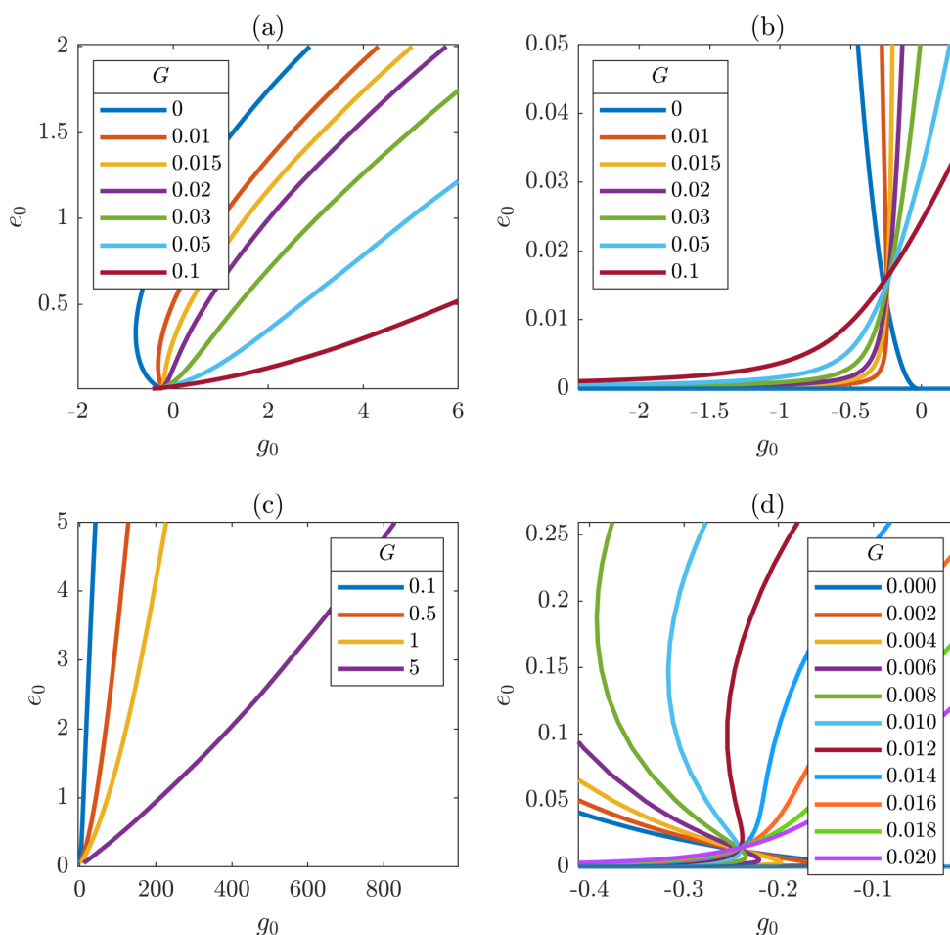


Fig. 6.1 Steady-state energies for constant G_0 , found using the expression for $g_0(e_0)$ given in (6.24). For this plot, $Pt^{-1} = 0.01$, $Ps^{-1} = 0.0001$ and $\varepsilon = 0.02$. (a) shows small values of G_0 , where e_0 is multivalued for some negative values of g_0 ; (b) shows the behaviour of the solutions in (a) for small e_0 ; (c) shows larger values of G_0 , where e_0 is always single-valued; (d) shows a selection of very small values of g_0 , near the point where they all take a similar value, and shows that the maximum G_0 for which there are values of g_0 with multiple solutions is 0.012.

is a double root where $p(e_0) = p_e(e_0) = 0$. Beyond this limiting case, there are three solutions, and it is necessarily true that $-p_e < 0$ for one of the solutions. Hence the energy mode is unstable by condition (5.11).

6.3.2 Unstable regions for the three-component system

To analyse the stability of the steady-state solutions, we express the three-component system (6.13)–(6.15) in the general form (5.1)–(5.3) by writing

$$f = \left(\frac{l^2 e}{le^{1/2} + Pt^{-1}} + Pt^{-1} \right) g, \quad (6.25)$$

$$c = \left(\frac{l^2 e}{le^{1/2} + Ps^{-1}} + Ps^{-1} \right) d, \quad (6.26)$$

$$\kappa = \left(\frac{l^2 e}{le^{1/2} + Re^{-1}} + Re^{-1} \right), \quad (6.27)$$

$$p = -\frac{l^2 e}{le^{1/2} + Pt^{-1}} g + \frac{l^2 e}{le^{1/2} + Ps^{-1}} d - (e - 1) e^{1/2} / l. \quad (6.28)$$

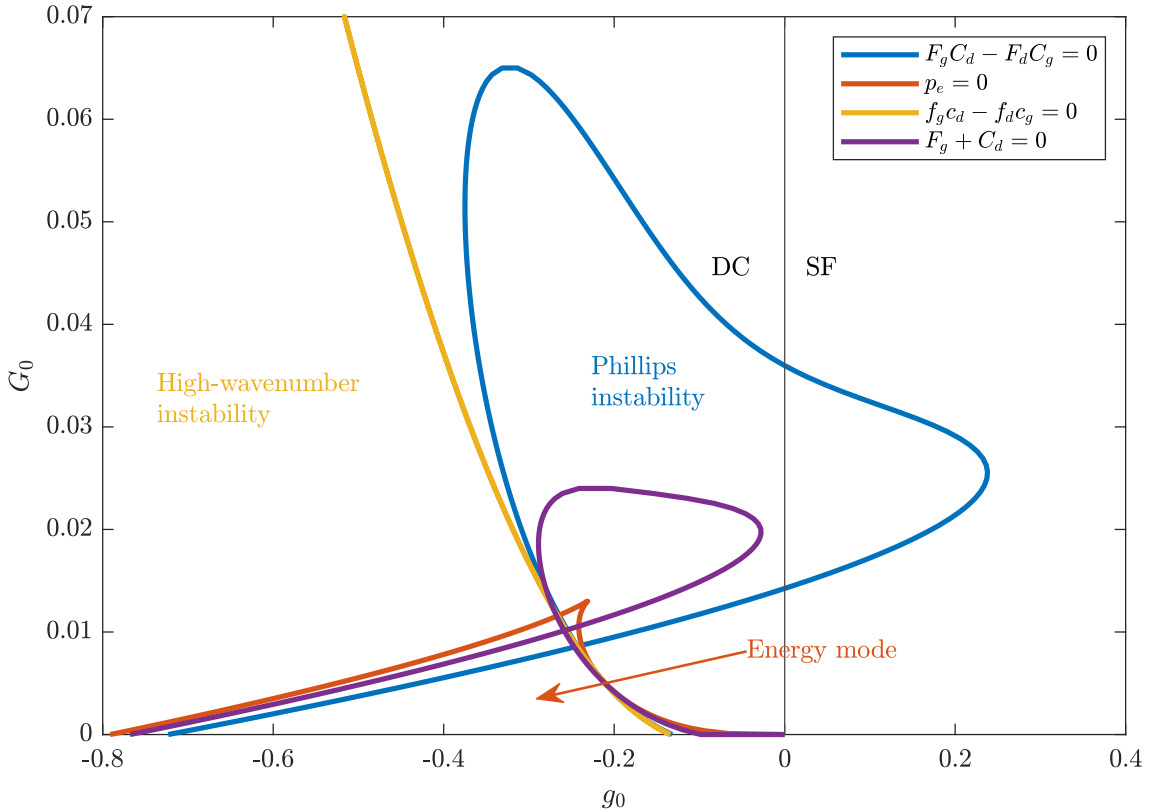


Fig. 6.2 Loci of marginal stability in g_0 - G_0 space, for parameter values $Pt^{-1} = 0.01$, $Ps^{-1} = 0.0001$ and $\varepsilon = 0.02$. Found by solving simultaneously (6.24) with the conditions for marginal stability $F_g C_d - F_d C_g = 0$, $p_e = 0$, $f_g c_d - f_d c_g = 0$ and $F_g + C_d = 0$.

Recall from Chapter 5 that the system is unstable to the Phillips instability if either $F_g C_d - F_d C_g < 0$ or $F_g + C_d < 0$, and the energy mode is unstable if $-p_e < 0$, where

$F_g = (f_g p_e - f_e p_g)/p_e$ and other quantities are defined similarly, and partial derivatives are taken in the steady-state (g_0, d_0, e_0) . If $f_g c_d - f_d c_g < 0$ then there is a high wavenumber instability. We investigate the stability boundaries for the system by finding loci of marginal stability for each condition. We first consider the Phillips instability, for which the system is marginally unstable at points where $F_g C_d - F_d C_g = 0$. We fix a value of G_0 and use (6.24) to write $g_0(e_0; G_0)$. This expression is substituted into the condition for marginal instability $F_g C_d - F_d C_g = 0$, which can then be solved for e . Now substituting this value of e_0 back into (6.24), we obtain a numerical value for $g_0(G_0)$ on the stability boundary. Repeating this process for a range of values of G_0 , and for all four instability conditions, we obtain a full picture of the unstable regions in $g - G$ space.

Fig. 6.2 shows the stability boundaries in $g_0 - G_0$ space for all four types of instability: the locus on which $F_g C_d - F_d C_g = 0$ is shown in blue, $p_e = 0$ in red, $f_g c_d - f_d c_g = 0$ in yellow and $F_g + C_d = 0$ in purple. Note that for $g_0 > 0$, i.e. in the salt fingering regime, only the Phillips instability ($F_g C_d - F_d C_g < 0$) occurs. In the diffusive convection regime ($g_0 < 0$), all types of instability are possible. Recall that an oscillatory Phillips instability occurs if and only if $F_g + C_d < 0$ and $F_g C_d - F_d C_g > 0$. The unstable region for $F_g + C_d < 0$ is a subset of the region where $F_g C_d - F_d C_g < 0$, so only a direct instability occurs. Additionally, for almost the entire unstable region for the Phillips mode, neither the energy mode nor high-wavenumber instability takes place. Note that in part of the unstable region, $0 < g_0 < G_0$, and hence $g_0 > 0$, $d_0 < 0$. This is the doubly stable region, where both components of the buoyancy gradient are individually stable. So the stirring produces instability even in the doubly stable regime.

Further, note that in the region where the energy mode is unstable, i.e. ($-p_e < 0$, red), we also have the high wavenumber instability ($f_g c_d - f_d c_g < 0$, yellow). According to the expression for the cutoff wavenumber (5.24), there is no real valued m_* , so there is instability for all wavenumbers $m > 0$.

Wavenumber-growth rate plots are shown in Fig. 6.3, in a range of steady states (g_0, d_0, e_0) , to demonstrate the different types of instability. Fig. 6.3(a) shows the Phillips instability, where $F_g C_d - F_d C_g < 0$; (b) where $F_g C_d - F_d C_g < 0$ and $F_g + C_d < 0$. In both Figs. 6.3(a) and (b), there is a clearly defined wavenumber of maximum growth rate which will set the scale for layering, as seen in Chapter 3. Fig. 6.3(c) shows the high wavenumber instability, where $f_g c_d - f_d c_g < 0$ and the growth rate diverges as $m \rightarrow \infty$. Figs. 6.3(d)–(f) show the stability of the three different steady states associated with $g_0 = -0.4$, $d_0 = -0.405$, where the steady-state energy is multivalued. Of the three steady states, only the middle one is unstable to the energy mode instability.

6.3.3 Why is there such a difference between SF and DC?

Figure 6.2 shows that in the salt fingering regime ($g, d > 0$), only the Phillips instability occurs, while all of the types of instability occur in the diffusive convection regime ($g, d < 0$). Why this happens is not initially clear from the form of the equations, which

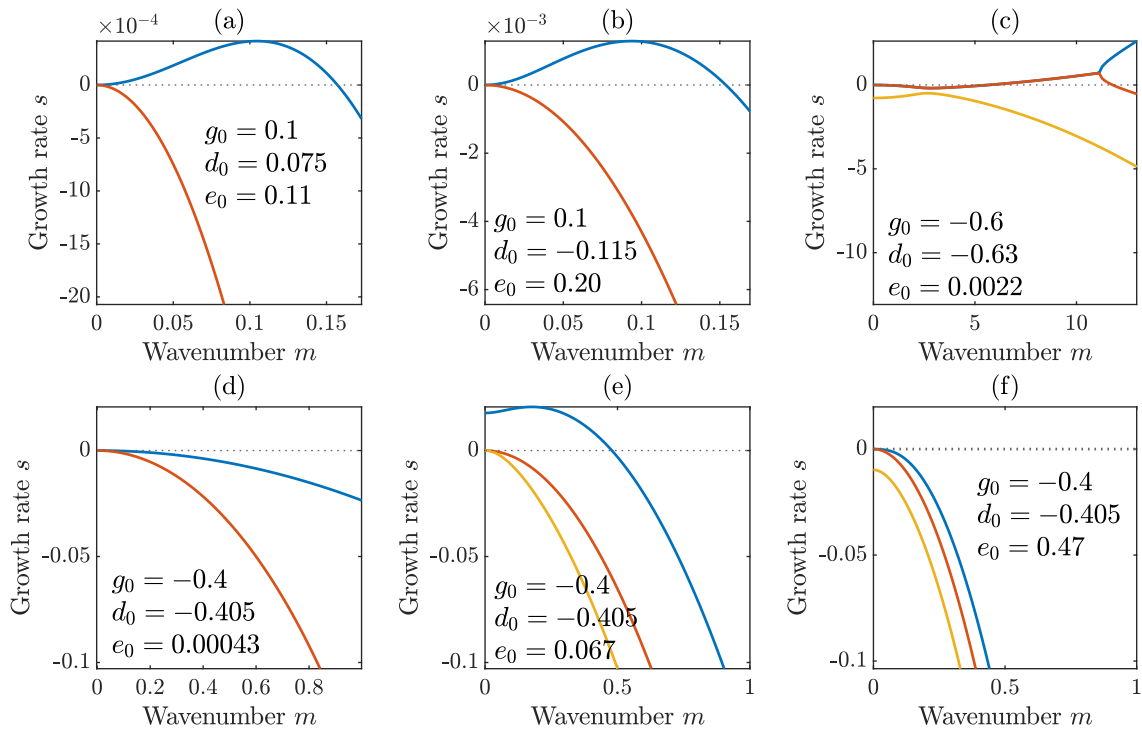


Fig. 6.3 Wavenumber-growth rate plots for the three-component system, demonstrating different types of instability, for parameter values $Pt^{-1} = 0.01$, $Ps^{-1} = 0.0001$, $\varepsilon = 0.02$ and $Re^{-1} = 0$. (a) $F_g C_d - F_d C_g < 0$; (b) $F_g C_d - F_d C_g < 0$ and $F_g + C_d < 0$; (c) $f_g c_d - f_d c_g < 0$. Panels (d)–(f) correspond to three different energies for the same values of g and d ; (d) and (f) show stable modes; (e) shows the energy mode instability $-p_e < 0$.

have a similar dependence on g and d . Upon closer inspection, all of the stability conditions depend on g and d not only through $G = g - d$, but also through the combination $\text{Ps}^{-1}g - \text{Pt}^{-1}d$. The total buoyancy gradient G is positive in either regime, but owing to the difference between Pt^{-1} and Ps^{-1} , we have:

$$\text{Ps}^{-1}g - \text{Pt}^{-1}d > 0 \quad \text{when} \quad g > \frac{\text{Pt}^{-1}}{\text{Ps}^{-1}}d = \frac{\kappa_T}{\kappa_S}d, \quad (6.29)$$

where κ_T and κ_S are the thermal and solutal diffusivities. The ratio $\kappa_T/\kappa_S > 1$, and is approximately 100 in salt water. In the DC regime, both g and d are negative. So for the total buoyancy gradient to be positive requires $g > d > \kappa_T d/\kappa_S$, so $\text{Ps}^{-1}g - \text{Pt}^{-1}d$ is always positive. Conversely, in the SF regime, both g and d are positive, and $g > \kappa_T d/\kappa_S$ in only a small segment of the region. Outside this segment, $\text{Ps}^{-1}g - \text{Pt}^{-1}d$ is negative, introducing an asymmetry between the regimes that accounts for the difference in stability behaviour.

6.3.4 Suppressing the high wavenumber instability with hyperdiffusion

As discussed in Chapter 5, it is possible to suppress the high wavenumber instability by the addition of hyperdiffusion terms $-Ag_{zzzz}$ and $-Bd_{zzzz}$ to the temperature and salinity equations (6.13) and (6.14) respectively. To demonstrate this suppression, Fig. 6.4 shows how the growth rate of perturbations varies with wavenumber, starting in the steady state $(g_0, d_0, e_0) = (-0.6, -0.63, 0.0022)$, which is susceptible to the high wavenumber instability (HWI). For simplicity, we take $B = A$. We see that for sufficiently large values of A , the HWI is suppressed entirely, while for smaller values there is an instability, but it is suppressed at high enough wavenumbers. Any positive value of A will cause the growth rate to be negative as $m \rightarrow \infty$. However, the choice of A is arbitrary, not being informed by any physical quantity. Further, the value of A has a significant effect on the maximally unstable wavenumber m_{\max} , with increasing A causing m_{\max} to decrease. Layers form on the scale of m_{\max} (cf. Chapter 3), so the introduction of hyperdiffusion introduces an artificial scale selection. Therefore we can say that the system with hyperdiffusion is less physically grounded than the system with $A = 0$.

6.3.5 The effect of changing parameters

The system (6.13)–(6.15) is governed by several dimensionless parameters. So far, we have considered these fixed at $\text{Pt}^{-1} = 0.01$, $\text{Ps}^{-1} = \text{Pt}^{-1}/100$, $\text{Re}^{-1} = 0$ and $\varepsilon = 0.02$, but in general these values may be varied. The Péclet numbers Pt^{-1} and Ps^{-1} depend on the diffusivity of the two components of buoyancy. In an oceanic setting, the ratio $\tau = \text{Ps}^{-1}/\text{Pt}^{-1} = 0.01$ is appropriate, but if the buoyancy gradients are provided by, for example, salt and sugar, then a diffusivity ratio of $\tau \approx 1/3$ is more appropriate. In

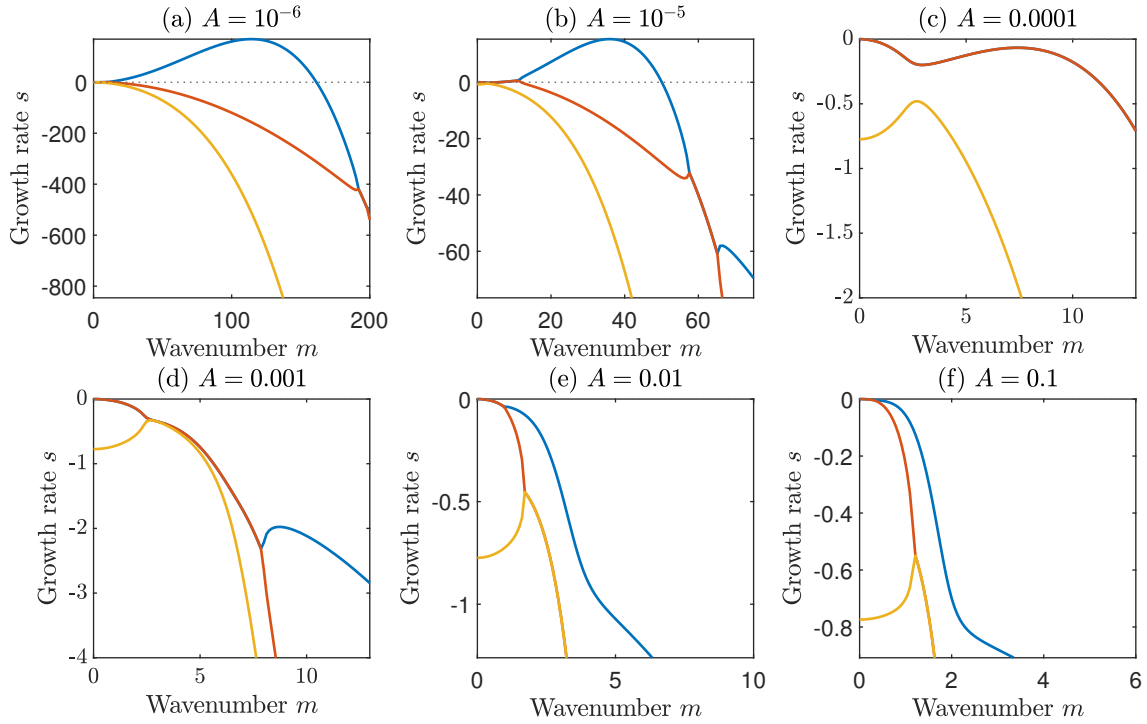


Fig. 6.4 Wavenumber-growth rate plots for $(g_0, d_0, e_0) = (-0.6, -0.63, 0.0022)$, for a range of values of A and parameter values $Pt^{-1} = 0.01$, $Ps^{-1} = 0.0001$, $\varepsilon = 0.02$ and $Re^{-1} = 0$. For perturbations to this steady state, increasing A beyond 10^{-4} is sufficient to suppress the high wavenumber instability for all wavenumbers.

Chapter 3, we saw that for the two-component system, increasing Pe^{-1} decreased the range of gradients where instability occurred. It is natural to expect that there will be a similar effect in the three-component system. We now investigate the effect on the stability of the system of changing τ and Pt^{-1} .

Varying the diffusivity ratio τ

The diffusivity ratio τ determines the strength of the double-diffusive effects, with $\tau = 0$ meaning that salt does not diffuse at all, and $\tau = 1$ the case where salt and temperature diffuse at the same rate, and can therefore evolve together as a single buoyancy field. Note that the system is invariant under the transformation $\tau \rightarrow 1/\tau$, $g \rightarrow -d$, $d \rightarrow -g$, $Ps^{-1} \rightarrow Pt^{-1}$, with ‘salt’ now the faster diffusing component, and ‘temperature’ diffusing more slowly.

Figure 6.5 shows the stability boundaries in g_0 – G_0 space for a range of values of τ . Increasing τ acts to flatten the unstable region, until at $\tau = 1$ the unstable region depends on G_0 alone. Note that as τ increases towards 1, the scale of the g axis increases significantly, until it is infinitely wide at $\tau = 1$. Continuing to increase τ beyond unity, the system flips, with the shape of the stability boundaries reflected in the $g = 0$ axis. Note that we take $Pt^{-1} = 0.01$ in Fig 6.5(a)–(d), and $Ps^{-1} = 0.01$ in Fig. 6.5(e)–(f), to allow this symmetry to be seen.

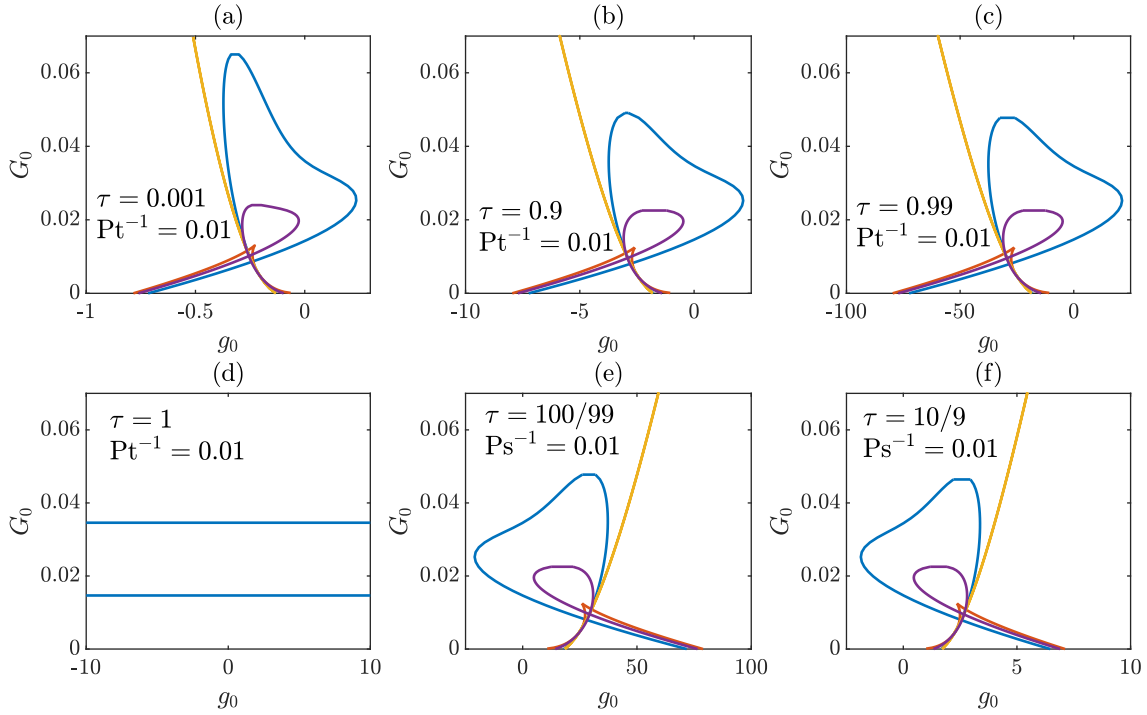


Fig. 6.5 Comparison of instability conditions (as shown in Fig. 6.2) for a range of values of τ , taking $Pt^{-1} = 0.01$ in panels (a)–(d), and $Ps^{-1} = 0.01$ in panels (e) and (f). $Re^{-1} = 0$ and $\varepsilon = 0.02$. Increasing τ ‘flattens’ the profile of the region, until $g - d$ does not vary with g when $\tau = 1$. Note that the plots in (e) and (f) are reflections of those in (c) and (b) respectively.

We have seen that changing τ has a significant effect on the unstable range of g_0 and d_0 , but have not yet seen its effect on the instability of perturbations in each steady state. Figure 6.6 shows how the growth rate of perturbations to the background state with $(g_0, d_0) = (0.1, 0.075)$ depends on wavenumber, for a range of values of τ . Increasing the value of τ increases the range of wavenumbers that is unstable, as well as the wavenumber of maximum growth rate. Thus, the larger the value of τ (i.e., the more similar the diffusivities of temperature and salt), the smaller the predicted scale of layers will be. So more strongly double-diffusive fluids will produce layers on a larger scale.

Varying the Péclet number Pt^{-1}

As discussed in Chapter 3, for the two-component system, increasing the Péclet number Pe^{-1} decreases the range of gradients that are susceptible to instability. Here, we expect that increasing Pt^{-1} while keeping τ fixed is likely to have a similar effect — shrinking the size of the unstable region in $g_0 - G_0$ space. Note that at $Pt^{-1} = 0$, if τ remains finite, then $Ps^{-1} = Pt^{-1} = 0$, recovering the two-component system.

Pt^{-1} measures the importance of thermal diffusion compared to advective transport, with larger values of Pt^{-1} corresponding to a system with more diffusion. Diffusion is a smoothing process, so it is to be expected that increasing the value of Pt^{-1} will act to suppress the layering instability.

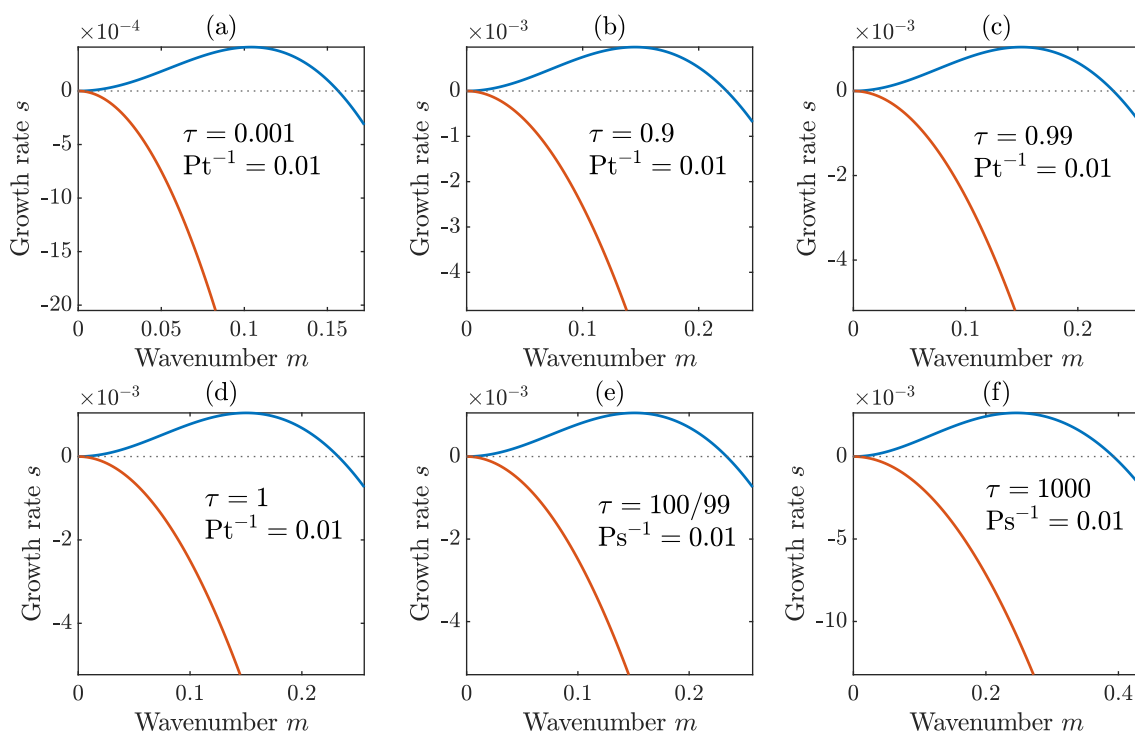


Fig. 6.6 Comparison of wavenumber-growth rate plots for a range of values of τ , taking $Pt^{-1} = 0.01$, $Re^{-1} = 0$ and $\varepsilon = 0.02$. Each plot is for the same point $(g_0, d_0) = (0.1, 0.075)$, roughly in the centre of the SF unstable region. Increasing τ increases both the range of unstable wavenumbers and the maximum growth rate

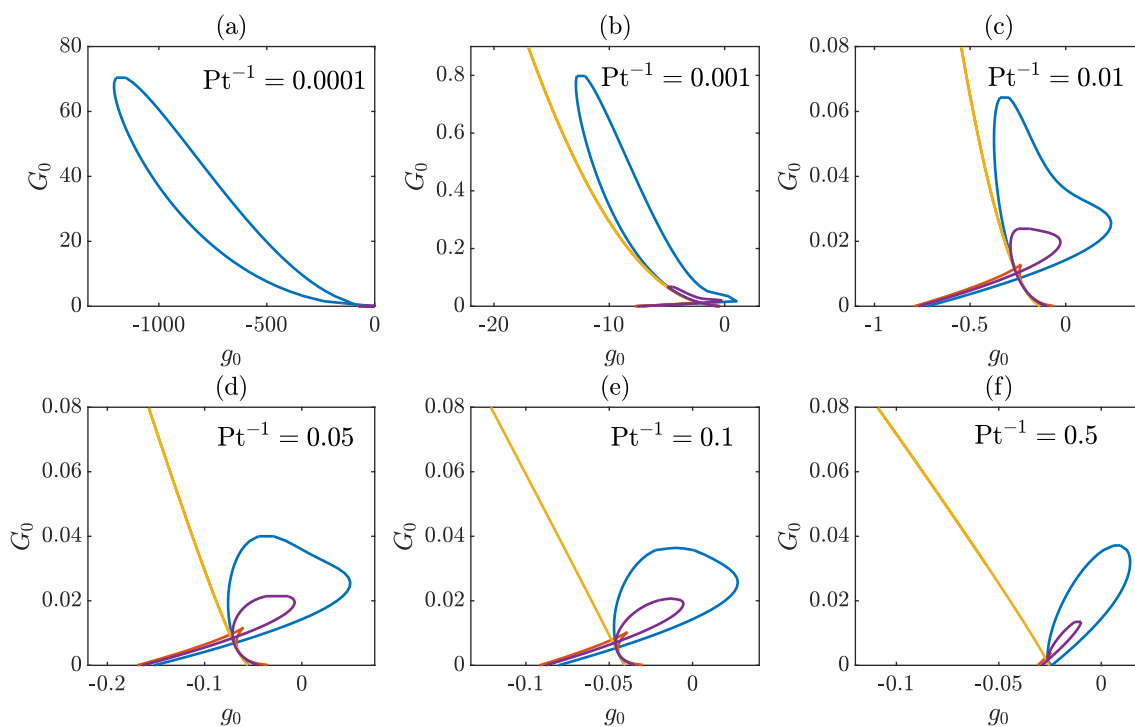


Fig. 6.7 Comparison of instability conditions for a range of values of Pt^{-1} , taking $\tau = 0.01$, $Re^{-1} = 0$ and $\varepsilon = 0.02$. Increasing Pt^{-1} shrinks the size of the unstable region (of both regimes) in g_0 - G_0 space.

Figure 6.7 shows the stability boundaries in g_0 – G_0 space for a range of values of Pt^{-1} . For very small values of Pt^{-1} there is a very large range of g_0 in the DC regime ($g_0 < 0$) where the Phillips instability occurs, while the size of the unstable region in the SF regime $g_0 > 0$ remains relatively small. As Pt^{-1} increases, the size of the unstable region of both regimes decreases, as expected. This is in keeping with the results of Chapter 3, where increasing Pt^{-1} also acted to suppress the layering instability.

6.4 Numerical Solutions

We have seen the conditions that are necessary for staircases to form in the three-component stirred system (6.13)–(6.15). To look beyond the initial instability, we now present long term nonlinear solutions, demonstrating the formation and subsequent evolution of staircases.

6.4.1 Numerical method to include hyperdiffusion

To solve the three-component system, we use the same MATLAB pdepe solver as in Chapter 3. This solver is designed to solve problems of the form:

$$c(x, t, u, u_x)u_t = x^{-m} (x^m f(x, t, u, u_x))_x + s(x, t, u, u_x), \quad (6.30)$$

with boundary conditions

$$p(x, t, u) + q(x, t) f(x, t, u, u_x) = 0. \quad (6.31)$$

It is straightforward to put the system (6.13)–(6.15) into this form. However, when hyperdiffusion is added, fourth derivatives are introduced. The pdepe solver is only designed to solve second order equations, so to tackle the fourth order system, we must rewrite it in terms of $T'' \equiv T_{zz}$ and $S'' \equiv S_{zz}$, and solve the five-component system

$$T_t = \left(\frac{l^2 e}{le^{1/2} + \text{Pt}^{-1}} T_z \text{Pt}^{-1} T_z \right)_z - A (T''_z)_z, \quad (6.32)$$

$$S_t = \left(\frac{l^2 e}{le^{1/2} + \text{Ps}^{-1}} S_z + \text{Ps}^{-1} S_z \right)_z - A (S''_z)_z, \quad (6.33)$$

$$e_t = \left(\frac{l^2 e}{le^{1/2} + \text{Re}^{-1} e_z} \right)_z - \frac{l^2 e}{le^{1/2} + \text{Pt}^{-1}} T_z + \frac{l^2 e}{le^{1/2} + \text{Ps}^{-1}} S_z + \text{Re}^{-1} e_{zz} - \varepsilon \frac{(e-1)e^{1/2}}{l}, \quad (6.34)$$

$$0 = (T_z)_z - T'', \quad (6.35)$$

$$0 = (S_z)_z - S''. \quad (6.36)$$

This new system (6.32)–(6.36) can be expressed in the form (6.30) by writing $u = (T, S, e, T'', S'')$.

For initial conditions, we take a uniform gradient background state (g_0, d_0, e_0) , perturbed by a sinusoidal perturbation with a single wavenumber. We choose the amplitude of the perturbation to be an eigenstate of the system for the chosen wavenumber $m = 2\pi n/H$. This eigenstate is found by considering the matrix equation for the growth rate of perturbations:

$$s \begin{pmatrix} g' \\ d' \\ e' \end{pmatrix} = M \begin{pmatrix} g' \\ d' \\ e' \end{pmatrix}, \quad (6.37)$$

where the matrix M takes the form:

$$M = \begin{pmatrix} -m^2 f_g - m^4 A & -m^2 f_d & -m^2 f_e \\ -m^2 c_g & -m^2 c_d - m^4 A & -m^2 c_e \\ p_g & p_d & -m^2 \kappa + p_e \end{pmatrix}, \quad (6.38)$$

and is evaluated in the steady state g_0, d_0, e_0 .

We use the MATLAB `eig` solver to find the eigenvalues s and eigenvectors of M , and choose the maximum eigenvalue s_{\max} , i.e. the one leading to the maximal growth of perturbations. Writing its eigenvector as $\mathbf{v}_{\max} = (v_1, v_2, v_3)^T$, the perturbation amplitudes are thus linked by the relation

$$\begin{pmatrix} g' \\ d' \\ e' \end{pmatrix} = \begin{pmatrix} 1 \\ v_2/v_1 \\ v_3/v_1 \end{pmatrix} g'. \quad (6.39)$$

We take the amplitude of the temperature perturbation to be $g' = 0.001g_0$; this coefficient is an arbitrary ‘small’ number, to make the perturbation small in comparison with the background state. Changing this simply changes the effective time origin of the perturbation. Values up to at least 0.1 are sufficiently small to ensure an initial linear growth phase in the two-component system. Combining this eigenstate-perturbation with

the background state gives the initial conditions for the numerical solutions as:

$$T(z, 0) = g_0 z - g' \sin\left(\frac{2\pi n z}{H}\right), \quad (6.40)$$

$$S(z, 0) = d_0 z - d' \sin\left(\frac{2\pi n z}{H}\right), \quad (6.41)$$

$$e(z, 0) = e_0 - e' \frac{2\pi n}{H} \cos\left(\frac{2\pi n z}{H}\right) \quad (6.42)$$

$$T''(z, 0) = g' \frac{4\pi^2 n^2}{H^2} \sin\left(\frac{2\pi n z}{H}\right), \quad (6.43)$$

$$T''(z, 0) = d' \frac{4\pi^2 n^2}{H^2} \sin\left(\frac{2\pi n z}{H}\right). \quad (6.44)$$

Based on our work on two-component stirred stratified convection (cf. Sec. 3.4.1), we take Dirichlet conditions to match the initial state:

$$T(0, t) = 0, \quad T(H, t) = g_0 H, \quad (6.45)$$

$$S(0, t) = 0, \quad S(H, t) = d_0(H), \quad (6.46)$$

$$e_z(0, t) = e_z(H, t) = 0. \quad (6.47)$$

$$T''(0, t) = T''(H, t) = 0, \quad (6.48)$$

$$S''(0, t) = S''(H, t) = 0. \quad (6.49)$$

The disadvantage of hyperdiffusion is that adding the extra two equations for T'' and S'' significantly increases the computational time needed. So in the SF region, where there is no HWI, we will solve the three equation system without hyperdiffusion (6.13)–(6.15), and we will only use the new five equation system (6.32)–(6.36) for the DC region. We will also show some results from DC without hyperdiffusion, to demonstrate how the HWI develops in the numerical solutions.

6.5 Numerical solutions in the salt fingering regime

We begin by considering states in the salt fingering regime, where $g > d > 0$. In this region, Fig. 6.2 shows that the only form of instability is the Phillips effect, which occurs in a finite region of $g_0 - d_0$ space, $0 < g_0 \lesssim 0.24$. As seen in Fig. 6.2, the range of G_0 where instability occurs is widest when $g_0 = 0$, with $0.014 \lesssim G_0 \lesssim 0.036$ susceptible to instability. As g_0 increases, the unstable range of G_0 decreases, until the tip of the unstable region is reached at $(g_0, d_0) \approx (0.24, 0.025)$. Of course, these values are specific to the parameters used ($\text{Pr}^{-1} = 0.01$, $\text{Ps}^{-1} = 0.0001$, $\varepsilon = 0.02$).

For the numerical integration, we take initial conditions (6.40)–(6.42), with fixed buoyancy and fixed energy boundary conditions (6.45), (6.46) and (6.47). We use the

MATLAB pdepe solver, with 4000 spatial steps over a depth of $H = 2000$ — the same as we used for the two-component system.

Figure 6.8 shows the evolution of solutions to the three-component model (6.13)–(6.15) for a range of initial conditions. Figure 6.8(a) has background state $(g_0, d_0, e_0) = (0.1, 0.075, 0.11)$, representing a point in the interior of the salt-fingering unstable region. Figure 6.8(b) has background state $(g_0, d_0, e_0) = (0.005, -0.03, 0.0403)$ — very close to the $g = 0$ boundary. Note that $d_0 < 0$ here, so both temperature and salinity gradients are statically stable, but the system is still unstable to perturbations due to the external stirring. Fig. 6.8(c) has $(g_0, d_0, e_0) = (0.23, 0.205, 0.17)$, near to the right hand boundary of the unstable region. The behaviour of all these solutions is qualitatively similar, with an initial stack of layers developing, and merging by Radko’s H-merger pattern, whereby neighbouring interfaces drift and combine, as seen in the two-component stirred model of Chapter 3.

Stirring dominates double-diffusion

To investigate the importance of double-diffusive effects versus stirring, we now take snapshots of solutions at fixed times. We compare the evolution of the temperature and salinity gradients by normalising them with respect to their background gradients. Figure 6.9 shows a snapshot of the normalised temperature and salinity gradients T_z/g_0 and S_z/d_0 , in solutions to (6.13)–(6.15). Three different values of the density ratio τ are considered, to demonstrate how the solutions change as the relative strength of the diffusivities is varied. In each case, the normalised temperature and salinity fields are almost identical, evolving together as a total buoyancy field, even when salt does not diffuse at all ($\tau = 0$). From this, we conclude that rather than double-diffusive effects being important, the layering dynamics are dominated by the stirring. Hence this model effectively produces the same results as the two-component model of Chapter 3. Recall the alternative form of the system (6.17)–(6.19); in this form, the model is clearly only a small perturbation away from the stirred two-component system (3.12)–(3.13). So it is not surprising that the results are very similar to those obtained in Chapter 3. As discussed in Chapter 1, Paparella & von Hardenberg (2014) proposed a two-component model based on that of BLY, in which the flux ratio γ was assumed to be constant, allowing the buoyancy to be modelled with a single equation. Here, we have separated the two components of buoyancy, but found them to evolve identically. As such, our third equation is not necessary, and instead the constant- γ assumption of Paparella & von Hardenberg (2014) would be appropriate for this stirred system. The additional equation makes the three-component system significantly more computationally expensive than a two-component system, so the model of Paparella & von Hardenberg (2014) is better suited to such stirred systems.

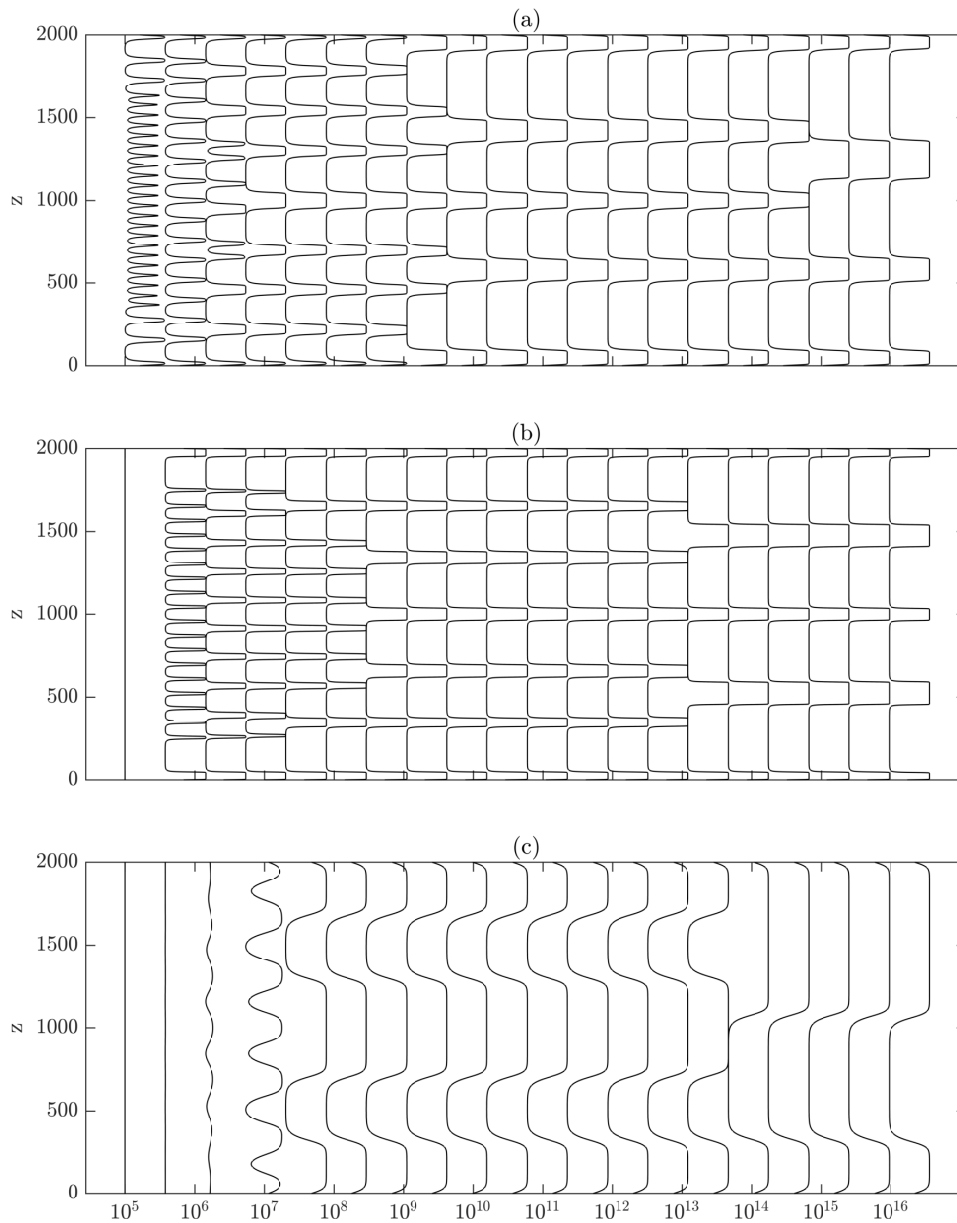


Fig. 6.8 Long-term evolution of the buoyancy gradient $b_z(z, t)$ in solutions of the three-component stirred system (6.13)–(6.15) with length scale (6.16), for parameter values $Pt^{-1} = 0.01$, $Ps^{-1} = 0.0001$, $\varepsilon = 0.02$ and $Re^{-1} = 0$. (a) Background state $(g_0, d_0, e_0) = (0, 1, 0, 0.75, 0, 11)$ and an $n = 33$ sinusoidal perturbation, near the centre of the SF unstable region; (b) $(g_0, d_0, e_0) = (0.005, -0.03, -0.043)$ and $n = 22$, with both temperature and salinity gradients stable; (c) $(g_0, d_0, e_0) = (0.23, 0.205, 0.17)$ and $n = 6$, near the right-hand boundary of the unstable region seen in Fig. 6.2. All three panels share a common time axis.

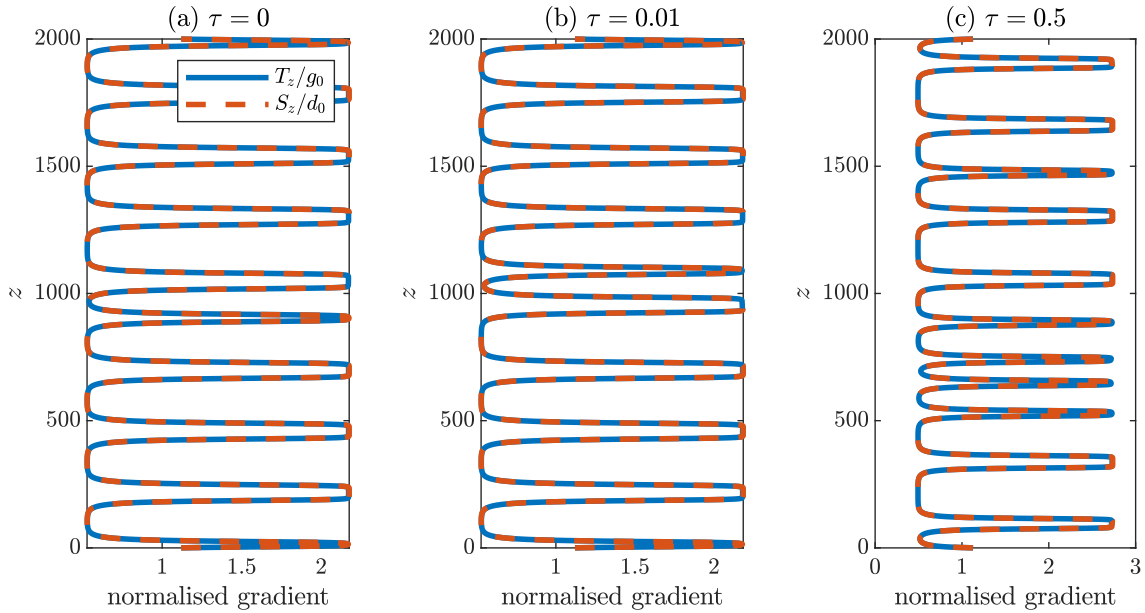


Fig. 6.9 Profiles of the temperature and salinity gradients in solutions to the three-component stirred system (6.13)–(6.15), at time $t = 10^7$, normalised by their background gradients. Each panel contains a snapshot at $t = 10^7$ of the solution with background gradients $(g_0, d_0) = (0.1, 0.075)$, with (a) $e_0 = 0.11$, $\tau = 0$; (b) $e_0 = 0.11$, $\tau = 0.01$; and (c) $e_0 = 0.095$, $\tau = 0.5$. Temperature and salinity fields track each other closely, with the normalised gradients being identical in all three cases.

6.6 Numerical solutions in the diffusive convection regime

In Sec. 6.3.2, we saw in Fig. 6.2 that there are regions of $g_0 - d_0$ space in the DC regime in which each of the possible instabilities takes place: the Phillips instability where $F_g C_d - F_d C_g < 0$, the energy mode where $p_e > 0$, and the high wavenumber instability where $f_g c_d - f_d c_g < 0$. In contrast, the SF regime admitted only the Phillips instability. In this section, we present numerical solutions in the DC regime for initial conditions with the HWI predicted (§ 6.6.1), and the Phillips instability (§ 6.6.2), both with and without hyperdiffusion terms in the equations.

6.6.1 Solution with high wavenumber instability

We begin by considering a solution for which the linear stability analysis predicts a high wavenumber instability. Fig. 6.2 shows a large region of the DC regime ($g_0 < 0$) in which the HWI is predicted by the stability analysis. We choose a background state in this region. Figure 6.10 shows two solutions to (6.32)–(6.36) starting with background state $(g_0, d_0, e_0) = (-0.6, -0.63, 0.0022)$. Fig. 6.10(a) shows the solution with no hyperdiffusion to counter the HWI; there is random growth of spikes in the gradient on the scale of the spatial mesh, which fits the expectation of the HWI producing growth on the smallest possible scales. Fig. 6.10(b) shows the solution with hyperdiffusion coefficient $A = 0.01$,

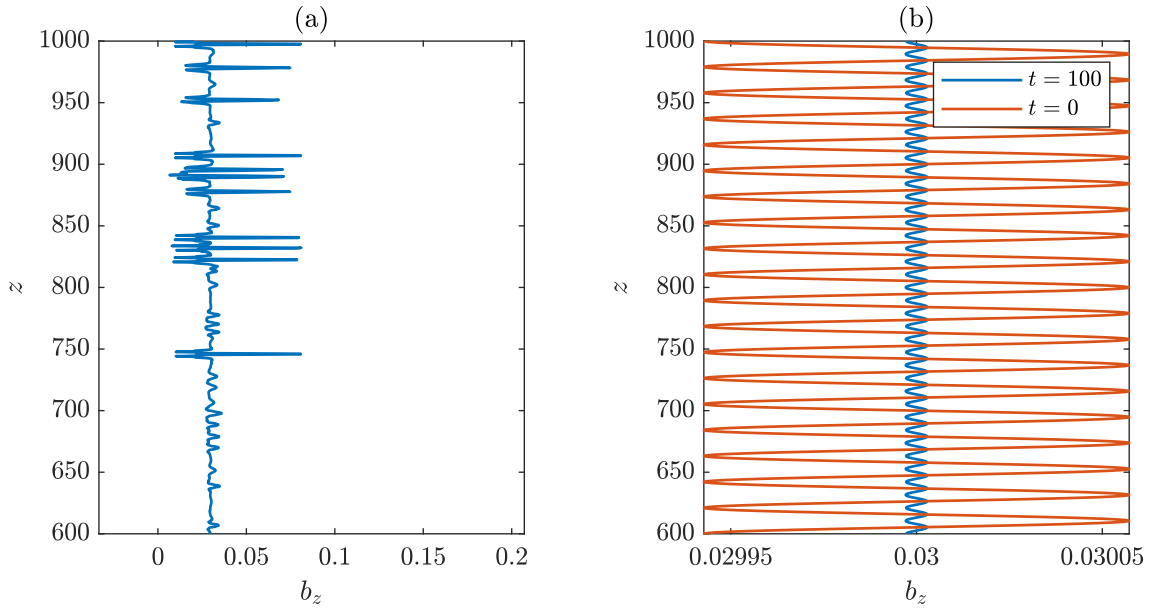


Fig. 6.10 Solutions to (6.32)–(6.36) in the DC regime, with background steady state $(g_0, d_0, e_0 = -0.6, -0.63, 0.0022)$ and parameter values $Pt^{-1} = 0.01$, $Ps^{-1} = 0.0001$, $\varepsilon = 0.02$ and $Re^{-1} = 0$. In this background state, a high wavenumber instability is expected. (a) Solution at time $t = 100$ for the system solved without hyperdiffusion terms to counter the HWI (i.e. $A = 0$). (b) Solution at time $t = 100$ for hyperdiffusion coefficient $A = 0.01$. The initial condition is shown in red for comparison.

as well as the initial condition. It is clear that the hyperdiffusion has suppressed the HWI, with the amplitude of the initial condition simply decaying.

6.6.2 Solution with Phillips instability

Now we consider a solution where the linear analysis predicts the Phillips instability, with no HWI expected. It would be reasonable to assume that with no HWI, the solutions will be similar to those in the SF regime with the Phillips instability. Figure 6.11 shows two solutions to (6.32)–(6.36), starting in the background state $(g_0, d_0, e_0) = (-0.1, -0.13, 0.033)$. Applying the stability analysis of Chapter 5, we find that this state is unstable to the Phillips effect, with most unstable wavenumber $m = 0.297$, predicting the formation of $n = 24$ layers across a domain depth of $H = 500$. Fig. 6.11(a) shows a solution with no hyperdiffusion. The solution evolves through the formation and merger of layers, but over time the interfaces gradually sharpen to the scale of the spatial mesh. This is surprising, as in all previous solutions interfaces the initial width of interfaces has been set by the linearly most unstable wavenumber, and interfaces have changed in width only via merger events. Contrary to expectation, it appears that the HWI does have an effect even when the background state is not linearly unstable at small scales. During the nonlinear evolution, the solution locally attains states that are unstable to the HWI, which then produce growth on infinitesimal scales. As such, it appears that it is necessary to include the hyperdiffusion terms to produce well-resolved layers in the DC regime.

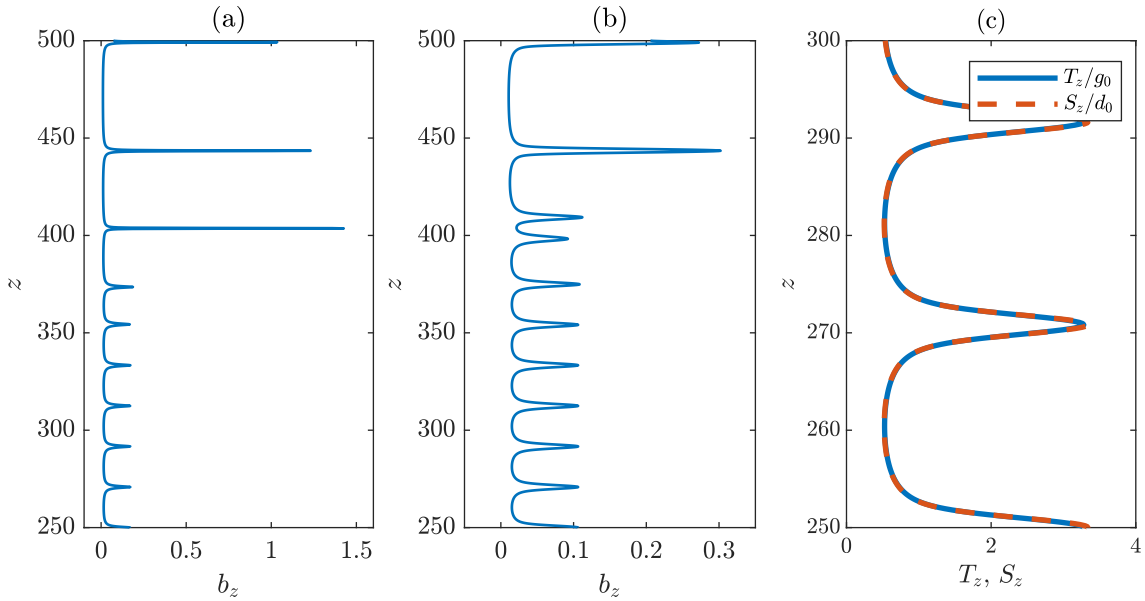


Fig. 6.11 Solutions to (6.32)–(6.36) in the DC regime, with background steady state $(g_0, d_0, e_0 = -0.1, -0.13, 0.032)$ and parameter values $Pt^{-1} = 0.01$, $Ps^{-1} = 0.0001$, $\varepsilon = 0.02$ and $Re^{-1} = 0$. In this background state, the Phillips instability is predicted by the linear stability analysis. (a) Solution at time $t = 10000$ for the system solved without hyperdiffusion terms (i.e. $A = 0$). Interfaces sharpen to the scale of the spatial mesh owing to the effect of the HWI. (b) Solution at time $t = 10000$ for hyperdiffusion coefficient $A = 0.01$. The hyperdiffusion regularises the sharpening, producing well-resolved layers. Note the plots show only a portion of the depth, to demonstrate most clearly the resolution of the interfaces. (c) Comparison of temperature and salinity gradients, normalised by their background gradients $T_z/-0.1$ and $S_z/0.13$, at time 10000, for the case with hyperdiffusion.

Figure 6.11(b) shows a solution with hyperdiffusion coefficient $A = 0.01$. Clear, well-resolved layers can now be seen. A disadvantage of the hyperdiffusion terms is that the system takes significantly longer to solve numerically, owing to the addition of the two extra equations (6.35)–(6.36). To produce the results in Fig. 6.11(b), the normal spatial resolution of 4000 meshpoints over $H = 2000$ was not sufficient, and the solver failed, so the domain depth was reduced to $H = 500$. To reach $t = 10^5$ in Fig. 6.11(b) took 2500s, compared to 90s for Fig. 6.11(a). Further increasing the time range leads to a nonlinear increase in the computational time. However, the dynamics of the solutions closely resemble those of the salt fingering solutions, so it is not necessary to show large numbers of solutions for DC.

Figure 6.11(c) shows a comparison of the normalised temperature and salinity gradient fields T_z/g_0 and S_z/d_0 at $t = 10000$. As in the SF case, the fields are almost identical, evolving together as a total buoyancy field, demonstrating that the dominant driving factor for the layering is the stirring, with double-diffusive dynamics being a secondary factor.

6.7 Discussion

In this chapter, we have investigated staircases in a double-diffusive system with an external energy source. We have used the same framework as in the two-component system presented in Chapter 3, adding an equation for the second component of density. We have applied the stability analysis of the three-component Phillips effect as discussed in Chapter 5.

In the salt fingering regime, the system is unstable to the Phillips instability for a wide range of parameter values. Numerical solutions of the three-component system produce results very similar to those shown for the two-component system with only a single independent component of buoyancy. In fact, by comparing the profiles of the temperature and salinity gradients in the solutions, we have seen that they are almost identical. Rather than evolving independently, both components of the buoyancy are merely carried together as part of the total buoyancy field. The stirring of the system is the driver behind the dynamics, with double-diffusive effects being secondary. Even for the extreme case where the diffusivity ratio $\tau = 0$ (i.e. no molecular diffusion of salt), there is only a very small difference between the two components of buoyancy. We will see in the next Chapter that for true salt fingering staircases to exist in the absence of stirring, it is necessary to reconsider the form of the length scale so that double-diffusive effects, rather than stirring, drive the Phillips instability.

In the diffusive convection regime, the system is unstable not only to the Phillips instability, but also to the energy mode and high wavenumber instabilities. The energy mode can be avoided by choice of suitable initial background gradients. The high wavenumber instability, on the other hand, can not be avoided. Even when the system is initialised in a state that is not linearly unstable to the HWI, the nonlinear evolution leads to states that are locally unstable at high wavenumbers. This leads to interfaces sharpening to the spatial mesh scale, rather than having a well-defined finite width. As such, the model must be regularised.

We saw in Chapter 5 that the high wavenumber instability can be regularised through the addition of hyperdiffusion terms to the temperature and salinity equations. By adding these terms with a suitable coefficient, the HWI is avoided and diffusive staircases can form. However, the addition of the hyperdiffusion makes the system significantly more computationally expensive. As in the salt fingering regime, we see that the dominant behaviour is due to stirring, rather than double-diffusive effects. In Chapter 8, we will present a model of DC layering where DDC effects are dominant.

Chapter 7

Thermohaline staircases: Salt fingering

7.1 Introduction

In Chapter 5, we extended the concepts of the Phillips effect and γ -instabilities to a three-component system in terms of temperature, salinity and kinetic energy. We demonstrated that the two instabilities are mathematically similar, with the physical difference coming from the driving energy source. The Phillips instability relies on forcing in the energy equation, for example via a direct energy source, as in the model of Balmforth *et al.* (1998), or from a constant salt finger flux, as assumed by Paparella & von Hardenberg (2014). We saw in Chapter 6 that in a three-component model, if stirring is retained, then the dynamics are almost identical to that of the two-component stirred system, with the temperature and salinity fields evolving together as a single buoyancy field. In this chapter, we present a new model for the evolution of thermohaline staircases without the need for such forcing, by reconsidering the form of the length-scale used to close the system. This is the first three-component mixing-length model for double-diffusive layering.

We begin by presenting a three-component model derived using the averaging process described in Chapter 2, and discussing an appropriate form for the length scale in the unstirred system. We apply this model to the salt fingering regime of double-diffusive convection. Applying the instability theory of Chapter 5, we analyse the linear stability of steady states, and demonstrate that the system is unstable for a range of parameter values within the salt fingering regime. Numerical solutions of the model to long times indicate that staircases evolve via the ‘B-merger’ pattern described by Radko (2007), whereby strong interfaces grow at the expense of weaker ones. Each layer merger causes the buoyancy gradient in surviving interfaces to increase, and the buoyancy flux through the layers to increase, so the staircase has significantly higher buoyancy flux than the initial unlayered state.

The chapter is arranged as follows. Section 7.2 contains a description of our three-component double-diffusive model and a discussion of the mixing length on which it depends. In Sec. 7.3 we apply the results of Chapter 5 to our model, demonstrating the expected regions of instability, and discussing the effect of changing the parameters of the

model. In Sec. 7.4, we present long-term numerical solutions and discuss the behaviour of the buoyancy flux through layer mergers. We end in Sec. 7.5 by summarising our key conclusions. The results presented in this chapter have been published as Pružina *et al.* (2023)

7.2 A three-component model for thermohaline staircases

To develop our model for the formation and evolution of thermohaline staircases, we consider a domain of height h , with a background dimensional temperature gradient Θ_z , salinity gradient Σ_z and reference density ρ_0 . The evolution of the velocity $\mathbf{u}(\mathbf{x}, t)$, temperature $T(\mathbf{x}, t)$ and salinity $S(\mathbf{x}, t)$ are governed by the Boussinesq equations

$$\mathbf{u}_t + \mathbf{u} \cdot \nabla \mathbf{u} = -\frac{1}{\rho_0} \nabla p + \frac{g(\rho - \rho_0)}{\rho_0} \mathbf{e}_z + \nu \nabla^2 \mathbf{u}, \quad (7.1)$$

$$T_t + \mathbf{u} \cdot \nabla T = \kappa_T \nabla^2 T, \quad (7.2)$$

$$S_t + \mathbf{u} \cdot \nabla S = \kappa_S \nabla^2 S, \quad (7.3)$$

$$\nabla \cdot \mathbf{u} = 0, \quad (7.4)$$

$$\frac{\rho - \rho_0}{\rho_0} = \beta S - \alpha T, \quad (7.5)$$

where $\rho(\mathbf{x}, t)$ is the density, and $p(\mathbf{x}, t)$ the pressure. The equations depend on the kinematic viscosity ν , the thermal and solutal diffusivities κ_T and κ_S , gravitational acceleration g , and thermal and solutal expansion coefficients α and β .

We nondimensionalise the system (7.1)–(7.5) via

$$\hat{t} = \frac{\kappa_T}{L^2} t, \quad \hat{z} = \frac{1}{L} z, \quad \hat{\mathbf{u}} = \frac{L}{\kappa_T} \mathbf{u}, \quad \hat{T} = \frac{\alpha g L^3}{\kappa_T \nu} T, \quad \hat{S} = \frac{\beta g L^3}{\kappa_T \nu} S, \quad \hat{p} = \frac{L^2}{\rho_0 \nu \kappa_T} p, \quad (7.6)$$

with hats denoting dimensionless quantities. The characteristic length L is taken to be the salt finger length, chosen such that the magnitude of the local Rayleigh number is equal to unity (Stern, 1960):

$$|\text{Ra}| = \frac{\alpha g |\Theta_z| L^4}{\kappa_T \nu} = 1. \quad (7.7)$$

With the choice of nondimensionalisation (7.6), the magnitudes of the dimensionless background temperature and salinity gradients are equal to the thermal and solutal Rayleigh numbers:

$$|\hat{\Theta}_z| = \frac{\alpha g |\Theta_z| L^4}{\kappa_T \nu} = |\text{Ra}| = 1, \quad (7.8)$$

$$|\hat{\Sigma}_z| = \frac{\beta g |\Sigma_z| L^4}{\kappa_T \nu} = |\text{Rs}| = \frac{1}{R_0}, \quad (7.9)$$

where R_0 is the density ratio. Dropping hats, we obtain the dimensionless form of the governing equations (7.1)–(7.5) as

$$\mathbf{u}_t + \mathbf{u} \cdot \nabla \mathbf{u} = -\sigma \nabla p + \sigma b \mathbf{e}_z + \sigma \nabla^2 \mathbf{u}, \quad (7.10)$$

$$T_t + \mathbf{u} \cdot \nabla T = \nabla^2 T, \quad (7.11)$$

$$S_t + \mathbf{u} \cdot \nabla S = \tau \nabla^2 S, \quad (7.12)$$

$$\nabla \cdot \mathbf{u} = 0, \quad (7.13)$$

$$b = T - S, \quad (7.14)$$

where $b(\mathbf{x}, t)$ is the nondimensional buoyancy field. These equations depend on the diffusivity ratio $\tau = \kappa_S / \kappa_T$ and the Prandtl number $\sigma = \nu / \kappa_T$. The dimensionless height of the domain is $H = h/L$.

We now present a one-dimensional model for double-diffusive layering of the form (5.1)–(5.3), developed using a horizontal averaging process. Oceanic observations of double-diffusive staircases show a horizontal extent far greater than the thickness of the individual layers (e.g. Schmitt *et al.*, 1987). As such, a horizontally averaged one-dimensional model is appropriate, providing insight to the physics of layering within a model that is relatively simple computationally. We once again apply the averaging process detailed in Chapter 2, to obtain the following system:

$$T_t = \left(\frac{l^2 e}{le^{1/2} + 1} T_z \right)_z, \quad (7.15)$$

$$S_t = \left(\frac{l^2 e}{le^{1/2} + \tau} S_z \right)_z, \quad (7.16)$$

$$e_t = \left(\frac{l^2 e}{le^{1/2} + \sigma} e_z \right)_z - \sigma \left(\frac{l^2 e}{le^{1/2} + 1} T_z - \frac{l^2 e}{le^{1/2} + \tau} S_z \right) + \sigma e_{zz} - \varepsilon \frac{e^{3/2}}{l}, \quad (7.17)$$

where T , S and e represent the horizontally averaged temperature, salinity and turbulent kinetic energy. The parameter ε controls the strength of the dissipation term. The system is closed by the mixing length l . The parameterisation of l is critical to the model, as it controls the form of the flux terms, and therefore the nature of any instability (cf. Chapter 5). For this turbulent model, we assume that the turbulent flux terms are more important than molecular diffusion, and have thus neglected the independent diffusion terms in (7.15) and (7.16).

It should be noted that this is a model of turbulent flow, relying on parameterisations of fluxes in terms of eddy diffusivities. As such, it should not be expected, and is not intended, to describe non-turbulent states accurately. Numerical simulations (e.g. Stellmach *et al.*, 2011) show that the salt fingering instability quickly leads to a highly turbulent state; although this form of model cannot capture the initial salt fingering stage of the evolution, it is nonetheless appropriate to describe all subsequent development, including the formation and evolution of staircases. Despite the fact that we are modelling a turbulent system,

observations and numerical simulations show that the diffusivity ratio τ is critical to the evolution of double-diffusive staircases, and hence it is important to keep it in the model. As such, the eddy diffusivities are not identical in each equation, as may be expected in a fully turbulent model. If $\tau = 1$, there would be no difference between the two components of buoyancy, and layering would not be possible without an external forcing.

The aim of this model is to describe layering within a mixing-length framework through the mechanism described in Chapter 5, which we have shown to be equivalent to the γ -instability of Radko (2003). Based on Radko's work, we propose to parameterise the flux functions, and therefore the length scale, in terms of the density ratio $R = T_z/S_z$, rather than in terms of the gradients individually. From a physical perspective, the mixing length l can be interpreted as a characteristic size of turbulent eddies, indicating that it should depend on e as well as R . Previous work on layering has shown that it is the qualitative form of the length scale that is important, rather than its precise parameterisation. For example, Balmforth *et al.* (1998), Paparella & von Hardenberg (2014) and Coclite *et al.* (2018) all used different prescriptions for $l(b_z, e)$ in models of stirred layering, producing very similar results. With this in mind, we propose a prescription for the length scale based on qualitative arguments, rather than a direct physical derivation.

In salt fingering systems, it has been established, both numerically and experimentally, that the temperature and salinity fluxes have a decreasing dependence on the density ratio $R = T_z/S_z$ (McDougall & Taylor, 1984; Kimura *et al.*, 2011). Furthermore, for the γ -style instability to be present, the flux ratio $\gamma = f/c$ should also decrease as a function of R . In our system (7.15)–(7.17), the temperature flux is $f = l^2 e T_z / (le^{1/2} + 1)$ and the salinity flux is $c = l^2 e S_z / (le^{1/2} + \tau)$. From these forms, f , c and γ are all increasing functions of the length scale l , and hence for $f(R)$, $c(R)$ and $\gamma(R)$ to be decreasing, $l(R)$ must also be decreasing. Real fingering staircases are generally observed in the range $1 < R < 2$, so we parameterise $l(R)$ to be decreasing within this range of interest. From a physical standpoint, the eddy diffusivities should increase as the amount of turbulence increases, so we parameterise l to also have an increasing dependence on e within the range of interest. Mathematically, a choice of l that depends on R alone would lead to the high-wavenumber instability discussed in Chapter 5, further motivating the dependence on both R and e . Based on these considerations, we adopt the parameterisation

$$l = \frac{(e^2 + \delta R^2)^{1/2}}{e^{1/2} R}, \quad (7.18)$$

where δ is a parameter chosen to be small such that, for $O(1)$ values of e and R , the mixing length $l \sim \sqrt{e}/R$. The value of δ must be non-zero, as otherwise $e = 0$ is a steady-state solution for all values of R_0 , susceptible to the energy-mode instability (5.11). For values of R close to unity, the prescription (7.18) is a decreasing function of R , giving a large length when $R \approx 1$, and smaller lengths for larger values of R , as required. We note that, while the model (7.15)–(7.17) was derived via averaging processes and physical arguments,

by contrast there is not such a clear physical motivation for the exact form of the length scale. The prescription (7.18) is therefore not the only possible choice, but is, nonetheless, a simple parameterisation with the appropriate qualitative dependence on e and R to model layers.

It should be noted that in double-diffusive convection described by the Boussinesq equations (7.1)–(7.5), the buoyancy anomalies leading to convective motions appear at or below the salt fingering length scale ($l = 1$, in our nondimensionalisation), while turbulent mixing is expected to occur on scales larger than this. Our turbulent model cannot describe these small scale dynamics directly, and instead assumes that turbulent motion continues down to the smallest scales to parameterise these motions. The length measures the scale of the turbulent motion, rather than the layers themselves, so that in these strongly convective regions, we expect l to represent the size of a turbulent eddy, which may be significantly smaller than the full layer depth.

At this stage, it is helpful to review the parameter values for which the two different regimes of double-diffusive convection occur. In the salt fingering regime, both temperature and salt gradients are positive. For the fluid to be statically stable, it is required that $b_z = 1 - 1/R_0 > 0$, and hence the background density ratio

$$R_0 > 1. \quad (7.19)$$

For diffusive convection, both gradients are negative. The overall buoyancy gradient is $b_z = -1 + 1/R_0$, so for the fluid to be statically stable, it is required that

$$0 < R_0 < 1. \quad (7.20)$$

The system (7.15)–(7.18) depends on four dimensionless parameters: τ , σ , δ and ε . The first two are material parameters of the fluid under consideration. For example, salt water has a diffusivity ratio of $\tau \approx 0.01$ and a Prandtl number of $\sigma = O(10)$, depending on the temperature and salinity. In this study, we focus primarily on illustrating the results of our model for the case of salt water, but we note that the choice of τ and σ can be adapted to model other physical contexts. The latter two parameters, δ and ε , are empirical modelling parameters introduced in the derivation to control the relative importance of turbulent dissipation and the form of the mixing length (7.18) (the parameter ε also appears in the model of BLY). We will determine values of δ and ε that lead to physically realistic behaviour in the solutions.

7.3 Steady states and their stability

To analyse the stability of the system (7.15)–(7.17), we begin by applying the general linear stability theory of three-component systems developed in Chapter 5. Equations (7.15)–

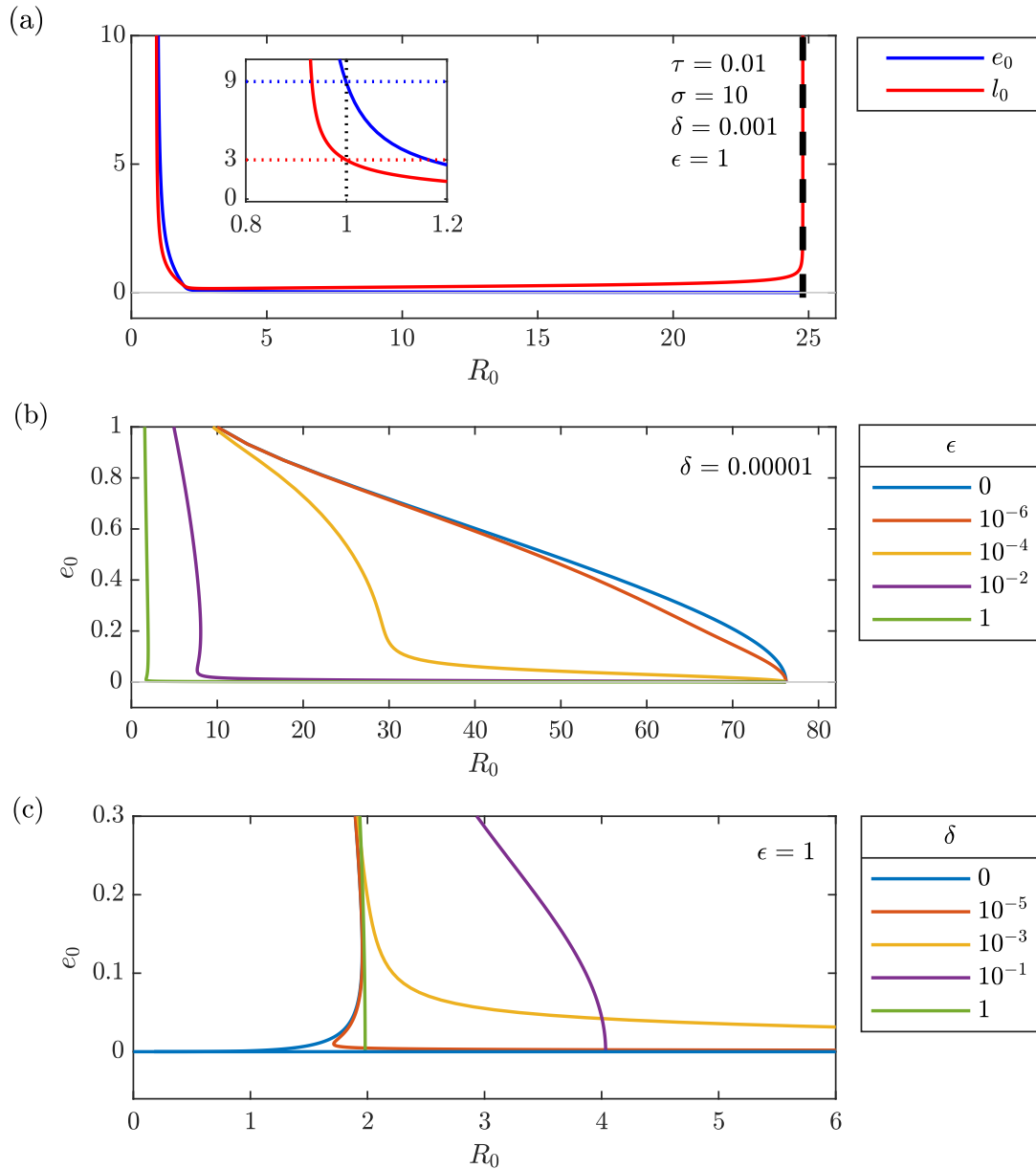


Fig. 7.1 Steady-state solutions to (7.25) with $\tau = 0.01$, $\sigma = 10$. (a) Energy e_0 and corresponding value of the length scale l_0 given by (7.18), as functions of R_0 for $\epsilon = 1$, $\delta = 0.001$. For small R_0 , e_0 and l_0 are large; as R_0 increases, e_0 decreases, with l_0 initially decreasing but $l_0 \rightarrow \infty$ as $e_0 \rightarrow 0$. Inset plot shows behaviour of e_0 and l_0 near $R_0 = 1$, with red and blue dotted lines showing the values $e_0 = \sigma/\epsilon - 1 = 9$ and $l_0 = \sqrt{\sigma/\epsilon - 1} = 3$. (b) e_0 as a function of R_0 , for a range of values of δ with $\epsilon = 1$ fixed. (c) e_0 as a function of R_0 , for a range of values of ϵ with $\delta = 0.001$ fixed. Sufficiently small values of δ and large values of ϵ lead to $e_0(R_0)$ being multi-valued.

(7.17) may be expressed in the form (3.17)–(3.18) by writing

$$f = \frac{l^2 e}{le^{1/2} + 1} g, \quad (7.21)$$

$$c = \frac{l^2 e}{le^{1/2} + \tau} d, \quad (7.22)$$

$$\kappa = \frac{l^2 e}{le^{1/2} + \sigma} + \sigma, \quad (7.23)$$

$$p = -\sigma \left(\frac{l^2 e}{le^{1/2} + 1} g - \frac{l^2 e}{le^{1/2} + \tau} d \right) - \varepsilon \frac{e^{3/2}}{l}, \quad (7.24)$$

where $g = T_z$ and $d = S_z$. For a given value of R_0 , the system admits the uniform steady state $(g_0, d_0, e_0) = (\pm 1, \pm 1/R_0, e_0(R_0))$.

7.3.1 Steady states

With the length scale prescribed by (7.18), the steady-state equation $p = 0$ for $e_0(R_0)$ leads to the following algebraic relation between e_0 and the parameter R_0 :

$$g_0(R_0 - 1)(e_0^2 + \delta R_0^2)^2 + g_0(\tau R_0 - 1)(e_0^2 + \delta R_0^2)^{3/2} R_0 + \frac{\varepsilon}{\sigma} R_0^3 e_0^2 (e_0^2 + \delta R_0^2) + (1 + \tau) \frac{\varepsilon}{\sigma} (e_0^2 + \delta R_0^2)^{1/2} e_0^2 + \frac{\varepsilon}{\sigma} R_0^5 \tau e_0^2 = 0, \quad (7.25)$$

where $g_0 = \pm 1$. We interpret the uniform-gradient steady state physically as a representation of the flow resulting from salt fingers. Individual fingers cannot be distinguished, but a mean fluid motion is supported by one stable and one unstable component of the buoyancy gradient.

Figure 7.1(a) shows e_0 as a function of R_0 . When there is no overall stratification ($R_0 = 1$), the energy $e_0 \approx \sigma/\varepsilon - 1$ (shown by the blue dotted line in the inset plot). As R_0 increases, e_0 decreases, reaching $e_0 = 0$ at $R_0 = (1 + \sqrt{\delta})/(\tau + \sqrt{\delta})$. However, it is important to note that such an unphysical ‘zero energy turbulent state’ is precluded in our time-dependent model. To see this, we consider the evolution of a state that begins with $e > 0$ for all z . At a given time, let $z = z_*$ denote the position of a local minimum of e , with $e_z(z_*) = 0$, $e_{zz}(z_*) > 0$, and $e(z_*)$ is near zero. Additionally, we note from (7.18) that $le^{1/2} \rightarrow \sqrt{\delta}$ as $e \rightarrow 0$. After some algebra, the governing energy equation (7.17) at $z = z_*$ gives

$$e_t(z_*) \sim \left(\frac{\delta}{\sqrt{\delta} + \sigma} + \sigma \right) e_{zz} - \sigma \left(\frac{\delta T_z}{\sqrt{\delta} + 1} - \frac{\delta S_z}{\sqrt{\delta} + \tau} \right). \quad (7.26)$$

Provided that $R_0 < (\sqrt{\delta} + 1)/(\sqrt{\delta} + \tau)$ (i.e. R_0 is in the range where uniform steady states exist), every term on the right-hand side of (7.26) is positive. It follows that $e_t(z_*) > 0$, implying that the minimum energy cannot decrease, precluding the energy from ever reaching zero. Hence, while zero energy and negative energy states can exist within the equations, they will never be attained from initial conditions starting with positive energy.

Nonetheless, the change of sign of e_0 when $R_0 > (\sqrt{\delta} + 1)/(\sqrt{\delta} + \tau)$ means that this model is applicable only for sufficiently low density ratios.

Figure 7.1(a) also shows the value of the length scale l_0 calculated from the energy using (7.18). As $R_0 \rightarrow 1$, $l_0 \sim \sqrt{e_0} \approx \sqrt{\sigma/\varepsilon - 1}$, which is shown by the red dotted line in the inset. As R_0 increases from 1, the length scale is decreasing in the range of interest near $R_0 = 1$, before reaching a minimum and increasing for larger values of R_0 , with $l_0 \rightarrow \infty$ and $e_0 \rightarrow 0$ as $R_0 \rightarrow (\sqrt{\delta} + 1)/(\sqrt{\delta} + \tau)$. The fact that l diverges as $e_0 \rightarrow 0$ is at on the surface a little concerning, however the length scale is decreasing as a function of R inside the range of interest, and the divergence occurs for much larger values of R than those for which we expect layering, so the parameterisation (7.18) is acceptable. Further, we have shown that the zero energy state is never reached, and hence this divergence in the mixing length will never occur in numerical solutions.

The relationship between e_0 and R_0 given by (7.25) is shown for various choices of the parameters ε and δ in figures 7.1(b)–(c). The results illustrate a strong dependence of e_0 on both ε and δ . As ε increases, the value of e_0 decreases for each R_0 , with $e_0 \approx \sigma/\varepsilon - 1$ at $R_0 = 1$, and $e_0 = 0$ at $R_0 = (1 + \sqrt{\delta})/(\tau + \sqrt{\delta})$. On the other hand, increasing the value of δ increases the energy at each R_0 . At smaller values of δ and larger values of ε , e_0 to be multi-valued for some range of R_0 . For example, the solution shown in purple in Fig. 7.1(b) is multi-valued near $R_0 \approx 8$. In cases where there are multiple steady-state energies, one steady state is unstable to the energy mode, leading to growth in energy on the domain scale. To investigate layering processes we wish to avoid this situation, so we set $\varepsilon = 1$ and $\delta = 0.001$. These are the parameters used in Fig. 7.1(a), where e_0 is clearly single-valued throughout.

In the diffusive convection regime, $T_z, S_z > 0$ and $0 < R_0 < 1$. Within these ranges, all the terms in (7.25) are negative, and hence there are no positive solutions for e_0 in the diffusive convection regime. This result holds in general for any system of the form (7.21)–(7.24), no matter what parameterisations are adopted for the length scale and dissipation term. As such, it appears that an unforced system of this form is not sufficient to model layering in diffusive convection, lending weight to the proposition of Ma & Peltier (2022) that external forcing may be necessary. In this chapter, we will restrict our focus to the salt fingering regime, with the modelling of layering in diffusive convection being revisited in Chapter 8.

7.3.2 Linear stability

The stability of the steady states of (7.15)–(7.17) can be analysed using the framework described in Chapter 5. For a range of values of R_0 , we first calculate $e_0(R_0)$ and substitute the value into the expressions for $-p_e$, $F_g C_d - F_d C_g$, $F_g + C_d$ and $f_g c_d - f_d c_g$; these quantities are plotted as functions of R_0 in Fig. 7.2(a). For a finite range of R_0 (between the red dots), $F_g C_d - F_d C_g < 0$, thereby satisfying the condition for the Phillips instability. By comparison with the schematic in Fig. 5.1(b), we see that our expectation of a finite unstable

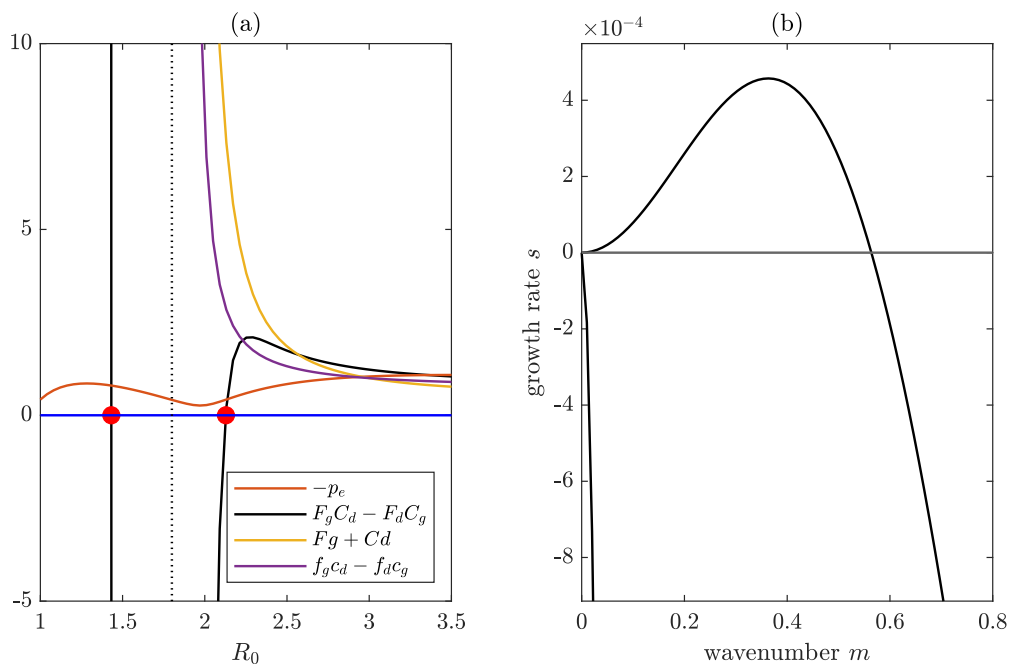


Fig. 7.2 (a) Various stability measures of the uniform steady state as R_0 varies, with $\tau = 0.01$, $\sigma = 10$, $\varepsilon = 1$, $\delta = 0.001$. The quantity $-p_e$ is shown in red, $F_g C_d - F_d C_g$ in black, $F_g + C_d$ in yellow, and $f_g c_d - f_d c_g$ in purple. The red circles mark the minimum and maximum values of R_0 for which condition (5.17) is satisfied. (b) The growth rate s against wavenumber m for the steady state with $R_0 = 1.8$ (marked with a dotted black line in (a)). There is a single unstable mode with maximum growth rate $s = 4.6 \times 10^{-4}$ at wavenumber $m = 0.363$.

region is met. Note that by our choice of nondimensionalisation, $|\text{Ra}| = 1$, so varying R_0 in Fig. 7.2(a) represents a single path through the unstable region of Ra – R_s space. The values of ε and δ are chosen so that the energy mode is not unstable (condition (5.11)), and neither condition (5.17b) nor (5.23) is met. Figure 7.2(b) shows a plot of growth rate against wavenumber for the case of $R_0 = 1.8$ — there is a single unstable mode, with a uniquely defined wavenumber of maximum growth rate, which can be used to predict the width of the fastest growing perturbations, and hence the width of the initial layers formed.

Recall from Chapter 5 that in a system of the general form (5.1)–(5.3), the layering instability (condition (5.17a)) may be caused by either the forcing mechanism of BLY and Paparella & von Hardenberg (2014), or the γ -instability of Radko (2003). With the specific system (7.15)–(7.17), this is no longer the case. For a model with no source term in the energy equation (7.17), the γ -mechanism is the only one in play.

We now investigate the effect on the stability of the system of varying the values of the material parameters, while fixing $\delta = 0.001$ and $\varepsilon = 1$. Figure 7.3 shows the effect on the critical values of R_0 for instability of changing τ and σ independently. The black line in Fig. 7.3(a) shows the minimum and maximum values of R_0 for which instability occurs, as τ is varied with all other parameters kept fixed. The critical value of τ at the tip of the curve is $\tau_c = 0.1055$. This critical value is independent of σ , although larger values of σ lead to larger unstable ranges of R_0 . Figure 7.3(b) shows the effect of varying σ on the critical values of R_0 . For $\sigma \ll 1$, only a very narrow range of R_0 leads to instability; at larger values of R_0 this range increases significantly, saturating at approximately $2 \lesssim R_0 \lesssim 14$ for large σ . The dashed line shows the lower boundary of the fingering regime, at $R_0 = 1$. Larger values of τ reduce the size of the unstable range of R_0 , but there is little qualitative change. For small σ , the entire unstable range lies below $R_0 = 1$, and is therefore not in the salt fingering regime. This result is consistent with those of Traxler *et al.* (2011), who studied salt fingering at low Prandtl number using three-dimensional numerical simulations. Traxler *et al.* (2011) found that the empirical flux ratio γ increased monotonically with density ratio R , so layering by the γ -instability was not expected at small σ . Instead, it was suggested that any layering was due to the collective instability of Stern (1969).

From Fig. 7.2, we see that staircases are predicted in our model for $1.4 \lesssim R_0 \lesssim 2.3$, given the parameter values $\tau = 0.01$, $\sigma = 10$, $\varepsilon = 1$, $\delta = 0.001$. This is in disagreement with the results of some previous studies that found instability much closer to the boundary $R_0 = 1$ (e.g. Stellmach *et al.*, 2011). However, Fig. 7.3 shows that the range for instability strongly depends on the values of σ and τ , and we saw in Sec. 7.3.1 that the values of δ and ε also have a strong effect on steady-state solutions. Hence given the difference in parameter values, it should not be worrying that the specific unstable range of R_0 found here does not match completely with previous works. A possible future adaptation of the model could include a more detailed parameter search with the goal of producing more quantitatively exact predictions.

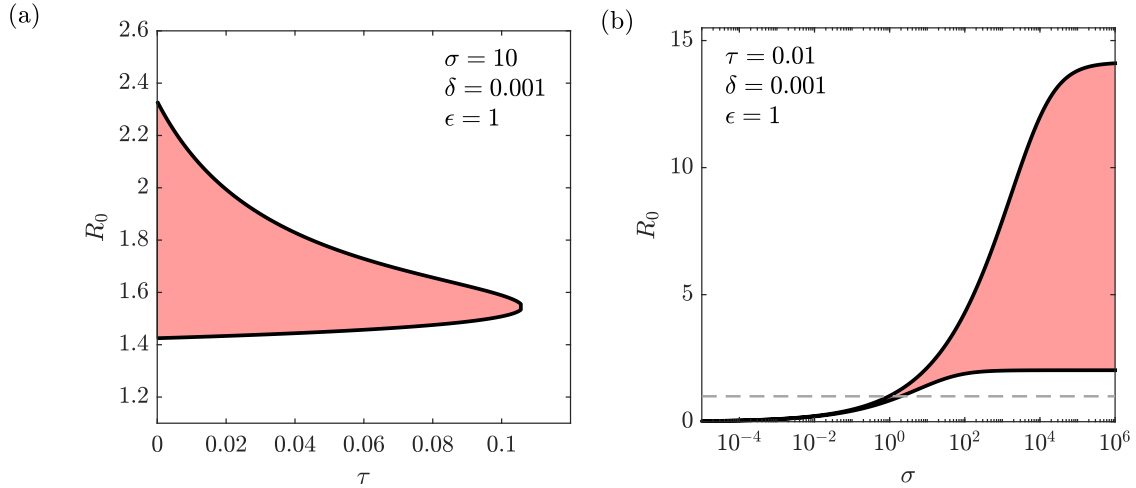


Fig. 7.3 Effect on the layering instability of changing (a) the diffusivity ratio τ , and (b) the Prandtl number σ . Black lines show the boundary of the unstable range of R_0 , as (a) τ is changed with fixed $\sigma = 10$, and (b) σ is changed for fixed $\tau = 0.01$. In each case, changing the value of the other parameter leads to no qualitative differences. The other model parameter values are $\delta = 0.001$ and $\epsilon = 1$; for these choices of δ and ϵ , there is no energy mode instability. The dashed line in (b) shows $R_0 = 1$, the lower boundary of the salt fingering regime.

7.4 Nonlinear evolution and long-term merger behaviour

A key advantage of the regularisation inherent in our mixing-length formulation (7.15)–(7.17) is that it allows the investigation of long-term dynamics of staircase evolution and merger beyond any initial instability. To investigate this long-term behaviour, we solve the system (7.15)–(7.17) with length scale (7.18) subject to the boundary conditions

$$T(0) = 0, \quad T(H) = H, \quad (7.27)$$

$$S(0) = 0, \quad S(H) = H/R_0, \quad (7.28)$$

$$e_z(0) = 0, \quad e_z(H) = 0, \quad (7.29)$$

and initial conditions

$$T = z - g' \sin\left(\frac{2n\pi z}{H}\right), \quad (7.30)$$

$$S = \frac{z}{R_0} - d' \sin\left(\frac{2n\pi z}{H}\right), \quad (7.31)$$

$$e = e_0 - e' \frac{2n\pi}{H} \cos\left(\frac{2n\pi z}{H}\right), \quad (7.32)$$

where the perturbation amplitudes (g', d', e') are chosen such that the initial condition is an eigenstate of the linear stability problem, with $2n\pi/H$ chosen to be the maximally unstable wavenumber based on the linear theory of Sec. 7.3. We solve the model numerically using the MATLAB pdepe solver, with 4000 spatial mesh points across a domain of depth 500,

which is sufficient for well-resolved solutions. The solver varies time steps dynamically to ensure adequate resolution.

7.4.1 Nonlinear evolution

Figure 7.4 shows the results of a numerical solution of (7.15)–(7.17), for the same parameters as used in Fig. 7.2(b). Figure 7.4(a) shows the buoyancy field $b = T - S$ plotted over a range of times. The plot illustrates the evolution from an initially uniform gradient to a layered staircase; the layers then proceed to undergo mergers over time. Eventually, at $t \approx 2 \times 10^6$, only a single interface remains, located at $z \approx 350$. Figure 7.4(b) shows the normalised buoyancy gradient at the same time points. Interfaces between layers are represented by sharp spikes in the gradient profile; these profiles reveal the fine structure at early times that is not visible in the overall temperature field in Fig. 7.4(a). The range in the buoyancy gradient, i.e. $\max(b_z) - \min(b_z)$, is shown in Fig. 7.4(c), measuring the difference between the gradients in the interfaces and the layers. There is a clear gradual increase in the maximum gradient, beginning at $t \approx 6 \times 10^5$ and ending at $t \approx 2 \times 10^6$, defining the range of times over which mergers occur. During a layer merger, the overall buoyancy variation across a region must be conserved, resulting in sharper interfaces with higher gradients after each merger. Referring to the unstable region shown in Fig. 7.2(a), there is no constraint individually on T_z and S_z , provided that R_0 stays within the bounds of the unstable region. Hence b_z can become arbitrarily large, resulting in ever steeper interfaces as successive merger events take place. This contrasts with the results of Chapters 3 and 6, where a well-defined maximum unstable gradient is determined, such that subsequent mergers produce thicker interfaces of fixed gradient. The long-term evolution of merger behaviour follows the same inverse logarithmic trend identified in Chapter 3, with the number of remaining interfaces N obeying the scaling $1/N \sim \log(t)$ as $t \rightarrow \infty$.

7.4.2 Merger dynamics

To understand the merging behaviour in more detail, we consider the results in the context of the analysis of Radko (2007), who identified two types of mergers: the B-merger, in which relatively strong interfaces grow at the expense of weaker neighbouring interfaces, and the H-merger, where neighbouring interfaces drift and collide. By considering a one-dimensional buoyancy conservation equation in a stepped basic state, and analysing the variation of the buoyancy flux across a step, Radko demonstrated the so-called merger theorem, showing that the B-merger has growth rate $\lambda_B \propto -\partial \tilde{F} / \partial \tilde{B}$, and the H-merger has growth rate $\lambda_H \propto \partial \tilde{F} / \partial \tilde{H}$, where $\tilde{F}(\tilde{B}, \tilde{H})$ is the buoyancy flux across a step, \tilde{B} the buoyancy jump, and \tilde{H} the height of the step.

To apply the merger theorem to the BLY model, Radko (2007) considered constant flux solutions, for which the model can be reduced to a nonlinear oscillator equation for $e(b)$. To apply the same analysis to our model, we adopt the same approach. Thus we seek

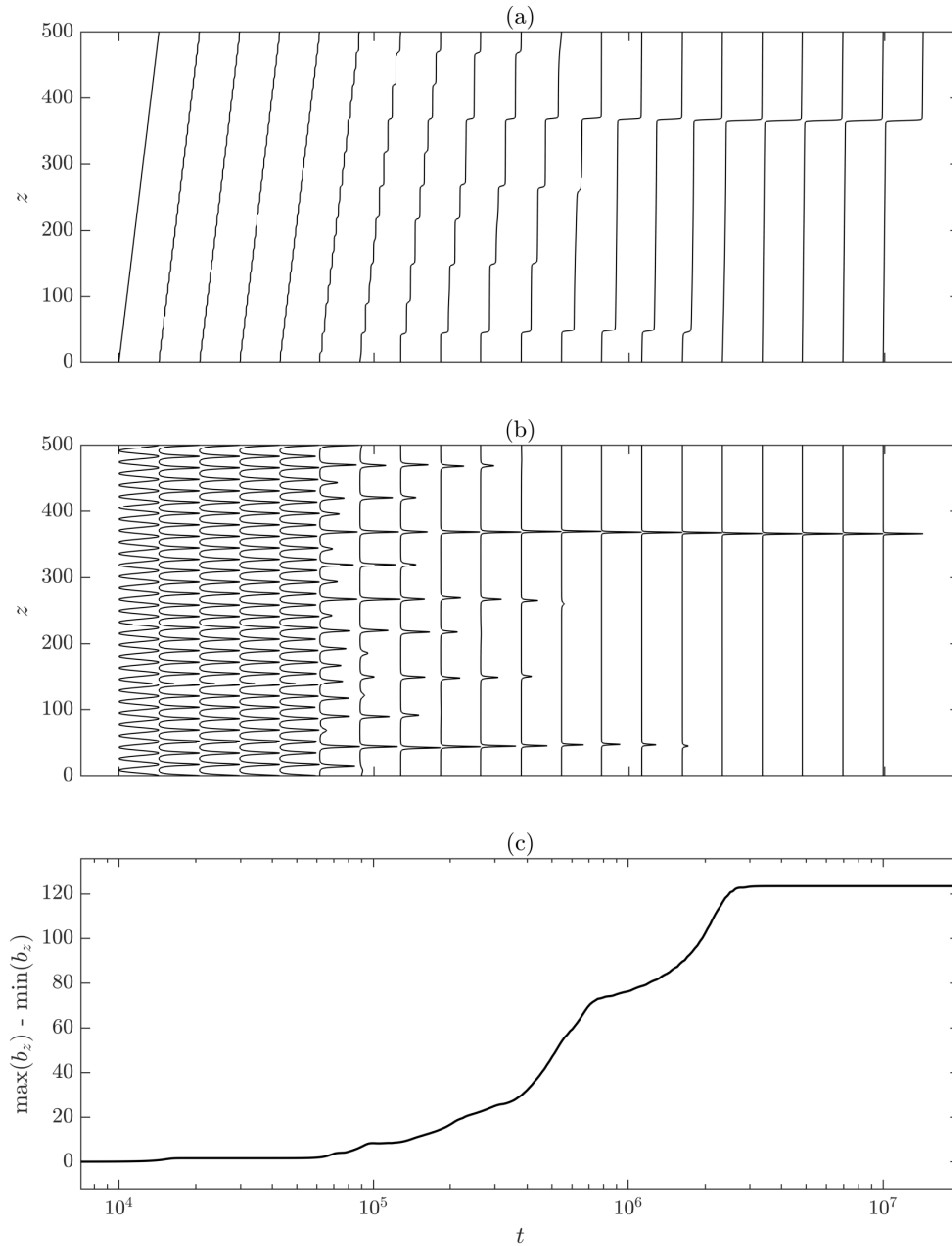


Fig. 7.4 Nonlinear evolution of the system (7.15)–(7.17), with length scale (7.18), subject to boundary conditions (7.27)–(7.29) and initial conditions (7.30)–(7.32), for parameter values $\tau = 0.01$, $\sigma = 10$, $\delta = 0.001$, $\varepsilon = 1$, $R_0 = 1.8$. (a) Depth profiles of the overall buoyancy field $b = T - S$ at a range of times logarithmically distributed between $t = 10^4$ and $t = 10^7$; (b) profiles of the buoyancy gradient $b_z = T_z - S_z$ scaled by the range of its values at each time, plotted at the same times as in (a); (c) range of gradients, i.e. $\max(b_z) - \min(b_z)$. The solution evolves from the initial condition into a dense stack of layers (seen as the first solution presented in (b)). At $t \approx 6 \times 10^5$, the layers begin to undergo mergers, which cause the maximum gradient to increase, until by $t \approx 2 \times 10^6$, only a single interface remains at $z \approx 350$, with $b_z \approx 120$.

steady-state solutions to the system (7.15)–(7.17) with uniform temperature and salinity fluxes f_0 and c_0 . Using a process mirroring that of BLY, the system can thus be reduced to a single equation. Whereas the derivation of BLY concerned their two-component system, the derivation given below includes the third equation of the model (7.15)–(7.17)

Assuming a steady state, the system (7.15)–(7.17) can be written as

$$f_0 = \frac{D^2}{D+1} T_z, \quad (7.33)$$

$$c_0 = \frac{D^2}{D+\tau} S_z, \quad (7.34)$$

$$0 = (\kappa e_z)_z - \sigma(f_0 - c_0) - \varepsilon \frac{e^2}{D}, \quad (7.35)$$

where $D = le^{1/2}$ and $\kappa = (D^2/(D+\sigma) + \sigma)$. Note that (7.33) uniquely defines $D(T_z)$ and (7.34) uniquely defines $S_z(D)$. The salt gradient is therefore tied to the temperature gradient, rather than the two fields being independent.

Dividing (7.33) by (7.34), we obtain

$$\gamma_0 = \frac{f_0}{c_0} = \frac{D+\tau}{D+1} R, \quad (7.36)$$

thus defining R in terms of D , where $\gamma_0 = f_0/c_0$ is the steady-state flux ratio. The prescription for the length scale (7.18), coupled with the definition of $D = le^{1/2}$, can be rearranged to give an expression for $e(D, R)$, namely,

$$e^2 = (D^2 - \delta) R^2. \quad (7.37)$$

Combining (7.37) with (7.36), we define the energy solely in terms of D by

$$e(D) = \frac{\sqrt{D^2 - \delta} (D+1)}{D+\tau} \gamma_0. \quad (7.38)$$

Multiplying the energy equation (7.35) by κe_z , integrating with respect to z , and changing variables such that $e_z dz = e_D dD$, we obtain

$$\frac{1}{2} (\kappa e_z)^2 + \int \left(-\sigma(f_0 - c_0) - \varepsilon \frac{e(D)^2}{D} \right) \kappa e_D dD = E, \quad (7.39)$$

where E is a constant.

To transform (7.39) to an equation for e_b , we could write $e_z = e_b b_z$ and divide all terms in (7.39) by $(\kappa b_z)^2$. However, when $b_z = 0$, this leads to a singularity in the potential. To avoid this, we note that $T_z \neq 0$ when $f_0 \neq 0$, and write $e_z = e_T T_z$ in terms of the temperature instead. This use of T instead of b as the ‘time’ variable is valid because D and S_z are defined as functions of T_z via (7.33)–(7.34). On using (7.33) to rewrite T_z as a function of

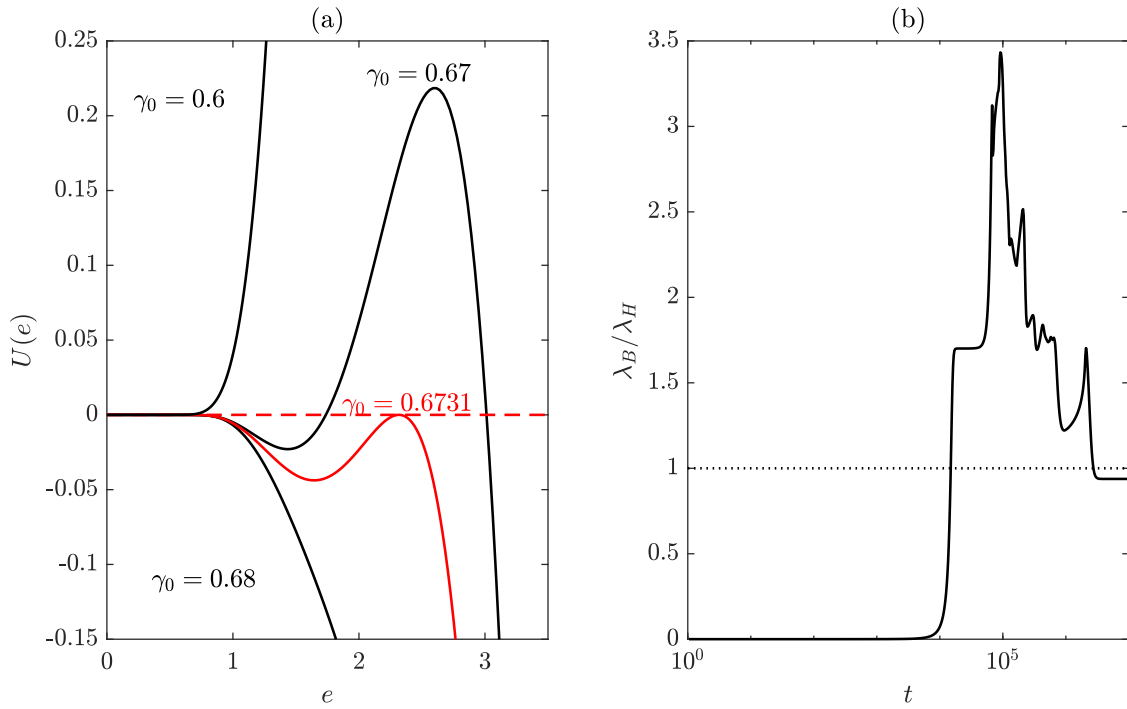


Fig. 7.5 (a) Potential $U(e)$ found by integrating (7.41) with respect to D , and coupling with (7.42) to find corresponding values of e . The red line has two peaks at e_1 and e_2 , where $U(e_1) = U(e_2)$. Parameter values are $f_0 = 0.45$, $\tau = 0.01$, $\sigma = 10$, $\varepsilon = 1$ and $\delta = 0.001$. (b) Plot of the ratio λ_B/λ_H calculated in the small-gradient case given by equation (7.43), for the solutions presented in Fig 7.4. The dotted line marks $\lambda_B/\lambda_H = 1$: above this line, the B-merger dominates; below it, the H-merger dominates.

D , we obtain

$$\frac{1}{2}e_T^2 + U(D) = E \left(\frac{D^2}{\kappa f_0 (D+1)} \right)^2, \quad (7.40)$$

where $D(e) = le^{1/2}$, the potential $U(D)$ is defined by

$$U(D) = \left(\frac{D^2}{\kappa f_0 (D+1)} \right)^2 \int \left(-\sigma(f_0 - c_0) - \varepsilon \frac{e(D)^2}{D} \right) \kappa dD, \quad (7.41)$$

and $e(D)$ is defined by

$$e(D) = \frac{\sqrt{D^2 - \delta(D+1)}}{D + \tau} \gamma_0. \quad (7.42)$$

Equation (7.40) represents a nonlinear oscillator for e as a function of temperature T , with variable weight. By inverting (7.42) for $D(e)$, (7.40) is transformed into an equation for e_T in terms of e . Analytically, this requires writing $D(e)$ as the root of a quartic, but the inversion is simple to do numerically by coupling (7.42) with (7.41).

The potential $U(e)$ is plotted in Fig. 7.5(a). For a narrow range of values of f_0 and γ_0 , $U(e)$ has two peaks, at e_1 and e_2 . With this two-peak shape for $U(e)$, the oscillator equation (7.40) has two stable steady states corresponding to the peaks of the potential: one with a smaller energy and the other with larger energy. These correspond to values of

the energy in interfaces and layers respectively. The profile of $U(e)$ depends sensitively on γ_0 and f_0 , but for each f_0 there is a precise value of γ_0 such that $U(e_1) = U(e_2)$; this value of U is shown by the red dashed line in Fig 7.5(a). For this critical value of γ_0 , the oscillator $e(T)$ has a special *kink* solution linking the two maxima (Balmforth *et al.*, 1998). By analogy with similar kink solutions to the Cahn-Hilliard equation, more complex solutions with gradient spikes also be constructed (e.g. Fraerman *et al.*, 1997).

With the potential taking this two-peak form, our three-component system maps directly to Radko's (2007) analysis of the merging behaviour of the BLY model, which is susceptible to both B- and H-mergers. Radko shows that, in this situation, the ratio of their growth rates is

$$\frac{\lambda_B}{\lambda_H} = \frac{\bar{g} - g_{\min}}{g_{\min}}, \quad (7.43)$$

where g_{\min} is the minimum gradient (in layers) and \bar{g} the background gradient (averaged across the whole layer-interface system). If the ratio λ_B/λ_H is greater than unity, B-mergers occur, and if the ratio is less than unity then H-mergers will dominate instead. In the solutions shown in Fig 7.4, it appears that the mergers occur via the B-merger pattern, with weaker interfaces shrinking without significant drifting. To show consistency with this condition on λ_B/λ_H , we calculate λ_B/λ_H at each time using (7.43). We take g_{\min} to be the global minimum gradient at each time, and $\bar{g} = 1$ as the background gradient. The ratio λ_B/λ_H is shown in Fig. 7.5(b), where we see that for times $10^4 \lesssim t \lesssim 2 \times 10^6$, the ratio $\lambda_B/\lambda_H > 1$, implying consistency with the numerical results, in which B-mergers dominate.

7.4.3 Increase of the buoyancy flux

In the full thermohaline system, it has been established that the existence of staircases leads to greater turbulent transport of both heat and salt through the fluid in comparison with an unlayered state (e.g. Rosenblum *et al.*, 2011; Hughes & Brummell, 2021). In the following section, we investigate this effect in our model, and provide an explanation for why it is the case. Figure 7.6 shows the evolution of the mean of the upward buoyancy flux

$$\frac{1}{H} \int_0^H (c - f) dz, \quad (7.44)$$

calculated at each time for the solution previously shown in Fig. 7.4. There is little change in the flux at early times, until the initial linear perturbation grows into a stack of layers at $t \approx 10^4$. As layers undergo mergers, the magnitude of the flux increases, with thicker mixed layers producing larger fluxes, consistent with simulations of salt fingering (e.g. Rosenblum *et al.*, 2011) Also plotted are the spatial profiles of the upward buoyancy flux $(c - f)$ at a range of times, showing that, in general, the flux is reasonably consistent across the different layers at each time, but with small perturbations in the interfaces.

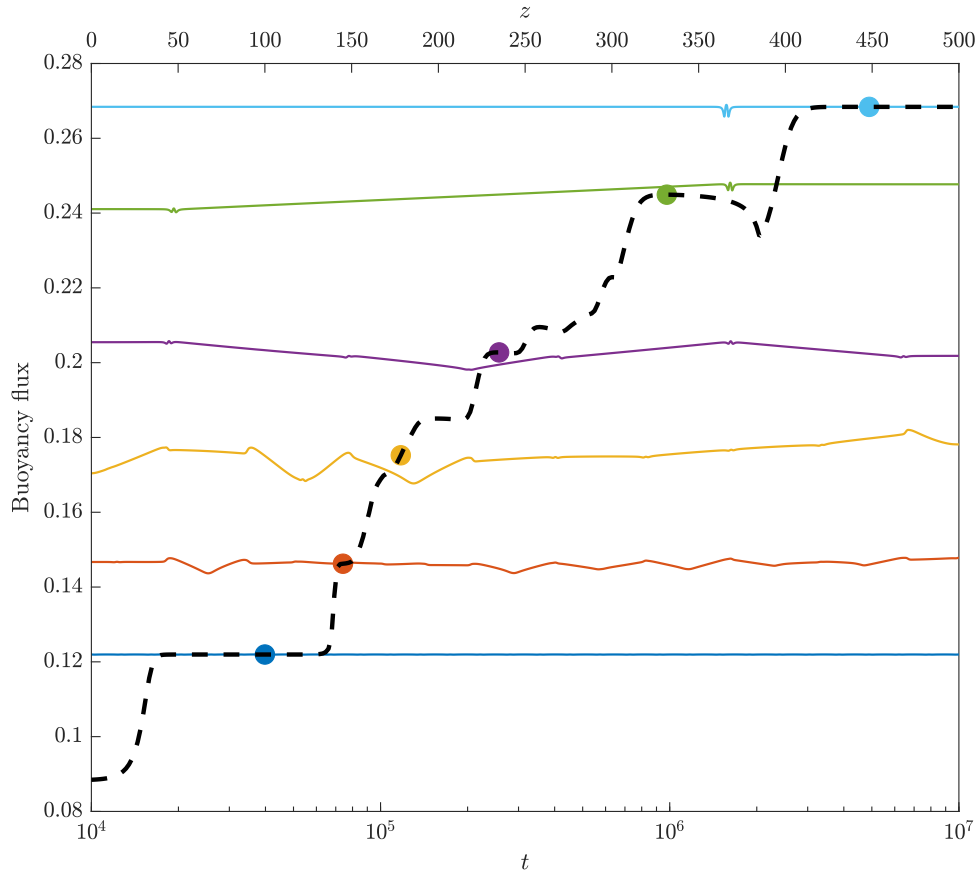


Fig. 7.6 Evolution of the buoyancy flux field for the solution shown in Fig. 7.4(a). The black dashed line shows the vertical mean of the upward buoyancy flux ($c - f$) defined by (7.44), plotted against time on the lower horizontal axis. The spatial profile of the buoyancy flux (with z on the upper horizontal axis) is also shown at a range of times, with the corresponding mean flux at each time marked with a dot of the same colour.

The increase in flux seen in Fig. 7.6 can be explained using the merger theorem of Radko (2007). We saw in Fig. 7.4 that layers undergo B-mergers, where weak interfaces decay with little vertical drift. To explain this, we consider a region of fluid initially containing two layers and one such weak interface. Initially, there is a buoyancy jump of B_1 across the interface. When a B-merger takes place, the resultant state is a single mixed layer, with the buoyancy variation from the top to the bottom now $B_2 \ll B_1$. The merger theorem states that the system is unstable to B-mergers if the buoyancy flux decreases as the buoyancy variation increases, and so this decrease of B during the merger must increase the flux in the region.

7.4.4 Variation of parameter values

An exploration of parameter space reveals that the solutions shown in Fig. 7.4 are representative of a large range of parameter values. To demonstrate this, we illustrate the solution for some extreme choices of parameters, shown in Fig. 7.7. Figure 7.7(a) takes a very large value of the Prandtl number σ , for which the scale of the most unstable mode is

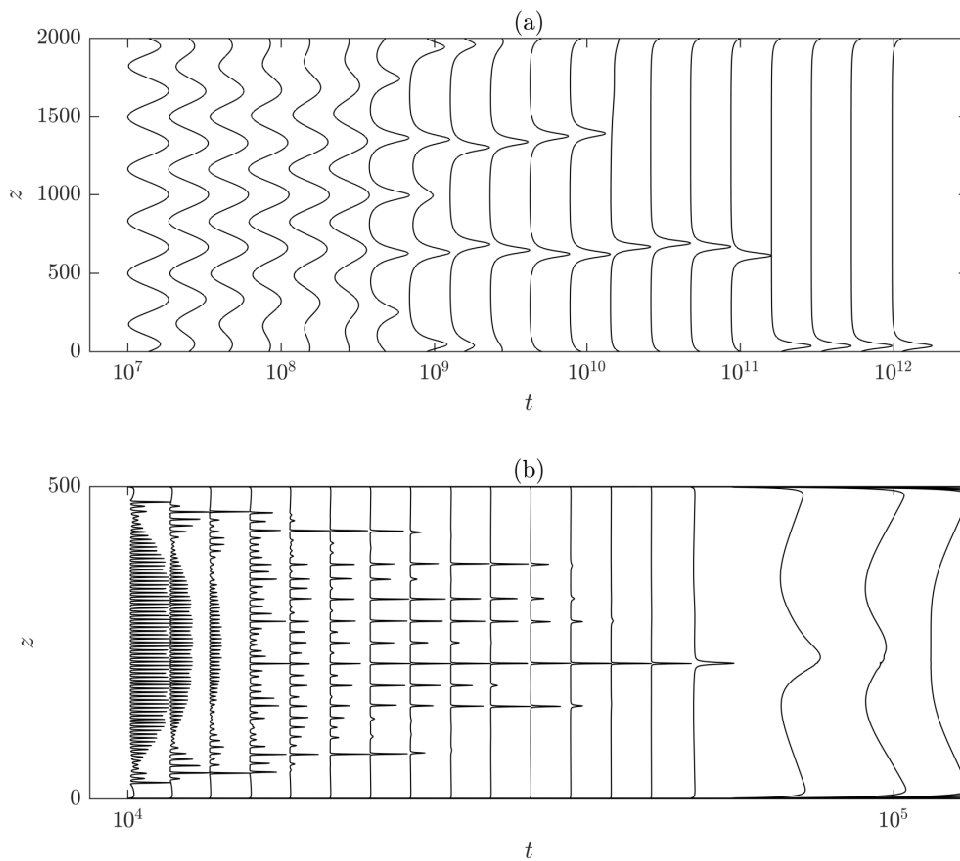


Fig. 7.7 Evolution of solutions to (7.15)–(7.17) with length scale (7.18), subject to boundary conditions (7.27)–(7.29) and initial conditions (7.30)–(7.32). (a) Very high Prandtl number case, with $\tau = 0.0001$, $\sigma = 10^4$, $\delta = 0.001$, $\varepsilon = 1$ and $R_0 = 3.64$, showing wide, smooth interfaces and layers. (b) No overall background buoyancy gradient, with $\tau = 0.01$, $\sigma = 1$, $\delta = 0.01$, $\varepsilon = 1$, $R_0 = 1$, in which the timescale for mergers is similar to that for layer growth. Layers merge quickly, eventually giving way to a single convective state across the entire domain.

very large, resulting in layers and interfaces that are wider and smoother in comparison with the results of Fig.7.4. Figure 7.7(b) shows the case with $R_0 = 1$, on the boundary between the salt fingering and statically unstable regimes. In this case, layers do form, but mergers occur on such a fast timescale that a regular staircase never develops, and the system transitions very quickly from the linear growth phase to a single interface in the middle, which then decays, forming a single layer across the entire domain depth. In both of the cases shown, while there are some quantitative differences from the results in Fig. 7.4, the qualitative behaviour is the same.

We selected the parameter values $\delta = 0.001$ and $\varepsilon = 1$ to prevent the energy mode from being unstable. If instead we choose parameters such that there is an energy mode instability, then there is energy growth on the domain scale, producing a wide interior

region with a large energy and constant temperature and salt gradients, with narrow boundary regions on either side to satisfy the boundary conditions (7.27)–(7.29).

7.5 Discussion

In this chapter we have presented a model for layering in salt fingering convection, derived from the Boussinesq equations using the averaging process of Chapter 2, and investigated its linear stability via the framework described in Chapter 5. In contrast to previous models, such as that of Paparella & von Hardenberg (2014), and the one discussed in Chapter 6, there is no forcing term, with instability being driven purely by interaction between the temperature and salinity fluxes. By suitable parameterisation of the length scale, the flux terms have the appropriate functional form to allow for the release of potential energy to drive instability via the γ -instability. This parameterisation of the length scale is a key ingredient of the model, and the form chosen (7.18) is not the only possibility. It is interesting to note that the length scale adopted by Balmforth *et al.* (1998), and used in Chapters 3 and 6 in models of stirred convection does not provide the appropriate release of potential energy from the flux terms to generate layering in (non-stirred) DDC. A prescription based on the density ratio R alone leads to a high wavenumber instability. However, a physically motivated and relatively simple parameterisation in terms of both R and e captures the essential physics of the layering process.

The multiscale analysis of Radko (2019a) provides an alternative method of regularising the high wavenumber instability by the inclusion of hyperdiffusion terms. This allowed a model in terms of temperature and salinity alone to produce realistic layering dynamics, without the need for the energy equation. Radko's model depends on the empirical calibration of several coefficients, requiring direct numerical simulations *a priori* to inform the choices of coefficients. By contrast, our model is derived using a spatial averaging process and the choice of a simple mixing length dependent on only one parameter. Both our model and that of Radko (2019a) provide similar numerical results, with staircases appearing and gradually reducing via the B-merger pattern of Radko (2007).

A slightly simpler mathematical model of layering could be produced by a reduced form of the model in which $e_t \equiv 0$. In this case, the energy equation becomes diagnostic, and e is determined directly at all times as a functional dependent on the global temperature and salinity fields. This modification does not affect the conditions for the layering instability (5.17), but removes the possibility of the energy mode instability (5.11). In this case, we are effectively left with a two-component system for T and S , closed via a functional parameterisation of e in the form of the steady energy equation. The layering instability, and its regularisation, are dependent entirely on the specific forms of f , c and p .

In Sec. 7.3, we showed that the model (7.15)–(7.17) admits uniform-gradient steady states $(T_z, S_z, e) = (z, z/R_0, e_0)$ in the salt fingering regime, with $e_0(R_0)$ being single-valued for appropriate choices of δ and ε . These steady states are unstable to perturbations for a

finite range of R_0 , with a well-defined wavenumber of maximum growth rate. Increasing the value of τ decreases the range of R_0 susceptible to instability, with no instability possible for $\tau \gtrsim 0.105$ (a value dependent on δ and ε). Larger values of σ give wider ranges of R_0 for instability. For values of the Prandtl number $\sigma \lesssim 1$, the unstable range of R_0 is very narrow, and exists only for $R_0 < 1$, i.e. outside of the salt fingering regime. Hence, for sufficiently small Prandtl number, there is no possibility for salt fingering staircases to form via the γ -instability, in agreement with the results of three-dimensional numerical simulations of the full thermohaline system (Traxler *et al.*, 2011).

We have presented numerical solutions to the model in Sec. 7.4, showing the initial development of a staircase and its subsequent evolution to late times. The staircase evolves via the B-merger process described by Radko (2007), eventually leaving a single strong interface with well-mixed layers on either side. During a merger event, the buoyancy gradient in the remaining interface increases, so that the gradient in the final interface is significantly higher than in the first interfaces to develop. The buoyancy flux through the system also shows sharp increases during merger events, which can be explained by the condition responsible for the B-merger that flux increases as buoyancy jump decreases. This increase in flux agrees with previous results (e.g. Rosenblum *et al.*, 2011), and is an important piece in the puzzle needed to understand transport processes through staircases.

To use the present model to make predictions for real staircases, we consider dimensional forms of the key parameters. With typical values of α , g , $|\Theta_z|$, κ_T and ν for an oceanic staircase, (7.7) gives a characteristic length of $L \approx 0.01m$, and hence a domain of depth 500 represents 5m—significantly smaller than the scale on which staircases are seen in the oceans. However, the parameters δ and ε can readily be varied, and it seems likely that such fine-tuning will allow the model to produce good predictions for real staircases. The value of $\sigma = 10$ used here is also slightly unrealistic, with a true oceanic value of $\sigma \approx 7$. With this reduced value, Fig. 7.3(b) shows a lower range of R_0 for instability, more in keeping with the range $1 < R_0 < 2$ in which observed staircases are found. With these changes to parameters it seems likely that the model can be adapted to produce good predictions of real staircase behaviour, which can easily be tested by comparison with observations.

Chapter 8

Thermohaline staircases: Diffusive convection

8.1 Introduction

In Chapter 7, we presented a model for layering in double-diffusive convection, and investigated staircase formation in the salt fingering regime. We saw in Sec. 7.3.1 that in the diffusive convection regime, no uniform-gradient steady-state solutions exist, no matter what parameterisations are used for the various terms in the equations. Ma & Peltier (2022) note that the value of the density ratio in observed diffusive staircases ($2 < 1/R < 7$) are significantly different from the range of R in which the basic diffusive convection instability takes place ($1 < 1/R < 1.14$, cf. Sec. 1.3). On this basis, they propose that rather than staircases being caused by diffusive-convection alone, some forcing is necessary, for example the imposition of an external flow, and that double-diffusive effects play only a secondary role in regularising the staircase. The lack of steady-state solutions in our model lends some support to this hypothesis.

Another suggestion for the mechanism driving diffusive layering is thermohaline-shear instability, where a flow stable to both shear and diffusive instabilities can become unstable due to a combination of both (Radko, 2016; Brown & Radko, 2019; Radko, 2019*b*). Numerical solutions have shown that these instabilities can then develop into layers. Another proposal is that layering is driven by the existence of horizontal density gradients, with thermohaline intrusions interacting with double-diffusive effects to form layers. This theory was originally developed in the SF regime (Merryfield, 2000), and has more recently been applied to diffusive staircases (Bebieva & Timmermans, 2017). Both of these alternative suggestions are dependent on horizontal structure — either with a mean shear flow or a horizontal temperature gradient, so naturally cannot be captured by the one-dimensional models discussed in this work.

However, three dimensional numerical simulations have produced diffusive layers in the absence of forcing (e.g. Rosenblum *et al.*, 2011). In Chapter 7 we interpreted the

uniform-gradient steady state as a representation of a salt-fingering field in a turbulent flow. In the DC regime, the analogous diffusive convection field cannot exist in our model without an external energy source driving the turbulence. As the layering instability develops from these uniform fields, it is possible that our model requires forcing not to drive layering, but simply to initialise the system in a uniform diffusive convective state.

In this chapter, we adapt the system (7.15)–(7.17) with length scale (7.18) to model staircases in the diffusive convection regime by reintroducing a constant power forcing term. In Chapter 6, we found that a model employing the BLY parameterisations for the length scale and stirring produced staircases, but led to a high-wavenumber instability in the diffusive regime, which could be suppressed by the addition of hyperdiffusion terms to the equations. In both regimes, the dynamics were dominated by the stirring, with the temperature and salinity fields evolving almost identically. For a realistic model of double-diffusive layering, the two components of buoyancy should be fully independent. We show here that with parameterisations for the length scale based on the density ratio R , as in Chapter 7, and an appropriate choice of source term, staircases form in the diffusive regime with the two components of density evolving separately, and no high wavenumber instability.

8.2 Model for DC layering incorporating an energy source

We begin with the same model as used in the salt fingering regime, with the addition of a energy source term P

$$T_t = \left(\frac{l^2 e}{le^{1/2} + 1} T_z \right)_z, \quad (8.1)$$

$$S_t = \left(\frac{l^2 e}{le^{1/2} + \tau} S_z \right)_z, \quad (8.2)$$

$$e_t = \left(\frac{l^2 e}{le^{1/2} + \sigma} e_z \right)_z - \sigma \left(\frac{l^2 e}{le^{1/2} + 1} T_z - \frac{l^2 e}{le^{1/2} + \tau} S_z \right) + \sigma e_{zz} - \varepsilon \frac{e^{3/2}}{l} + P. \quad (8.3)$$

These equations are nondimensionalised according to (7.6) such that in the DC regime, the background temperature gradient is $g_0 = -1$, and the background salinity gradient is $d_0 = -1/R_0$, for R_0 the density ratio. For a statically stable buoyancy gradient, $b_z \equiv -(1 - 1/R_0) > 0$, so $R_0 < 1$.

Once again we use the length scale

$$l = \frac{(e^2 + \delta R^2)^{1/2}}{e^{1/2} R}, \quad (8.4)$$

chosen to provide the appropriate release of potential energy to drive layering, as discussed in Chapter 7.

To parameterise the energy source, we take the simplest possible option — a constant power source term $P = W$. We will keep all other parameters fixed at the values used in Chapter 7, but will investigate the effect of changing the value of W . This constant power parameterisation for the energy source was considered by Balmforth *et al.* (1998) (BLY) in their work on stirred stratified layering, but in that case the range of uniform steady-state gradients unstable to perturbations was unbounded, leading to the development of infinite gradients in a finite time. We will see in Sec. 8.3.2 that beside allowing the existence of steady-state solutions to (8.1)–(8.4), this constant power source does not affect any of the conditions for instability. We choose this constant power parameterisation as the minimal possible addition to the model that will allow staircases to form; in future work more physically-motivated forms should be considered.

8.3 Steady states and their stability

8.3.1 Uniform gradient steady states

The system (8.1)–(8.4) admits uniform steady states $(g_0, d_0, e_0) = (-1, -1/R_0, e_0(R_0))$ such that $p(g_0, d_0, e_0) = 0$, where

$$p = -\sigma \left(\frac{l^2 e}{le^{1/2} + 1} T_z - \frac{l^2 e}{le^{1/2} + \tau} S_z \right) - \varepsilon \frac{e^{3/2}}{l} + W. \quad (8.5)$$

Recall from Chapter 7 that in the DC regime $g_0 < 0$, $d_0 < 0$, $R_0 < 1$, there are no positive solutions e_0 when $W = 0$, as the bracketed term in (8.5) is negative. Adding any positive value of W allows positive solutions e_0 to exist. Setting $e_0 = 0$, $g_0 = -1$, $d_0 = -1/R_0$ in (8.5), we find that $e_0 = 0$ at

$$R_c = \frac{\sigma \delta (1 + \sqrt{\delta})}{(W (1 + \sqrt{\delta}) + \sigma \delta) (\tau + \sqrt{\delta})}. \quad (8.6)$$

Uniform gradient steady-state solutions exist for all values of $R_0 \leq R_c$. Steady states exist in the DC regime ($0 < R_0 < 1$) for $W > W_c$, where W_c is given by

$$W_c = \frac{(1 - \tau) \sigma \delta}{(1 + \sqrt{\delta}) (\tau + \sqrt{\delta})}. \quad (8.7)$$

For parameter values $\tau = 0.01$, $\sigma = 10$, $\varepsilon = 1$ and $\delta = 0.001$, this critical value is $W_c \approx 0.23$. Figure 8.1(a) shows the steady-state energy as a function of R_0 for a range of values of W . As W increases, the value of R_c decreases, thus expanding the range of R_0 for which steady states exist.

For each value of W , $e_0(R_0)$ increases for small values of R_0 . For the higher values of W , the profile is not monotonic, with $e_0(R_0)$ peaking, then decreasing for larger values of R_0 . However, this peak and decrease happens only for $R_0 > 1$, so not in the region of interest for DC. Note that no matter the value of R_0 , a higher value of W produces a greater energy. This makes sense physically, with a larger power source giving a more energetic state. From here onwards, we adopt the value $W = 1$.

Figure 8.1(b) shows the form of the length scale (8.4) corresponding to each of the steady-state energies in Fig. 8.1(a). As $e_0 \rightarrow 0$, $l_0 \rightarrow \infty$, while $l_0 e_0^{1/2} \rightarrow \sqrt{\delta}$. For all except the largest value of W shown, the length scale decreases monotonically as R_0 increases. This is contrary to expectation; when R_0 is near zero, there is a large difference between the two components of buoyancy, producing a relatively large buoyancy gradient, so we would expect a small length as in interfaces. Similarly, when R_0 is close to 1, the buoyancy gradient is smaller, so we expect a longer length scale. However, this argument does not take into account variation in the magnitude of T_z . With a sufficiently large value of T_z a large buoyancy gradient is possible even for R_0 near 1. Conversely, a small enough value of T_z can produce a very small buoyancy gradient for values of R_0 near zero, where we had previously assumed b_z to be large. Although the length scale does not have the expected dependence on R_0 , we shall see in Sec. 8.4 that it does produce the appropriate lengths in numerical staircase solutions.

8.3.2 Stability

We analyse the stability of the steady state $(g_0, d_0, e_0) = (-1, -1/R_0, e_0(R_0))$ using the framework developed in Chapter 5. Writing the equations in the general form (5.1)–(5.3), f , c and κ are unchanged from the expressions (7.21)–(7.23), while p picks up the source term, as given by (8.5).

For a range of values of R_0 we first calculate $e_0(R_0)$ and substitute the value into the expressions for $-p_e$, $F_g C_d - F_d C_g$, $F_g + C_d$ and $f_g c_d - f_d c_g$; these quantities are plotted as functions of R_0 in Fig. 8.2(a). There is a finite range of R_0 where $F_g C_d - F_d C_g < 0$, so (5.17a) is satisfied. As well as a portion of the DC regime, this unstable range includes values where $R_0 > 0$ and the fluid is statically unstable. None of the other instability conditions (5.11), (5.17b) or (5.23) are satisfied anywhere. Figure 8.2(b) shows how the growth rate s of sinusoidal perturbations varies with wavenumber m . There is a clear finite range of m for instability where $s > 0$, and a well-defined maximally unstable wavenumber.

Note that all of the stability conditions (5.11), (5.17a, b) and (5.23) depend only on partial derivatives of the functions $f(g, d, e)$, $c(g, d, e)$ and $p(g, d, e)$. The constant power source W in (8.5) vanishes when any derivative is taken, so has no direct effect on the stability of the system. The source term is necessary in order to produce uniform steady states with positive energies, but the instability comes entirely from the double-diffusive interaction of the fluxes, rather than the energy source. This contrasts with the stirred models of BLY, and Chapters 3 and 6, where the source term was parameterised as a

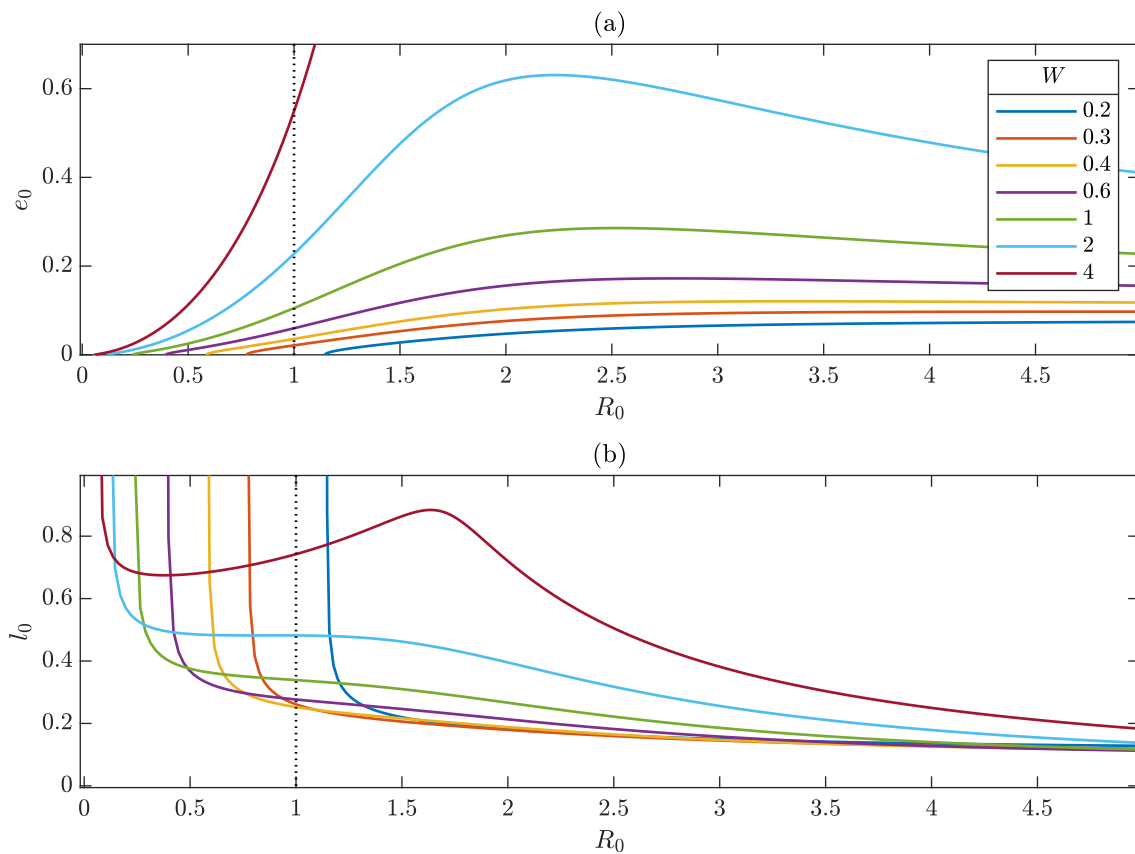


Fig. 8.1 (a) Steady-state solutions $e_0(R_0)$ to the DC steady-state equation (8.5), for a range of values of the constant power source W . Other parameter values are $\tau = 0.01$, $\sigma = 10$, $\varepsilon = 1$ and $\delta = 0.001$. The black dotted line shows the boundary of the DC region $R_0 < 1$. (b) Values of $l_0(R_0)$, corresponding to each line shown in (a).

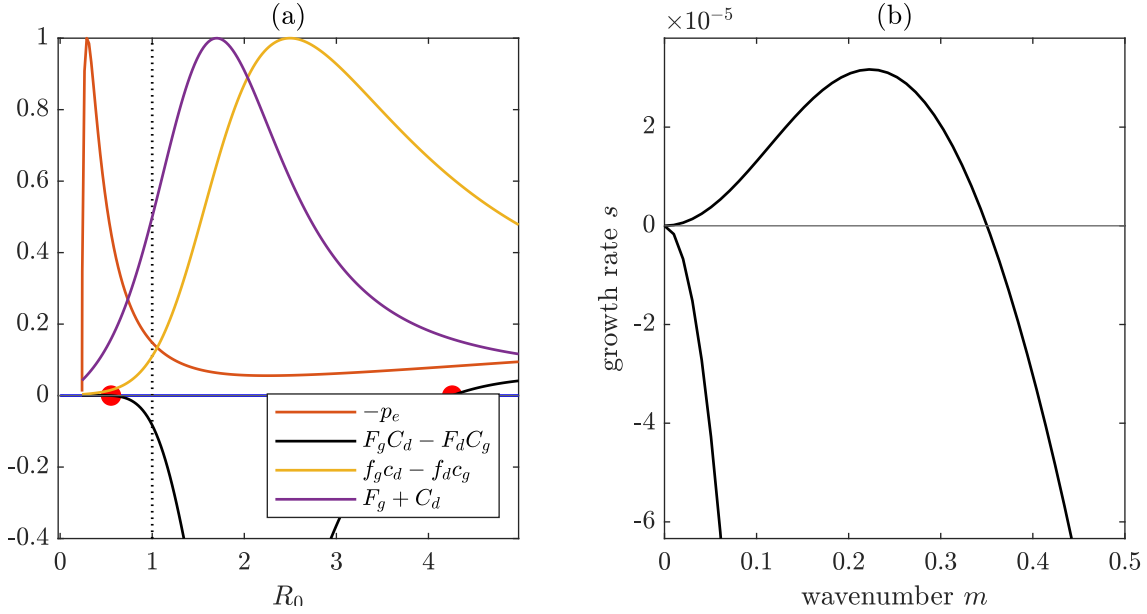


Fig. 8.2 (a) Stability conditions for the state $(g_0, d_0, e_0) = (-1, -1/R_0, e_0(R_0))$, for parameters $\tau = 0.01$, $\sigma = 10$, $\varepsilon = 1$, $\delta = 0.001$ and $W = 1$. Condition (5.17a) is satisfied for values of R_0 between the red dots. (b) Growth rate of perturbations to the steady state with $R_0 = 0.9$. There is a single unstable mode, with maximally unstable wavenumber $m = 0.222$.

function of b_z and e . BLY demonstrated that alternative forms for the energy source (including the constant power option used in this chapter) do not lead to the well-resolved layers seen when their ‘equipartition’ source $P = \varepsilon e^{1/2}/l$ is used. Here, by adopting the constant power source, we ensure that all the instability is due to double-diffusive effects. The only effect of the constant power source is in supporting uniform-gradient steady states in the DC regime.

In Chapter 5, we presented the ‘three-component Phillips effect’ — an extension of the stability analysis of Balmforth *et al.* (1998) to a three-component system of temperature, salinity and kinetic energy. A linear instability in such a system can follow either the Phillips mechanism, where the layering instability is driven by an energy source, or the γ -instability, where interaction between steady-state temperature and salinity fluxes causes the release of potential energy allowing for layers to form. The stirred three-component model of Chapter 6 produced staircases by the Phillips mechanism. By contrast, the energy source here does not affect the conditions for instability directly, with layering being caused by the γ -instability.

8.4 Nonlinear evolution

We solve the system (8.1)–(8.4) with boundary conditions (7.27)–(7.29) and initial conditions (7.30)–(7.32). The perturbation amplitudes (g', d', e') are chosen to be an eigenstate of the linear stability problem for the background state $(g_0, d_0, e_0) = (-1, -1/R_0, e_0(R_0))$,

with $m = 2n\pi/H$ the maximally unstable wavenumber. As before, we use the MATLAB pdepe solver.

Figure 8.3 shows the solution for background state $(g_0, d_0, e_0) = (-1, -1/0.9, 0.0861)$, with the $n = 35$ sinusoidal perturbation across a domain depth $H = 1000$, using 4000 spatial mesh points. The results show some similarities to those for the SF regime shown in Fig. 7.4, but there are some notable differences. At early times, a stack of layers and interfaces forms, which gradually undergoes mergers until by $t \approx 10^{13}$ there are two interfaces remaining, at the top and bottom of the domain. The interfaces appear very different to those seen in the SF regime in Chapter 7: rather than a single spike in the buoyancy gradient, they are characterised by two spikes separated by a region of lower gradient. In the SF regime, successive mergers increased the maximum buoyancy gradient in an interface, with the width remaining approximately constant. Conversely, Fig. 8.3(c) shows that in the DC regime, the maximum buoyancy gradient remains $O(1)$, with a slight decrease as mergers occur. Instead, interfaces get wider with each successive merger. This difference in behaviour is discussed in Sec 8.5. The mergers seen here follow the H-merger pattern described by Radko (2007), where neighbouring interfaces drift and combine. By contrast, in the SF regime, mergers followed the B-merger pattern of strong interfaces growing at the expense of weaker ones. In comparison to the SF solutions seen in Chapter 7, the difference in gradient between layers and interfaces is very small, with $\max(b_z) - \min(b_z) \approx 0.7$ at late times.

8.4.1 Profile of the layers and interfaces

We now discuss the profile of the layers and interfaces in a snapshot of the solution at fixed time. Figure 8.4 shows the profile of the solution shown in Fig. 8.3 at $t = 10^8$, showing (a) the density ratio and length scale, (b) the temperature, salinity and buoyancy fields, and (c) their gradients.

As discussed in Sec. 8.3.1, we initially expect that R should be close to 1 in layers to produce a small overall buoyancy gradient, while R should be near zero in interfaces to give a large gradient. However, this does not account for the magnitude of each of the components of buoyancy. We see in Fig. 8.4(a) that in the wide, well-mixed layers, R is near zero and l is large, while in the narrower interfaces, R approaches unity and l is near zero. This matches well with the picture seen in Fig. 8.1(b), where $l \rightarrow \infty$ as $R \rightarrow 0$, and l decreases as R increases.

In the solution shown in Fig. 8.3(b), the interfaces display two large spikes in the buoyancy gradient, either side of a region with lower gradient. To investigate this profile, we consider the temperature and salinity fields individually. Figure 8.4 shows (b) the individual fields and (c) their gradients at time $t = 10^8$, after several mergers have taken place. The buoyancy field in (b) and buoyancy gradient in (c) have been normalised to have the same horizontal scale as the salinity field. In both the temperature and salinity fields, a clear staircase structure can be seen. However, the steps in the buoyancy field are

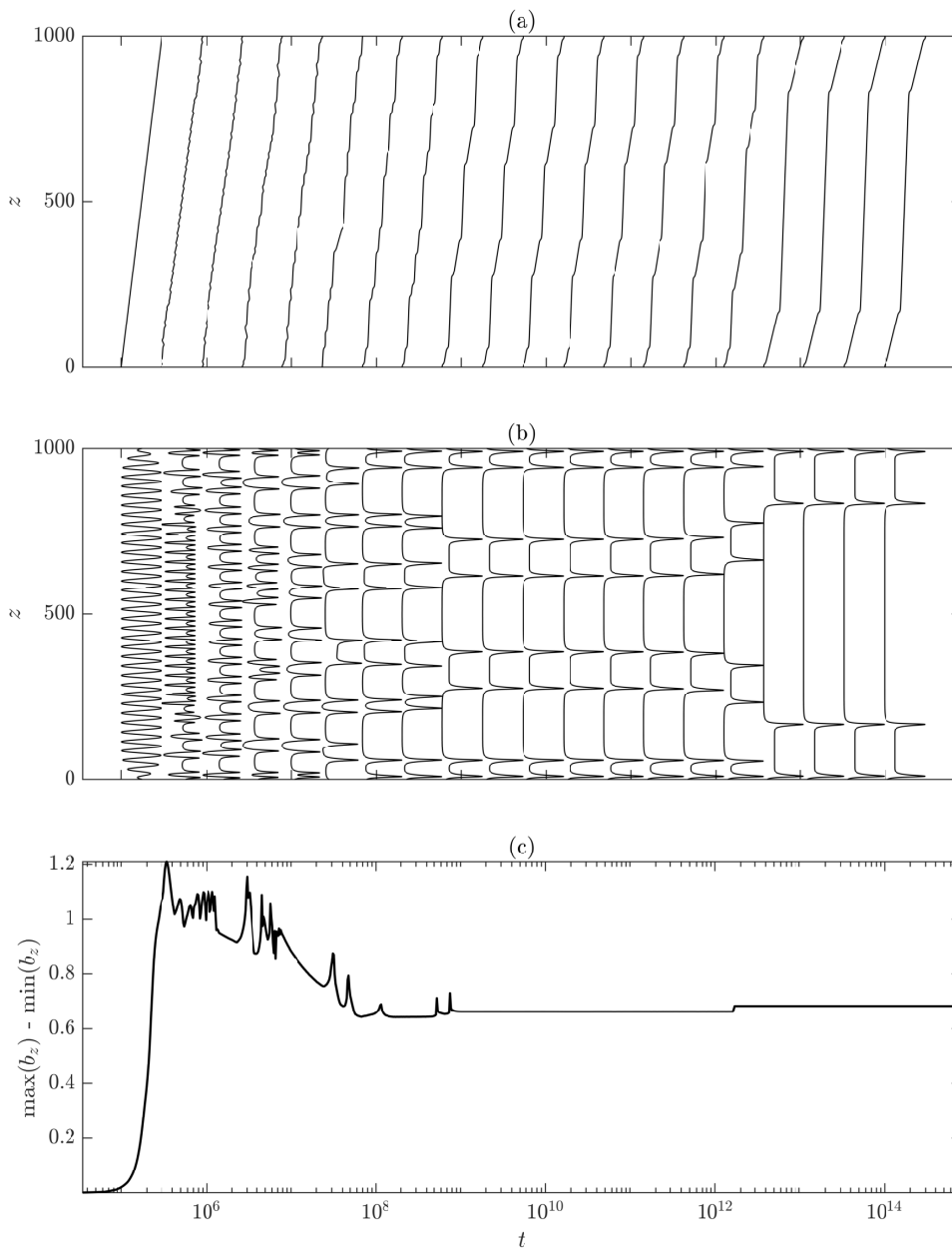


Fig. 8.3 Nonlinear evolution of the system (8.1)–(8.3), with length scale (8.4), subject to boundary conditions (7.27)–(7.29) and initial conditions (7.30)–(7.32), for parameter values $R_0 = 0.9$, $\tau = 0.01$, $\sigma = 10$, $\varepsilon = 1$, $\delta = 0.001$ and $W = 1$. (a) Overall buoyancy field $b = T - S$; (b) buoyancy gradient $b_z = T_z - S_z$ scaled by the range of its values at each time; (c) range of gradients, i.e. $\max(b_z) - \min(b_z)$. The time axes of all panels are aligned. Profiles in (a) and (b) are shown corresponding to the time at which they intersect the time axis. The solution evolves from the initial condition into a dense stack of layers (seen as the first solution presented in (b)). At $t \approx 10^6$, the layers begin to undergo mergers, which cause the maximum gradient to increase, until by $t \approx 10^{13}$ two interfaces remain on the edges of the domain. Interfaces are characterised by two spikes of equal magnitude in the buoyancy gradient b_z , with a lower gradient region in between.

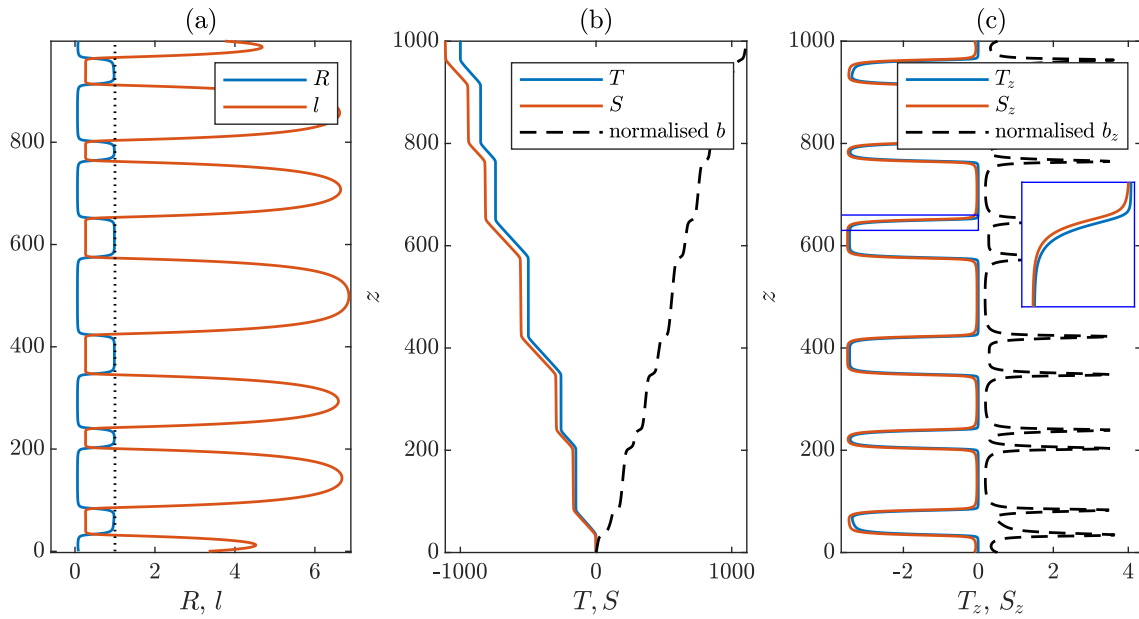


Fig. 8.4 Snapshot of the solution from Fig. 8.3, showing (a) the density ratio R and length scale l ; (b) T , S and b ; and (c) T_z , S_z and b_z at $t = 10^8$. The b and b_z fields have been normalised to have the same scale as S and S_z . The box outlined in blue in (c) shows a larger scale view of the range $630 \leq z \leq 660$.

less well-formed. We see from Fig. 8.4(c) that the interfaces in T and S are smooth but the salinity interfaces are slightly wider than the interfaces in the temperature. As such, when the total buoyancy gradient is calculated, there are two spikes, corresponding to the edges of the interfaces where S_z is much greater than T_z . In the centre of the interface, $T_z \approx S_z$, so b_z is smaller than in the edges of the interface. Note that $|S_z| \geq |T_z|$ everywhere, so the total buoyancy gradient b_z remains positive. That the interfaces in the salt field are wider than in the temperature field is somewhat surprising — previous numerical studies have found interfaces to be sharper in the salt than the temperature field (e.g. Hughes & Brummell, 2021). It has been argued that this is because the molecular diffusivity of temperature is much higher than that of salt, so peaks in the temperature gradient become more spread out (e.g. Wood *et al.*, 2013).

This two-spike interface profile is generic for the entire unstable range of R_0 . Fig. 8.5 shows snapshots of solutions for two different values of R_0 to illustrate this. For $R_0 = 0.8$, Fig. 8.5(a) clearly shows the two-spike structure. In comparison to Fig. 8.4, the spikes are smaller, with the interior of the interface having a larger gradient than the $R_0 = 0.9$ case. Fig. 8.5(b)–(c) show the profile of solutions with $R_0 = 0.6$; (b) shows the whole solution, and (c) a close-up on a single interface. The two-spike profile cannot be seen from the global form in Fig. 8.5(b), in which it appears that interfaces have an approximately rectangular profile. However the close-up view in Fig. 8.5(c) shows that the two-spike profile does still exist, but the gradient in the middle of the interface is almost identical to that in the spikes. In both Figs. 8.5(a) and (b), the interfaces in the salinity gradient appear

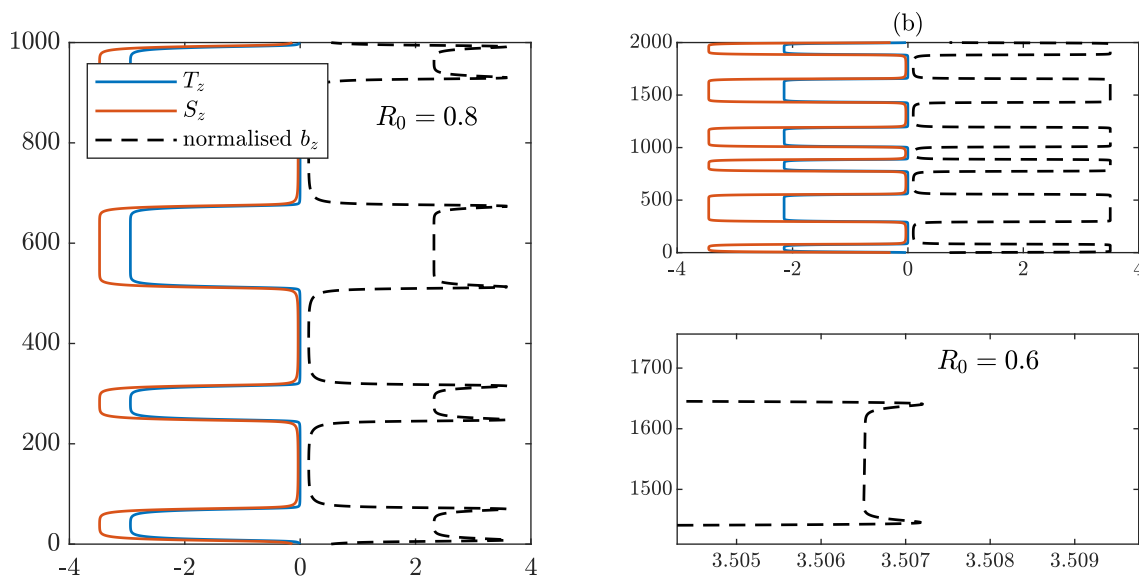


Fig. 8.5 Snapshots of solutions to (8.1)–(8.3) at time $t = 10^{10}$, for (a) $R_0 = 0.8$ and (b,c) $R_0 = 0.6$. T_z , S_z and b_z are plotted, with the buoyancy gradient fields been normalised to have the same scale salinity gradient. (b) and (c) show the same solution, with (c) giving a close-up view of the profile of a single interface.

to be marginally wider than those in the temperature gradient, leading to the two-spike profiles.

The two-spike profile can be explained by noticing that the interfaces in the salinity staircase are wider than those in the temperature staircase. However, this leads to the new question: why are the salt interfaces wider? To answer this, we consider the forms of the temperature and salinity fluxes given by (7.21)–(7.22). When $le^{1/2}$ is large, as in layers, $f/g \approx c/d$. So in layers, temperature and salinity are transported at similar rates. However as $le^{1/2} \rightarrow 0$, $f/g \sim c/\tau d$. Hence in small-length, low-energy interfaces, the ratio of temperature flux to salinity flux is much smaller than in layers. So temperature and salinity are transported at similar rates from the layers and into interfaces, but less temperature is transported through interfaces than salinity. As such, the density ratio in the interfaces R^I is heightened in comparison with the background ratio R_0 . The solutions shown above confirm this, with measured values of $R^I = 0.94, 0.84$ and 0.62 , compared to background values $R_0 = 0.9, 0.8$ and 0.6 in Figs. 8.4, 8.5(a) and 8.5(b) respectively.

Now we have established that $R^I > R_0$ in interfaces, we shall demonstrate why the interfaces in the salinity profile are wider than those in the temperature. For simplicity, we assume a rectangular structure to the temperature and salinity gradient profiles (although a

similar argument to the following may be made with smoother profiles), so that

$$\text{In layers} \begin{cases} T_z = 0, \\ S_z = 0, \\ R = 1. \end{cases} \quad (8.8)$$

$$\text{In interfaces} \begin{cases} T_z = T_z^I, \\ S_z = S_z^I, \\ R = R^I. \end{cases} \quad (8.9)$$

We additionally write h_i^T as the thickness of the i th interface in the temperature, and h_i^S as the thickness of the i th salinity interface, for $i = 1, 2, \dots, N$, where N is the total number of interfaces. Thus, the total temperature and salinity gradients are

$$T(H) - T(0) = \sum_{i=1}^N h_i^T T_z^I, \quad (8.10)$$

$$S(H) - S(0) = \sum_{i=1}^N h_i^S S_z^I. \quad (8.11)$$

By the choice of nondimensionalisation (7.6), the background temperature gradient is fixed as -1 , with background salinity gradient $-1/R_0$. Taking T_z^I and S_z^I to be constants (once again, non-constant profiles are possible), conservation of temperature and salinity requires

$$\sum_{i=1}^N h_i^T = -\frac{H}{T_z^I}, \quad (8.12)$$

$$\sum_{i=1}^N h_i^S = -\frac{H}{R_0 S_z^I} = -\frac{R^I H}{R_0 T_z^I}. \quad (8.13)$$

Recalling that $R^I > R_0$, it follows from (8.12)–(8.13) that

$$\sum_{i=1}^N h_i^T < \sum_{i=1}^N h_i^S, \quad (8.14)$$

i.e. the total width of temperature interfaces must be less than the total width of salinity interfaces. In the numerical solutions shown in Figs. 8.3–8.5, condition (8.14) is satisfied by having $h_i^T < h_i^S$ in every interface, yielding the two-spike profile in the buoyancy gradient.

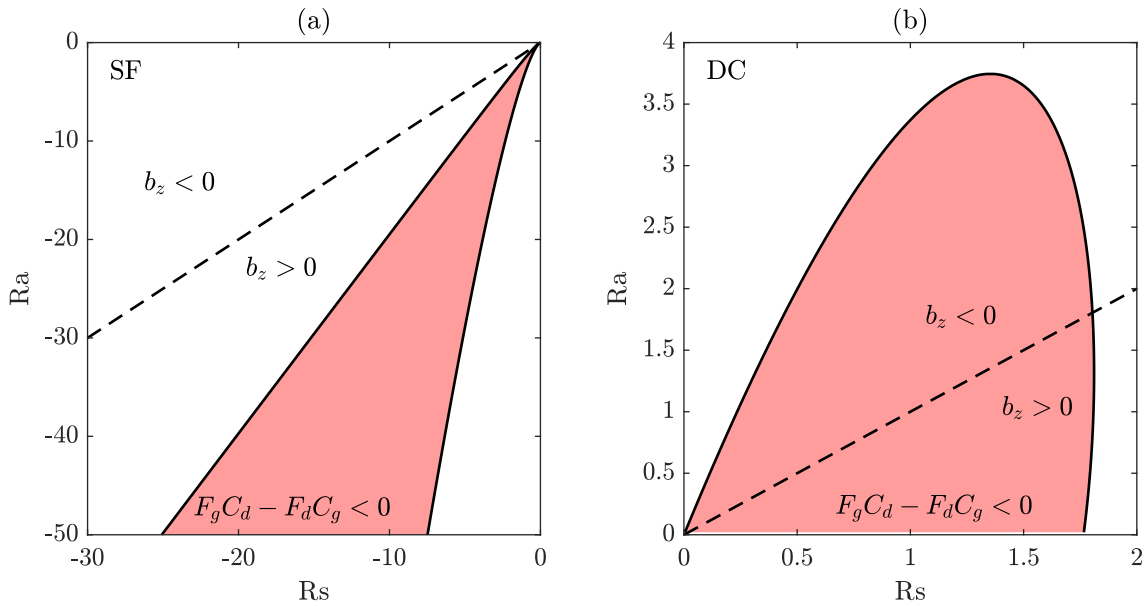


Fig. 8.6 Regions of Ra–Rs space unstable to the layering instability (5.17a), with parameter values $\tau = 0.01$, $\sigma = 10$, $\varepsilon = 1$, $\delta = 0.001$ in (a) the unforced SF system (7.15)–(7.17), and (b) the forced DC system (8.1)–(8.3) with $W = 1$. Dashed lines show $g_0 = d_0$; above these lines the fluid is statically unstable.

8.5 Difference in behaviour between salt fingering and diffusive convection

We have seen that there are significant differences in the solutions of the forced DC system (8.1)–(8.3) and the unforced SF system (7.15)–(7.17). Most notably, in the SF regime, successive mergers led to an increase in the gradient in interfaces, while in the DC regime there is no significant increase in gradient, but the thickness of interfaces increases. Both of these behaviours ensure that the buoyancy jump across the interface is conserved during a merger event. To investigate the cause of this difference, we consider the stability boundaries in Ra–Rs space.

Recall that the system (7.15)–(7.17) was nondimensionalised such that in the background state, the Rayleigh number Ra had unit magnitude, with the salinity Rayleigh number $Rs = Ra/R_0$. In all the analysis so far, we have considered only background states with $g_0 \equiv -Ra = \pm 1$. However, in the nonlinear phase of evolution, $g(z, t)$ is not fixed at ± 1 , and may evolve freely subject to the boundary condition (7.27). Assuming that a locally uniform state $(g_0, d_0, e_0(g_0, d_0))$ exists across some region of the domain, we can extend the stability analyses of sections 7.3 and 8.3.2 to find unstable regions in g_0 – d_0 space. These are shown in Fig. 8.6.

We see from Fig. 8.6 that in the SF regime (a), the unstable region takes the form of a wedge of Ra–Rs space, extending to arbitrarily large values of $|Ra|$ and $|Rs|$. Hence, b_z can attain any value $b_z \in \mathbb{R}^+$ within the unstable region. By comparison, in the DC regime (b), the unstable region is a bounded region with $0 \lesssim Ra \leq 3.7$ and $0 \lesssim Rs \leq 1.8$. With

these constraints on the Rayleigh numbers, the total buoyancy gradient can exist only in the range $-2.5 \lesssim b_z \lesssim 1.8$. So when a merger takes place, the buoyancy gradient cannot increase every time. To ensure total buoyancy conservation, the interface must instead grow in thickness. This reduced range of unstable buoyancy gradients also explains the very small difference between the gradient in interfaces and layers seen in the numerical results of Fig. 8.3.

The picture in the DC regime shown in Fig. 8.6 is a little concerning. As $Ra \rightarrow 0$, the system is unstable to layering for a finite range of Rs . Arguing based on continuity and smoothness, it appears that there may also be an unstable region where $Rs > 0$ and $Ra < 0$ (and hence $R_0 < 0$). This is the doubly stable regime, in which both components of the buoyancy have stable gradients, so instability here is not expected. Of course, we saw in Chapter 6 that stirring produced instability for some parts of the doubly stable regime (cf. Fig. 6.2), so it is possible that the same will happen with the parameterisations used here. However, considering the form of the length scale (8.4), $l < 0$ when $R_0 < 0$, which is clearly not physically valid as a length scale. Naïvely ignoring this problem, and seeking steady-state solutions anyway, we find that there are indeed steady states in the doubly stable regime that are unstable to layering — so the inclusion of an energy source allows instability where none is expected. However, we saw in Sec. 8.3.1 that $l \rightarrow \infty$ as $R \rightarrow 0$. So by continuity, it will not be possible to reach negative values of l in solutions. Hence, the doubly stable regime cannot be reached. This is a limitation of the model, where ideally the same equations would be applicable to all regions of Ra – Rs space. As an aside, if the forced system (8.1)–(8.3) is applied in the salt fingering regime, the results are not significantly different from those presented in Chapter 7. The steady-state solutions are changed, but, as discussed in Sec. 8.3.2, the constant power source does not directly impact the γ -instability.

Furthermore, the shape of the unstable region in Fig. 8.6(b) is unexpected. Whereas in the SF regime, there is a semi-infinite wedge in Ra – Rs space where layering is predicted, the unstable region in the DC regime is fully bounded, and contains only relatively small values of Ra and Rs . Referring to Fig. 1.3, we see that for a basic double-diffusive instability, both Ra and Rs are $O(1000)$ — significantly larger than the $O(1)$ values seen in Fig. 8.6(b).

In summary, while the addition of a constant power source does allow staircases to form in the DC regime, the overall stability picture does not provide a good model for real staircases. This is a useful first step, but leaves work to be done.

8.6 Discussion

In Chapter 7 we presented a model for layering in salt fingering, but showed that it does not have any uniform steady states in the diffusive convection regime. Ma & Peltier (2022) suggested that diffusive staircases are not in fact due to an initial DC instability, but rather

require some external forcing in order to form. By adding a constant power source term to the energy equation, we have adapted the model to produce staircases in the DC regime.

The system is unstable to the γ -instability for a range of values of the density ratio, in both the DC and statically unstable regimes. Solutions follow the characteristic pattern of layers initially forming, then evolving through mergers, gradually reducing the number of layers over time. Mergers follow the H-merger pattern of interfaces drifting and colliding. The interfaces in the salinity field are slightly thicker than those in the temperature field, producing interfaces in the buoyancy field characterised by two sharp spikes either side of a smooth region. We have established that this difference in interface thickness between the two components of buoyancy is due to a difference in the turbulent fluxes, such that the ratio of temperature to salinity flux is much smaller in interfaces than in layers. However, this stands at odds with the results of previous numerical studies, where the small diffusivity ratio τ has produced sharper interfaces in the salt than in the temperature (e.g. Wood *et al.*, 2013; Hughes & Brummell, 2021). In deriving the model (8.1)–(8.3) we neglected the independent molecular diffusion terms in the temperature and salinity equations, assuming that the turbulent fluxes would be significantly more important. It seems likely that this approximation was not valid for these diffusive interfaces, and molecular diffusion should be retained to produce the sharper saline interfaces seen in simulations. In the SF regime (cf. Chapter 7), the neglect of molecular diffusion appears to remain valid, as interfaces are not wide, but sharp, with a single peak.

During a merger, the interface width increases, in contrast with the SF regime where the maximum buoyancy gradient increased. Considering the unstable regions of the whole of Ra – Rs space (i.e., considering locally uniform states, rather than global states across the whole domain, where the temperature gradient is fixed at ± 1 by the nondimensionalisation), we found that the unstable region of the SF quadrant is a semi-infinite wedge, while the unstable region of the DC regime is fully bounded. In the SF regime, temperature and salinity gradients may combine to produce any arbitrary value for the buoyancy gradient; in the DC regime, only a finite range of buoyancy gradients is available. As such, when two interfaces merge, the new single interface cannot increase in gradient beyond a certain level, so the interface instead must thicken to ensure buoyancy conservation.

In this chapter, we included an energy source in the model (8.1)–(8.4). However, numerical studies of layering in the diffusive regime have shown that no such source term is necessary, with staircases forming in solutions to the unforced Boussinesq equations (Rosenblum *et al.*, 2011; Mirouh *et al.*, 2012). For the system to develop layers, an initial diffusive convective state is needed, which cannot exist in our model without some forcing. We have adopted a constant power source term, which allows uniform-gradient diffusive convection states to exist in the turbulent model, while having no effect on the linear stability of these states. As in the SF regime (cf. Chapter 7), staircase formation occurs via the γ -instability, in contrast with the proposal of Ma & Peltier (2022) that the layering instability itself requires forcing in the DC regime.

We have now presented two different three-component systems with energy sources to model staircases in diffusive convection. The first, in Chapter 6, relied on the BLY forms for the length scale and source term. These parameterisations were designed specifically to describe the dynamics of a stirred system, and were based on characteristic scales derived from the stirring motion. By contrast, the model in this chapter used the length scale parameterised in terms of the density ratio, with scales based on double-diffusive physics. The constant power source term here was chosen as the simplest possible form, and has no effect on the system's stability beyond enabling the existence of basic diffusive convection states. The first model (Chapter 6) can be considered a stirred model with some possibility for double-diffusion, while the second (Chapter 8) is a double-diffusive model, with an energy source added to 'help'. In solutions to the model in Chapter 6, the temperature and salinity fields evolved identically as a single buoyancy field; in the double-diffusive model presented here, the two components of buoyancy evolve independently to create true double-diffusive staircases.

To summarise, the model presented in this chapter is an extension of that presented in Chapter 7 for salt fingers, extended to model the diffusive regime. The system (8.1)–(8.3) represents the minimum change to the salt fingering model that is required for staircase solutions to exist. However, the results in this chapter cannot be viewed as conclusive, and have some serious shortcomings that must be acknowledged.

First, the numerical solutions show interfaces in the salinity field to be wider than in the temperature, where simulations and observations in fact show the opposite, with salinity interfaces being sharper. In the derivation of the model, we ignored the additional molecular diffusion terms (i.e., T_{zz} and τS_{zz} on the right hand sides of (8.1) and (8.2) respectively), as they were considered to have a significantly smaller contribution than the flux terms. This assumption was appropriate in the SF regime, and produced solutions with a good resemblance to real staircases. It has been suggested that the differences in molecular diffusivity is the key factor driving the different interface thicknesses in the two components of density, so neglecting these diffusive terms has resulted in incorrect predictions. To develop a more physically relevant model, the obvious first step is to retain these molecular diffusion terms. In this case, the form of the length scale (8.4) may need to be reconsidered; it was developed for the particular fluxes in (8.1)–(8.2), so may not necessarily produce the same behaviour if the diffusive terms are retained.

Another obvious issue is the unstable regions shown in Fig. 8.6(b). The figure shows instability only for a very small range of $O(1)$ values of Ra and Rs . In reality, the values of the Rayleigh numbers for the basic diffusive convective instability are $O(1000)$ (cf. Fig. 1.3). With a more detailed investigation of parameter space (i.e. ε , δ) it may be possible to produce more realistic results. In addition, it is concerning that the system is unstable as $Ra \rightarrow 0$. By continuity, it appears that there may also be a layering instability when $Ra < 0$ and $Rs > 0$, i.e. the doubly stable regime, where no instability should be exist. It seems most likely that this problem stems from the inclusion of forcing, with the

constant power source term allowing diffusive convective states to exist where none are expected, which can then become unstable by the same layering instability.

With these limitations in mind, the results presented in this chapter should be seen as an interesting extension of our salt fingering model, and an investigation into the limits of its applicability, rather than as a serious physical prediction. There is certainly room for future work on this style of model for diffusive layering. By reconsidering the assumptions in the model, and retaining the molecular diffusion terms, it seems likely that a more accurate model can be developed, with the potential for making physically relevant predictions. As discussed in Chapter 7, the prescription for the length scale (7.18) is not the only possible option, so the model could be tuned further by investigating different forms for the length scale.

A further alteration to the model could be through reconsidering the form of stirring. While the constant power form used in this chapter has advantages as the minimum forcing necessary, individual physical situations could be modelled with more specific forcing terms. As an example, recent measurements have shown the existence of DC staircases in river outflows in the Caribbean, strongly forced by diurnal heating (Taylor, 2022, personal correspondence). By forcing instead with a time and depth-dependant heat source, the model could be adapted to produce a more realistic representation of this physical scenario.

Chapter 9

Conclusions

Summary

From stratified layers in a laboratory tank, to thermocompositional layers in the interiors of stars, the dynamics of staircases represent a challenge to mathematicians with far reaching effects across different areas of physics. In a geophysical context, understanding the conditions under which double-diffusive staircases form, and the transport properties through them, has important consequences for climate modelling. In the Arctic, accurate parameterisations of the ocean-ice heat flux are important in determining the fate of polar ice cover, so knowing accurately where diffusive staircases can be found, and how much heat is transported through them will play an important part (e.g. Stranne *et al.*, 2017). In general, as a changing climate alters oceanic salt and heat distributions, changes in double-diffusive fluxes have the potential to destabilise existing oceanic circulation (e.g. van der Boog *et al.*, 2021). Likewise, $\mathbf{E} \times \mathbf{B}$ staircases form transport barriers, and are thus important in the context of plasma confinement—a key problem for nuclear fusion (e.g. Dif-Pradalier *et al.*, 2010). Between producing better climate models and helping to make fusion power viable, staircase physics has the potential to play a large role in adaption to the climate crisis in the coming years.

In this thesis we have made developments in two areas: stirred stratified convection, and double-diffusive convection. In Chapter 2, we presented a spatial averaging process to develop one-dimensional models for density staircases from the Boussinesq equations. In subsequent chapters, we applied this model to different contexts by varying the parameterisation of a turbulent mixing length. Our model relies on the related phenomena of the Phillips effect and γ -instability, in which parameterisations of density fluxes produce a negative turbulent diffusivity, leading to sharpening of the density profile, and eventually to the formation of layers.

In Chapter 3, we investigated stirred stratified convection, using a mixing length that interpolates between a scale based on the stirring motion, and the emergent Ozmidov length based on the stratification, and including an explicit forcing term in the equations. We investigated the influence of boundary conditions on staircase solutions. In particular,

we found that certain choices allow investigation of the behaviour of staircases to very long times. We showed that the inclusion of molecular and viscous diffusion acts to suppress the instability that leads to layering. Staircase solutions evolve by layer mergers, in which adjacent layers combine into one. We showed that these mergers happen on a logarithmic timescale, which is consistent with other models of layering.

In Chapter 4, we presented an experimental study to test a prediction of Chapter 3, namely that the system is unstable to layering for only a finite range of Richardson number. Equipment constraints allowed us to access only a small region of parameter space, in which our results are consistent with the hypothesis. However, further experimental work for a wider range of parameters is necessary to confirm and extend our results, and to produce a more quantitative study.

To tackle the problem of double-diffusive layering, it is necessary to consider the two components of density (temperature and salinity) separately. As such, a two-component model such as that used in Chapter 3 (for buoyancy and energy) is not sufficient, and a third equation must be added. In Chapter 5 we presented a linear stability analysis of a general three-component system of equations, finding conditions for the equivalent of the Phillips instability. We showed that the ‘ γ -instability’ based on the ratio of fluxes, and the Phillips instability, are mathematically equivalent, with the physical difference being the energy source driving the instability. While the Phillips instability relies on some large scale stirring or energy production, the γ -instability is driven by the release of potential energy from the background temperature and salinity fields. We also found that a high-wavenumber instability can occur in a three-component system, and demonstrated how it can be regularised by the inclusion of hyperdiffusion terms.

In Chapter 6, we applied the analysis of Chapter 5 to a three-component model with stirring retained. By retaining a stirring term, while adding an extra equation for a second component of density, we hoped to produce a ‘halfway house’ between the externally forced and double-diffusive problems. However, when solved numerically, this model produces solutions almost identical to those in the stirred case with a single component of buoyancy, with temperature and salinity fields evolving as a single buoyancy field. The dynamics are dominated by the stirring, with double-diffusion playing a much smaller role.

To produce a true model for double-diffusive staircases, we removed the forcing term entirely. Previously, the mixing-length had been parameterised based on assumptions about the stirring behaviour. In Chapter 7, we presented a new choice of length scale appropriate for double-diffusive physics. This new length allows for the release of potential energy from the background density fields to drive the γ instability so that staircases can form. The inclusion of an energy equation regularises the system, avoiding the high wavenumber instability found in models of temperature and salinity alone. Numerical solutions in the salt fingering regime show the evolution of staircases via mergers. We demonstrated that each merger increases the buoyancy flux through the staircase, thus explaining the heightened fluxes found in observed staircases compared to non-layered regions.

We found that the model presented in Chapter 7 did not produce staircase solutions in the diffusive convection regime. Previous work has suggested that the layering instability in the DC regime is not in fact the result of a basic double-diffusive instability, but requires something else to drive it, for example a background shear flow. In Chapter 8 we showed that introducing a simple constant-power forcing term does produce staircase structures in DC. These DC staircases appear quite different to the SF staircases of Chapter 7, with interfaces becoming wider, rather than sharper with successive mergers, owing to differences in the unstable regions of parameter space.

Outlook

There is significant potential for future research to build on the results presented in this thesis. One particular direction to take is an extension of the experiments of Chapter 4 to a fuller study, to demonstrate more conclusively the existence of an upper limit on the Richardson number for staircase formation. Two simple ways to access new parameter spaces are by changing the geometry, and hence the characteristic scales, and by changing the solute, allowing a wider range of densities. Another improvement would be to take quantitative measurements of the fluid density, potentially allowing finer structures to be seen than are visible in the shadowgraph images.

Another important direction for further study is a comparison of the models presented here with direct numerical simulations. In the salt fingering model, there are two physical parameters (σ and τ), which are set by the fluid, and two free parameters (ε and δ). By comparison with simulations and observations, these free parameters may be calibrated to produce more quantitative results, enabling more accurate predictions to be made for real staircase structures.

The study of diffusive convection in Chapter 8 produced results with some worrying characteristics. Most notably, the interfaces in the salinity field are wider than those in the temperature field, which is contrary to what is observed in real oceanic staircases. To improve this model and produce more realistic results, some of the assumptions in the derivation of the model should be reconsidered. Specifically, when developing the salt fingering model, we neglected the molecular diffusive terms in the temperature and salinity equations, assuming that the contribution from diffusion would be of secondary importance in comparison to the turbulent fluxes. However, the difference in molecular diffusion is suggested as the key factor influencing the different thickness of salt and temperature interfaces, so to reproduce this characteristic, these terms should be retained in the model. To further develop the DC model, an obvious step is to focus on the forcing term. The constant-power forcing was chosen as a minimal addition to the SF model to allow it to produce staircase solutions in the DC regime, and an extended investigation should consider a different way of forcing the fluid. As an example, some oceanic systems may be strongly forced by diurnal heating (for example in river outflows, where cold, fresh water is flowing above warmer, salty water). This could be represented in the equations by a

time- and space-dependent forcing in the temperature equation, rather than a direct kinetic energy source.

More generally, the stability analysis of Chapter 5 and the model of Chapter 7 could be used to inform the study of layering in other systems. For example, several models of layering in other contexts rely on arbitrary forcing terms to drive the layering instability. Our work on salt fingering staircases has shown that such forcing is not necessary for the formation of layers, and so our choice of length scale could be used to inform parameterisations in other models.

An ultimate goal would be the creation of a ‘grand unified model’ for layering that could be applicable in several different contexts. One promising direction could be to construct a model that makes use of available potential energy (the fraction of potential energy that may be converted to kinetic energy). Instead of a model based on density fields, or potential vorticity, a system written only in terms of energy could be applied across all contexts. A range of physical setups could be modelled with a single set of equations, allowing their behaviours to be compared, and knowledge from one area to be applied to others. With large numbers of researchers working on staircase physics from a wide range of areas, the future looks bright for new developments in the field.

Bibliography

- ASHOURVAN, A. & DIAMOND, P. H. 2016 How mesoscopic staircases condense to macroscopic barriers in confined plasma turbulence. *Phys. Rev. E* **94**, 051202.
- ASHOURVAN, A. & DIAMOND, P. H. 2017 On the emergence of macroscopic transport barriers from staircase structures. *Phys. Plasmas* **24**, 012305.
- BALMFORTH, N. J., LLEWELLYN SMITH, S. G. & YOUNG, W. R. 1998 Dynamics of interfaces and layers in a stratified turbulent fluid. *J. Fluid Mech.* **355**, 329–358.
- BALMFORTH, N. J. & YOUNG, Y.-N. 2005 Stratified Kolmogorov flow. Part 2. *J. Fluid Mech.* **528**, 23–42.
- BARENBLATT, G. I., BERTSCH, M., DAL PASSO, R., PROSTOKISHIN, V. M. & UGHI, M. 1993 A mathematical model of turbulent heat and mass transfer in stably stratified shear flow. *J. Fluid Mech.* **253**, 341–358.
- BEBIEVA, Y. & TIMMERMANS, M.-L. 2017 The relationship between double-diffusive intrusions and staircases in the arctic ocean. *J. Phys. Oceanogr* **47** (4), 867 – 878.
- VAN DER BOOG, C. G., DIJKSTRA, H. A., PIETRZAK, J. D. & KATSMAN, C. A. 2021 Double-diffusive mixing makes a small contribution to the global ocean circulation. *Comm. Earth Environ.* **2** (1), 46.
- BROWN, J. M. & RADKO, T. 2019 Initiation of diffusive layering by time-dependent shear. *J. Fluid Mech.* **858**, 588–608.
- COCLITE, G., PAPARELLA, F. & PELLEGRINO, S. 2018 On a salt fingers model. *Nonlinear Analysis* **176**, 100 – 116.
- DIF-PRADALIER, G., DIAMOND, P. H., GRANDGIRARD, V., SARAZIN, Y., ABITEBOUL, J., GARBET, X., GHENDRIH, P., STRUGAREK, A., KU, S. & CHANG, C. S. 2010 On the validity of the local diffusive paradigm in turbulent plasma transport. *Phys. Rev. E* **82**, 025401.
- DIF-PRADALIER, G., HORNUNG, G., GHENDRIH, P., SARAZIN, Y., CLAIRET, F., VERMARE, L., DIAMOND, P. H., ABITEBOUL, J., CARTIER-MICHAUD, T., EHRLACHER, C., ESTÈVE, D., GARBET, X., GRANDGIRARD, V., GÜRCAN, O. D., HENNEQUIN, P., KOSUGA, Y., LATU, G., MAGET, P., MOREL, P., NORSCINI, C., SABOT, R. & STORELLI, A. 2015 Finding the elusive $\mathbf{E} \times \mathbf{B}$ staircase in magnetized plasmas. *Phys. Rev. Lett.* **114**, 085004.
- DRITSCHEL, D. G. & MCINTYRE, M. E. 2008 Multiple jets as PV staircases: the Phillips effect and the resilience of eddy-transport barriers. *J. Atmos. Sci* **65**, 855–874.
- FRAERMAN, A., MEL'NIKOV, A., NEFEDOV, I., SHERESHEVSKII, I. & SHPIRO, A. 1997 Nonlinear relaxation dynamics in decomposing alloys: One-dimensional Cahn-Hilliard model. *Phys. Rev. B* **55**, 6316.

- GARAUD, P. 2018 Double-diffusive convection at low Prandtl number. *Ann. Rev. Fluid Mech.* **50**, 275–298.
- GUO, W., DIAMOND, P. H., HUGHES, D. W., WANG, L. & ASHOURVAN, A. 2019 Scale selection and feedback loops for patterns in drift wave-zonal flow turbulence. *Plasma Phys. Control. Fusion* **61**, 105002.
- HAYNES, P. & SHUCKBURGH, E. 2000 Effective diffusivity as a diagnostic of atmospheric transport: 1. stratosphere. *J. Geophys. Res. Atmos.* **105** (D18), 22777–22794.
- HOLFORD, J. M. & LINDEN, P. 1999a The development of layers in a stratified fluid. In *Inst. Math. Appl. Conference Series*, vol. 68, pp. 165–180. Oxford University Press.
- HOLFORD, J. M. & LINDEN, P. 1999b Turbulent mixing in a stratified fluid. *Dyn. Atmospheres Oceans* **30** (2-4), 173–198.
- HUGHES, D. W. & BRUMMELL, N. H. 2021 Double-diffusive magnetic layering. *Astrophys. J.* **922**, 195.
- HUPPERT, H. E. & LINDEN, P. F. 1979 On heating a stable salinity gradient from below. *J. Fluid Mech.* **95**, 431–464.
- JONES, W. P. & LAUNDER, B. E. 1972 The prediction of laminarization with a two-equation model of turbulence. *Int. J. Heat Mass Transf.* **15**, 301–314.
- KAWAKATSU, T. & MUNAKATA, T. 1985 Kink dynamics in a one-dimensional conserved TDGL system. *Prog. Theor. Phys.* **74**, 11–19.
- KIMURA, S., SMYTH, W. & KUNZE, E. 2011 Turbulence in a sheared, salt-fingering-favorable environment: Anisotropy and effective diffusivities. *J. Phys. Oceanogr.* **41** (6), 1144–1159.
- KOSUGA, Y., DIAMOND, P. H. & GÜRCAN, Ö. D. 2013 How the propagation of heat-flux modulations triggers $\mathbf{E} \times \mathbf{B}$ flow pattern formation. *Phys. Rev. Letters* **110**, 105002.
- LINDEN, P. F. 1979 Mixing in stratified fluids. *Geophys. Astrophys. Fluid Dyn* **13**, 3–23.
- MA, Y. & PELTIER, W. R. 2022 Thermohaline staircase formation in the diffusive convection regime: a theory based upon stratified turbulence asymptotics. *J. Fluid Mech.* **931**.
- MALKOV, M. A. & DIAMOND, P. H. 2019 Dynamics of potential vorticity staircase evolution and step mergers in a reduced model of beta-plane turbulence. *Phys. Rev. Fluids* **4**, 044503.
- MANUCHARYAN, G. & CAULFIELD, C. 2015 Entrainment and mixed layer dynamics of a surface-stress-driven stratified fluid. *J. Fluid Mech.* **765**, 653–667.
- MARCUS, P. S. 1993 Jupiter’s Great Red Spot and other vortices. *Ann. Rev. Astron. Astrophys.* **31**, 523–573.
- MCDUGALL, T. J. & TAYLOR, J. R. 1984 Flux measurements across a finger interface at low values of the stability ratio. *J. Mar. Res.* **42** (1), 1–14.
- MERRYFIELD, W. J. 2000 Origin of thermohaline staircases. *J. Phys. Oceanogr.* **30**, 1046–1068.

- MIROUH, G. M., GARAUD, P., STELLMACH, S., TRAXLER, A. L. & WOOD, T. S. 2012 A new model for mixing by double-diffusive convection (semi-convection). i. the conditions for layer formation. *Astroph. J.* **750** (1), 61.
- NAGAI, T. & KAWASAKI, K. 1983 Molecular dynamics of interacting kinks. I. *Physica A* **120**, 587–599.
- NAYAR, K. G., SHARQAWY, M. H., BANCHIK, L. D. & OTHERS 2016 Thermophysical properties of seawater: a review and new correlations that include pressure dependence. *Desalination* **390**, 1–24.
- NEAL, V. T., NESHYBA, S. & DENNER, W. 1969 Thermal stratification in the arctic ocean. *Science* **166**, 373–374.
- OGLETHORPE, R., CAULFIELD, C. & WOODS, A. W. 2013 Spontaneous layering in stratified turbulent Taylor–Couette flow. *J. Fluid Mech.* **721**, R3.
- OSTER, G. 1965 Density gradients. *Sci. Am.* **213** (2), 70–79.
- OZMIDOV, R. V. 1965 On the turbulent exchange in a stably stratified ocean. *Izv. Acad. Sci. USSR. Atmos. Oceanic Phys.* **1**, 861–871.
- PAPARELLA, F. & VON HARDENBERG, J. 2014 A model for staircase formation in fingering convection. *Acta Appl. Math.* **132**, 457–467.
- PAPARELLA, F. & VON HARDENBERG, J. 2012 Clustering of salt fingers in double-diffusive convection leads to staircaselike stratification. *Phys. Rev. Lett.* **109**, 014502.
- PARK, Y., WHITEHEAD, J. A. & GNANADESKIAN, A. 1994 Turbulent mixing in stratified fluids: layer formation and energetics. *J. Fluid Mech.* **279**, 279–311.
- PHILLIPS, O. M. 1972 Turbulence in a strongly stratified fluid—is it unstable? *Deep Sea Res.* **19**, 79–81.
- POSMENTIER, E. S. 1977 The generation of salinity finestructure by vertical diffusion. *J. Phys. Oceanogr.* **7**, 298–300.
- RADKO, T. 2003 A mechanism for layer formation in a double-diffusive fluid. *J. Fluid Mech.* **497**, 365–380.
- RADKO, T. 2007 Mechanics of merging events for a series of layers in a stratified turbulent fluid. *J. Fluid Mech.* **577**, 251–273.
- RADKO, T. 2013 *Double-Diffusive Convection*. Cambridge University Press.
- RADKO, T. 2016 Thermohaline layering in dynamically and diffusively stable shear flows. *J. Fluid Mech.* **805**, 147–170.
- RADKO, T. 2019a Thermohaline layering on the microscale. *J. Fluid. Mech* **862**, 672–695.
- RADKO, T. 2019b Thermohaline-shear instability. *Geophys. Res. Lett.* **46** (2), 822–832.
- RAMSING, N. & GUNDERSON, J. 2020 Unisense seawater and gases table. <https://unisense.com/wp-content/uploads/2021/10/Seawater-Gases-table.pdf>.
- LORD RAYLEIGH 1916 On convection currents in a horizontal layer of fluid, when the higher temperature is on the under side. *Lond. Edinb. Dublin Philos. Mag. J. Sci.* **32** (192), 529–546.

- ROSENBLUM, E., GARAUD, P., TRAXLER, A. & STELLMACH, S. 2011 Turbulent mixing and layer formation in double-diffusive convection: three-dimensional numerical simulations and theory. *Astrophys. J.* **731**, 66.
- RUDDICK, B. R., MCDUGALL, T. J. & TURNER, J. S. 1989 The formation of layers in a uniformly stirred density gradient. *Deep Sea Res. A* **36**, 597–609.
- SCHMITT, R., PERKINS, H., BOYD, J. & STALCUP, M. 1987 C-salt: An investigation of the thermohaline staircase in the western tropical North Atlantic. *Deep Sea Research Part A. Oceanographic Research Papers* **34** (10), 1655–1665.
- SCHMITT, R. W. 1994 Double diffusion in oceanography. *Annu. Rev. Fluid Mech* **26**, 255–285.
- SHARQAWY, M. H., LIENHARD, J. H. & ZUBAIR, S. M. 2010 Thermophysical properties of seawater: a review of existing correlations and data. *Desalination Water Treat.* **16**, 354–380.
- SOMMERIA, J., MEYERS, S. D. & SWINNEY, H. L. 1989 Laboratory model of a planetary eastward jet. *Nature* **337**, 58–61.
- STELLMACH, S., TRAXLER, A., GARAUD, P., BRUMMELL, N. & RADKO, T. 2011 Dynamics of fingering convection. Part 2. The formation of thermohaline staircases. *J. Fluid Mech.* **677**, 554–571.
- STERN, M. E. 1960 The “salt-fountain” and thermohaline convection. *Tellus* **12**, 172–175.
- STERN, M. E. 1969 Collective instability of salt fingers. *J. Fluid Mech.* **35**, 209–218.
- STERN, M. E. & TURNER, J. S. 1969 Salt fingers and convecting layers. *Deep Sea Res.* **16**, 497 – 511.
- STRANNE, C., MAYER, L., WEBER, T. C., RUDDICK, B. R., JAKOBSSON, M., JERRAM, K., WEIDNER, E., NILSSON, J. & GÄRDFELDT, K. 2017 Acoustic mapping of thermohaline staircases in the arctic ocean. *Sci. Rep.* **7** (1), 15192.
- TAIT, R. & HOWE, M. 1968 Some observations of thermo-haline stratification in the deep ocean. *Deep Sea Res.* **15**, 275 – 280.
- TIMMERMANS, M. L., TOOLE, J., PROSHUTINSKY, A., KRISHFIELD, R. & PLUEDDEMANN, A. 2008 Eddies in the Canada Basin, Arctic Ocean, observed from ice-tethered profilers. *J. Phys. Oceanogr.* **38**, 133.
- TRAXLER, A., GARAUD, P. & STELLMACH, S. 2011 Numerically determined transport laws for fingering (“thermohaline”) convection in astrophysics. *Astrophys. J.* **728**, L29.
- TURNER, J. 1967 Salt fingers across a density interface. *Deep Sea Res.* **14** (5), 599–611.
- TURNER, J. S. 1973 *Buoyancy Effects in Fluids*. Cambridge University Press.
- TURNER, J. S. & STOMMEL, H. 1964 A new case of convection in the presence of combined vertical salinity and temperature gradients. *Proc. Natl. Acad. Sci.* **52**, 49–53.
- VERONIS, G. 1965 On finite amplitude instability in thermohaline convection. *J. Mar. Res* **23**, 1–17.
- PRUŽINA, P., HUGHES, D. W. & PEGLER, S. S. 2022 Development and long-term evolution of density staircases in stirred stratified turbulence. *Phys. Rev. Fluids* **7**, 104801.

- PRUŽINA, P., HUGHES, D. W. & PEGLER, S. S. 2023 Salt fingering staircases and the three-component phillips effect. *Journal of Fluid Mechanics* **968**, A16.
- WATSON, S. J., OTTO, F., RUBINSTEIN, B. Y. & DAVIS, S. H. 2003 Coarsening dynamics of the convective Cahn-Hilliard equation. *Physica D* **178**, 127–148.
- WOOD, T. S., GARAUD, P. & STELLMACH, S. 2013 A new model for mixing by double-diffusive convection (semi-convection). II. The transport of heat and composition through layers. *Astroph. J.* **768** (2), 157.
- ZATSEPIN, A., DIKAREV, S., POYARKOV, S., SHEREMET, N., DMITRENKO, I., GOLOVIN, P. & KASSENS, H. 1999 Step-like vertical structure formation due to turbulent mixing of initially continuous density gradients. In *Land-Ocean Systems in the Siberian Arctic*, pp. 93–99. Springer.
- ZHURBAS, V. M. & OZMIDOV, R. V. 1984 Step-like structure forms of the oceanic thermocline and their generation mechanisms. *Okeanologiya* **24**, 197–203.